Kinetic Studies of the Gas Phase CH_2OO Criegee Intermediate Relevant to Atmospheric Chemistry Using Time-Resolved UV and IR Absorption Spectroscopy

Zara Sultana Mir

Submitted in accordance with the requirements for the degree of Doctor of Philosophy

The University of Leeds
School of Chemistry

June 2021

Contributions to Published Work

The candidate confirms that the work submitted is her own, except where work which has formed part of jointly-authored publications has been included. The contribution of the candidate and the other authors to this work has been explicitly indicated below. The candidate confirms that appropriate credit has been given within the thesis where reference has been made to the work of others.

Chapters 4 and 5 of this thesis include work which has appeared in the publication:

> Mir, Z. S.; Lewis, T. R.; Onel, L.; Blitz, M. A.; Seakins, P. W.; Stone, D., CH_2OO Criegee intermediate UV absorption cross-sections and kinetics of CH_2OO + CH_2OO and CH_2OO + I as a function of pressure. *Physical Chemistry Chemical Physics* **2020**, *22* (17), 9448-9459

My role in this publication was that I carried out all experiments, processed the raw data and carried out all the data analysis.

Chapter 6 of this thesis includes work forming the basis of a paper in preparation:

> Mir, Z. S.; Jamieson, M.; Greenall, N. R.; Seakins, P. W.; Blitz, M. A.; Stone, D., Identification, monitoring, and reaction kinetics of reactive trace species using time-resolved mid-infrared quantum cascade laser absorption spectroscopy: Development, characterisation, and initial results. **In Production**

My role in this work was that I carried out all experiments, processed the raw data and carried out all the data analysis.

Work which is not the subject of this thesis, however, contributed to the publication:

> Howes, N. U. M.; Mir, Z. S.; Blitz, M. A.; Hardman, S.; Lewis, T. R.; Stone, D.; Seakins, P. W., Kinetic studies of C_1 and C_2 Criegee intermediates with SO_2 using laser flash photolysis coupled with photoionization mass spectrometry and time resolved UV absorption spectroscopy. *Physical Chemistry Chemical Physics* **2018**, *20* (34), 22218-22227

My role in this publication was that I carried out the experiments, processed the raw data and carried out the data analysis for the work using time resolved UV absorption spectroscopy.

Acknowledgements

بِسْمِ اللَّهِ الرَّحْمَٰنِ الرَّحِيمِ ۝ الْحَمْدُ لِلَّهِ رَبِّ الْعَالَمِينَ ۝

Qu'ran [1:1-2]

In the name of Allah, the most beneficent, the most merciful.
All praise and thanks are for Allah, Lord of the worlds.
First and foremost, through it all, Allah has always been with me, and it is only by His will that I have come this far.

There are also a number of people who are owed a thank you for their contribution in getting me to this point. Without the constant encouragement, patience and support of these select few individuals, this PhD would not have been possible.

The first people I would like to express my gratitude to are my supervisors Doctor Daniel Stone and Professor Paul Seakins, for giving me the opportunity to be part of such an amazing research group, and for their help and support over the course of this PhD. I owe a huge thanks to my primary supervisor Dan in particular, for the infinite patience, invaluable advice and constant words of reassurance he has provided throughout this research project. I am immensely grateful for his positive attitude from which I have learned and benefitted greatly. I would also like to thank Dr Mark Blitz for all his help in the lab and his seemingly endless knowledge of all things related to instrumental physical chemistry.

Next I would like to thank all my friends. A big thank you to the wonderful friends I have made during my time in Leeds, in particular those in the Dainton lab and members of the Seakins, Stone and Heard research groups, both past and present. Thank you to the great friends I was fortunate enough to have met during my policy internship at the Parliamentary Office of Science and Technology. Also, thank you to all my incredible friends outside of academia, whose support, encouragement and advice over the years has meant a lot and continues to be appreciated.

Finally, I would like to thank my family who have always been tremendous in their love, support and belief in me. I am indebted to them for their endless wisdom, guidance and duas. Particular thanks are owed to my mother, for her kind and understanding nature, and to my sister, for all that she does for me. To my father, thank you for everything, and this one is for you. I hope I've made you proud.

Abstract

The chemistry of Criegee intermediates, produced in the atmosphere *via* oxidation of unsaturated volatile organic compounds by ozone, has potentially important impacts on atmospheric composition and thus on air quality and climate. In recent years, there have been significant advances in our understanding of the properties and chemistry of Criegee intermediates following the advent of photolytic sources for use in laboratory experiments. Since the discovery of this photolytic production method of Criegee intermediates, various methods have been employed for their detection, which have yielded vast information on Criegee spectra and the kinetics of Criegee reactions with other atmospheric species. However, discrepancies persist in Criegee intermediate spectra, rate coefficients of Criegee intermediate reactions and also in product yields.

In this work, the UV absorption cross-sections of the simplest Criegee intermediate CH_2OO, and kinetics of the CH_2OO self-reaction and the reaction of CH_2OO with I are reported as a function of pressure. Measurements were made at 298 K using 248 nm pulsed laser flash photolysis of $CH_2I_2/O_2/N_2$ gas mixtures coupled with time-resolved broadband UV absorption spectroscopy at pressures between 6 and 300 Torr. Results give a peak absorption cross-section of $(1.37 \pm 0.29) \times 10^{-17}$ cm^2 at ~340 nm and a rate coefficient for the CH_2OO self-reaction of $(8.0 \pm 1.1) \times 10^{-11}$ cm^3 s^{-1}, with no significant pressure dependence of the absorption cross-sections or the self-reaction kinetics over the range investigated. On the contrary, the rate coefficient for the reaction between CH_2OO and I demonstrates pressure dependence over the range investigated, with a Lindemann fit giving $k_0 = (4.4 \pm 1.0) \times 10^{-29}$ cm^6 s^{-1} and $k_\infty = (6.7 \pm 0.6) \times 10^{-11}$ cm^3 s^{-1}. The origins of IO in the system have been investigated, the implications of which are discussed.

Additionally, the $CH_2OO + SO_2$ reaction at room temperature was selected to develop and characterise a robust and economical instrument that can be applied to a wide range of problems in atmospheric chemistry and beyond. The development, characterisation and initial results from the experiment using 266 nm pulsed laser flash photolysis coupled with time-resolved mid-IR quantum cascade laser (QCL) absorption spectroscopy are reported. The IR absorption spectrum of CH_2OO and rate coefficient of the $CH_2OO + SO_2$ reaction with respect CH_2OO loss and SO_3

production are reported at 298 K and pressures in the range 20-100 Torr. Results indicate the CH_2OO spectrum to be in good agreement with that of a previously reported measurement in terms of relative peak heights and positions in the wavenumber region 1285.5917-1286.0605 cm^{-1}, and a rate coefficient for the $CH_2OO + SO_2$ reaction of $(3.8 \pm 0.5) \times 10^{-11}$ cm^3 s^{-1} from both CH_2OO and SO_3 measurements, with no significant pressure dependence over the pressure range investigated. The product yield of SO_3 from the reaction of $CH_2OO + SO_2$ is determined to be independent of pressure over the range investigated, with an SO_3 absorption cross-section of $(5.5 \pm 2.3) \times 10^{-19}$ cm^2 at ~1388.7 cm^{-1}.

Table of Contents

List of Figures

Chapter 1

Chapter 2

Chapter 3

Chapter 4

Chapter 5

List of Tables

Chapter 1

Chapter 2

Chapter 4

Chapter 5

Chapter 6

Chapter 1

Introduction

The study of the Earth's atmosphere and air is one of the oldest realms of science and the ever-changing nature of the atmosphere has been of interest to humans for millennia. Over the last 200 years, it has been recognised that anthropogenic activity, resulting in emissions of trace gases, has led to significant changes in the natural environment and the composition of the Earth's atmosphere and climate. In today's society there exists a global consensus that fossil fuel combustion and emissions of radiatively active species, commonly referred to as greenhouse gases (GHGs), produced by anthropogenic means are causing changes to the Earth's climate and contributing to rising global temperatures and diminishing air quality.[1]

Atmospheric composition is established, controlled and defined by emissions, meteorology and chemistry, meaning changes to atmospheric composition can occur both directly, through the release and movement of pollutants, and indirectly, through the chemical transformation of pollutants, and can potentially result in environmental issues such as ozone depletion, smog formation and climate change. The chemistry occurring can differ vastly depending on which layer of the atmosphere is being investigated i.e. the altitude from the Earth's surface, and chemistry and emissions can vary from region to region e.g. an urban environment such as a busy megacity compared to a remote environment such as a tropical rainforest. Understanding atmospheric chemistry is integral to addressing climate change and issues relating to air quality and human health, along with the accompanying legislative measures and policies which arise from the effort to rectify such issues. An introduction to the Earth's atmosphere and a brief discussion of the chemistry occurring within this atmosphere are provided in this chapter.

1.1 The Earth's Atmosphere and Climate System

The Earth's atmosphere refers to the layer of gases surrounding the Earth. Retained by gravitational interactions with Earth, the atmosphere is perpetually changing due to dynamic processes and chemical reactions. This atmosphere is of fundamental

importance to protecting and sustaining life on Earth as we know it, by creating pressure allowing liquid water to exist on the Earth's surface, absorbing solar radiation warming the surface through heat retention, known as the greenhouse effect which is described in detail below, and reducing temperature extremes between day and night.

Air composition, atmospheric temperature and pressure all vary with altitude, and Earth's atmosphere is often classified into different layers which can be described by their characteristic vertical temperature gradients.[2] While the temperature in the atmosphere varies by a factor of less than two, the pressure changes by six orders of magnitude,[3] however the vertical temperature profile of the atmosphere is more complex than the pressure profile, which essentially decreases exponentially with increasing altitude. Consequently, most of the mass of the atmosphere is found at low altitudes with over 99 % of the mass of the atmosphere residing below 50 km in altitude. The variation in the vertical temperature and pressure profiles of the atmosphere are shown in Figure 1.1.

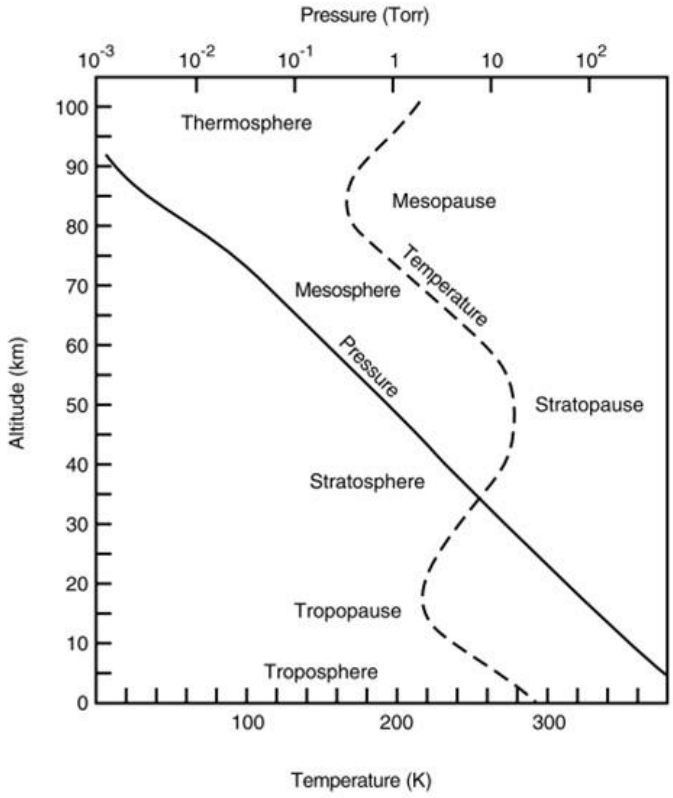

Figure 1.1: Typical variation of the vertical temperature profile and total pressure of the Earth's atmosphere with altitude in the range 0-100 km. Reproduced from reference 2.[2]

The lowest layer of the atmosphere, stretching out from the Earth's surface at 0 km to an altitude of approximately 7 km at the poles and 15 km at the equator and containing 85-90 % of the atmosphere's mass, is known as the troposphere. The gradient of the tropospheric temperature profile is negative as it features a decrease in temperature with increasing altitude since the primary heating source in this region is a result of energy transfer from the Earth's surface, thus the lowest part of the troposphere, i.e. the Earth's surface, is typically the warmest section with an average temperature of approximately 15 °C or 288 K, and as the distance from the source or altitude is increased, the temperature decreases.[2] Rapid vertical movement of gases by convection is promoted in the troposphere due to the negative temperature gradient, meaning that all species within this layer are vertically well mixed, with nearly all atmospheric water vapour (H_2O) or moisture found in this layer making it the region where most of the Earth's weather takes place. The troposphere is often further divided into three layers, namely the Earth's surface layer, the boundary layer and the free troposphere. The boundary layer can extend up to 2 km in altitude and is the region of the atmosphere closest to ground level, i.e. Earth's surface, and is directly affected by it mainly through highly turbulent and fast mixing, hence interactions between the Earth's surface and its atmosphere are greatest here.[3] During the day, the Earth heats the surface layer by thermal conduction (heat transfer *via* direct physical contact i.e. molecular collisions) which mixes with the region above through thermal convection (heat transfer *via* bulk flow of a fluid i.e. mass motion of molecules within a gas or liquid), meaning the boundary layer is well mixed. The free troposphere is the region above the boundary layer where interactions between the surface and atmosphere are less significant, since the change in temperature with altitude, or temperature gradient inversion, above the boundary layer is usually small resulting in slow transfer of species from the boundary layer to the free troposphere, effectively trapping pollutants. During the night, the Earth's surface cools and the boundary layer becomes stably stratified, minimising heat transfer and mixing to only weak or intermittent levels thereby reducing the height of the boundary layer to the surface layer and hence confining pollutants to this region.

The region of the atmosphere above the troposphere is the stratosphere, approximately 15 to 50 km in altitude and separated from the troposphere by the

tropopause. Interactions between the atmosphere and solar radiation lead to a positive temperature gradient in the stratosphere, meaning the temperature increases with increasing altitude, in particular due to absorption of solar ultraviolet (UV) light by atmospheric ozone (O_3),[2] the majority of which is contained within the stratosphere in what is referred to as the ozone layer, which restricts turbulence and mixing.[3] Although the temperature may be -60 °C or 213 K at the tropopause, the top of the stratosphere is much warmer at temperatures typically near 0 °C or 273 K. Located directly above the stratosphere is the mesosphere, extending approximately from 50 to 90 km in altitude within which rapid mixing is also experienced. The mesosphere is bounded below by the stratopause and above by the mesopause, and has a negative temperature gradient with the temperature cooling to approximately -85 °C or 188 K in this region.[3]

Beyond the mesosphere lie the thermosphere and exosphere, the upper-most regions of the Earth's atmosphere at altitudes of 90 to 700 km and 700 to 10,000 km respectively. The air is so rarefied and atoms and/or molecules are so far apart in these layers that they can travel 1 km and hundreds of kilometres in the thermosphere and exosphere respectively before colliding with another species. The temperature in the thermosphere is reliant on solar activity[2] and gradually increases with altitude to as high as 1500 °C or 1773 K, again giving a positive temperature gradient, which is in fact a direct consequence of the low-pressure conditions, since molecular collisions are so infrequent that any absorption of solar radiation by species in this region leads to high translational velocities and high apparent temperatures.[3] However, thermal equilibration between translational, vibrational and rotational modes of species does not occur in the thermosphere given the low number densities present, therefore this layer of the Earth's atmosphere does not store much energy. Due to the lesser still number of collisions between species in the exosphere, this region no longer behaves like a gas and the particles constantly escape into space, i.e. they are free-moving particles. The thermosphere and exosphere are the regions where many of the satellites orbiting the Earth are contained. It should be noted that the majority of the atmospheric chemistry described within this chapter, and indeed this thesis, concerns the chemical transformations occurring predominantly in the planetary boundary layer and the free troposphere.

As well as physical properties such as pressure and temperature, optical properties also vary throughout the atmosphere, such as absorption, emission and scattering of solar radiation. Solar actinic flux, which is measured in quanta s^{-1} cm^{-2} nm^{-1} and varies as a function of altitude i.e. between the bottom and top of the atmosphere as shown in Figure 1.2, is the sum of the direct solar flux, the downward scattered solar flux *via* Rayleigh and Mie scattering and the upward diffuse flux from reflection and radiation from the Earth's surface.[4]

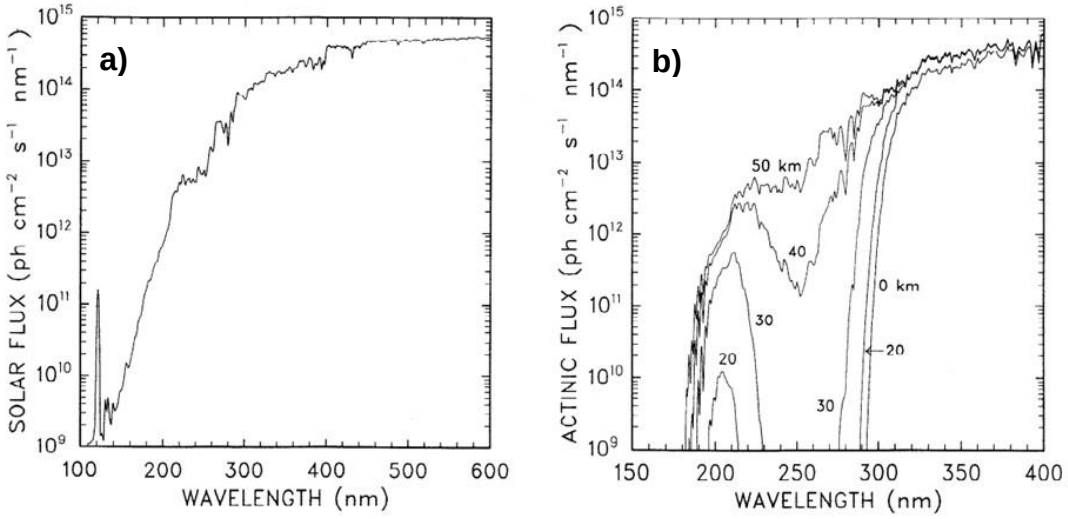

Figure 1.2: Solar actinic flux a) at the top of the Earth's atmosphere in the wavelength range 100-600 nm and b) at various altitudes within the Earth's atmosphere and at the Earth's surface in the wavelength range 150-400 nm, illustrating the decreases in the actinic flux resulting from strong absorption of solar energy by O_2 below ~180 nm and by O_3, which is predominantly in the stratosphere, between 220 and 300 nm. Reproduced from reference 4.[4]

The atmosphere surrounding the Earth is responsible for moderating its climate, with the principal energy input being through solar radiation, as shown in Figure 1.3. Prior to the industrial revolution which marked a period of development in the latter half of the 18th century, the Earth's surface temperature had remained relatively constant and stable since the end of the last glacial period approximately 12,000 years ago,[5] suggesting that an equilibrium had been reached between the incoming radiation from the Sun and the outgoing emission from the Earth and its atmosphere, achieving what is referred to as a radiation balance. Of the energy the Earth receives from the Sun, just under half is absorbed by the Earth's surface, 30 % is reflected

back out of the Earth's atmosphere and the remaining approximately 20 % is absorbed by gas molecules within the atmosphere,[6] with different molecules absorbing different wavelengths of radiation, such as stratospheric ozone which absorbs much (> 97 %) of the ultraviolet (UV) light at wavelengths between 200 nm and 315 nm.[7]

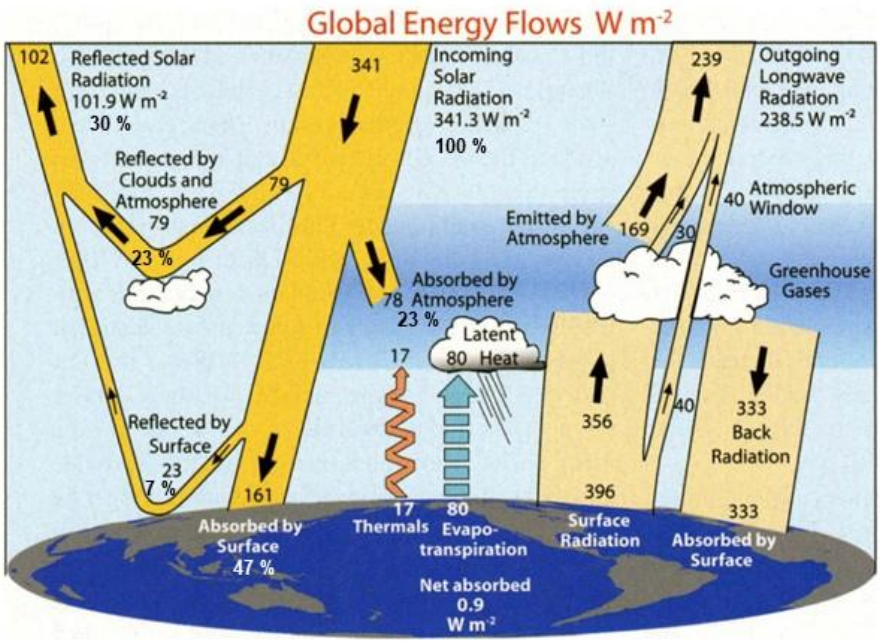

Figure 1.3: A schematic representation of the Earth's energy budget. Adapted and reproduced from reference 6.[6]

UV and visible energy from the Sun is absorbed by the Earth's surface, which re-emits this energy as infrared (IR) radiation. Although most of the IR emitted is radiated directly into space, some is trapped in the Earth's atmosphere by certain naturally occurring molecules known as greenhouse gases (GHGs), e.g. carbon dioxide (CO_2), water vapour (H_2O) and ozone (O_3), which absorb it, and then re-radiate or convert it to thermal energy, warming up the Earth's surface and lower atmosphere in a phenomenon referred to as the greenhouse effect.[8] Without any 'natural' greenhouse effect, the Earth would be too cold (-18 °C or 255 K) for liquid water to exist and therefore uninhabitable, meaning the greenhouse effect is integral to the balance of incoming and outgoing radiation which supports life on Earth.[9] Unfortunately, problems arise when there are changes to this natural system, described in detail further in this chapter.

1.1.1 Air Quality

Air quality refers to the state of the air at any given time and in a particular place, with good air quality describing clean unpolluted air which is vital to the maintenance of the delicate balance of life on Earth, for humans, vegetation, wildlife, water and soil alike.[10] Ambient air quality standards are legal guidelines proposed by international and/or regional organisations, such as the World Health Organisation (WHO) and the European Commission respectively, for concentrations of pollutants in the air. Limits for selected pollutants set by the latter are summarised in Table 1.1.[11] Failing to meet these criteria results in poor air quality, which is when pollutants reach high enough concentrations to endanger human health and/or the environment, with one such result of air pollution being acid rain.[8] Adverse effects of air pollution on human health include aromatics which are carcinogenic, nitrogen dioxide which leads to cardiovascular effects and ozone which causes damage to crops and can trigger respiratory health problems in humans.[1] Air quality is controlled by the composition of the atmosphere which in turn is controlled by emissions, meteorology and chemistry, therefore an improvement in air quality can only be achieved by first understanding the chemistry occurring in the air and then strictly regulating emissions of pollutants found to be detrimental to air quality, including both primary pollutants such as nitrogen oxides (NO + NO_2) and sulfur oxides (SO + SO_2), collectively known as NO_X and SO_X respectively, and volatile organic compounds (VOCs), and secondary pollutants such as ground level ozone (O_3) and particulate matter ($PM_{2.5}$ for small or fine particles with a diameter of 2.5 μm or less and PM_{10} for large or coarse particles with a diameter of 10 μm or less).

Pollutant	Concentration	Averaging Period
Carbon monoxide (CO)	10 mg m^{-3}	Maximum daily 8 hour mean
Ozone (O_3)	120 μg m^{-3}	Maximum daily 8 hour mean
Nitrogen dioxide (NO_2)	200 μg m^{-3}	1 hour
	40 μg m^{-3}	1 year
Sulfur dioxide (SO_2)	350 μg m^{-3}	1 hour
	125 μg m^{-3}	24 hours

Table 1.1: European Commission standards for concentrations of selected pollutants in the air. Reproduced from reference 11.[11]

1.1.2 Climate Change

Climate change refers to a change in the usual climate patterns on a global or regional scale, resulting in a long-term shift in weather patterns.[8] These changes include temperature, precipitation patterns, and wind and storm force and frequency, and are accompanied by major alterations in sea levels associated with melting ice sheets and glaciers. More specifically, it refers to anthropogenic climate change rather than natural climate change, i.e. any change apparent from the mid to late 20th century onwards and attributed principally to human use of fossil fuels consequentially leading to increased levels of atmospheric GHGs such as CO_2. Global warming is the process by which the overall temperature of the Earth's atmosphere exhibits a gradual increase, generally attributed to the greenhouse effect caused by increased levels of CO_2, chlorofluorocarbons (CFCs), and other GHGs. In particular, global warming is the enhanced greenhouse effect caused by high atmospheric concentrations of GHGs, such as CO_2, methane (CH_4), nitrous oxide (N_2O) and O_3 produced *via* anthropogenic sources, resulting in additional warming of the Earth's atmosphere over 'natural' conditions leading to the observed temperature increase.[1] Radiative forcing (RF) is the change in the net irradiance (difference between incoming and outgoing radiation energy) compared with an unperturbed atmosphere (taken as pre-industrial 1750). There is much uncertainty in RF values for many forcing agents such as aerosols, the direct and indirect effects of which both have negative RF values as shown in Figure 1.4, since aerosols cool the atmosphere and offset climate change.[12, 13]

The Intergovernmental Panel on Climate Change (IPCC) fifth assessment report 2013 concluded a total increase in RF of approximately 2.4 W m^{-2} relative to the start of the industrial era in 1750 as shown in Figure 1.4.[12] It was claimed that the dominant cause of the observed climate change and warming since the mid-20th century was extremely likely to be human influence (>95% probability).

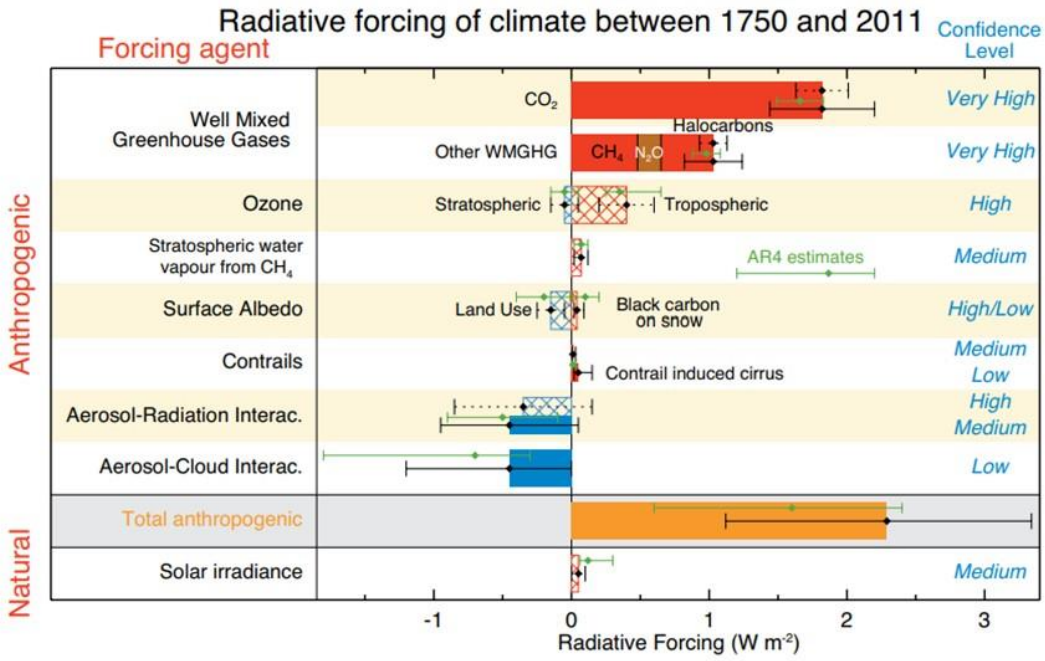

Figure 1.4: A schematic radiative forcing diagram from the IPCC 5th assessment report 2013, showing the most significant factors contributing to global warming and the radiative forcing value associated with each forcing agent. Reproduced from reference 12.[12]

In 2010, parties to the United Nations Framework Convention on Climate Change (UNFCCC) agreed that warming should be limited to below 2 °C in order to avoid dangerous levels of climate change, with the year 2015 seeing the first time since records began that the annual global average temperature reached the halfway mark to this limit with a 1 °C anomaly since pre-industrial times.[14] The IPCC sixth assessment report is due to be finalised and published in full by 2022 in time for the 2023 Global Stocktake by the UNFCCC,[15] when countries will review progress towards the Paris Agreement, which is a legally binding international treaty on climate change signed in 2016 with the goal of keeping global warming to well below 2 °C while pursuing efforts to limit it to 1.5 °C compared to pre-industrial levels.[16]

The above two phenomena, air quality and climate change, are well established in their own right, with links and feedbacks across each. However, their causes are similar, that is the release of air pollutants originating from a variety of anthropogenic sources and human activities. Burning of fossil fuels such as coal, oil and natural gas is the major source common to both.

1.1.3 Atmospheric Composition and Trace Atmospheric Species

The composition of the Earth's atmosphere primarily consists of nitrogen (78.1 %), oxygen (20.9 %) and argon (0.9 %). The remainder of the atmosphere comprises what are known as trace species, several of which are listed in Table 1.2.[17] Despite their low abundance, it is these trace species present in the atmosphere which dictate much of the atmospheric chemistry taking place, thereby having a profound influence on the atmosphere and major implications for air quality and climate change. There are many different types of trace gases present in the atmosphere, namely those which are produced naturally, i.e. from geothermal sources such as volcanoes emitting SO_2, or extreme heat of lightning during thunderstorms producing NO, and biogenic sources such as plants and micro-organisms emitting VOCs, including isoprene and monoterpenes, and those which are produced from anthropogenic sources such as fossil fuel combustion emitting NO, NO_2, SO_2, CO_2 and unburnt fuel.[17] These reactive species have a role to play in the atmospheric composition of other trace species through chemical and photochemical reactions.

Constituent	Chemical Formula	Volume Mixing Ratio in Dry Air*	Major Sources
Nitrogen	N_2	78.084 %	Biological
Oxygen	O_2	29.948 %	Biological
Argon	Ar	0.934 %	Inert
Carbon dioxide	CO_2	416 ppmv**	Combustion, ocean, biosphere
Neon	Ne	18.18 ppmv	Inert
Helium	He	5.24 ppmv	Inert
Methane	CH_4	1.7 ppmv	Biogenic, anthropogenic
Hydrogen	H_2	0.55 ppmv	Biogenic, anthropogenic, photochemical
Ozone (stratosphere)	O_3	0.5-10 ppm	Photochemical
Nitrous oxide	N_2O	0.31 ppmv	Biogenic, anthropogenic
Carbon monoxide	CO	50-200 ppbv	Photochemical, anthropogenic
Ozone (troposphere)	O_3	10-500 ppbv	Photochemical
VOCs	RH	5-500 ppbv	Biogenic, anthropogenic
Nitrogen oxides	NO_X	10 pptv-1 ppmv	Soils, lightning, anthropogenic
Ammonia	NH_3	10 pptv-1 ppbv	Biogenic, anthropogenic
Hydroxyl	OH	0.1-10 pptv	Photochemical
Hydroperoxyl	HO_2	0.1-10 pptv	Photochemical
Formaldehyde	HCHO	0.1-1 ppbv	Photochemical
Sulfur dioxide	SO_2	10 pptv-1ppbv	Photochemical, volcanic, anthropogenic

*Excludes water vapour

**This is the atmospheric concentration of CO_2 as measured in April 2021

Table 1.2: Chemical composition of the atmosphere. Adapted and reproduced from reference 17.[17]

Of the trace species in the atmosphere, water vapour, H_2O, which is the most potent greenhouse gas and typically constitutes a few percent of the troposphere, exerts the greatest influence on atmospheric chemistry through its roles as a reactant, in the formation of hydroxyl radicals, and a catalyst, since it can significantly alter reaction mechanisms and pathways of important atmospheric reactions through the catalytic effect.[18] It is also constantly transferred between the troposphere and terrestrial reservoirs in the water or hydrological cycle, which describes the continuous movement of water between land and ocean surfaces and the atmosphere. Water

vapour is much less abundant in the stratosphere, with typical concentrations on the order of a few ppmv (parts per million by volume) and the primary stratospheric source of H_2O thought to be the oxidation of methane.[12] Another important trace species is carbon dioxide, CO_2, which is also a greenhouse gas, the concentration of which has seen a constant and steady increase since the industrial revolution, and which has the largest radiative forcing effect on the atmosphere (Figure 1.4).

Similarly, ozone, O_3, is a greenhouse gas, and is an important trace gas which is naturally occurring and present throughout the Earth's atmosphere, however it is not uniformly distributed since it exists in varying concentrations within the atmosphere strongly depending on altitude, with the maximum concentration found in what is known as the stratospheric ozone layer. Stratospheric ozone is formed naturally by solar UV radiation breaking apart oxygen molecules (O_2) to produce two highly reactive oxygen atoms (O) which then combine with another oxygen molecule to produce O_3.[19] A steady-state stratospheric concentration of ozone, known as the Chapman mechanism, is set up since this continual production is balanced by its equally continual destruction *via* reactions with sunlight and a wide variety of naturally occurring and man-made chemicals in the stratosphere, such as hydrogen and nitrogen oxides and those containing chlorine and bromine. Tropospheric O_3 production cannot occur following solar photolysis of O_2 molecules due to the reduced solar intensity at wavelengths below 250 nm, which is a direct result of UV absorption by O_3 and O_2 in the stratosphere. Instead, the presence of tropospheric O_3 is partially due to regular downward transportation from the stratosphere, with significant contribution from chemical formation,[19] which is discussed in detail further in this chapter. Another reactive trace species which, although only present in small concentrations in the atmosphere, controls much of its oxidative chemistry, is the hydroxyl radical, OH, with the primary tropospheric source being solar photolysis of ozone, as discussed in detail further in this chapter.

1.2 Atmospheric Emissions of Volatile Organic Compounds

One important class of trace atmospheric species is volatile organic compounds (VOCs). These are organic species with a high vapour pressure present in the gas

phase at room temperature and atmospheric pressure. Emissions of VOCs can occur *via* natural processes or human/industrial processes, with some anthropogenic VOCs being regulated by the law and various bodies such as the VOC Solvents Emissions Directive in the European Union, the Environmental Protection Agency (EPA) in the US, and the World Health Organisation (WHO), as some VOCs can be harmful to human health and/or the environment.[20, 21] It is necessary to know and understand the chemistry of both biogenic and anthropogenic VOCs in order to accurately assess the competition in reactions and their relative impacts in different regions or environments.

Total VOC emissions from biogenic sources, which are those made in life processes by nature i.e. produced by living organisms such as plants, animals, microbes and fungi, are estimated to be more than 8 times as much as the total anthropogenic VOC emissions, which are those originating in or from human activity.[22] Excluding methane (CH_4), approximately 1150 teragrams of carbon per year (Tg C/yr) is released into the atmosphere in the form of VOCs which can be credited to biological sources. Comparatively, anthropogenic sources account for only approximately 142 Tg C/yr in the form of VOCs.[22]

1.2.1 Biogenic VOCs from Plants

The majority of biogenic VOCs are released by plants with the most abundant compound emitted being isoprene (2-methyl-1,3-butadiene, C_5H_8).[23] Isoprene is produced and emitted by many (but not all) perennial plants, such as various species of trees e.g. oaks, poplars and eucalyptus, and shrubs. It has been reported that of the 1150 Tg C/yr of VOCs emitted globally by biological sources, approximately 528 Tg C/yr is solely due to isoprene emissions, equating to 600 Tg per year of isoprene,[24] half of which is from tropical broadleaf trees.

A major class of VOCs is terpenes, which are derived biosynthetically from units of isoprene, and are mainly hydrocarbons, although some contain alcohol, aldehyde and ketone functional groups. Hence terpenes are classified sequentially by increasing chain of isoprene units.[25] One such type of terpenes are monoterpenes, consisting of two isoprene units (dimers of isoprene), with the molecular formula $C_{10}H_{16}$. Examples of monoterpenes include limonene (present in citrus fruits),

linalool (present in lavender), myrcene (present in hops) and pinene (present in pine trees and existing as one of two isomers, either α-pinene or β-pinene).

1.2.2 Anthropogenic VOCs from Fossil Fuels and Other Sources

Use of fossil fuels such as coal, oil and gas can emit VOCs in two ways: either directly as products e.g. gasoline, or indirectly as by-products such as from vehicle exhaust gas emissions e.g. benzene which is a known human carcinogen. VOCs, including those from fossil fuels, influence climate through their production of organic aerosols and their involvement in photochemistry and photochemical smog formation, which is characterised by high concentrations of O_3 and fine particles. Photochemical production of tropospheric O_3 occurs in the presence of NO_X (NO_X = NO + NO_2, nitric oxide and nitrogen dioxide respectively), carbon monoxide (CO) and light, along with VOCs.[26] The chemistry which occurs and its mechanism is discussed further in this chapter.

Chlorofluorocarbons (CFCs) were used widely in the 20th century as cleaning products, refrigerants, solvents and propellants in aerosol applications. It was later discovered that CFCs contribute to ozone depletion in the upper atmosphere and hence the manufacture and use of such products has been strictly regulated, phased out and in some cases banned under the Montreal Protocol 1989, and replaced with the counterpart hydrofluorocarbons (HFCs).[27] Although this legally binding document was introduced due to the role of CFCs in ozone depletion, their atmospheric impacts are not restricted to their part as active ozone reducers. This class of anthropogenic VOCs is also a very potent greenhouse gas with a potential for increasing the greenhouse effect larger than that of CO_2.[28-30]

Another major source of anthropogenic VOCs are paints and solvents. Many building materials emit formaldehyde (HCHO) and paint solvents include acetone and ethyl acetate,[31, 32] all of which are irritants, therefore, unsurprisingly, the paint industry is progressively shifting towards the use of aqueous solvents in paints. Dichloromethane (CH_2Cl_2) is found in adhesive removers and aerosol spray paints and metabolises to carbon monoxide (CO) in the human body. VOCs are of concern as both indoor and outdoor air pollutants and their effects on air quality are severely concerning. Evidently, atmospheric emissions of VOCs are abundant, diverse and

ubiquitous, with most if not all VOCs creating adverse effects, either directly in the form of the VOC itself, or through the chemical transformations of such emissions, which will ultimately determine their impacts on air quality and climate. Not only are there implications of this chemistry in the atmosphere, but also for human health.

1.3 Atmospheric Chemistry and Oxidation

The atmospheric fate of most VOCs is to undergo oxidation, leading to cascades of complex reactions and conversion into highly reactive oxidation products,[33, 34] influencing other atmospheric trace constituents.[35, 36] The removal and main atmospheric degradation process for VOCs, or indeed any atmospheric trace species which can undergo oxidation, is the reaction with the hydroxyl radical (OH), which is the principal oxidant of the troposphere under sunlit conditions.[37-39]

OH radicals are highly reactive and consequently short-lived. Atmospheric generation of OH (R1.1-1.2) is primarily through solar photolysis of ozone forming the electronically excited oxygen atom $O(^1D)$ which reacts with water vapour to produce two OH radicals[40]:

$$O_3 + h\nu\ (\lambda \leq 340\ \text{nm}) \rightarrow O(^1D) + O_2 \qquad \text{(R1.1)}$$

$$O(^1D) + H_2O \rightarrow 2\ OH \qquad \text{(R1.2)}$$

Most of the $O(^1D)$ atoms formed in the initial step by ozone photolysis are quenched to ground state $O(^3P)$ which reacts with O_2 to form ozone (R1.3), with only a small proportion (approximately 1-4 %) proceeding to the formation of OH.

$$O(^3P) + O_2 \xrightarrow{+M} O_3 \qquad \text{(R1.3)}$$

Since the formation of OH *via* the above reaction scheme is dependent upon radiation from the sun, this suggests that OH production will occur primarily during the day. This is evident in observed time profiles of OH over the course of a day, which typically illustrate a diurnal cycle i.e. OH concentration is highest during the day reaching its peak at midday and reaching a minimum during the night when no sunlight is present.[37, 40] Along with the hydroxyl radical, OH, the two other leading oxidising species in the air are the nitrate radical, NO_3, and ozone, O_3. Although O_3 is also active during the day, O_3 and NO_3 become more significant during the night.

As OH is highly reactive towards atmospheric trace species, it is not surprising that the atmospheric concentration of OH is very low, at approximately 10^6 molecules cm^{-3}, equivalent to a mixing ratio of ~0.04 pptv (parts per trillion by volume).[40] The reactive nature of the OH radical means it reacts rapidly following formation hence its atmospheric lifetime is often less than one second, on the order of 0.01 to 1 s.[41, 42]

1.3.1 Reactions of the OH Radical

Oxidation chemistry is responsible for the removal of VOCs and other primary pollutants such as CH_4, SO_2 and NO_X from the atmosphere, whilst also potentially leading to the production of secondary pollutants such as ozone and secondary organic aerosol (SOA) as part of the oxidation chain. The oxidation of many species emitted into the atmosphere is initiated by reaction with OH. Many of these reactions produce hydroperoxy (HO_2) and peroxy (RO_2) radicals, which are key intermediates in the formation of secondary atmospheric pollutants. HO_2 and RO_2 formation reactions are represented in R1.4-1.5 and R1.7-1.10 respectively.

OH radicals are closely coupled with HO_2 radicals, with OH and HO_2 collectively referred to as HO_X (HO_X = OH + HO_2).[40-42] A major process for HO_2 formation is reaction of OH with CO:

$$OH + CO \overset{+M}{\rightleftharpoons} (HOCO) \rightarrow H + CO_2 \quad (R1.4)$$

$$H + O_2 \overset{+M}{\longrightarrow} HO_2 \quad (R1.5)$$

In clean air, OH can be reformed from HO_2 *via* reaction with ozone:

$$HO_2 + O_3 \rightarrow OH + 2\,O_2 \quad (R1.6)$$

Tropospheric OH is also consumed in another important removal process which is reaction with CH_4, forming the methyl peroxy radical (RO_2):

$$OH + CH_4 \rightarrow H_2O + CH_3 \quad (R1.7)$$

$$CH_3 + O_2 \overset{+M}{\longrightarrow} CH_3O_2 \quad (R1.8)$$

Similar reactions to that of CH_4 occur for most hydrocarbons or saturated VOCs, RH, with OH. The hydroxyl radical has a strong tendency to remove or abstract a hydrogen atom from the organic species (RH) forming an organic alkyl radical (R),

which then reacts rapidly with molecular oxygen (O_2) in the atmosphere forming RO_2 radicals *via* the following generic mechanism[40-42]:

$$OH + RH \rightarrow H_2O + R \quad (R = \text{organic group}) \quad (R1.9)$$

$$R + O_2 \xrightarrow{+M} RO_2 \quad (R1.10)$$

In polluted or industrial environments with high concentrations of NO, reactions R1.11-R1.13 are important. These ensuing reactions constitute the exclusive pathway for chemical formation of ozone in the troposphere:

$$HO_2 + NO \rightarrow OH + NO_2 \quad (R1.11)$$

$$RO_2 + NO \rightarrow RO + NO_2 \quad (R1.12)$$

$$RO + O_2 \rightarrow R'CHO + HO_2 \quad (R1.13)$$

Both HO_2 and RO_2 compounds are an essential part of the ozone cycle as their chemistry can lead to O_3 production through reactions R1.14-R1.15.[40-42] Ozone, which is a tropospheric pollutant and a greenhouse gas, is a component of photochemical smog.

$$NO_2 + h\nu\ (\lambda < 420\ \text{nm}) \rightarrow NO + O(^3P) \quad (R1.14)$$

$$O(^3P) + O_2 \xrightarrow{+M} O_3 \quad (R1.15)$$

The series of reactions R1.4-R1.5 and R1.9-R1.13 are radical chain reactions (indicated by red arrows in Figure 1.5) which oxidise CO, VOCs and NO, but also cause a cycling or interconversion between OH, HO_2 and RO_2 radicals. Including reactions R1.14-R1.15, this leads to a coupling of O_3, HO_X and NO_X cycles. Radical recycling *via* reactions R1.11-R1.13 is of particular relevance as it constitutes a secondary source of OH, significantly enhancing the oxidation efficiency of the troposphere.[43]

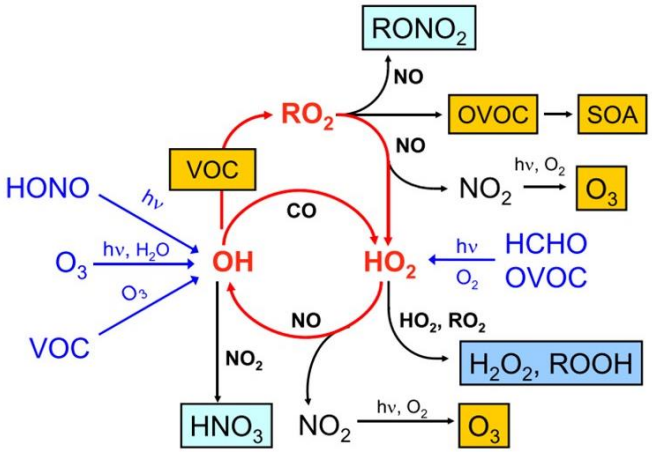

Figure 1.5: Schematic representation of atmospheric HO_X chemistry, illustrating initiation of radical chemistry (shown by the blue arrows), chain reactions (shown by the red arrows) and termination steps (shown by the black arrows). Reproduced from reference 43.[43]

Alkoxy radicals, RO, produced in reaction R1.12, are generally converted to OVOCs (oxygenated VOCs) either by rapid reaction with O_2 yielding carbonyl compounds, R'CHO (reaction R1.13) or by unimolecular decomposition and isomerisation reactions. OVOCs are important in atmospheric chemistry as they can contribute significantly to organic reactivity in various tropospheric regions, thereby affecting the atmospheric lifetime of OH. Furthermore, photolysis of OVOCs can be an important source of radicals in urban conditions, and OVOCs are precursors to secondary organic aerosols (SOA) which play a role in air quality and climate.[43]

RO_X (= OH + HO_2 + RO + RO_2) loss processes in remote, clean environments with very low concentrations of NO are a source of peroxides (H_2O_2, ROOH), as shown in reactions R1.16-R1.17. These represent termination of radical chemistry through recombination reactions of peroxy radicals.

$$HO_2 + HO_2 \xrightarrow{+M} H_2O_2 + O_2 \qquad \text{(R1.16)}$$

$$HO_2 + RO_2 \rightarrow ROOH + O_2 \qquad \text{(R1.17)}$$

In polluted regions with high NO concentrations recombination reactions are a source of nitric acid (HNO_3) and organic nitrates ($RONO_2$), as shown in reactions R1.18-R1.19. Such chain termination reactions suppress concentrations of OH, HO_2 and RO_2 radicals.

$$OH + NO_2 \xrightarrow{+M} HNO_3 \qquad (R1.18)$$

$$RO_2 + NO \xrightarrow{+M} RONO_2 \qquad (R1.19)$$

1.3.1.1 Oxidation of Unsaturated VOCs

Unsaturated VOCs or alkenes, such as isoprene, can undergo a different reaction mechanism with the OH radical. Instead of abstraction of a hydrogen atom as with alkanes (R1.9-R1.10) where the reaction involves breaking of a hydrogen-carbon bond, alkenes react typically *via* addition of OH across the carbon-carbon double bond[39]:

$$OH + R_2C = CR_2 \rightarrow OHR_2C - CR_2 \qquad (R1.20)$$

$$OHR_2C - CR_2 + O_2 \rightarrow OHR_2C - CR_2OO \qquad (R1.21)$$

As well as this main addition reaction pathway (reactions R1.20-R1.21), hydrogen abstraction can also occur as with alkanes, but to a lesser extent as the addition reaction takes precedence,[44] however both reaction pathways result in the formation of RO_2 radicals. Atmospheric oxidation of unsaturated VOCs can also be initiated by other oxidising species such as O_3 and NO_3, both of which react *via* addition across the C=C double bond.[37-39] As mentioned previously, although O_3 is an active oxidant during the day, oxidation reactions of VOCs initiated by O_3 and NO_3 become more important under conditions of low intensity of solar radiation, i.e. during the night and in winter, when OH-initiated oxidation of VOCs is limited as a result of reduced photochemistry.

The nitrate radical, NO_3, is an atmospheric oxidant produced *via* the reaction of NO_2 with ozone (R1.22), and subsequently reacts with NO_2 to rapidly establish a chemical equilibrium with N_2O_5 (R1.23):[38, 45, 46]

$$NO_2 + O_3 \rightarrow NO_3 + O_2 \qquad (R1.22)$$

$$NO_3 + NO_2 \overset{+M}{\rightleftharpoons} N_2O_5 \qquad (R1.23)$$

During the day, the NO_3 produced is rapidly photolysed by solar radiation (R1.24), leading to low day time concentrations since NO_3 is heavily suppressed:[45, 46]

$$NO_3 + h\nu\ (\lambda < 590\ nm) \rightarrow NO_2 + O(^3P) \qquad (R1.24)$$

However, during the night, NO_3 radicals accumulate and are present at significant concentrations,[39, 46] in contrast to OH radicals which are formed following photolysis of ozone resulting in high day time and low night time concentrations. NO_3-initiated oxidation of unsaturated VOCs occurs *via* addition across the C=C double bond and results in the formation of RO_2 radicals.[38, 39, 46] Oxidation of unsaturated VOCs through reaction with O_3 is discussed in the following section.

1.3.2 Ozonolysis in the Gas Phase

Ozone displays high reactivity towards unsaturated VOCs, meaning it has great capacity to be a major atmospheric degradation pathway of such compounds, with oxidation of alkenes by ozone known as ozonolysis.[37-39] Globally, the O_3-initiated oxidation of unsaturated VOCs in ozonolysis removes ~10 % of isoprene (C_5H_8), the most abundant and dominant VOC emitted into the atmosphere, and is a substantially larger sink for monoterpenes ($C_{10}H_{16}$) and sesquiterpenes ($C_{15}H_{24}$) owing to the faster rate coefficients for reaction with ozone compared to isoprene.[47] Oxidation by ozone is also significant for alkenes such as ethene (C_2H_4) and propene (C_3H_6) which are emitted anthropogenically in vehicle exhausts. Oxidation of alkenes by ozone leads to cleavage of C=C double bonds, resulting in production of a carbonyl product and a carbonyl oxide, referred to as a Criegee intermediate.[48]

Ozonolysis reactions have long been predicted to produce carbonyl oxides or Criegee intermediates,[48] and proceed *via* a 1,3-dipolar cycloaddition of the O_3 molecule across the unsaturated C=C bond in the VOC to form an intermediate called a molozonide or a primary ozonide. Subsequently the primary ozonide undergoes a retro 1,3-dipolar cycloaddition leading to cleavage, forming the corresponding carbonyl oxide or Criegee intermediate, and an organic compound in which the carbon-carbon double bond is replaced by a carbonyl group i.e. a C=O double bond as part of an aldehyde if the R group is a H, or a ketone. The general reaction (R1.25) and mechanism (Figure 1.6) for atmospheric ozonolysis of alkenes are shown below:

$$R_2C = CR_2 + O_3 \rightarrow (C_2R_4O_3) \rightarrow CR_2OO + CR_2O \qquad \text{(R1.25)}$$

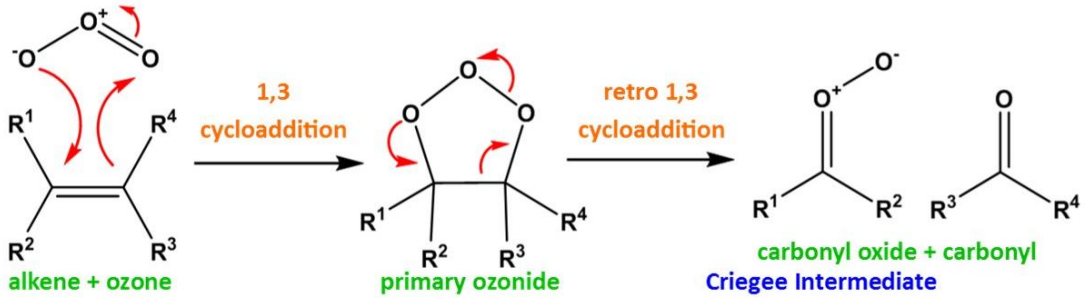

Figure 1.6: Reaction scheme for the gas phase ozonolysis of alkenes. Adapted from reference 49.[49]

Ozonolysis reactions make particularly significant contributions to the tropospheric oxidising capacity at night and in winter when photochemistry is limited by the low intensity of solar radiation,[38, 39, 45, 50, 51] making ozonolysis an important atmospheric process with significant implications for the atmospheric oxidation of VOCs.

1.4 Criegee Intermediates

Criegee intermediates are an important reactive species in the atmosphere with the generic formula CR_2OO.[48] The simplest Criegee intermediate is formaldehyde oxide, CH_2OO. Criegee intermediates were first postulated in 1949 by Rudolf Criegee,[48] after whom they are named, as key intermediates in the ozonolysis of alkenes, to explain the formation of observed products upon investigating the reaction of the alkene 9,10-octalin ($C_{10}H_{16}$) with ozone. Criegee also later suggested a mechanism for ozonolysis reactions,[49] which is summarised in Figure 1.6.

In early work on Criegee intermediates carried out in 1975, it was proposed that the Criegee had a biradical structure, i.e. a molecule containing two radical centres.[52] However, after great speculation over the nature of this species, a recent investigation in 2013 employing infrared spectroscopy has suggested that the electronic structure is zwitterionic in character rather than biradical, with a strengthened (shorter) C-O bond and a weakened (longer) O-O bond.[53] A zwitterion is a neutral molecule with two charge centres, giving it simultaneous positive and negative electrical charges, making it a dipolar ion with both cationic and anionic states and hence an overall charge of zero. The resonance structures of the simplest Criegee intermediate CH_2OO where R = H are shown in Figure 1.7.

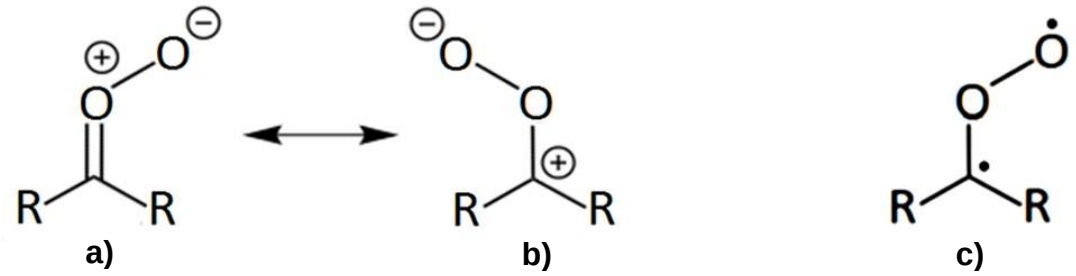

Figure 1.7: Structure of the Criegee a) and b) zwitterion, and c) biradical. Adapted from references 49 and 52 respectively.[49, 52]

Typically, the Criegee intermediate is initially produced vibrationally excited with high internal energy, owing to the high exothermicity of the reaction, 200 – 250 kJ mol^{-1} as shown in the potential energy surface (PES) diagram in Figure 1.8,[54] leading to a subsequent competition between decomposition, producing various atmospheric trace constituents such as OH, HO_2, CO and CO_2, and collisional stabilisation.[55] Unimolecular decomposition/dissociation of Criegee intermediates has implications for non-photolytic OH production at night and in winter,[40, 45, 50, 56] discussed in detail below. Collisional stabilisation, the rate of which depends on the overall pressure (i.e. concentration of inert bath gas species M, often N_2, He or Ar), removes excess energy from a proportion of the excited Criegee intermediate molecules, forming a small steady-state concentration of stabilised Criegee intermediates (SCIs), which can then undergo bimolecular reactions. The yield of SCIs formed is also dependent on the size of the carbonyl coproduct. The various bimolecular reactions of SCIs and their atmospheric implications are discussed in detail further in this chapter.

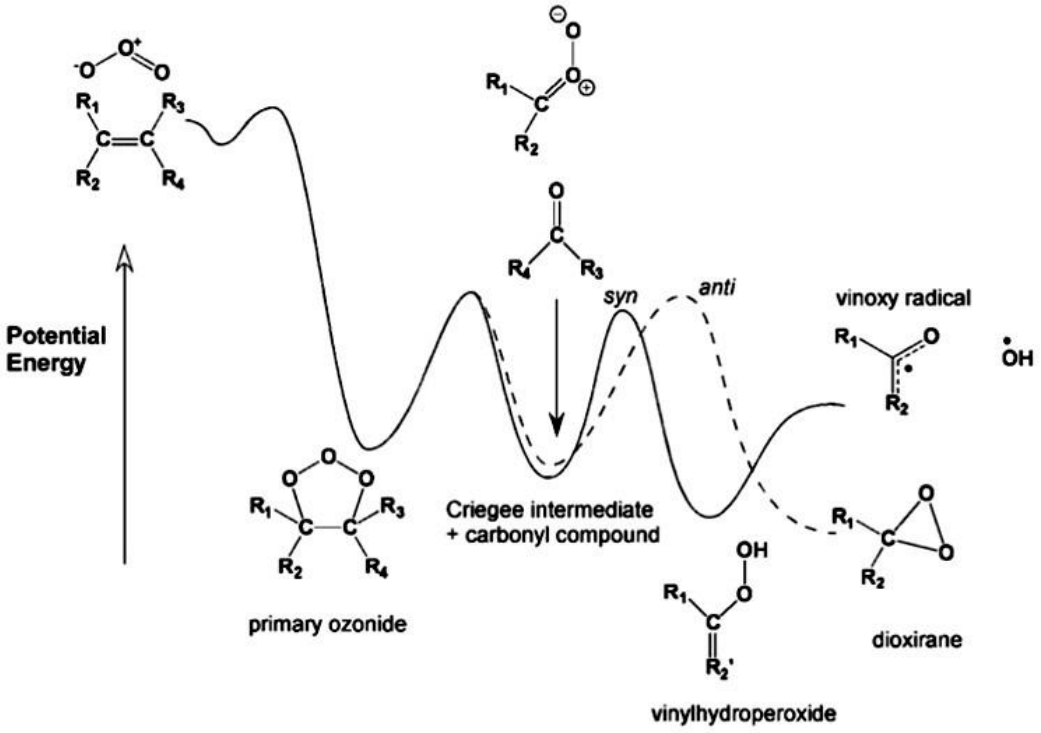

Figure 1.8: A potential energy diagram (PES) of generic alkene ozonolysis (R represents any alkyl substituent or H atom) forming a Criegee intermediate. Typical exothermicity for primary ozonide formation from reactants is > 200 kJ mol^{-1}, with this well being ~60 kJ mol^{-1} deep relative to Criegee formation, and the barrier to isomerisation of Criegees typically being 60-80 kJ mol^{-1}. The Criegee intermediate shows R_1 and R_2 in the *syn*- and *anti*- positions respectively, with the pathway along the PES taken by each conformer labelled. Reproduced from reference 54.[54]

Vibrationally excited Criegee intermediates undergo decomposition to produce important atmospheric species such as OH and HO_2. The mechanism does not require solar radiation and hence provides an important route for OH production in the absence of sunlight. Field measurements at an urban site of both summer and winter time OH and HO_2 radicals taken during the PUMA (Pollution of the Urban Midlands Atmosphere) campaigns held in summer 1999 and winter 2000 showed the noon time concentration of OH during winter to be only a factor of 2 less than during summer despite a factor of 15 reduction in OH production from the photolysis of ozone.[50] The measured noon time concentrations of HO_2 were similar for summer and winter. A detailed box-model of the fast reaction chemistry was able to quantitatively reproduce the high winter time concentrations measured for OH,

showing that the winter radical pool (OH, HO_2 and RO_2) is sustained by reactions of unsaturated hydrocarbons with ozone and by the photolysis of carbonyls, and it was concluded that the high OH concentrations evidenced that there is significant chemical processing of VOCs in winter in regions where emissions are high. This was the first report in the literature revealing decomposition of Criegee intermediates formed from alkene ozonolysis as a source of radicals during winter.

Another campaign in which the relevance of ozonolysis reactions on tropospheric oxidation was highlighted is the RONOCO (ROle of Nighttime chemistry in controlling the Oxidising Capacity of the atmOsphere) aircraft campaign, investigating tropospheric night time oxidation chemistry and the role of radical species at night. Observations of OH, HO_2, NO_3, N_2O_5 and a number of supporting measurements were made during a series of night time and day time flights over the UK in summer 2010 and winter 2011, reflecting the first simultaneous airborne measurements of these species, and observed concentrations of these short-lived species were compared with those calculated by a box model using a detailed chemical scheme. Initiation of night time tropospheric oxidation chemistry through production of HO_X and RO_X radicals, although mainly due to the reaction of NO_3 with unsaturated VOCs, included a significant contribution from the reaction of O_3 with unsaturated VOCs as well.[45] Alkene ozonolysis reactions reportedly influenced the night time HOx radical budget both indirectly, *via* production of RO_2 radicals which, under night time conditions, react with NO_3 to produce RO radicals which react with O_2 to produce HO_X, and directly, through decomposition of Criegee intermediates to produce OH and HO_2. Loss of HO_X and RO_X radicals occurred through a combination of processes including HO_2 + RO_2 reactions and radical propagation was primarily achieved through reactions of NO_3 with RO_2 radicals. Thus, it was concluded that the NO_3 radical at night plays a similar role to both OH and NO during the day in that it acts both as a chain initiator in RO_X radical production (like OH during the day) and the chain propagator in tropospheric oxidation (like NO during the day).[45] A separate comparison of day time and night time oxidation analysing the rates of reaction of OH, O_3 and the NO_3 radical with measured alkenes during the campaign indicated that the summer night time troposphere can be as important for the processing of VOCs as the winter day time troposphere.[57] Furthermore, the analysis showed that while on average, oxidation

reactions of NO_3 with alkenes dominated the night time production of HO_2 during summer, oxidation reactions of O_3 with alkenes dominated the night time production of HO_2 during winter.

1.4.1 Atmospheric Concentration of Criegee Intermediates

The atmospheric processes by which Criegee intermediates are produced in, and removed from, the atmosphere control and dictate the concentration of Criegee intermediates present in the atmosphere. Ozonolysis rate coefficients are small, on the order of 10^{-17}-10^{-18} cm^3 s^{-1},[58] whereas rate coefficients of secondary reactions such as bimolecular reactions between SCIs and some key trace atmospheric species such as $(H_2O)_2$, SO_2, NO_2 and organic acids may be large, on the order of 10^{-10}-10^{-12} cm^3 s^{-1}. This slow rate of formation of SCIs by ozonolysis and fast rate of destruction by various reactions (unimolecular or bimolecular) results in a small steady-state concentration of SCIs in the atmospheric ozonolysis of alkenes, and is reflected in ozonolysis experiments carried out in laboratory chamber studies, as discussed below, since SCIs are formed in these experiments in the same way they are formed in the atmosphere. Difficulties in measuring SCIs in the atmosphere at all, and particularly of measuring SCIs directly in the laboratory, are indicative of the low concentration of Criegees present. In the first direct experimental measurement of CH_2OO in the gaseous ozonolysis of ethene reported in 2015, a feat which had previously proven difficult, Womack *et al.*[55] employed Fourier transform microwave spectroscopy and a modified pulsed nozzle to facilitate high reactant concentrations with rapid sampling and sensitive detection. Despite researchers being able to directly detect the Criegee intermediate, it was the least abundant species detected in the system, and the relatively small abundance of this compared to that of the most abundant species in the system, HCHO, in the ratio $1:3.3 \times 10^6$ CH_2OO:HCHO,[55] clearly indicated the challenges in detection of CH_2OO from ozonolysis reactions in the gas phase.

In the atmosphere, however, since the trace species which contribute to formation of SCIs, namely O_3 and unsaturated VOCs, have been measured, a reasonable estimation of the concentration of SCIs can be made from a combination of theoretical and field studies, i.e. using the steady-state approximation (refer to

Chapter 2 for further details) with detailed chemical modelling.[59] Various estimations of SCI concentrations have been made based on the availability of experimental measurements and quantum calculations of the formation and loss processes of SCIs, with the estimated concentration of Criegee intermediates in the atmosphere calculated to be in the range 10^3-10^5 cm^{-3}.[59-61] Figure 1.9 shows the global variation of the simulated annual-average boundary layer production rate of Criegee intermediates, illustrating the Criegee intermediate production rate to be on the order of 10^4-10^5 cm^{-3} s^{-1} in forests and industrial regions, consisting of high concentrations of Criegee intermediate precursor species, outside of which the Criegee intermediate production rates are several orders of magnitude slower.[60]

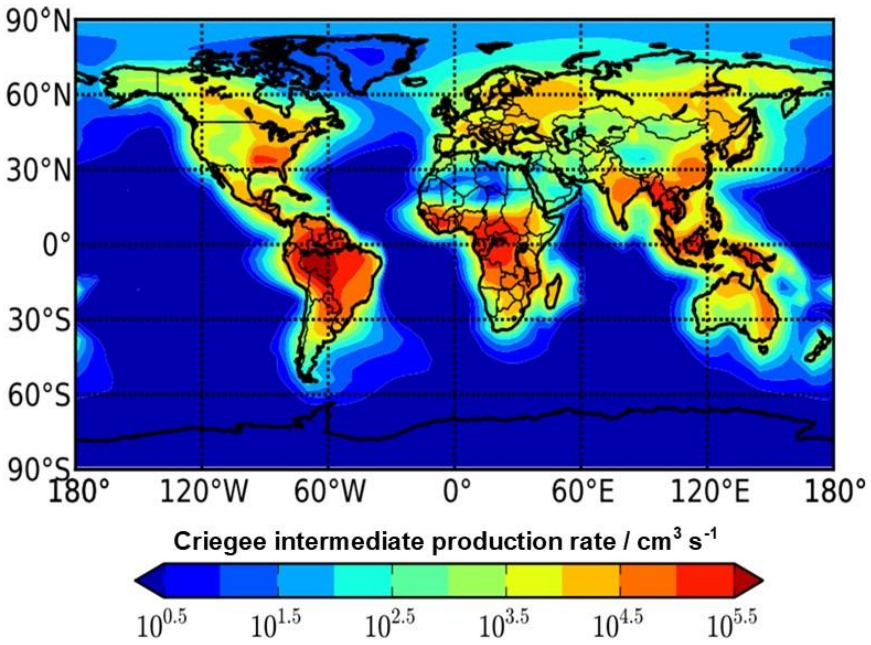

Figure 1.9: The annual average production rate of Criegee intermediates in the atmospheric boundary layer simulated using a global transport model. Reproduced from reference 60.[60]

Furthermore, measurements of VOC and O_3 concentrations in urban and rural sites along with the estimated SCI concentration based on these measurements, and the daily, weekly and annual variation of these species has shown the highest concentration of SCIs was expected in a polluted urban site, impacted by high levels of VOCs from vehicle exhausts, whereas the lowest concentration was predicted at a rural site.[62] The levels of annual average SCI concentrations for the urban and rural UK sites estimated to be in the range 100-2980 cm^{-3} and 30-730 cm^{-3} respectively.

Results suggested that SCIs exhibit a diurnal cycle with peaks during the afternoon given the higher concentration of both VOCs from anthropogenic emissions at urban sites and O_3 from photochemical production, giving an average day to night time ratio of the concentration of SCI of ~1.5. Weekly cycles indicated higher concentrations of SCIs at the weekend than during the weekdays for urban sites by ~10-20 % due to reduced vehicular traffic hence low NO_X emissions increasing the VOC/NO_X ratio and resulting in higher O_3 production. On the contrary, no significant difference between weekday and weekend SCI concentrations were predicted at the rural site lacking vehicular traffic, thus minimising the role of NO_X for altering O_3 concentrations between weekdays and the weekend. A clear seasonal cycle of the concentration of SCIs peaking in May was predicted, the main factor in which was the increased levels of O_3 during Spring months since the change in VOC concentration throughout the year was not significant.[62]

As stated above, the atmospheric concentration of SCIs is dependent on the processes which effectively remove Criegees from the atmosphere. In turn, the importance and significance of the various potential Criegee intermediate reactions in the atmosphere is not only dependent on the rate coefficient for the reaction but also the relative atmospheric concentrations of each species. Relative rates of the bimolecular reactions of SCIs determine which will play the more dominant role in the atmosphere, and the competition between reactions of SCIs with trace atmospheric species is expected to vary from one Criegee intermediate to another. The various bimolecular channels of SCI reactions are discussed in detail further in this chapter, along with their relative rates and hence relative importance in the atmosphere, and the atmospheric impacts of these reactions in terms of product formation and its implications on atmospheric chemistry.

1.5 Previous Studies of Criegee Intermediate Chemistry

In early studies of ozonolysis reactions, Criegee intermediates eluded direct detection due to their highly reactive nature and the lack of a method suitable for direct detection. For this reason, only indirect experimental evidence of Criegee chemistry was available, resulting in reaction rates with large uncertainties as a

result of an absence in detailed and evidenced understanding of the mechanisms related to Criegee production and loss. As stated above, rate coefficients of ozonolysis are relatively small whereas bimolecular reactions of SCIs may be rapid, often leading to a small steady-state concentration of stabilised Criegee intermediates (SCIs) in ozonolysis systems, indicative of the atmospheric SCI concentration. The effects of Criegee intermediate chemistry in the troposphere remained uncertain despite access to, and support from, decades of theoretical studies and indirect experimental measurements.[63]

1.5.1 Indirect Measurements of Criegee Intermediates

Initial investigations used Criegee intermediate scavengers to investigate the bimolecular reactions of SCIs in experiments in atmospheric simulation chambers. However, such experiments of Criegee intermediates in ozonolysis reactions proved challenging given the low steady-state concentration of Criegees formed in the chamber during ozonolysis, therefore reaction kinetics of Criegee chemistry were inferred by observation and quantification of the formation of stable products.[63, 64] Scavengers such as SO_2, HCHO and H_2O were used and products such as H_2SO_4, hydroxy methyl formate (HCO_2CH_2OH) and hydroperoxide (H_2O_2) respectively were used to quantitatively derive information on Criegee kinetics.[63] The main fate of Criegee intermediates was expected to be the reaction with water due to the high concentration of water vapour in the troposphere, with an expected rate coefficient on the order of 10^{-16} cm^3 s^{-1},[63, 65] however, the rates of Criegee reactions with most atmospheric trace species were largely thought to be relatively slow, such as rate coefficient of the reaction of Criegee with NO_2, inferred from the yield of the carbonyl product formed, determined to be on the order of 10^{-14} cm^3 s^{-1}.[66]

One study by Cox and Penkett investigated the reactions of various Criegee + SO_2 systems,[67] inferring the rate of reaction by reference to measurement of the sulfuric acid aerosol formed in the oxidation of SO_2 to H_2SO_4. It was concluded that the rates of sulfuric acid aerosol formation are greater for internally unsaturated alkenes, 2-methyl-2-butene and cis-pent-2-ene, than for the terminally unsaturated 4-methyl-1-pentene and propene.[67] This was confirmed in a subsequent study, which investigated the reaction of the Criegee intermediate CH_3CHOO, formed from

ozonolysis of *cis*-but-2-ene, with SO_2 in detail. A rate coefficient of $(4.3 \pm 0.7) \times 10^{-15}$ cm^3 s^{-1} was reported, and it was concluded that the effects of the ozone-alkene reaction could have a significant contribution to atmospheric oxidation of SO_2.[68]

Further adding to the complications of using ozonolysis chamber experiments to study Criegee intermediates in the laboratory, modelling of these experiments to interpret observations and results was difficult due to the complex ozonolysis mechanism with multiple reactions occurring simultaneously resulting in several routes to production of these stable products within the chamber. The exact nature of the mechanisms and extent of reactions within the system, by way of production, stabilisation and removal of Criegee intermediates, was not well understood, therefore kinetics determined from these experiments were highly uncertain. Due to the transient nature of Criegee intermediates, large uncertainties persisted in reaction kinetics and overall chemistry and hence their impacts on atmospheric composition.[63, 64]

1.5.2 First Direct Detection of Criegee Intermediates and Reaction Kinetics

Criegee intermediates were not directly detected in the gas phase until 2008 when Taatjes *et al*. measured the simplest Criegee, CH_2OO, by tunable synchrotron photoionisation mass spectrometry (PIMS)[69] (for further detail refer to Chapter 3). The CH_2OO intermediate was produced following photolysis of oxalyl chloride, $(COCl)_2$ (R1.26), generating Cl atoms, which then reacted with dimethyl sulfoxide, $(CH_3)_2SO$ (DMSO), in excess oxygen:

$$(COCl)_2 + h\nu\ (\lambda{=}248\ nm) \rightarrow COCl + CO + Cl \qquad (R1.26)$$

$$CH_3SOCH_3 + Cl \rightarrow CH_3SOCH_2 + HCl \qquad (R1.27)$$

$$CH_3SOCH_2 + O_2 \rightarrow CH_2OO + CH_3SO \qquad (R1.28)$$

The mass to charge ratio (*m/z*) signal for H_2CS^+, a by-product of the reaction system observed in the photoionisation mass spectrum, was found to interfere with the CH_2OO^+ signal. Moreover, the yield of CH_2OO obtained was too small for this method to be considered as a convenient source of CH_2OO.

Direct detection of Criegee intermediates in the gas phase with kinetic analysis was documented by the same group in 2012, with Welz *et al*. reporting a sought-after source for the selective production of CH_2OO.[70] The reactive species CH_2I was produced by photolysis of diiodomethane, CH_2I_2, at a wavelength of 248 nm (R1.29) at 298 K and a pressure of 4 Torr. Reaction of iodomethyl radicals and excess oxygen (R1.30) formed an isomer of CH_2O_2 detected by tunable synchrotron photoionisation mass spectrometry which was identified to be the CH_2OO Criegee intermediate based on its threshold energy for photoionisation.

$$CH_2I_2 + h\nu\ (\lambda{=}248\ \text{nm}) \rightarrow CH_2I + I \qquad \text{(R1.29)}$$

$$CH_2I + O_2 \rightarrow CH_2OO + I \qquad \text{(R1.30)}$$

The species CH_2O_2 has three potential structural isomers all with *m/z* = 46, dioxirane, formic acid and the Criegee intermediate formaldehyde oxide, and Welz *et al*. identified the species detected in the time-resolved mass spectrum as the third isomer, the CH_2OO Criegee, based on the ionisation energy of the product conforming to theoretical predictions of CH_2OO.[70] Dioxirane and formic acid have considerably higher ionisation energies, 10.82 eV and 11.33 eV respectively,[71, 72] than that observed for the CH_2O_2 isomer in the photoionisation spectrum of ~10 eV, which matched closely to the calculated ionisation energy for CH_2OO of 9.98 eV.

Kinetics of CH_2OO reactions with SO_2 and NO_2 were measured under pseudo-first order conditions by Welz *et al*.[70] Rate coefficients of $(3.9 \pm 0.7) \times 10^{-11}$ cm^3 s^{-1} for $CH_2OO + SO_2$ and $(7^{+3}_{-2}) \times 10^{-12}$ cm^3 s^{-1} for $CH_2OO + NO_2$, at 298 K and 4 Torr, were determined, showing CH_2OO to be much more reactive than previously anticipated, with SO_2 and NO_2 reacting more than 1000 times faster than expected according to previous indirect measurements.[67, 68] These increased rates of reaction could have implications for atmospheric production of sulfate and nitrate aerosols, as the final products of these reactions were suggested to be SO_3 and HCHO or NO_3 and HCHO respectively. Both rates of reaction suggest more diverse and reactive Criegee chemistry than anticipated with implications for understanding atmospheric fates of trace species. Other reactions investigated included CH_2OO with NO and H_2O, postulated to produce NO_2 and HCHO, and hydroxymethyl hydroperoxide ($HOCH_2OOH$, HMHP) respectively, for which upper limits for the rate coefficients of $< 6 \times 10^{-14}$ cm^3 s^{-1} and $< 4 \times 10^{-15}$ cm^3 s^{-1} were determined respectively.[70]

1.5.2.1 Photolytic Production Method of Criegee Intermediates Using Di-iodoalkane Precursors

The high reactivity of Criegee intermediates makes direct measurements challenging, and therefore requires preparation of the Criegee intermediate *in situ* and in relative isolation with rapid and sensitive monitoring. The photolytic method of production for SCIs in laboratory experiments, identified and introduced by Welz *et al*. in 2012,[70] whereby flash photolysis of a di-iodoalkane precursor in the presence of a large excess of O_2 is employed, has enabled the direct detection of Criegee intermediates. This photolytic source of SCIs produces the Criegee in high yield resulting in concentration of SCIs several orders of magnitude higher than in chamber experiments employing ozonolysis reactions, making it possible to directly detect, measure and monitor the Criegee intermediate itself using analytical techniques which are well established in the field of atmospheric chemistry. This pioneering technique has stimulated active research into Criegee intermediates, consequently allowing for Criegee chemistry to be at the forefront of modern research after over 60 years of its proposal. Photolytic generation of SCIs has opened avenues for new opportunities and increased laboratory kinetic studies of these species in isolation.

Application of this new reaction scheme is not limited to the simplest Criegee CH_2OO for which the precursor is diiodomethane, CH_2I_2,[53, 73-76] its discovery has encouraged similar schemes to be tested and applied to the formation of other larger alkyl substituted SCIs: e.g. for CH_3CHOO the precursor is 1,1-diiodoethane, CH_3CHI_2,[77-81] for $(CH_3)_2COO$ the precursor is 2,2-diiodopropane, $(CH_3)_2CI_2$,[82-84] and for C_2H_5CHOO the precursor is 1,1-diiodopropane, $C_2H_5CHI_2$.[82] Promoting synthesis of some larger Criegees *via* this method, more specifically those which do not have the same R groups such as CH_3CHOO and C_2H_5CHOO, comprises differences to the production of the simplest CH_2OO Criegee and other symmetrical intermediates such as $(CH_3)_2COO$, in that more than one conformer can exist and hence be produced.[85] For example, the CH_3CHOO Criegee has two conformers, namely *syn*-CH_3CHOO and *anti*-CH_3CHOO, the structures for which are shown in Figure 1.10, and each of which is produced in differing yields following photolysis of the di-iodoalkane precursor and has differing reactivities towards co-reactants.

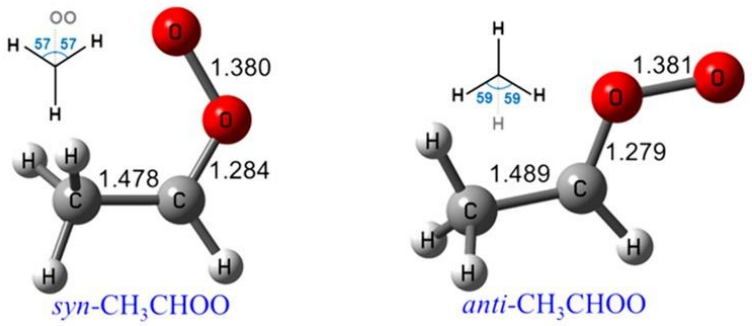

Figure 1.10: Structures for *syn*-CH_3CHOO and *anti*-CH_3CHOO with bond lengths in Å. Reproduced from reference 85.[85]

Flash photolysis experiments investigating Criegee kinetics indicate much higher reactivity than previously expected on the basis of chamber ozonolysis experiments. Furthermore, although the high concentrations of SCIs generated using this method are advantageous and required to study Criegees in the laboratory e.g. in terms of spectroscopy and kinetics, this leads to the potential for Criegee self-reactions to take place under laboratory conditions.[86-89] Due to the relatively low steady-state concentration of Criegee intermediates generated during atmospheric ozonolysis of alkenes, the Criegee self-reaction is not itself atmospherically relevant as it is unlikely to compete with other processes under atmospheric conditions and so is likely to play an insignificant role in the atmosphere. Nonetheless, since it has the potential to be important under laboratory conditions owing to the high concentrations of SCIs formed, this reaction can potentially impact all Criegee reaction kinetics determined in the laboratory. Hence Criegee self-reaction kinetics are important as they can largely influence Criegee kinetics under laboratory conditions, therefore must be taken into account to ensure that the Criegee self-reaction has no impact in experiments of Criegee + X, where X is a trace atmospheric species whose reaction with SCIs is atmospherically significant such as SO_2, NO_2 and $(H_2O)_2$. The Criegee self-reaction can also be closely coupled to Criegee spectra, i.e. Criegee absorption cross-sections,[73-76] since significant changes in concentration can occur on the timescale of the absorption measurements, making Criegee self-reaction kinetics important for determination of Criegee spectra and for further studies of Criegee reaction kinetics using spectroscopy. The UV absorption cross-sections and self-reaction kinetics of the simplest Criegee intermediate

CH_2OO are discussed in detail in Chapters 4 and 5 respectively, along with the experiments and analysis carried out and results obtained for their determination in this work.

The yield of SCI produced following photolysis of a di-iodoalkane precursor in the presence of excess O_2 has been of interest since the introduction of this scheme as a method for producing Criegees in the laboratory since this information is required to quantify the concentration of SCI produced in the system. Consequently, this yield is crucial in determination of both spectral and kinetic data on Criegee intermediates for systems investigated under laboratory conditions in which the photolytic production method of Criegees is employed. The yield of CH_2OO from the reaction of CH_2I radicals with O_2 as a function of total pressure haa been measured previously in this laboratory by Stone *et al*.[90] at 295 K and pressures between 25 and 450 Torr following 248 nm photolysis of CH_2I_2 in the presence of excess oxygen using three complementary methods. Results from the three methods were found to be similar, with the yield of CH_2OO decreasing with increasing pressure and an 18 % CH_2OO yield being reported at atmospheric pressure.

1.6 Spectral Detection Methods of Criegee Intermediates

In recent years, there have been significant advances in our knowledge and understanding of the properties of Criegee intermediates and substantial progress has been achieved in the proficiency of Criegee chemistry following the advent of photolytic sources for use in laboratory experiments. In the study by Welz *et al*.,[70] tunable synchrotron photoionisation mass spectrometry (PIMS) was used to explicitly assign the Criegee intermediate, and although exceptionally useful and important in the initial assessment and results of direct Criegee investigations and for devising and orchestrating the future of Criegee chemistry, this technique is not universal. The instrumentation used in such a setup is very specialist and expensive, with limited and restricted accessibility and availability, and operating the pressure and temperature controls for such a system is challenging. Alternative analytical techniques exist which are much more widely applicable than the PIMS method,

such as absorption and fluorescence spectroscopy, the principles for which are discussed in detail in Chapter 3.

Since the introduction of the photolytic production method of SCIs, many spectroscopic techniques have been successfully implemented to investigate the Criegee intermediate itself and the reactions of Criegee intermediates. Spectroscopic detection of Criegee intermediates has been achieved in varying regions of the electromagnetic spectrum, employing methods including ultraviolet (UV) absorption spectroscopy,[73-77, 79, 81, 82, 84] infrared (IR) absorption spectroscopy,[53, 80, 83] microwave spectroscopy,[55, 91] and laser induced fluorescence (LIF) spectroscopy of reaction products.[92] Using a combination of these methods, spectra of CH_2OO,[53, 73-76] CH_3CHOO,[77-81] $(CH_3)_2COO$[82-84] and C_2H_5CHOO[82] have been reported.

Such detection methods have the potential to enable direct detection of SCIs in chamber experiments to investigate the discrepancies between kinetic results of flash photolysis and chamber measurements, as stated above. This also has implications for investigations of Criegees which cannot be generated photolytically in the laboratory, such as larger SCIs since their photolytic production may be more challenging as it is contingent on the availability of analogously larger di-iodo-substituted precursors which are more difficult to synthesise, but in particular those from biogenic sources such as isoprene and monoterpenes for which ozonolysis is a significant atmospheric sink. For this reason, accurate spectroscopic data along with accurate kinetic information are required for evaluation of Criegee reactions which will occur in chamber experiments. Measurements of UV absorption spectra of Criegee intermediates have indicated that the UV absorption cross-sections of SCIs are relatively large, on the order of ~10^{-17} cm^2,[73-76] thus giving UV absorption spectroscopy vast potential for use in the measurement of atmospherically relevant SCI reaction kinetics. Exploitation of this property has led to UV detection methods as a basis for kinetic measurements and determining rates of Criegee reactions in the laboratory. However, significant uncertainties exist in Criegee UV absorption spectra reported in the literature. The UV absorption cross-sections of the simplest Criegee, CH_2OO, are the focus of Chapter 4 of this thesis, where they are discussed in detail.

1.7 Criegee Chemistry and its Atmospheric Impacts

The field of Criegee chemistry is an exciting one, and the recent discovery of the photolytic production method to produce collisionally stabilised Criegee intermediates in the laboratory has enabled direct detection of SCIs. Although extensive investigations into the reactions of Criegee intermediates have been carried out since this discovery, these studies are far from comprehensive in their analysis of Criegee intermediates and their reaction rate coefficients, and many unanswered questions still remain. Many bimolecular reaction pathways of SCIs are known to exist, however mechanistic features and kinetics have been difficult to study until recently. There have been a number of studies of SCI reaction kinetics utilising a wide range of direct detection methods, investigating the reactions of SCIs with several atmospheric inorganic species, such as SO_2, NO_2, NO, water (H_2O) and water dimer ($(H_2O)_2$), and organic species, such as carboxylic acids and carbonyl compounds. Kinetics and products of oxidation reactions of SCIs with SO_2,[70, 74, 78, 79, 84, 89, 92-95], NO_2,[70, 78, 92] $(H_2O)_2$,[96-99] and organic acids,[100, 101] have been reported to be significant in the atmosphere. Relative rates of the bimolecular reactions of SCIs determine the extent of the competition between different atmospheric loss pathways, and dictate which will be dominant in the atmosphere. The reaction with water dimer is expected to be the dominant chemical sink for SCIs in the troposphere since the atmospheric concentration of H_2O and $(H_2O)_2$ is significantly higher than that of SO_2, and hence the higher concentration compensates for a lower rate coefficient for this bimolecular reaction. Table 1.3 summarises the rate coefficients, $k_{reaction}$, of the atmospherically relevant bimolecular reactions of the simplest Criegee intermediate, CH_2OO, with key atmospheric species, and provides details of estimations of the effective first-order rate coefficients, k_{eff}, for these reactions.

Co-reactant	$k_{reaction}$ / $cm^3\ s^{-1}$	Assumed concentration	Number density / cm^{-3}	k_{eff} / s^{-1}
$(H_2O)_2$ [96]	6.5×10^{-12}	$H_R \geq 36$ % *	$\geq 1.6 \times 10^{14}$	1040
SO_2 [70]	3.9×10^{-11}	50 ppbv	1.2×10^{12}	47
NO_2 [70]	7×10^{-12}	50 ppbv	1.2×10^{12}	8
Carboxylic acids [100]	1×10^{-10}	5 ppbv	1.2×10^{11}	12

*H_R = relative humidity

Table 1.3: Estimations for the effective first-order rate coefficient, k_{eff}, for the reactions of CH_2OO with key atmospheric species at 298 K and 760 Torr, calculated by multiplication of the rate coefficient for the reaction, $k_{reaction}$, by the typical number density of each species in the atmosphere. Adapted and reproduced from reference 96.[96]

Criegee intermediates may have an important role in the atmospheric chemistry of sulfates, nitrates and organic acids. Studies probing the kinetics of reactions with SO_2 and NO_2 provide evidence that SCIs not only contribute to pollutant removal but also to aerosol formation, since these bimolecular reactions result in SOA production of sulfate and nitrate,[59, 70] and hence may be involved in offsetting global warming by way of planetary cooling through increased aerosols,[13] but also lead to poor air quality and respiratory health issues. Thus, this chemistry is likely to affect the formation of new atmospheric particles, the production of secondary cloud condensation nuclei and ultimately, the climate. This demonstrates the connection between anthropogenic activities such SO_2 emissions, natural ecosystems such as biogenic VOC emissions and SOA formation, and climate, from cloud properties to radiative forcing.

Bimolecular reactions of Criegee intermediates with SO_2 also play an essential and important role in the implications of SO_2 oxidation to sulfur trioxide, SO_3, potentially revealing a previously unknown route for SO_3 production in the atmosphere, with consequences for the global H_2SO_4 budget since SO_3 reacts with water vapour to produce gaseous sulfuric acid,[59] usually deposited through acid rain or snow which can damage ecosystems and materials. Independently, recent field measurements of sulfuric acid in regions impacted by high emissions of unsaturated

VOCs have supported this notion, as unknown oxidants of SO_2 have been indicated.[102]

Unimolecular decomposition reactions of excited Criegee intermediates have also been investigated and are of particular interest as they can lead to formation of formic acid which dissociates into various products, one of which is OH.[40, 55, 56, 64] Hence Criegee chemistry, which is driven by ozone and so does not require solar photolysis like OH driven chemistry, has been associated with non-photolytic OH production, especially under low solar radiation conditions such as in the winter time and at night. Despite the efficiency drop in the reactions involved in photolytically generated OH during winter, field measurements have shown OH concentrations in winter to be much higher than expected, with this difference in production of OH attributed to ozonolysis of alkenes, dominated by Criegee chemistry.

Alkene ozonolysis is the dominant source of Criegee intermediates in the atmosphere, and so inclusion of this chemistry in regional and global chemical transport models is vital to accurately obtain radical concentrations, branching ratios of product channels for the oxidation of unsaturated VOCs by ozone, kinetics for Criegee reactions and the overall effect of Criegee chemistry from alkene ozonolysis on atmospheric composition.[103] Certain atmospherically relevant questions, such as this fractional yield of excited Criegee intermediate and SCI from the alkene ozonolysis of various VOCs, can only be investigated by probing the alkene-ozone system, requiring the use of chamber studies.[103] Chamber studies, such as those conducted in the EUPHORE (EUropean PHOtoREactor) atmospheric simulation chamber, generally tend to be relative rate experiments (for further information refer to Chapter 3), employing indirect methods of Criegee detection.[103-106] Such relative rate studies are complementary to direct studies and can yield a vast amount of valuable information. However absolute studies and direct measurements of SCIs and their reaction kinetics, such as those carried out with techniques used and developed in this work (for further information refer to Chapters 3 and 6), are required to make full use of the information provided by these relative rate studies.

Since the recent discovery of the photolytic method of Criegee intermediate production, which brought to light the faster reactivity of Criegee intermediates than

previously anticipated, for example for the reaction between SCIs and SO_2, incorporation of these faster kinetics into relative rate studies has allowed detailed and in-depth investigations of Criegee chemistry and its atmospheric impacts. Relative rate studies measuring the loss of SO_2 in the presence of various alkene-ozone systems as a function of water vapour or humidity have enabled quantification of the relative rates of reaction of various SCIs, including conformer specific reactivity, with SO_2 and water, and their decomposition rates.[104-106]

Modelling Criegee chemistry in all its complexity is important to accurately gauge its overall atmospheric impacts, and modelling studies necessitate the availability of accurate kinetic parameters such as rate coefficients and branching ratios for alkene ozonolysis reactions and Criegee intermediate reactions alike. Information is required for the various types of Criegee intermediate reactions, such as those stated above, in order to model the impact of Criegee chemistry on e.g. production of OH, SOA and H_2SO_4.

Reactions of various Criegee intermediates which have been investigated via direct probing of the Criegee indicate a number of important channels for the atmospheric loss of Criegees. Reported rate coefficients in the literature of some reactions are in agreement, however discrepancies remain for others. One such reaction is the CH_2OO self-reaction, which, although itself is unlikely play a significant role in the atmosphere owing to the small steady-state concentration of SCI present, is important under laboratory conditions owing to the higher concentration of SCI formed.[86-89] This reaction can potentially impact all CH_2OO reaction kinetics investigated under laboratory conditions and hence requires accurate quantification. The CH_2OO self-reaction and its kinetics are the focus of Chapter 5 of this thesis, where they are discussed in detail.

1.8 Overview of this Thesis

This thesis will describe the kinetics of Criegee intermediate reactions relevant to atmospheric chemistry. The kinetics of the reaction of the simplest Criegee intermediate, CH_2OO, with itself and with SO_2 will be discussed and experimental determination of the rate coefficients of these reactions using time-resolved UV and IR absorption spectroscopy respectively will be described. The UV and IR absorption spectra of CH_2OO will be discussed. The characterisation and development of a time-resolved mid-IR absorption spectroscopy instrument will also be described.

The experimental work described in this thesis employed production of CH_2OO from photolysis of CH_2I_2 in excess O_2 at either 248 nm or 266 nm. All experiments were carried out at room temperature and a range of pressures below atmospheric pressure.

A summary of the chapters presented in this thesis is as follows:

Chapter 2 introduces theories of chemical reactions and photochemistry.

Chapter 3 describes methods used to investigate gas phase kinetics and detect reactive species, including those used throughout this thesis, and provides details of the apparatus used in the UV detection of CH_2OO described in this thesis.

Chapter 4 provides details of the experimental determination of the UV absorption cross-sections of CH_2OO.

Chapter 5 discusses the experimental determination of the kinetics of the CH_2OO self-reaction and the reaction between CH_2OO and I using time-resolved absorption spectroscopy.

Chapter 6 gives details of the development, characterisation and initial results of a time-resolved mid-IR absorption method with respect to the IR absorption spectrum of CH_2OO and the kinetics of the reaction between CH_2OO and SO_2.

Chapter 7 summarises the work presented in this thesis and the key findings from it, and outlines possible future work.

1.9 References

1. IPCC Climate change 2014: Synthesis report. Contribution of working groups I, II and III to the fifth assessment report of the Intergovernmental Panel on Climate Change; Geneva, Switzerland, 2014.

2. Finlayson-Pitts, B. J.; James N. Pitts, J., Chemistry of the upper and lower atmosphere: theory, experiments, and applications. Academic Press: San Diego, California, 1999.

3. Seinfeld, J. H.; Pandis, S. N., Atmospheric chemistry and physics: from air pollution to climate change. John Wiley & Sons, Incorporated: New Jersey, USA, 2016.

4. DeMore, W. B.; Sander, S. P.; Howard, C. J.; Ravishankara, A. R.; Golden, D. M.; Kolb, C. E.; Hampson, R. F.; Kurylo, M. J.; Molina, M. J. Chemical kinetics and photochemical data for use in stratospheric modeling- Evaluation number 12- Publication 97-4; Jet Propulsion Laboratory: Pasadena, California, 1997.

5. Severinghaus, J. P.; Brook, E. J., Abrupt climate change at the end of the last glacial period inferred from trapped air in polar ice. Science **1999,** 286 (5441), 930-934.

6. Trenberth, K. E.; Fasullo, J. T.; Kiehl, J., Earth's global energy budget. Bulletin of the American Meteorological Society **2009,** 90 (3), 311-324.

7. Wayne, R. P., Chemistry of atmospheres: An introduction to the chemistry of the atmosphere of Earth, the planets, and their satellites. Third ed.; Oxford University Press: Oxford, 2000.

8. Barry, R. G.; Chorley, R. J., Atmosphere, weather and climate. Ninth ed.; Routledge: London, 2009.

9. Kweku, D. W.; Bismark, O.; Maxwell, A.; Desmond, K. A.; Danso, K. B.; Oti-Mensah, E. A.; Quachie, A. T.; Adormaa, B. B., Greenhouse effect: Greenhouse gases and their impact on global warming. Journal of Scientific Research and Reports **2017,** 17 (6), 1-9.

10. Jacob, D. J.; Winner, D. A., Effect of climate change on air quality. Atmospheric Environment **2009,** 43 (1), 51-63.

11. European Environment Agency, Directive 2008/50/EC of the European Parliament and of the Council of 21 May 2008 on ambient air quality and cleaner air for Europe. European Commission, Ed. Official Journal of the European Union: 2008.

12. Stocker, T. F.; Dahe, Q.; Plattner, G.-K.; Alexander, L. V.; Allen, S. K.; Bindoff, N. L.; Bréon, F.-M.; Church, J. A.; Cubasch, U.; Emori, S.; Forster, P.; Friedlingstein, P.; Gillett, N.; Gregory, J. M.; Hartmann, D. L.; Jansen, E.; Kirtman, B.; Knutti, R.; Kanikicharla, K. K.; Lemke, P.; Marotzke, J.; Masson-Delmotte, V.; Meehl, G. A.; Mokhov, I. I.; Piao, S.; Ramaswamy, V.; Randall, D.; Rhein, M.; Rojas, M.; Sabine, C.; Shindell, D.; Talley, L. D.; Vaughan, D. G.; Xie, S.-P., Technical summary. In Climate change 2013: The physical science basis. Contribution of working group I to the fifth assessment report of the Intergovernmental Panel on Climate Change, Cambridge University Press: Cambridge, United Kingdom and New York, USA, 2013.

13. Park, C. C., The environment: principles and applications. Second ed.; Routledge: London, 2001.

14. MET Office Global climate in context as the world approaches 1°C above pre-industrial for the first time. https://www.metoffice.gov.uk/research/news/2015/global-average-temperature-2015 (accessed 17th May 2021).

15. IPCC The IPCC and the sixth assessment cycle; https://www.ipcc.ch/assessment-report/ar6/, 2020.

16. UNFCCC, Paris Agreement. 2015.

17. Brasseur, G. P.; Orlando, J. J.; Tyndall, G. S., Atmospheric chemistry and global change. Oxford University Press: New York, USA, 1999.

18. Buszek, R. J.; Francisco, J. S.; Anglada, J. M., Water effects on atmospheric reactions. International Reviews in Physical Chemistry **2011,** 30 (3), 335–369.

19. Salawitch, R. J.; Fahey, D. W.; Hegglin, M. I.; McBride, L. A.; Tribett, W. R.; Doherty, S. J., Twenty questions and answers about the ozone layer: 2018 update. In Scientific Assessment of Ozone Depletion: 2018, World Meteorological Organization: Geneva, Switzerland, 2019.

20. Kneller, R.; Manderson, E., Environmental regulations and innovation activity in UKmanufacturing industries. Resource and Energy Economics **2012,** 34 (2), 211-235.

21. Carnell, E.; Vieno, M.; Vardoulakis, S.; Beck, R.; Heaviside, C.; Tomlinson, S.; Dragosits, U.; Heal, M. R.; Reis, S., Modelling public health improvements as a result of air pollution control policies in the UK over four decades - 1970 to 2010. Environmental Research Letters **2019,** 14 (7), 074001.

22. Goldstein, A. H.; Galbally, I. E., Known and unexplored organic constituents in the Earth's atmosphere. Environmental Science and Technology **2007,** 41 (5), 1514–1521.

23. Sharkey, T. D.; Wiberley, A. E.; Donohue, A. R., Isoprene emission from plants: Why and how. Annals of Botany **2008,** 101 (1), 5-18.

24. Guenther, A.; Karl, T.; Harley, P.; Wiedinmyer, C.; Palmer, P. I.; Geron, C., Estimates of global terrestrial isoprene emissions using MEGAN (Model of Emissions of Gases and Aerosols from Nature). Atmospheric Chemistry and Physics **2006,** 6, 3181–3210.

25. Kandi, S.; Godishala, V.; Rao, P.; Ramana, K. V., Biomedical significance of terpenes: An insight. Biomedicine and Biotechnology **2015,** 3 (1), 8-10.

26. Guo, H., Volatile organic compounds (VOCs) emitted from petroleum and their influence on photochemical smog formation in the atmosphere. Journal of Petroleum and Environmental Biotechnology **2012,** 3 (1), 1000e104.

27. United Nations Environment Programme, Handbook for the Montreal protocol on substances that deplete the Ozone layer. Fourteenth ed.; Ozone Secretariat: Nairobi, Kenya, 2020.

28. Lu, Q.-B., Cosmic-ray-driven reaction and greenhouse effect of halogenated molecules: Culprits for atmospheric ozone depletion and global climate change. International Journal of Modern Physics B **2013,** 27 (17), 1350073-1350111.

29. Ramanathan, V., Greenhouse effect due to chlorofluorocarbons: Climatic implications. Science **1975,** 190 (4209), 50-52.

30. Ramanathan, V.; Feng, Y., Air pollution, greenhouse gases and climate change: Global and regional perspectives. Atmospheric Environment **2009,** 43 (1), 37-50.

31. Xiong, J.; Wang, L.; Bai, Y.; Zhang, Y., Measuring the characteristic parameters of VOC emission from paints. Building and Environment **2013,** 66, 65-71.

32. Qian, H.; Fiedler, N.; Moore, D. F.; Weisel, C. P., Occupational exposure to organic solvents during bridge painting. Annals of Occupational Hygiene **2010,** 54 (4), 417–426.

33. Kesselmeier, J.; Staudt, M., Biogenic volatile organic compounds (VOC): An overview on emission, physiology and ecology. Journal of Atmospheric Chemistry **1999,** 33 (1), 23-88.

34. Koppmann, R., Volatile organic compounds in the atmosphere. Blackwell Publishing: Oxford, UK, 2007.

35. Calvert, J. G.; Atkinson, R.; Becker, K. H.; Kamens, R. M.; Seinfeld, J. H.; Wallington, T. H.; Yarwood, G., The mechanisms of atmospheric oxidation of the aromatic hydrocarbons. Oxford University Press: 2002.

36. Calvert, J. G.; Derwent, R. G.; Orlando, J. J.; Tyndall, G. S.; Wallington, T. J., Mechanisms of atmospheric oxidation of the alkanes. Oxford University Press: Oxford, UK, 2008.

37. Lelieveld, J.; Butler, T. M.; Crowley, J. N.; Dillon, T. J.; Fischer, H.; Ganzeveld, L.; Harder, H.; Lawrence, M. G.; Martinez, M.; Taraborrelli, D.; Williams, J., Atmospheric oxidation capacity sustained by a tropical forest. Nature **2008,** 452, 737–740.

38. Waring, M. S.; Wells, J. R., Volatile organic compound conversion by ozone, hydroxyl radicals, and nitrate radicals in residential indoor air: Magnitudes and impacts of oxidant sources. Atmospheric Environment **2015,** 106, 382-391.

39. Mellouki, A.; Wallington, T. J.; Chen, J., Atmospheric chemistry of oxygenated volatile organic compounds: Impacts on air quality and climate. Chemical Reviews **2015,** 115 (10), 3984–4014.

40. Stone, D.; Whalley, L. K.; Heard, D. E., Tropospheric OH and HO2 radicals: field measurements and model comparisons. Chemical Society Reviews **2012,** 41 (19), 6348-6404.

41. Gligorovski, S.; Strekowski, R.; Barbati, S.; Vione, D., Environmental implications of hydroxyl radicals (OH). Chemical Reviews **2015,** 115 (24), 13051–13092.

42. Gligorovski, S.; Strekowski, R.; Barbati, S.; Vione, D., Addition and correction to Environmental implications of hydroxyl radicals (OH). Chemical Reviews **2018,** 118 (4), 2296.

43. Lu, K. D.; Rohrer, F.; Holland, F.; Fuchs, H.; Bohn, B.; Brauers, T.; Chang, C. C.; Häseler, R.; Hu, M.; Kita, K.; Kondo, Y.; Li, X.; Lou, S. R.; Nehr, S.; Shao, M.; Zeng, L. M.; Wahner, A.; Zhang, Y. H.; Hofzumahaus, A., Observation and modelling of OH and HO2 concentrations in the Pearl River Delta 2006: a missing OH source in a VOC rich atmosphere. Atmospheric Chemistry and Physics **2012,** 12 (3), 1541–1569.

44. McGillen, M. R.; Percival, C. J.; Shallcross, D. E.; Harvey, J. N., Is hydrogen abstraction an important pathway in the reaction of alkenes with the OH radical? Physical Chemistry Chemical Physics **2007,** 9 (31), 4349-4356.

45. Stone, D.; Evans, M. J.; Walker, H.; Ingham, T.; Vaughan, S.; Ouyang, B.; Kennedy, O. J.; McLeod, M. W.; Jones, R. L.; Hopkins, J.; Punjabi, S.; Lidster, R.; Hamilton, J. F.; Lee, J. D.; Lewis, A. C.; Carpenter, L. J.; Forster, G.; Oram, D. E.; Reeves, C. E.; Bauguitte, S.; Morgan, W.; Coe, H.; Aruffo, E.; Dari-Salisburgo, C.; Giammaria, F.; Carlo, P. D.; Heard, D. E., Radical chemistry at night: comparisons between observed and modelled HOX, NO3 and N2O5 during

the RONOCO project. Atmospheric Chemistry and Physics **2014,** 14 (3), 1299–1321.

46. Ball, S. Atmospheric chemistry at night (ECG Environmental Brief No 3); 2014.

47. Nguyen, T. B.; Tyndall, G. S.; Crounse, J. D.; Teng, A. P.; Bates, K. H.; Schwantes, R. H.; Coggon, M. M.; Zhang, L.; Feiner, P.; Millller, D. O.; Skog, K. M.; Rivera-Rios, J. C.; Dorris, M.; Olson, K. F.; Koss, A.; Wild, R. J.; Brown, S. S.; Goldstein, A. H.; Gouw, J. A. d.; Brune, W. H.; Keutsch, F. N.; Seinfeld, J. H.; Wennberg, P. O., Atmospheric fates of Criegee intermediates in the ozonolysis of isoprene. Physical Chemistry Chemical Physics **2016,** 18 (15), 10241-10254.

48. Criegee, R.; Wenner, G., Die Ozonisierung des 9,10-Oktalins. Justus Liebigs Annalen der Chemie **1949,** 564 (1), 9-15.

49. Criegee, R., Mechanism of ozonolysis. Angewandte Chemie International Edition **1975,** 14 (11), 745-752.

50. Heard, D. E.; Carpenter, L. J.; Creasey, D. J.; Hopkins, J. R.; Lee, J. D.; Lewis, A. C.; Pilling, M. J.; Seakins, P. W.; Carslaw, N.; Emmerson, K. M., High levels of the hydroxyl radical in the winter urban troposphere. Geophysical Research Letters **2004,** 31 (18), L18112.

51. Harrison, R. M.; Yin, J.; Tilling, R. M.; Cai, X.; Seakins, P. W.; Hopkins, J. R.; Lansley, D. L.; Lewis, A. C.; Hunter, M. C.; Heard, D. E.; Carpenter, L. J.; Creasey, D. J.; Lee, J. D.; Pilling, M. J.; Carslaw, N.; Emmerson, K. M.; Redington, A.; Derwent, R. G.; Penkett, S. A., Measurement and modelling of air pollution and atmospheric chemistry in the U.K. West Midlands conurbation: Overview of the PUMA Consortium project. Science of The Total Environment **2006,** 360 (1-3), 5-25.

52. Wadt, W. R.; Goddard-III, W. A., Electronic structure of the Criegee intermediate. Ramifications for the mechanism of ozonolysis. Journal of the American Chemical Society **1975,** 97 (11), 3004–3021.

53. Su, Y.-T.; Huang, Y.-H.; Witek, H. A.; Lee, Y.-P., Infrared absorption spectrum of the simplest Criegee intermediate CH2OO. Science **2013,** 340 (6129), 174-176.

54. Osborn, D. L.; Taatjes, C. A., The physical chemistry of Criegee intermediates in the gas phase. International Reviews in Physical Chemistry **2015,** 34 (3), 309-360.

55. Womack, C. C.; Martin-Drumel, M.-A.; Brown, G. G.; Field, R. W.; McCarthy, M. C., Observation of the simplest Criegee intermediate CH2OO in the gas-phase ozonolysis of ethylene. Science Advances **2015,** 1 (2), e1400105.

56. Malkin, T. L.; Goddard, A.; Heard, D. E.; Seakins, P. W., Measurements of OH and HO2 yields from the gas phase ozonolysis of isoprene. Atmospheric Chemistry and Physics **2010,** 10 (3), 1441–1459.

57. Walker, H. M.; Stone, D.; Ingham, T.; Vaughan, S.; Cain, M.; Jones, R. L.; Kennedy, O. J.; McLeod, M.; Ouyang, B.; Pyle, J.; Bauguitte, S.; Bandy, B.; Forster, G.; Evans, M. J.; Hamilton, J. F.; Hopkins, J. R.; Lee, J. D.; Lewis, A. C.; Lidster, R. T.; Punjabi, S.; Morgan, W. T.; Heard, D. E., Night-time measurements of HOX during the RONOCO project and analysis of the sources of HO2. Atmospheric Chemistry and Physics **2015,** 15 (14), 8179–8200.

58. Atkinson, R.; Baulch, D. L.; Cox, R. A.; Crowley, J. N.; R. F. Hampson, J.; Hynes, R. G.; Jenkin, M. E.; Kerr, J. A.; Rossi, M. J.; Troe, J. Summary of evaluated kinetic and photochemical data for atmospheric chemistry: IUPAC subcommittee on gas kinetic data evaluation for atmospheric chemistry; 2006.

59. Khan, M. A. H.; Percival, C. J.; Caravan, R. L.; Taatjes, C. A.; Shallcross, D. E., Criegee intermediates and their impacts on the troposphere. Environmental Science: Processes and Impacts **2018,** 20 (3), 437-453.

60. Pierce, J. R.; Evans, M. J.; Scott, C. E.; D'Andrea, S. D.; Farmer, D. K.; Swietlicki, E.; Spracklen, D. V., Weak global sensitivity of cloud condensation nuclei and the aerosol indirect effect to Criegee + SO2 chemistry. Atmospheric Chemistry and Physics **2013,** 13 (6), 3163–3176.

61. Vereecken, L.; Novelli, A.; Taraborrelli, D., Unimolecular decay strongly limits the atmospheric impact of Criegee intermediates. Physical Chemistry Chemical Physics **2017,** 19 (47), 31599-31612.

62. Khan, M. A. H.; Morris, W. C.; Galloway, M.; Shallcross, B. M. A.; Percival, C. J.; Shallcross, D. E., An estimation of the levels of stabilized Criegee

intermediates in the UK urban and rural atmosphere using the steady-state approximation and the potential effects of these intermediates on tropospheric oxidation cycles. International Journal of Chemical Kinetics **2017,** 49 (8), 611-621.

63. Johnson, D.; Marston, G., The gas-phase ozonolysis of unsaturated volatile organic compounds in the troposphere. Chemical Society Reviews **2008,** 37 (4), 699-716.

64. Donahue, N. M.; Drozd, G. T.; Epstein, S. A.; Presto, A. A.; Kroll, J. H., Adventures in ozoneland: down the rabbit-hole. Physical Chemistry Chemical Physics **2011,** 13 (23), 10848-10857.

65. Ryzhkova, A. B.; Ariya, P. A., A theoretical study of the reactions of parent and substituted Criegee intermediates with water and the water dimer. Physical Chemistry Chemical Physics **2004,** 6 (21), 5042-5050.

66. Presto, A. A.; Donahue, N. M., Ozonolysis fragment quenching by nitrate formation: The pressure dependence of prompt OH radical formation. The Journal of Physical Chemistry A **2004,** 108 (42), 9096–9104.

67. Cox, R. A.; Penkett, S. A., Oxidation of atmospheric SO2 by products of the ozone–olefin reaction. Nature **1971,** 230 (5292), 321–322.

68. Cox, R. A.; Penkett, S. A., Aerosol formation from sulphur dioxide in the presence of ozone and olefinic hydrocarbons. Journal of the Chemical Society, Faraday Transactions 1 **1972,** 68 (0), 1735-1753.

69. Taatjes, C. A.; Meloni, G.; Selby, T. M.; Trevitt, A. J.; Osborn, D. L.; Percival, C. J.; Shallcross, D. E., Direct observation of the gas-phase Criegee intermediate (CH2OO). Journal of the American Chemical Society **2008,** 130 (36), 11883–11885.

70. Welz, O.; Savee, J. D.; Osborn, D. L.; Vasu, S. S.; Percival, C. J.; Shallcross, D. E.; Taatjes, C. A., Direct kinetic measurements of Criegee intermediate (CH2OO) formed by reaction of CH2I with O2. Science **2012,** 335 (6065), 204-207.

71. Nguyen, M. T.; Nguyen, T. L.; Ngan, V. T.; Nguyen, H. M. T., Heats of formation of the Criegee formaldehyde oxide and dioxirane. Chemical Physics Letters **2007,** 448 (4-6), 183-188.

72. Cool, T. A.; Wang, J.; Nakajima, K.; Taatjes, C. A.; AndrewMcllroy, Photoionization cross sections for reaction intermediates in hydrocarbon combustion. International Journal of Mass Spectrometry **2005,** 247 (1-3), 18-27.

73. Beames, J. M.; Liu, F.; Lu, L.; Lester, M. I., Ultraviolet spectrum and photochemistry of the simplest Criegee intermediate CH2OO. Journal of the American Chemical Society **2012,** 134 (49), 20045-20048.

74. Sheps, L., Absolute ultraviolet absorption spectrum of a Criegee intermediate CH2OO. The Journal of Physical Chemistry Letters **2013,** 4 (24), 4201-4205.

75. Ting, W.-L.; Chen, Y.-H.; Chao, W.; Smith, M. C.; Lin, J. J.-M., The UV absorption spectrum of the simplest Criegee intermediate CH2OO. Physical Chemistry Chemical Physics **2014,** 16 (22), 10438-10443

76. Foreman, E. S.; Kapnas, K. M.; Jou, Y.; Kalinowski, J.; Feng, D.; Gerber, R. B.; Murray, C., High resolution absolute absorption cross sections of the B1A'–X1A' transition of the CH2OO biradical. Physical Chemistry Chemical Physics **2015,** 17 (48), 32539-32546.

77. Beames, J. M.; Liu, F.; Lu, L.; Lester, M. I., UV spectroscopic characterization of an alkyl substituted Criegee intermediate CH3CHOO. The Journal of Chemical Physics **2013,** 138 (24), 244307.

78. Taatjes, C. A.; Welz, O.; Eskola, A. J.; Savee, J. D.; Scheer, A. M.; Shallcross, D. E.; Rotavera, B.; Lee, E. P. F.; Dyke, J. M.; Mok, D. K. W.; Osborn, D. L.; Percival, C. J., Direct measurements of conformer-dependent reactivity of the Criegee intermediate CH3CHOO. Science **2013,** 340 (6129), 177-180.

79. Sheps, L.; Scully, A. M.; Au, K., UV absorption probing of the conformer-dependent reactivity of a Criegee intermediate CH3CHOO Physical Chemistry Chemical Physics **2014,** 16 (48), 26701-26706.

80. Liu, F.; Beames, J. M.; Petit, A. S.; McCoy, A. B.; Lester, M. I., Infrared-driven unimolecular reaction of CH3CHOO Criegee intermediates to OH radical products. Science **2014,** 345 (6204), 1596-1598.

81. Smith, M. C.; Ting, W.-L.; Chang, C.-H.; Takahashi, K.; Boering, K. A.; Lin, J. J.-M., UV absorption spectrum of the C2 Criegee intermediate CH3CHOO. The Journal of Chemical Physics **2014,** 141 (7), 074302.

82. Liu, F.; Beames, J. M.; Green, A. M.; Lester, M. I., UV spectroscopic characterization of dimethyl- and ethyl-substituted carbonyl oxides. The Journal of Physical Chemistry A **2014,** 118 (12), 2298–2306.

83. Liu, F.; Beames, J. M.; Lester, M. I., Direct production of OH radicals upon CH overtone activation of (CH3)2COO Criegee intermediates. The Journal of Chemical Physics **2014,** 141 (23), 234312.

84. Smith, M. C.; Chao, W.; Takahashi, K.; Boering, K. A.; Lin, J. J.-M., Unimolecular decomposition rate of the Criegee intermediate (CH3)2COO measured directly with UV absorption spectroscopy. The Journal of Physical Chemistry A **2016,** 120 (27), 4789–4798.

85. Lee, Y.-P., Perspective: Spectroscopy and kinetics of small gaseous Criegee intermediates. The Journal of Chemical Physics **2015,** 143 (2), 020901.

86. Su, Y.-T.; Lin, H.-Y.; Putikam, R.; Matsui, H.; Lin, M. C.; Lee, Y.-P., Extremely rapid self-reaction of the simplest Criegee intermediate CH2OO and its implications in atmospheric chemistry. Nature Chemistry **2014,** 6 (6), 477–483.

87. Buras, Z. J.; Elsamra, R. M. I.; Green, W. H., Direct determination of the simplest Criegee intermediate (CH2OO) self reaction rate. The Journal of Physical Chemistry Letters **2014,** 5 (13), 2224-2228.

88. Ting, W.-L.; Chang, C.-H.; Lee, Y.-F.; Matsui, H.; Lee, Y.-P.; Lin, J. J.-M., Detailed mechanism of the CH2I + O2 reaction: Yield and self-reaction of the simplest Criegee intermediate CH2OO. The Journal of Chemical Physics **2014,** 141 (10), 104308.

89. Chhantyal-Pun, R.; Davey, A.; Shallcross, D. E.; Percival, C. J.; Orr-Ewing, A. J., A kinetic study of the CH2OO Criegee intermediate self-reaction,

reaction with SO2 and unimolecular reaction using cavity ring-down spectroscopy. Physical Chemistry Chemical Physics **2015,** 17 (5), 3617-3626.

90. Stone, D.; Blitz, M.; Daubney, L.; Ingham, T.; Seakins, P., CH2OO Criegee biradical yields following photolysis of CH2I2 in O2†. Physical Chemistry Chemical Physics **2013,** 15 (44), 19119-19124.

91. Nakajima, M.; Endo, Y., Communication: Determination of the molecular structure of the simplest Criegee intermediate CH2OO. The Journal of Chemical Physics **2013,** 139 (10), 101103.

92. Stone, D.; Blitz, M.; Daubney, L.; Howes, N. U. M.; Seakins, P., Kinetics of CH2OO reactions with SO2, NO2, NO, H2O and CH3CHO as a function of pressure. Physical Chemistry Chemical Physics **2014,** 16 (3), 1139-1149.

93. Liu, Y.; Bayes, K. D.; Sander, S. P., Measuring rate constants for reactions of the simplest Criegee intermediate (CH2OO) by monitoring the OH radical. The Journal of Physical Chemistry A **2014,** 118 (4), 741–747.

94. Huang, H.-L.; Chao, W.; Lin, J. J.-M., Kinetics of a Criegee intermediate that would survive high humidity and may oxidize atmospheric SO2. Proceedings of the National Academy of Sciences **2015,** 112 (35), 10857-10862.

95. Chhantyal-Pun, R.; Welz, O.; Savee, J. D.; Eskola, A. J.; Lee, E. P. F.; Blacker, L.; Hill, H. R.; Ashcroft, M.; Khan, M. A. H.; Lloyd-Jones, G. C.; Evans, L.; Rotavera, B.; Huang, H.; Osborn, D. L.; Mok, D. K. W.; Dyke, J. M.; Shallcross, D. E.; Percival, C. J.; Orr-Ewing, A. J.; Taatjes, C. A., Direct measurements of unimolecular and bimolecular reaction kinetics of the Criegee intermediate (CH3)2COO. the Journal of Physical Chemistry A **2017,** 121 (1), 4-15.

96. Chao, W.; Hsieh, J.-T.; Chang, C.-H.; Lin, J. J.-M., Direct kinetic measurement of the reaction of the simplest Criegee intermediate with water vapor. Science **2015,** 347 (6223), 751-754.

97. Lewis, T. R.; Blitz, M. A.; Heard, D. E.; Seakins, P. W., Direct evidence for a substantive reaction between the Criegee intermediate, CH2OO, and the water vapour dimer. Physical Chemistry Chemical Physics **2015,** 17 (7), 4859-4863.

98. Smith, M. C.; Chang, C.-H.; Chao, W.; Lin, L.-C.; Takahashi, K.; Boering, K. A.; Lin, J. J.-M., Strong negative temperature dependence of the simplest Criegee intermediate CH2OO reaction with water dimer. The Journal of Physical Chemistry Letters **2015,** 6 (14), 2708–2713.

99. Sheps, L.; Rotavera, B.; Eskola, A. J.; Osborn, D. L.; Taatjes, C. A.; Au, K.; Shallcross, D. E.; Khan, M. A. H.; Percival, C. J., The reaction of Criegee intermediate CH2OO with water dimer: primary products and atmospheric impact. Physical Chemistry Chemical Physics **2017,** 19 (33), 21970-21979.

100. Welz, O.; Eskola, A. J.; Sheps, L.; Rotavera, B.; Savee, J. D.; Scheer, A. M.; Osborn, D. L.; Lowe, D.; Booth, A. M.; Xiao, P.; Khan, M. A. H.; Percival, C. J.; Shallcross, D. E.; Taatjes, C. A., Rate coefficients of C1 and C2 Criegee intermediate reactions with formic and acetic acid near the collision limit: Direct kinetics measurements and atmospheric implications. Angewandte Chemie International Edition **2014,** 53 (18), 4547-4550.

101. Chhantyal-Pun, R.; McGillen, M. R.; Beames, J. M.; Khan, M. A. H.; Percival, C. J.; Shallcross, D. E.; Orr-Ewing, A. J., Temperature-dependence of the rates of reaction of trifluoroacetic acid with Criegee intermediates. Angewandte Chemie International Edition **2017,** 56 (31), 9044-9047.

102. Mauldin-III, R. L.; Berndt, T.; Sipilä, M.; Paasonen, P.; Petäjä, T.; Kim, S.; Kurtén, T.; Stratmann, F.; Kerminen, V.-M.; Kulmala, M., A new atmospherically relevant oxidant of sulphur dioxide. Nature **2012,** 488 (7410), 193–196.

103. Newland, M. J.; Nelson, B. S.; Muñoz, A.; Ródenas, M.; Vera, T.; Tárrega, J.; Rickard, A. R., Trends in stabilisation of Criegee intermediates from alkene ozonolysis. Physical Chemistry Chemical Physics **2020,** 22 (24), 13698-13706.

104. Newland, M. J.; Rickard, A. R.; Alam, M. S.; Vereecken, L.; Muñoz, A.; Ródenas, M.; Bloss, W. J., Kinetics of stabilised Criegee intermediates derived from alkene ozonolysis: reactions with SO2, H2O and decomposition under boundary layer conditions. Physical Chemistry Chemical Physics **2015,** 17 (6), 4076-4088.

105. Newland, M. J.; Rickard, A. R.; Vereecken, L.; Muñoz, A.; Ródenas, M.; Bloss, W. J., Atmospheric isoprene ozonolysis: impacts of stabilised Criegee intermediate reactions with SO2, H2O and dimethyl sulfide. Atmospheric Chemistry and Physics **2015,** 15 (16), 9521–9536.

106. Newland, M. J.; Rickard, A. R.; Sherwen, T.; Evans, M. J.; Vereecken, L.; Muñoz, A.; Ródenas, M.; Bloss, W. J., The atmospheric impacts of monoterpene ozonolysis on global stabilised Criegee intermediate budgets and SO2 oxidation: experiment, theory and modelling. Atmospheric Chemistry and Physics **2018,** 18 (8), 6095–6120.

Chapter 2

Theory of Gas Phase Kinetics and Photochemistry

The ability to understand the chemistry occurring in the atmosphere requires knowledge and understanding of the kinetics and photochemistry of atmospheric species. This chapter introduces the concepts of chemical kinetics, i.e. the rate at which species interact with each other and chemical reactions take place, and photochemistry, i.e. the ways in which species interact with radiation and the chemical effects of light.

2.1 Rate Theory of Gas Phase Kinetics

Reaction kinetics is a branch of physical chemistry concerning the measurement of rates of chemical reactions where a chemical reaction is defined as the transformation of chemical compounds from reactants to products. Chemical reactions in atmospheric chemistry can occur over a vast range of different timescales.[1] Although reaction kinetics was limited to the study of relatively slow reactions until the mid-20th century, the development of new techniques exploiting faster electronics, lasers and more sensitive detection techniques has allowed for the kinetics of increasingly reactive species to be probed.[2] Advances in the field of measuring increasingly fast rates of reaction has in fact surpassed reaction kinetics and led to the observation of reaction dynamics, i.e. the mechanism by which a reaction takes place, on the femtosecond timescale (10^{-15} s).[3]

A general gas phase chemical reaction can be described as:

$$a\mathrm{A} + b\mathrm{B} \rightarrow c\mathrm{C} + d\mathrm{D} \qquad \text{(R2.1)}$$

where A, B, C, and D are chemical species and *a*, *b*, *c*, and *d* are the absolute values of the stoichiometric coefficients for each species, which are negative for reactants and positive for products.

The rate of reaction, *r*, is defined as the rate of decrease in the concentration of reactants per unit time, $-\frac{d[\mathrm{A}]}{dt}$, or the rate of increase in the concentration of products

per unit time, $+\frac{d[C]}{dt}$. A generic rate equation describing r can be written for all chemical reactions, which, for the general reaction shown above is:

$$r = -\frac{1}{a}\frac{d[A]}{dt} = k[A]^{\alpha}[B]^{\beta} \qquad \text{(Equation 2.1)}$$

where $-\frac{d[A]}{dt}$ is the rate of change of A, k is the rate coefficient (which can vary with both temperature and pressure), [A] and [B] are the concentrations of reactants A and B respectively, and α and β are the orders of the reaction with respect to [A] and [B] respectively. The exponents α and β can only be determined experimentally and provide information on how the rate of reaction varies with the concentration of the associated reactant. It should be noted, however, that the rate equation of certain limited reactions can be predicted provided that the mechanism of the reaction is well understood. The overall order of the reaction is given by the sum of the exponents in the rate equation ($\alpha + \beta$).

An elementary reaction is a one-step chemical reaction, in which one or more chemical reactant species react directly to form products in a single reaction step and with a single transition state, where a transition state is defined as a particular configuration along the reaction coordinate corresponding to the maximum potential energy along the minimum energy pathway, so represents a saddle point on the potential energy surface (PES). A reaction coordinate is an abstract one-dimensional coordinate which represents progress along the reaction pathway upon conversion from reactants to products. A PES is defined as a surface analogous to a landscape which describes the energy of a system, particularly a collection of atoms, as a function of certain parameters known as reaction coordinates, typically the progress of the reaction, the positions of the atoms or the bond lengths between atoms.

For an elementary reaction, the order of the reaction with respect to a particular reactant is equivalent to the absolute value of the stoichiometric number for that reactant. The molecularity of a reaction or step is described as the number of species (molecules, ions, atoms or free radicals) which come together to collide and react. It follows then, that for an elementary reaction, the molecularity of the reaction corresponds to the total number of reactant molecules participating in the reaction, and is equivalent to the overall order of the reaction. An elementary reaction involving

only one reactant species is termed a unimolecular reaction and is first-order, an elementary reaction involving two species is termed a bimolecular reaction and is second-order, and an elementary reaction involving three species is termed a termolecular reaction and is third-order. For bimolecular reactions, rate coefficients can be made simpler to determine by monitoring the reaction under pseudo-first-order conditions under which pseudo-first-order kinetics apply. Under such pseudo-first-order conditions, the concentration of one reactant species is in large excess relative to the concentration of the other reactant species, hence the concentration of the species in excess is, in effect, considered to be constant.

For an elementary reaction, the rate law or rate equation, which is the equation that links the initial or forward rate of reaction with the concentration or pressures of the reactant species taking part in the chemical reaction and the constant parameters of the reaction such as rate coefficients, can be predicted from the stoichiometry of each participating reactant species. On the other hand, for a complex reaction, which is described in further detail below, the rate equation and overall order of reaction cannot be reliably deduced from the stoichiometry of the overall reaction and must be determined experimentally, since the unknown reaction mechanism for the reaction comprises more than one elementary step. Once the experimental rate equation has been determined, it if often useful for establishing the reaction mechanism by which the reaction takes place.

A complex reaction, otherwise known as a multistep, stepwise or overall reaction, is a chemical reaction with one or more reaction intermediates and consists of at least two consecutive known elementary reactions. In complex reactions, not all bonds are broken and formed at the same time as in elementary reactions, hence one or more reaction intermediates appear within the reaction pathway upon going from the reactants to the products. A reaction intermediate is defined as a molecular entity that is formed from the reactants, or preceding intermediates, and reacts further to give the products, or succeeding intermediates, of a chemical reaction, i.e. it is the reaction product of each of the steps in a multistep reaction, except for the last one which forms the final product(s). Since reactive intermediates are usually short lived, they are very seldom isolated.

In general, there is one relatively very slow elementary step within the sequence of elementary steps making up the complex reaction. This slowest individual elementary reaction within the reaction mechanism is referred to as the rate-determining step (RDS) of the reaction, i.e. the overall reaction cannot proceed any faster than this RDS proceeds, and can often be used to approximately determine the overall rate of the reaction. Species involved in, or prior to, this RDS will normally appear in the rate equation; conversely species involved after the RDS do not appear in the rate equation, i.e. the reaction rate is independent of, and hence zero-order with respect to, the concentration of these species.

Experimental investigations and modelling of such complex reactions require understanding of the fundamental elementary reactions making up the complex reaction. Techniques employed to investigate the rates of complex reactions in relative isolation involve simplification of the reaction *via* detailed knowledge of each of the elementary processes taking place. Details of such experiments within the scope of this thesis are provided alongside the details of the corresponding reaction system in Chapter 5, in which the kinetics of the $CH_2OO + CH_2OO$ and the $CH_2OO + I$ reactions are discussed in detail, with the mechanism used to describe the reactions occurring in this complex system including the reaction of $CH_2I + O_2$ to generate CH_2OO and the subsequent reactions of the simultaneously generated CH_2IO_2 peroxy radical.

2.1.1 The Steady State Approximation

For a complex reaction, it is often possible to derive the overall rate equation from a combination of each of the multiple elementary rate equations making up the complex rate equation, using the steady-state approximation (SSA). The SSA describes a situation in which it is assumed that, after an initial induction period, the concentrations of reactive reaction intermediates in a system reach a small and constant level. Thus, for a reaction consisting of the elementary reactions:

$$A + B \rightarrow C \qquad \text{(R2.2)}$$

$$C + D \rightarrow P_1 + P_2 \qquad \text{(R2.3)}$$

$$C \rightarrow P_3 + P_4 \qquad \text{(R2.4)}$$

the rate equation for the rate of formation of products can be written as:

$$r = +\frac{d[P_1]}{dt} = +\frac{d[P_2]}{dt} = k_{2.3}[C][D]$$
$$r = +\frac{d[P_3]}{dt} = +\frac{d[P_4]}{dt} = k_{2.4}[C] \qquad \text{(Equation 2.2)}$$

The SSA requires that the intermediate species have a small and invariant concentration. For this to be true, the rate of removal of the intermediate species must far exceed its rate of production, i.e. the step(s) or elementary reaction(s) constituting loss of the intermediate species (R2.3 and R2.4) are much faster than those constituting its formation (R2.2) hence $k_{2.3} >> k_{2.2}$ and $k_{2.4} >> k_{2.2}$ with a criterion commonly used being that $k_{2.3}/k_{2.2} \geq 10$ and $k_{2.4}/k_{2.2} \geq 10$. This is often the case for reactive intermediate species since they are formed slowly and react readily, so their concentration does not build up and remains low. Application of the SSA involves setting the net rate of change of the concentration of the reaction intermediate in the reaction mechanism equal to zero, i.e. its concentration as constant, so that the kinetic equations can be simplified by setting the rate of formation of the intermediate equal to the rate of its destruction. It is assumed that the time required to achieve this steady-state concentration is negligible compared to the total reaction time.

In this case, the rate equation can be simplified by applying the SSA to species C:

$$+\frac{d[C]}{dt} = k_{2.2}[A][B] - (k_{2.3}[C][D] + k_{2.4}[C]) \approx 0 \qquad \text{(Equation 2.3)}$$

which, upon rearranging, gives the steady state concentration of species C as:

$$[C] = \frac{k_{2.2}[A][B]}{k_{2.3}[D]+k_{2.4}} \qquad \text{(Equation 2.4)}$$

which can be substituted back into the rate equation for the formation of products. This thesis focuses on the direct detection of the reaction kinetics of Criegee intermediates, discussed in detail in Chapter 1. The SSA is applied to intermediate species in reaction systems and since Criegee intermediates are intermediate species in atmospheric reactions, they can be thought to exist in a steady state concentration in the atmosphere. For complex systems, such as those in Criegee intermediate reactions presented in this thesis and discussed further in Chapter 5, application of the SSA can give complex rate equations such as that shown above. This is true for any number of product channels for an overall reaction with any combination of reactions.

2.2 Temperature and Pressure Dependence of Rate Coefficients

Rate coefficients often depend on temperature and/or pressure conditions, which can be probed by studying rates of reactions over a range of temperatures and pressures. Indeed, the rate coefficients of many atmospheric and combustion reactions can vary considerably over a relatively narrow range of temperatures and pressures.[4] Since both temperature and pressure within the Earth's atmosphere vary sufficiently enough to cause significant changes to rate coefficients of certain reactions (as shown in Figure 1.1 in Chapter 1), it is important to understand the fundamental concepts behind the temperature and pressure dependence of rate coefficients. The experiments reported in this thesis were conducted at room temperature and a range of pressures below atmospheric pressure. Despite determination of chemical kinetics and hence rates of chemical reactions relying upon experimental measurements, theoretical approaches can also be utilised to determine rate coefficients. As with experimental measurements, advances in technology has enabled theoretical calculations to be carried out much quicker, cheaper and more accurately than in previous years.

2.2.1 Temperature Dependence

In reaction kinetics, the Arrhenius equation is used to describe positive temperature dependence. An empirical experimental observation is that, for many reactions, the rate coefficient, *k*, varies with temperature according to this Arrhenius equation[5]:

$$k = A \exp\left(-{}^{E_a}/_{RT}\right) \qquad \text{(Equation 2.5)}$$

where *A* is the pre-exponential factor and represents the frequency of collisions between reactant species whether they result in product formation or not but occurring with the correct orientation to react, E_a is the activation energy of the reaction and is the minimum amount of energy that is required by and must be provided to reactant species to overcome the reaction barrier and result in a chemical reaction, *R* is the gas constant and *T* is the absolute temperature.

The pre-exponential factor and the activation energy are collectively described as the Arrhenius parameters, and are used to parameterise the temperature dependence of the rate coefficient *k* for a particular reaction. It can be seen from the formula for the

Arrhenius equation that the exponential term, exp(-E_a/RT), increases with temperature, therefore the rate of reaction will also increase as temperature increases for a reaction involving species which exhibit Arrhenius behaviour, as depicted in Figure 2.1. Several theories have been advanced to explain this temperature dependence, with two of the fundamental theories commonly used to determine rate coefficients of elementary reactions exhibiting positive temperature dependence being simple collision theory (SCT) and transition state theory (TST), brief summaries for which are provided below.

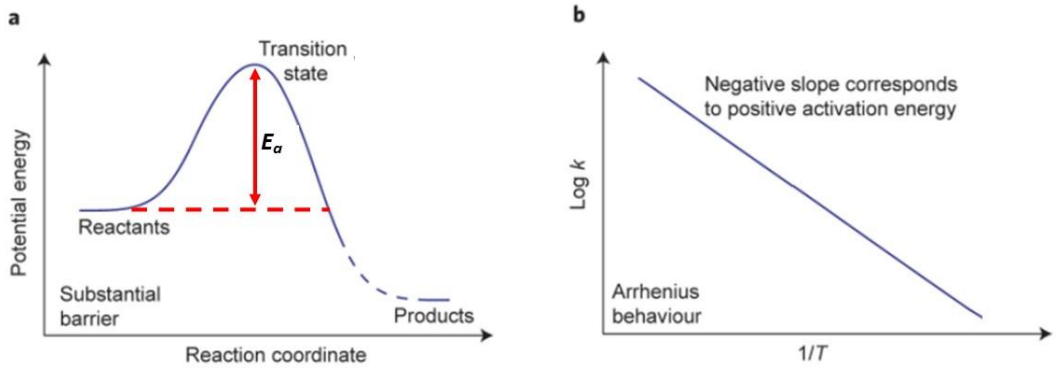

Figure 2.1: Schematic representation of a) a typical reaction coordinate or potential energy surfaces (PES) for an exothermic reaction with a substantial barrier to reaction products, which adheres approximately to the Arrhenius equation (Equation 2.5), showing the potential energy of the system as the reaction takes place, and b) the typical Arrhenius plot corresponding to this system where an Arrhenius plot is defined as a plot of the log of the rate coefficient k as a function of the inverse of the temperature T, and should be linear with a slope equal to -E_a/R for reactions which exhibit Arrhenius behaviour. Adapted from reference 6.[6]

2.2.1.1 Simple Collision Theory

At the simplest and most basic level, rate coefficients for elementary chemical reactions in the gas phase can be rationalised in terms of, and calculated by using, simple collision theory (SCT). It is assumed in SCT that the reacting species (atoms and molecules) behave as hard, structureless spheres undergoing elastic collisions, and that a reaction may only occur upon/during a collision, i.e. that no intermolecular forces are in operation between the species. SCT states that when reactant species collide, only a certain fraction of collisions, called successful collisions, result in a perceptible or notable change. In order to break the existing bonds and form the new

bonds, at the moment of impact these successful collisions must have enough energy, also known as the activation energy, to overcome the energy barrier to reaction, resulting in the reaction products being formed. Increasing the concentration of the reactant(s) leads to more collisions overall and hence more successful collisions, while increasing the temperature increases the average kinetic energy of the reactant species and hence the number of collisions with enough energy to form products, both of which lead to an increase in the overall reaction rate.

An estimation of the rate coefficient, k, for a reaction between two species A and B can thus be calculated using SCT,[7] by equating the rate of reaction, r, for the reaction between these two species to the total number of collisions between the reactants per unit volume and time, also known as the collision frequency, Z_{AB}, multiplied by the fraction of species with sufficient energy to react upon collision, F:

$$r = Z_{AB}\, F \qquad \text{(Equation 2.6)}$$

The collision frequency, Z_{AB}, is obtained from the kinetic theory of gases and is given by:

$$Z_{AB} = V_{col}\, N_A{}^2\, [A][B] \qquad \text{(Equation 2.7)}$$

where V_{col} is the collision volume which describes the notional volume swept out by a moving molecule in unit time, N_A is Avogadro's constant, and [A] and [B] are the concentrations of reactant species A and B in molar units respectively. The collision volume is determined by the product of the collisional area of the reaction between species A and B, also known as the collision cross-section, σ_{AB}, and the mean relative speed of species A and B, $\bar{c}_{rel}$:

$$V_{col} = \sigma_{AB}\, \bar{c}_{rel} = \sigma_{AB} \left(\frac{8 k_B T}{\pi \mu_{AB}} \right)^{1/2} \qquad \text{(Equation 2.8)}$$

where $\sigma_{AB} = \pi(r_A + r_B)^2$, r_A and r_B are the radii of species A and B respectively, k_B is the Boltzmann constant, T is the temperature (K), μ_{AB} is the reduced mass of reactant species A and B, $\mu_{AB} = \frac{m_A m_B}{m_A + m_B}$, m_A and m_B are the masses of species A and B respectively, and the term $\left(\frac{8k_BT}{\pi\mu_{AB}}\right)^{1/2}$ represents the mean relative speed of A and B. Substituting this formula for collision volume into the equation for the collision frequency gives:

$$Z_{AB} = \sigma_{AB} \left(\frac{8k_B T}{\pi \mu_{AB}} \right)^{1/2} N_A{}^2 \, [A][B] \qquad \text{(Equation 2.9)}$$

The fraction of colliding species with sufficient energy to overcome an energy barrier (the activation energy) to rearrangement of electrons during the reaction, *F*, is given by the fraction of species with a kinetic energy above a certain critical value, ε, within a distribution of kinetic energies. This distribution of kinetic energies, $f(E)$ is described by:

$$f(E) = \frac{1}{k_B T} \exp\left(-E/k_B T\right) \qquad \text{(Equation 2.10)}$$

Integration of this distribution of kinetic energies between limits of ε, the critical energy for reaction, and infinity, gives the fraction of species, *F*, with kinetic energy above the critical value:

$$F = f(E \geq \varepsilon) = \int_{\varepsilon}^{\infty} \frac{1}{k_B T} \exp\left(-E/k_B T\right) dE \qquad \text{(Equation 2.11)}$$

$$= \frac{1}{k_B T} \int_{\varepsilon}^{\infty} \exp\left(-E/k_B T\right) dE \qquad \text{(Equation 2.12)}$$

$$= \exp\left(-\varepsilon/k_B T\right) \qquad \text{(Equation 2.13)}$$

SCT therefore predicts the rate of reaction, r, of the elementary chemical reaction between two species A and B to be given by:

$$r = \sigma_{AB} \left(\frac{8k_B T}{\pi \mu_{AB}} \right)^{1/2} N_A{}^2 \, [A][B] \exp\left(-\varepsilon/k_B T\right) \qquad \text{(Equation 2.14)}$$

When this expression for rate of reaction is compared to the rate equation for an elementary reaction, it is derived that, for such a reaction, SCT predicts the rate coefficient, *k*, to be given by:

$$k = \sigma_{AB} \left(\frac{8k_B T}{\pi \mu_{AB}} \right)^{1/2} N_A{}^2 \exp\left(-\varepsilon/k_B T\right) \qquad \text{(Equation 2.15)}$$

which compares well with the experimentally determined Arrhenius equation given above. This expression offers the first theoretical explanation for the Arrhenius equation on a molecular basis.

Upon comparison of rate coefficients calculated by SCT with known rate coefficients determined experimentally, it is evident that this theory fails to estimate rate coefficients accurately, with reaction rate coefficients of more complex species being increasingly more inaccurate. This can be explained by the fact that in the SCT, species have been treated as spherical and so able to react in all directions, which is not the case since the orientation of the collisions is not always proper for the reaction, i.e. a reaction will only occur between species A and B until and unless they are oriented in the correct manner.

A new concept must be introduced into the SCT to rectify this problem, termed the steric factor, ρ_S, which represents the probability that the two reacting species will collide with the proper orientation to yield the corresponding product(s), and is defined as the ratio between the experimental value for the pre-exponential factor A from the Arrhenius equation and the calculated value for the collision frequency Z_{AB}:

$$\rho_S = \frac{A_{\text{experimental}}}{Z_{\text{AB, calculated}}} \qquad \text{(Equation 2.16)}$$

The result of the steric factor is often less than unity, and is usually lower for more complex reactant species. This is reasonable since the more complex and unsymmetrical the structure for a reactant, the more orientational restrictions it is likely to have and the more precise the correct orientation is likely to be. It should be noted that the steric factor does try to account for the discrepancy between experimentally determined and theoretically calculated rate coefficients, but it is not predictive and there is no generic formula to calculate it, it is simply the ratio between two differently determined results, one empirically and the other theoretically. Difficulty in assessing this steric factor still leaves the SCT imperfect for the calculation of reaction rate coefficients.

Using the SCT is a good starting point for the estimation of reaction rate coefficients since it provides insight into the physical description and significance of the Arrhenius parameters, and can qualitatively predict the broad features of many rate coefficients, particularly the exponential dependence of k on temperature. However, given that it

cannot make accurate quantitative predictions of rate coefficients, its use presents challenges in that it is not practically applicable beyond a certain point, and that results determined *via* its use may potentially be inaccurate. The limitations of the theory are embedded in its assumptions that reacting species are equivalent to hard spheres which react instantaneously on collision if sufficient energy is available, and that intermolecular forces and internal energy distributions are negligible. These assumptions ignore the structure of the reactant species and overlook the importance of intermolecular forces, both of which can, to some extent, control if and how reactions involving these species materialise.

In reality, reactions will in fact only occur if the reacting species collide in such a way that certain steric requirements are met, and reactions will not be instantaneous since a finite time is required for structural and energetic redistributions to occur. Furthermore, there are often long-distance interactive forces occurring between the reacting species, leading to both temporary and permanent changes. Incorporation of these ideas into SCT has proven to be problematic, hence a more sophisticated model is required to obtain more accurate theoretical estimations of reaction rate coefficients.

2.2.1.2 Transition State Theory

Transition state theory (TST), sometimes referred to as activated complex theory, explains the reaction rates of elementary chemical reactions in the gas phase by considering the reaction to take place as a trajectory across a PES. The PES for the co-linear reaction $A + BC \rightarrow AB + C$ is shown in Figure 2.2. Unlike SCT, TST accounts for the formation of an intermediary species between the reactants and products of a reaction, termed the activated complex, $ABC^{\ddagger}$, which is the cluster of atoms around the highest energy point along the reaction coordinate in the PES. For the reaction shown, as A and BC come into proximity they distort, and the potential energy rises to this maximum point or peak in the PES, at which the exact configuration of the cluster is called the transition state.

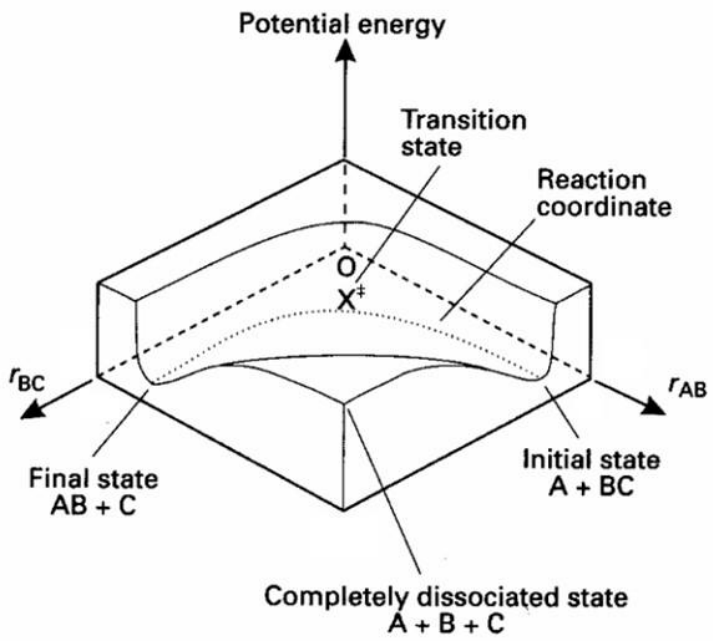

Figure 2.2: 3D potential energy surface (PES) for the reaction A + BC. Reproduced from reference 7.[7]

It should be noted that the terms transition state and activated complex are sometimes used interchangeably, however they mean different things, so it is important to highlight the specific differences between them. The transition state, located at the peak of the PES for the reaction, refers only to the highest potential energy of the atoms participating in the chemical reaction and is the one and only molecular configuration that occurs at this point, whereas the activated complex covers a range of configurations that the atoms form on their way from reactants to products and may be present at any point near the transition state.

TST treats the activated complex as existing in a special type of chemical equilibrium, known as the quasi-equilibrium, with the reactants, and assumes that once the transition state has been reached, it is impossible for this to re-form reactants and so inevitable that the reaction will proceed towards the formation of products. A quasi-equilibrium is described as a thermodynamic process during which the system only deviates from the equilibrium by an infinitesimal amount, i.e. a process that takes place so slowly such that the system appears to be static. It is also assumed in TST that the energy distribution of the reactant molecules is described by a Boltzmann distribution, and that a single reactive vibration of the activated complex, considered to be separable from all other vibrations and rotations of the complex, is responsible

for the motion over the energy barrier to reaction, i.e. this motion over the barrier is a classical process.

The overall reaction:

$$A + BC \rightarrow AB + C \qquad \text{(R2.5)}$$

upon applying the TST to fully describe the system, can be written as:

$$A + BC \rightleftharpoons ABC^{\ddagger} \rightarrow AB + C \qquad \text{(R2.6)}$$

and the rate equation, r, can be written as:

$$r = -\frac{d[A]}{dt} = -\frac{d[BC]}{dt} = k_{bimol}[A][BC]$$
$$r = +\frac{d[AB]}{dt} = +\frac{d[C]}{dt} = k^{\ddagger}[ABC^{\ddagger}] \qquad \text{(Equation 2.17)}$$

Since a quasi-equilibrium is present between the reactants and the intermediary species, the equilibrium constant for the quasi-equilibrium, K_{eq}, is:

$$K_{eq} = \frac{[ABC^{\ddagger}]}{[A][BC]} \qquad \text{(Equation 2.18)}$$

rearrangement of which means that the concentration of $ABC^{\ddagger}$ can be expressed in terms of the concentration of A and BC and the equilibrium constant:

$$[ABC^{\ddagger}] = K_{eq}[A][BC] \qquad \text{(Equation 2.19)}$$

Combining Equation 2.17 - Equation 2.19 derives a formula describing the rate of reaction:

$$r = k^{\ddagger}[ABC^{\ddagger}] = k^{\ddagger}K_{eq}[A][BC] = k_{bimol}[A][BC] \qquad \text{(Equation 2.20)}$$

from which it is evident that the bimolecular rate coefficient for the reaction, k_{bimol}, is given by:

$$k_{bimol} = k^{\ddagger}K_{eq} \qquad \text{(Equation 2.21)}$$

It follows that before this rate coefficient k_{bimol} can be determined using TST, there are two parameters which must be defined, the rate coefficient $k^{\ddagger}$ and the equilibrium constant K_{eq}.

The equilibrium constant K_{eq} can be described, *via* a temperature dependent expression using the general result from statistical mechanics, as a product of an exponential function dependent upon the size of the activation barrier (denoted by ε in Equation 2.22), i.e. the energy difference between the zero-point energy of the reactants (A + BC) and the products (AB + C), determined by spectroscopy, and the total molecular partition functions of species A, BC and the activated complex $ABC^{\ddagger}$ which are called Q_A, Q_{BC} and $Q_{ABC^{\ddagger}}$ respectively, each made up of the product of the translational, rotational and vibrational partition functions of each species, calculated using statistical mechanics and spectroscopic data:

$$K_{eq} = \frac{Q_{ABC^{\ddagger}}}{Q_A Q_{BC}} \exp\left(-\varepsilon / k_B T\right) \qquad \text{(Equation 2.22)}$$

Since it is assumed that a single vibration, which is independent of all other vibrations and rotations in the activated complex, leads to dissociation of this activated complex $ABC^{\ddagger}$ to form products AB + C, the total partition function for the activated complex, $Q_{ABC^{\ddagger}}$, can be separated into two components, namely q, the vibrational partition function of $ABC^{\ddagger}$ describing the reactive vibration that leads to dissociation, and $Q_{ABC^{\ddagger}}'$, the total partition function of $ABC^{\ddagger}$ excluding the contribution from this reactive vibration:

$$Q_{ABC^{\ddagger}} = q\, Q_{ABC^{\ddagger}}' \qquad \text{(Equation 2.23)}$$

The vibrational partition function q can be approximated to:

$$q = \frac{k_B T}{h\nu} \qquad \text{(Equation 2.24)}$$

where ν is the frequency of the reactive vibration.

The rate coefficient $k^{\ddagger}$ is directly proportional to the frequency of the vibrational mode responsible for converting the activated complex to products, ν. However, every vibration does not necessarily lead to the formation of products, AB + C, as a fraction of the vibrations also lead to the formation of reactants, A + BC, so a proportionality constant, referred to as the transmission coefficient, κ, is introduced to account for the proportion of reactive vibrations, with vibrational frequency ν, which lead to product formation. It is worth noting that the transmission coefficient is often assumed to be unity. $k^{\ddagger}$ is thus determined to be:

$$k^{\ddagger} = \kappa\nu \qquad \text{(Equation 2.25)}$$

The overall rate coefficient for the reaction, k_{bimol}, is therefore determined by substituting the above factors into Equation 2.21, and can be defined as:

$$k_{\text{bimol}} = \kappa \frac{k_B T}{h} \frac{Q_{ABC^{\ddagger}}'}{Q_A Q_{BC}} \exp\left(-\varepsilon/k_B T\right) \qquad \text{(Equation 2.26)}$$

which again resembles the experimentally determined Arrhenius equation provided above. It is clear from the TST and SCT variations of the Arrhenius equation that rate coefficients often exhibit temperature dependence, a dependence which is proportional to the activation barrier of the reaction and can potentially be predicted for reactions which exhibit Arrhenius behaviour using these theories, however an advantage of TST over SCT is that it inherently includes molecular complexity.

Although there is generally good agreement between results of rate coefficients calculated using TST and experimentally determined rate coefficients, especially for small reaction systems for which accurate PESs are available, and certainly better agreement with experimental results than when compared to rate coefficients obtained using SCT, accurate predictions of rate coefficients are still not achieved. This is because the statistical mechanical formulation of TST, as described above, requires both the structure and vibrational frequencies of the transition state to be known accurately. This is very difficult in reality, particularly since many PESs are not accurate enough to provide such information. For many reactions, especially those involving larger species, it is often difficult to employ this form of TST in a meaningful manner due to the fact that the number of variables is too large. As such, despite it becoming increasingly possible to calculate transition state structures with reasonable reliability and comparison of the magnitude of the calculated and experimental rate coefficients providing information about the mechanism of the reaction, this form of TST is still not a fully predictive tool, particularly when used to explain the temperature dependence of rate coefficients of complex reactions.

Rather than employing this statistical mechanical method of extracting parameters for TST, involving calculation of partition functions, which is not only difficult but also computationally expensive, TST can also be used in conjunction with thermodynamic quantities. The thermodynamic form of TST is designed for use in the interpretation of kinetic data from more complex systems. The rate coefficient $k^{\ddagger}$ remains the same

as before in the thermodynamic formulation of TST, therefore only the equilibrium constant K_{eq} needs to be determined, this time without the use of partition functions but by using thermodynamic quantities instead. It is worth noting that the thermodynamic formulation of TST involved thermodynamic quantities specifically for the formation of the transition state and not for the formation of the product(s) of the reaction.

For a system at chemical equilibrium, the change in Gibbs free energy, ΔG, which is the energy associated with a chemical reaction which can be used to do work, is defined as:

$$\Delta G = -RT\ln K_{eq} \qquad \text{(Equation 2.27)}$$

which, when modified to represent terms for an activated system with a transition state, and rearranged, gives:

$$K_{eq} = \exp\left(-\Delta G^{\ddagger}/_{RT}\right) \qquad \text{(Equation 2.28)}$$

The standard definition for the Gibbs free energy is given by the sum of the enthalpy, H, defined as the heat evolved (either released of absorbed) by a chemical reaction at constant pressure and temperature, plus the product of the temperature and the entropy, S, defined as the degree of disorder or randomness, of the system:

$$\Delta G = \Delta H - T\Delta S \qquad \text{(Equation 2.29)}$$

Upon substituting the Gibbs free energy of activation term with this standard definition, and again modifying to represent terms for an activated system with a transition state, the equilibrium constant, K_{eq}, can be defined as:

$$K_{eq} = \exp\left(-\Delta H^{\ddagger}/_{RT}\right)\exp\left(\Delta S^{\ddagger}/_{R}\right) \qquad \text{(Equation 2.30)}$$

which, when substituted into Equation 2.21, the overall rate coefficient for the reaction, gives:

$$k_{bimol} = \kappa\frac{k_B T}{h}\exp\left(\Delta S^{\ddagger}/_{R}\right)\exp\left(-\Delta H^{\ddagger}/_{RT}\right) \qquad \text{(Equation 2.31)}$$

Consequently, if the changes in entropy and enthalpy of transition state formation, $\Delta S^{\ddagger}$ and $\Delta H^{\ddagger}$ respectively, are known, the overall rate coefficient for the reaction, k_{bimol}, can be calculated directly. It is worth noting that the entropy of activation, $\Delta S^{\ddagger}$,

and the enthalpy of activation, $\Delta H^{\ddagger}$, are related to the pre-exponential factor, A, and the activation energy, E_a, in the Arrhenius equation respectively. It is also important to clarify that both the enthalpy and entropy terms in this thermodynamic formulation of the TST relate only to the enthalpy and entropy of the transition state of the system, and not to the enthalpy and entropy of the reaction as a whole.

While TST is a widely applicable theory which has provided a conceptual foundation for understanding how reactions occur, it does have limitations. According to TST, atomic nuclei behave according to classical mechanics, and it is assumed that a reaction does not occur unless and until reactant species collide with enough energy to form the transition structure. This is not strictly true since quantum mechanics states that for any barrier with a finite amount of energy, it is feasible that particles can tunnel through the barrier. This means that for a chemical reaction in which reactants do not collide with enough energy to traverse the energy barrier, there is still a possibility that the reaction will proceed. Tunnelling probability increases with decreasing barrier height, making it an important phenomena for reactions with relatively low energy barriers, and negligible for reactions with large activation barriers.

TST also fails for some reactions at high temperature, since it assumes the reaction system will pass over the lowest energy saddle point on the PES. Although for reactions occurring at relatively low temperatures, this description is consistent, molecules populate higher energy vibrational modes at high temperatures, which means that their motion becomes more complex and it is possible for collisions to generate transition states far away from the lowest energy saddle point.

When applied to each elementary step of a complex reaction, TST assumes that each intermediate is long-lived enough to reach a Boltzmann distribution of energies before continuing to the next step, which is not always true. In cases where the intermediates are in fact very short-lived, the momentum of the reaction trajectory from the reactants to the intermediate can carry forward to affect product selectivity. Given these limitations, several alternative versions of TST have been proposed to account and correct for these fundamental issues faced when considering reactions for which TST does not work, e.g. for reactions with low energy barriers, for reactions at high temperatures and for complex reactions with short-lived reaction intermediates.

Examples of these are microcanonical variational TST, canonical variational TST, improved canonical variational TST, nonadiabatic TST and semiclassical TST.

2.2.1.3 Theory of Barrierless Reactions

A fundamental concept of both SCT and TST is the assumption of the presence of an energy barrier to reaction, i.e. that on the reaction path between the initial and final arrangements of atoms and molecules, there exists a barrier, separating the minima of the PES pertaining to the initial and final states of the reaction, with the magnitude of this barrier relating to the activation energy, which is the minimum amount of energy that must be provided to reactant species for a chemical reaction to occur. It then follows that for a chemical reaction exhibiting such behaviour to proceed at a reasonable rate, the temperature of the system should be high enough such that there exists an appreciable number of reactant species with translational energy equal to or greater that the activation energy, and that upon increasing the temperature of the system, since the number of reactant species with this energy or more increases, so does the rate of reaction.

However, not all reactions behave in this manner. Indeed, some reactions, including those of interest in atmospheric and combustion systems, exhibit negative temperature dependences, meaning they occur faster at lower temperatures, i.e. the rate of reaction increases with decreasing temperature. When following an approximately exponential relationship so that the rate coefficient can still be fit to an Arrhenius expression, this results in an apparent negative value for activation energy since there is no energy requirement for bonds to be broken before molecular rearrangement can occur to give products. Elementary reactions exhibiting such behaviour are typically called barrierless reactions, given the lack of an energy barrier to reaction, with PESs such as that depicted in Figure 2.3. Various processes occurring in the atmosphere and in combustion systems can be barrierless reactions, e.g. reactions between two reactive radicals and addition reactions such as those between radicals and O_2. To interpolate between determinations of rate coefficients for barrierless processes or to extrapolate beyond the measured range, the temperature dependence can be parameterised using empirical descriptions of the reaction in the form:

$$k = A\left(\frac{T}{298\ \mathrm{K}}\right)^{-\mathrm{n}} \qquad \text{(Equation 2.32)}$$

where A and n are determined through fitting to experimental observations.

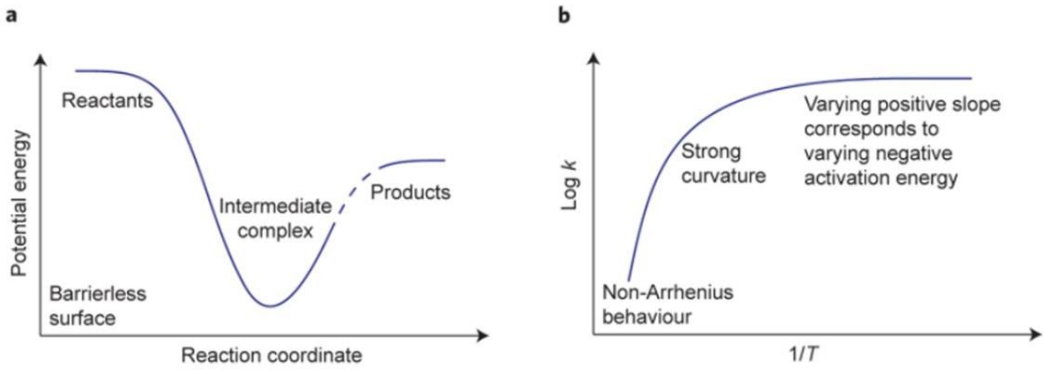

Figure 2.3: Schematic representation of a) a typical potential energy surface (PES) for an exothermic reaction with no energy barrier, showing the potential energy of the system as the reaction takes place and exhibiting strong non-Arrhenius behaviour, and b) the typical Arrhenius plot corresponding to this system, where an Arrhenius plot is defined as a plot of the log of the rate coefficient k as a function of the inverse of the temperature T, and should be linear with a slope equal to $-E_a/\mathrm{R}$ for reactions which exhibit Arrhenius behaviour. Adapted from reference 6.[6]

Although originally developed to explain reactions with energy barriers, SCT and TST can still provide good descriptions of barrierless reactions, however kinetic treatment of such reactions is more difficult and determination of reaction rate coefficients for barrierless reactions is not best achieved *via* the use of conventional TST. A fundamental flaw within TST is the assumption that during the course of a reaction, the transition state is not crossed more than once, and so any crossing of this transition state is counted as a reaction from reactants to products. For reactions where the energy within the system is small compared to the large activation energy, this assumption is a fairly accurate description of the system, however it becomes less accurate for reactions where the activation energy is small, since, in reality, it is possible for a species to cross the surface at which the transition state exists and turn around, or cross multiple times and only truly react once. As such, rate coefficients calculated using unadjusted TST tend to be upper limits, or in the case of reactions with insignificant energy barriers, they are overestimated. Additionally, in reactions with barriers, the saddle point is taken as the transition state, and although it is still

possible to assign a transition state in a barrierless reaction, this is no longer a saddle point. To account for these issues and determine the temperature dependence of such barrierless reactions, variational TST (VTST) can be used to locate the position of the transition state that defines a successful reaction on the PES. Distinctly, for a barrierless reaction, the transition state is determined more from entropy than enthalpy, since the enthalpy term, which is related to the activation energy in the Arrhenius equation as defined and described above, becomes negligible for a barrierless reaction.

It has been shown that even certain reactions with activation barriers can demonstrate a strong negative temperature dependence at very low temperatures due to an effect predicted in the early 20th century known as quantum mechanical tunnelling (QMT), which is defined as a quantum mechanical phenomenon where a species is able to penetrate through the potential energy barrier to reaction which is higher in energy than the species' own kinetic energy. Work at the University of Leeds has also demonstrated this effect of reactions adhering to the Arrhenius equation at high temperatures with non-Arrhenius behaviour at low temperature.[8]

2.2.2 Pressure Dependence

Gas phase kinetics includes two types of reactions for which the rate coefficients exhibit pressure dependence. These are unimolecular dissociation/recombination fall-off reactions and chemically activated bimolecular reactions. In principle, both these reactions are both temperature and pressure dependent, however the pressure dependence may be insignificant under certain conditions. Dissociation reactions are defined as processes in which large species, such as molecules or complexes, separate or split to form smaller species, such as atoms, ions or radicals, often in a reversible manner, with the opposite of dissociation reactions being termed association or recombination reactions. Chemically activated reactions are processes by which vibrationally excited species are produced from the reaction of precursor species, with the excited species being so due to the energy released by the reaction being channelled into the products, giving them energy greater than would be thermally predicted, hence an increased propensity to undergo further chemical reactions.

Among the reactions which display this pressure dependence are dissociation reactions, elimination reactions, isomerisation reactions, radical-radical recombination reactions and addition reactions of radicals to multiple bonds. All of these reactions can be considered as a sequence of at least two steps with one being an excitation process followed by either a deactivation step, in which excess energy is removed by a bath gas to stabilise the excited species, or by a reaction, producing generally two or more products. Of note is that the detail which distinguishes a pressure dependent reaction from a pressure independent one is the process of energy transfer, which is the relocation of energy from one system to another. Generally, rates of dissociation/recombination reactions increase with increasing pressure while those of chemically activated reactions decrease with increasing pressure. In both cases, various expressions are available which allow for the high- and low-pressure limiting rates to be connected.

2.2.2.1 The Lindemann Mechanism

Gas phase dissociation and isomerisation reactions often display first-order kinetics at high pressures, with the rates of such reactions also typically increasing with temperature, demonstrating the requirement for reactant species to acquire adequate energy to overcome an energy barrier to reaction. However, the observed first-order kinetics apparently preclude collisional activation, which is defined as a bimolecular process in which the energy is transferred from a collision partner, usually a bath gas, to the reactant species, such that the reactant species is left with an excess of energy, i.e. internally excited.

The first and simplest kinetic model to qualitatively describe the pressure dependence of a chemical reaction was proposed by Lindemann[9] in the 1920s, which splits the overall unimolecular reaction:

$$AB \rightarrow A + B \qquad \text{(R2.7)}$$

which designates either a dissociation or an elimination reaction, into two elementary steps:

$$AB + M \underset{k_{-1}}{\overset{k_1}{\rightleftharpoons}} AB^* + M \qquad \text{(R2.8)}$$

$$AB^* \xrightarrow{k_2} A + B \qquad \text{(R2.9)}$$

where M is any other species, often a bath gas, which is able to produce or deactivate the energised species AB* (* denotes a species in the excited state). Note that the first step is a reversible reaction with rate coefficients k_1 and and k_{-1} in the forward and backward directions respectively.

The first step, a strong collision between the reactant species AB and the bath gas M, transfers enough energy to AB to reach a state above the reaction barrier and produces the excited species AB*, constituting the excitation step. This energised state then either loses energy in a subsequent collision to re-form AB, i.e. undergoes the reverse of the first step otherwise known as deactivation, or it rearranges to the products A + B, i.e. undergoes a reaction.

The rate of formation of the products A and B from this mechanism are both given by:

$$+\frac{d[A]}{dt} = +\frac{d[B]}{dt} = k_2[AB^*] \qquad \text{(Equation 2.33)}$$

After a short time, formation and consumption of the excited species AB* will be in balance, i.e. the concentration of AB*, [AB*], reaches the steady-state concentration, the details for which are provided above. Application of the SSA to AB* gives:

$$[AB^*] = \frac{k_1[AB][M]}{k_{-1}[M]+k_2} \qquad \text{(Equation 2.34)}$$

which, when substituted into the original equation for rate of formation of the products, gives:

$$+\frac{d[A]}{dt} = +\frac{d[B]}{dt} = k_2[AB^*] = \frac{k_2k_1[AB][M]}{k_{-1}[M]+k_2} \qquad \text{(Equation 2.35)}$$

The rate coefficient which is actually measured experimentally, $k_{AB,obs}$, is defined as a unimolecular rate coefficient since the rate of reaction is observed to be dependent on the concentration of reactant species AB:

$$+\frac{d[A]}{dt} = +\frac{d[B]}{dt} = k_{AB,obs}[AB]$$

$$\text{where } k_{AB,obs} = \frac{k_2k_1[M]}{k_{-1}[M]+k_2} \qquad \text{(Equation 2.36)}$$

from which it is evident that $k_{AB,obs}$ is dependent on the concentration of species M, which is any collision partner and usually refers to the bath gas.

The two limiting cases of low- and high-pressure, equating to low and high concentration of collision partner, usually bath gas, where [M] tends towards zero ([M]→0) and infinity ([M]→∞) respectively, lead to expressions for the low- and high-pressure rate coefficients, k_0 and k_∞ respectively.

At low pressures, since [M]→0, this means that $k_{-1}[M] << k_2$, therefore the rate of formation of products is simplified to:

$$+\frac{d[A]}{dt} = +\frac{d[B]}{dt} = k_1[AB][M] = k_{AB,obs}[AB]$$

$$\text{where } k_{AB,obs} = k_0 = k_1[M] \qquad \text{(Equation 2.37)}$$

demonstrating that the reaction exhibits effectively second-order kinetics overall, with the Lindemann mechanism predicting that the rate coefficient increases as the pressure is increased in this low-pressure region since $k_{AB,obs}$ is directly proportional to [M]. As such, when expressed as a function of [M], the rate coefficient takes the form of an apparent first-order rate coefficient.

At high pressures, since [M]→∞, this means that $k_{-1}[M] >> k_2$, allowing simplification of the rate of formation of products to:

$$+\frac{d[A]}{dt} = +\frac{d[B]}{dt} = \frac{k_2 k_1}{k_{-1}}[AB] = k_{AB,obs}[AB]$$

$$\text{where } k_{AB,obs} = k_\infty = \frac{k_2 k_1}{k_{-1}} \qquad \text{(Equation 2.38)}$$

for which the rate coefficient is, in fact, a unimolecular rate coefficient since it is first order with respect to [AB]. This rate coefficient is termed the high-pressure limit, since at these high pressures, the rate coefficient becomes independent of pressure.

A schematic representation of the experimentally observed rate coefficient, $k_{AB,obs}$, as a function of total pressure, [M], is shown in Figure 2.4. The plot illustrates an initially linear dependence of $k_{AB,obs}$ on [M] at low pressure, with curvature where $k_{AB,obs}$ departs from this linear relationship at a certain pressure and falls off, leading to the limiting value of $k_{AB,obs}$ at high pressure. The transition region in which $k_{AB,obs}$

switches from the low-pressure to the high-pressure regime is called the fall-off region.

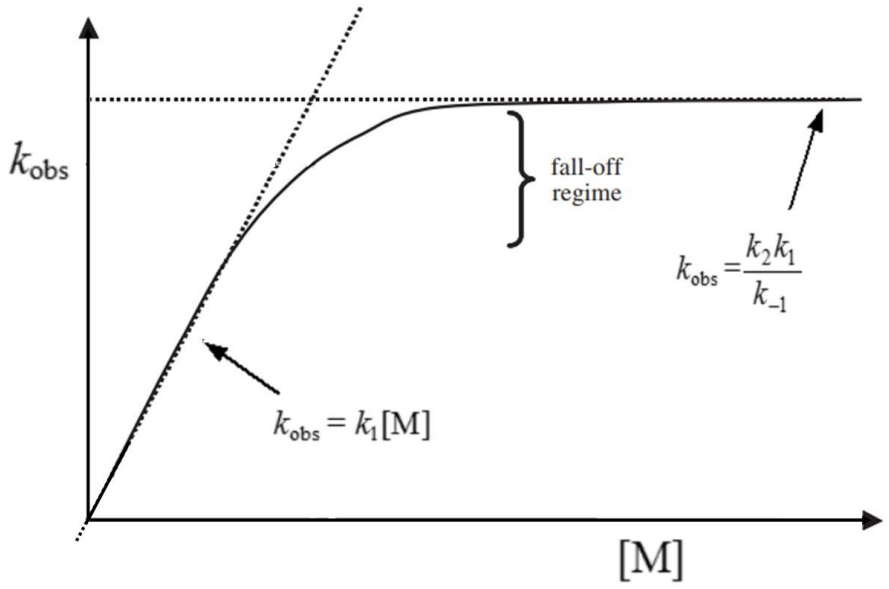

Figure 2.4: Schematic diagram of the apparent first-order or unimolecular rate coefficient, $k_{AB,obs}$, as a function of total pressure, [M], showing that the observed rate is second-order at low pressures and tends to a limiting first-order value at high pressures. Reproduced and adapted from reference 10.[10]

The unimolecular rate coefficient $k_{AB,obs}$ at any pressure is usually expressed in terms of both k_0 and k_∞, or alternatively, in terms of the reduced pressure, p_r, defined as:

$$k_{AB,obs} = k_\infty \frac{p_r}{1+p_r} \qquad \text{where } p_r = \frac{k_0[M]}{k_\infty} \qquad \text{(Equation 2.39)}$$

which, when substituted in to the expression for $k_{AB,obs}$, gives:

$$k_{AB,obs} = \frac{k_0[M]k_\infty}{k_0[M]+k_\infty} \qquad \text{(Equation 2.40)}$$

Termolecular recombination or association is the reverse reaction of unimolecular dissociation, as described above. The principle of detailed balancing ties both reactions together by the thermodynamic equilibrium constant:

$$K_{eq} = \frac{k_{AB,obs}}{k_{A+B,obs}} \qquad \text{(Equation 2.41)}$$

Consequently, $k_{A+B,obs}$, like $k_{AB,obs}$, is pressure dependent. As characterised above, a pressure-dependent reaction is a process that is composed of an excitation step followed by either deactivation or reaction to, often multiple, products. Upon close inspection of the generic termolecular recombination or association reaction:

$$A + B + M \rightarrow AB + M \qquad \text{(R2.10)}$$

in terms of the underlying scheme of elementary reactions:

$$A + B \underset{k_2}{\overset{k_{-2}}{\rightleftharpoons}} AB^* \qquad \text{(R2.11)}$$

$$AB^* + M \overset{k_{-1}}{\rightarrow} AB + M \qquad \text{(R2.12)}$$

it is evident that these criteria of what constitutes a pressure-dependent reaction are met. In three-body, or termolecular, reactions two reactant species, A and B, react to yield one single product species, AB, with the reaction requiring a third body, M, to stabilise the excited product, AB*, by collision. Once again, M is any species, often a bath gas, which is able to produce or deactivate the energised species AB*. Note again that the first step is a reversible reaction with rate coefficients k_{-2} and and k_2 in the forward and backward directions respectively, and that both the elementary steps making up the association reaction are in the opposite order to those making up a dissociation reaction shown earlier, since association and dissociation are opposite reactions of each other. The excitation step here is called chemical activation since the energised AB* species is created upon the formation of a new bond during the recombination or association process, whereas for a dissociation reaction, the excitation occurs due to collisions with the bath gas, known as collisional activation.

A similar mechanism to that proposed by Lindemann for unimolecular kinetics can be used to explain the observed pressure dependence of many termolecular association reactions, *via* application of the SSA to species AB* and substitution into the equation for rate of formation of products, giving:

$$+\frac{d[AB]}{dt} = k_{-1}[AB^*] = \frac{k_{-1}k_{-2}[A][B][M]}{k_2 + k_{-1}[M]} \qquad \text{(Equation 2.42)}$$

The experimentally observed termolecular rate coefficient, $k_{A+B,obs}$, is therefore given by:

$$+\frac{d[\mathrm{AB}]}{dt} = k_{\mathrm{A+B,obs}}[\mathrm{A}][\mathrm{B}]$$

$$\text{where } k_{\mathrm{A+B,obs}} = \frac{k_{-1}k_{-2}[\mathrm{M}]}{k_2+k_{-1}[\mathrm{M}]} \qquad \text{(Equation 2.43)}$$

In a similar fashion to unimolecular reactions, at low pressures, since $k_{-1}[\mathrm{M}] << k_2$, the rate of formation of products is simplified to:

$$+\frac{d[\mathrm{AB}]}{dt} = \frac{k_{-1}k_{-2}}{k_2}[\mathrm{A}][\mathrm{B}][\mathrm{M}] = k_{\mathrm{A+B,obs}}[\mathrm{A}][\mathrm{B}]$$

$$\text{where } k_{\mathrm{A+B,obs}} = k_0 = \frac{k_{-1}k_{-2}}{k_2}[\mathrm{M}] \qquad \text{(Equation 2.44)}$$

resulting in a third-order rate equation.

Equally, at high pressures, since $k_{-1}[\mathrm{M}] >> k_2$, the rate of formation of products is simplified to:

$$+\frac{d[\mathrm{AB}]}{dt} = k_{-2}[\mathrm{A}][\mathrm{B}] = k_{\mathrm{A+B,obs}}[\mathrm{A}][\mathrm{B}]$$

$$\text{where } k_{\mathrm{A+B,obs}} = k_\infty = k_{-2} \qquad \text{(Equation 2.45)}$$

resulting in a second-order rate equation.

Similarly to the dissociation rate coefficient $k_{\mathrm{AB,obs}}$, the association rate coefficient $k_{\mathrm{A+B,obs}}$ at any pressure can also be expressed in terms of both k_0 and k_∞. This is demonstrated in this thesis to explain the pressure dependence of the rate coefficient for the reaction between CH_2OO and I, further details for which are provided in Chapter 5.

When compared to experimental results of observed rate coefficients of unimolecular dissociation and termolecular association reactions as a function of total pressure, it is apparent that although the Lindemann model is qualitatively correct, its quantitative assessment is sometimes not accurate. In other words, although it can explain the occurrence of a fall-off region, for a unimolecular dissociation reaction, it predicts the location of the fall-off region to occur at pressures which are several orders of magnitude higher than experimentally observed and for cases in which the high-pressure limit k_∞ is known from experiments, the calculated rate coefficient k_2 is found to be unrealistically large. For such unimolecular dissociation reactions, the

Lindemann mechanism predicts that $k_{AB,obs}$ decreases with pressure and that its reciprocal, $1/k_{AB,obs}$, is a linear function of the reciprocal of pressure, or equivalently 1/[M], *via* inversion and rearrangement of the equation to give:

$$\frac{1}{k_{AB,obs}} = \frac{k_{-1}[M]+k_2}{k_2 k_1[M]} = \frac{k_{-1}}{k_2 k_1} + \frac{1}{k_1[M]} \qquad \text{(Equation 2.46)}$$

and substitution for an expression equating to a straight-line plot:

$$\frac{1}{k_{AB,obs}} = \frac{1}{k_\infty} + \frac{1}{k_1} \cdot \frac{1}{[M]} \qquad \text{(Equation 2.47)}$$

Experimentally, however, for many reactions, although $k_{AB,obs}$ does decrease at low pressure, the graph of $1/k_{AB,obs}$ as a function of 1/[M] is quite often curved rather than linear.

In the simplest form, the Lindemann mechanism fails for two main reasons. Firstly, the treatment of the rate of activation and deactivation is too simplistic in that the theory assumes that the rate coefficients for the bimolecular activation and deactivation steps, k_1 and k_{-1} respectively, do not depend on energy and can be directly calculated from kinetic collision theory, hence the internal degrees of freedom of the reactant species are completely neglected and so the theory consequently underestimates the rate of activation. Secondly, according to the theory it is assumed that the unimolecular step is not energy dependent since it takes no account for the fact that a unimolecular reaction specifically involves one particular form of molecular motion, meaning that the process is in fact energy dependent. Subsequent theories of unimolecular reactions have attempted to address these problems by recognising the need to consider how energy is distributed in an energised model, taking into account the requirement for energy to be located in the correct bond for a reaction to occur and the fact that the probability of this happening depends on how much energy is available and how big the species carrying the energy is.

2.2.2.2 The Hinshelwood Theory

The Hinshelwood theory[11] further develops the Lindemann mechanism by taking into account the energy distributed among vibrational degrees of freedom, and thus offers a solution for the first problem regarding the bimolecular step of the Lindemann

mechanism. The Lindemann theory neglects the vibrational modes of the reacting species, since in collision theory, it is assumed that only translational energy is available to surmount the energy barrier to reaction. The model inherently assumes that AB can be treated as different species to AB*, when, in reality, AB* and AB are the same species with the only difference being that AB* contains additional internal energy, mainly stored in vibrational modes. Hinshelwood suggested that the internal energy of the reacting species AB, contained in its vibrations, can assist it to overcome this activation barrier. A given amount of excess energy in AB* can be stored in many different combinations of vibrations, or states, and the number of states increases rapidly with energy. Since AB* exists in many different states, the probability to excite AB to AB* therefore increases as it scales with the number of states, with the probability of forming a particular state given by the Boltzmann distribution.

Hinshelwood derived an expression for this probability of the reacting species AB being collisionally activated to the reactive state AB* based on the assumption that all vibrations are classical or simple harmonic oscillators at equilibrium. A further assumption made is the strong collision assumption meaning that every collision can form AB in any state, i.e. that the probability of deactivation of AB* in any given collision is unity. The result of the Hinshelwood adaptation to the Lindemann theory is that theoretical value of the rate of activation, k_1, increases compared to the initial Lindemann model, that of the rate of deactivation, k_{-1}, remains unchanged due to the strong collision assumption, and that of the rate of the unimolecular reaction, k_2, decreases due to the increase in k_1 via rearrangement of the high-pressure rate coefficient, k_∞. This modification improves the some of the issues with the original model since it moves the fall-off regime to a lower pressure range, leads to a more realistic value for k_2, and accounts for vibrational degrees of freedom in reactant species leading to the increase in k_1 being more pronounced for larger species since they have more oscillators or vibrations, i.e. more ways of distributing energy. An important consequence of the Lindemann-Hinshelwood treatment is that the probability of activating AB to AB* depends on the number of oscillators, i.e. on the size of the reacting species AB, with larger species more easily activated than smaller ones. In general, when compared to experimental results of unimolecular rate coefficients, the Lindemann-Hinshelwood model reproduces the location of the

fall-off region well, however the shapes of experimental fall-off curves are still not accurately captured.

2.2.2.3 The Rice-Ramsperger-Kassel-Marcus Theory

A further refinement to the Lindemann mechanism to account accurately for pressure dependence of rate coefficients for unimolecular reactions was made by Rice and Ramsperger,[12] Kassel,[13] and Marcus,[14] leading to the development of the more elaborate RRK, and later RRKM theory. It was developed by Rice and Ramsperger in 1927 and Kassel in 1928 to give the RRK theory and was generalised into the RRKM theory in 1952 by Marcus who took into account TST, details for which are provided above.

The second reason why the Lindemann mechanism on its own fails can be addressed by recognising that a minimum amount of energy must be localised in specific modes of molecular motion in order for the unimolecular step to take place. RRK theory considers the internal energy distribution of the energised species AB*, and separates the formation of the generally excited species AB*, with enough energy to react but not in the correct mode, from that of the specifically excited activated complex $AB^{\ddagger}$, with sufficient energy located in the correct mode or bond for the reaction to occur, leading to the modified reaction scheme:

AB + M	$\underset{k_{-1}}{\overset{k_1}{\rightleftharpoons}}$	AB* + M	(R2.8)
AB*	$\xrightarrow{k_3}$	$AB^{\ddagger}$	(R2.13)
$AB^{\ddagger}$	$\xrightarrow{k_4}$	A + B	(R2.14)

The basic idea of RRK theory is that conversion of AB* to products is thought to proceed *via* a critical geometry $AB^{\ddagger}$, with AB* and $AB^{\ddagger}$ having the same energy, but in AB* this energy is randomly distributed among all oscillators whereas in $AB^{\ddagger}$ a specific amount of energy is localised into the reactive mode. The localisation probability decreases as the number of oscillators or modes increases since there are more modes to spread the energy across, and consequently, the rate coefficient for the unimolecular step, k_2, becomes smaller as the reacting species becomes larger and more complex, in contrast to the behaviour of the rate coefficient for activation, k_1.

RRK theory was then modified to what is known as the RRKM theory, in which $AB^{\ddagger}$ is identified as the transition state of the reaction, where a transition state is defined as the dividing surface between the reactants and products of the reaction, with its location being determined by the condition that every trajectory or flux which passes this surface will form products, i.e. undergo reaction, without recrossing. The second assumption of RRKM theory is the ergodicity assumption, which requires fast and complete randomisation of the available freely distributable energy among only all active modes after excitation, and recognises that only part of the internal energy can be freely distributed among different modes, i.e. that contributions to the internal energy exist which are assigned to a particular mode and hence are not distributable, such as the zero-point energy of vibrations. As such, the energy of the reacting species is partitioned into fixed and non-fixed components, with only the latter energy, which can flow freely among the various modes of motion of the reacting species, being able to contribute to the reaction. Hence, RRKM theory uses vibrational and rotational partition functions to separate contributions from various modes and obtain population distributions amongst various energy levels, for which, detailed and accurate thermodynamic data for both stable species as well as for the transition state is required as input.

As a result, when such reliable thermodynamic information is available, RRKM theory can often accurately reproduce experimental results. Unfortunately, however, such data are not available for many of the transient species within the reaction and so often, RRKM theory cannot be used to determine the pressure dependence of rate coefficients for unimolecular reactions.

2.2.2.4 The Troe Fall-off Form

A general description for any fall-off curve is provided by the Troe fall-off form,[15] which demonstrates that the introduction of a broadening factor, F, itself a function of k_0 and k_∞, applied to Equations 2.36 and 2.43 for a unimolecular and termolecular reaction respectively, and in the same form as Equation 2.40, can accurately replicate the pressure dependence of many experimentally determined rate coefficients, k_{obs}:

$$k_{obs} = \frac{k_0[M]k_\infty}{k_0[M]+k_\infty}F \qquad \text{(Equation 2.48)}$$

where

$$F = F_c \left[1 + \left(\log_{10} \left(\frac{k_0[\mathrm{M}]}{k_\infty} \right) \right)^2 \right]^{-1} \qquad \text{(Equation 2.49)}$$

Although the exact value of F_c depends on the specific reaction which is being investigated, it has been shown that taking the value of F_c to be 0.6 provides an adequate description for most atmospheric reactions of interest.[16] For rate coefficients with broad fall-off curves, a more detailed description of the broadening factor F has also been provided by Troe[15]:

$$F = \frac{\left(1 + \frac{k_0[\mathrm{M}]}{k_\infty} \right)}{\left[1 + \left(\frac{k_0[\mathrm{M}]}{k_\infty} \right)^n \right]^{1/n}} \qquad \text{(Equation 2.50)}$$

where

$$n = \left(\frac{\ln(2)}{\ln\left(2/F_c \right)} \right) \left[(1-b) + b \left(\frac{k_0[\mathrm{M}]}{k_\infty} \right)^q \right] \qquad \text{(Equation 2.51)}$$

where

$$q = \frac{(F_c - 1)}{\ln\left(F_c/10 \right)} \qquad \text{(Equation 2.52)}$$

The role of the broadening factor in the Troe fall-off form is to correct the shape of the Lindemann fall-off curve to match the experimental data.

2.3 Theory of Photochemistry

Atmospheric composition, which is determined by atmospheric emissions and chemistry, impacts air quality. Air quality, in turn, is driven primarily by photochemistry, with two of the main atmospheric oxidants, O_3 and OH, being formed in the atmosphere *via* photochemistry (further details are provided in Chapter 1). Other important atmospheric processes such as global warming and the production of stratospheric ozone are also impacted by photochemistry. This section will introduce the concept of photochemistry, and the importance of molecular absorption of solar

radiation on the composition and chemistry of the atmosphere. Photochemistry is the branch of chemistry concerned with the chemical effects of light and the interaction of chemical species with electromagnetic radiation. Electromagnetic radiation is also referred to as photons and light, with photons being the elementary particles which carry electromagnetic energy, manifesting as light across a wide range of energies, frequencies or wavelengths, which can be organised onto a spectrum. Generally, the term photochemistry is used to describe a chemical reaction caused by absorption of ultraviolet (UV), visible light or infrared (IR) radiation, of wavelengths in the ranges 100-400 nm, 400-750 nm and 750-2500 nm respectively.

2.3.1 The Beer-Lambert Law

Absorbance of a species at wavelength λ, A_λ, is defined as the natural logarithm of the ratio of intensities of light without and with the attenuating or absorbing species present, $I_{0,\lambda}$ and $I_{l,\lambda}$ respectively, and is given by:

$$A_\lambda = \ln\left(\frac{I_{0,\lambda}}{I_{l,\lambda}}\right) \qquad \text{(Equation 2.53)}$$

where $I_{0,\lambda}$ is the average light intensity of the incident light at wavelength λ and $I_{l,\lambda}$ is the light intensity at wavelength λ after transmission through the sample of length l.

For a species at homogeneous concentration $[C]$, the total attenuation of light or total absorbance at a given wavelength λ, A_λ, is determined by and related to the properties of the medium through which the light is travelling *via* The Beer-Lambert law. These properties are the probability that each attenuating species in the medium, i, will absorb a photon of light at wavelength λ, i.e. the absorption cross-section of the species at wavelength λ, $\sigma_{i,\lambda}$, the concentration of each attenuating species i in the medium, $[C]_i$, and the total distance or path length travelled by the light through the attenuating or absorbing medium, l, and are described by the Beer-Lambert law:

$$A_\lambda = \sum_{i=1}^{i=\mathrm{n}} \sigma_{i,\lambda}\,[C]_i\,l \qquad \text{(Equation 2.54)}$$

In the atmosphere, absorbance can occur as a result of absorption of electromagnetic or solar radiation by a species such as an atom, molecule or radical, or by scattering

of this radiation due to various species such as atoms, molecules or particles. It can be seen from the Beer-Lambert law that absorbance is linearly dependent on both the absorption cross-section and concentration of the absorbing species, and on the path length of the light through the absorbing sample. Measurement of species concentrations both in the atmosphere and in the laboratory can therefore be made possible by virtue of absorption spectroscopy if the absorption cross-sections for the corresponding species are known. Absorption spectroscopy in the UV/visible region of the electromagnetic spectrum, resulting in electronic excitation of the species under consideration, is particularly useful in atmospheric science for determination of species concentration since UV/visible absorption cross-sections are well known for many atmospherically important species.

2.3.2 Absorption of Electromagnetic Radiation by Molecules

A significant portion of the chemistry leading to atmospheric change is often initiated by the interaction of atmospheric species with solar radiation. The principle of photochemical transformations is that the mechanism by which the activation energy required for the reaction is provided is through light. Absorption of this electromagnetic radiation by atmospheric species involves interaction between an incident photon and the absorbing molecule leading to a transition between energy levels within the molecule. Since electromagnetic radiation is quantised, meaning it can only have certain discrete values and is not continuous, energy can be gained or lost, i.e. absorbed or emitted respectively, only in integral multiples of the smallest unit of energy, known as a quantum. The energy of a quantum is proportional to the frequency of the radiation, v, with the fundamental proportionality constant being h, known as Planck's constant. Electromagnetic radiation is composed of indivisible quantum packets called photons, which are particles of light with a particular, fixed and quantised energy:

$$E = hv = \frac{hc}{\lambda} = hc\tilde{v} \qquad \text{(Equation 2.55)}$$

where v is the frequency of the light, λ is the wavelength of the light, $\tilde{v}$ is the wavenumber of the light, h is Planck's constant and c is the speed of light. Most importantly, this leads to the conclusion that electromagnetic radiation must be

absorbed as an integer number of photons, and absorption of a photon occurs only if the energies of the levels of the absorbing species allow a transition equivalent in energy to that of the incident photon.

When molecules are supplied by an external source with photons of energy, the photons are absorbed by the ground state electrons in the molecules, ending in a higher energy excited state. In the broad sense, there exists three distinct types of excitations which arise from transitions involving changes in the electronic, vibrational and rotational energy levels of the absorbing molecule, most often corresponding to the UV/visible, IR and microwave regions of the electromagnetic spectrum respectively.[17] Hence, photon absorption by a molecule AB results in production of an excited molecule AB*, depending on the photon energy:

$$AB + h\nu \rightarrow AB^* \qquad \text{(R2.15)}$$

Electronic and vibrational excitations are often coupled, giving rise to vibronic transitions, which involve simultaneous changes in electronic and vibrational energy levels of the molecule, resulting in the spectrum of the molecule in the UV/visible region. In the gas phase, vibronic transitions are also accompanied by changes in rotational energy, and although all three types of transitions are present, rotational fine structure cannot always be resolved and observed, as is the case for the experimentally observed CH_2OO UV absorption spectrum discussed in Chapter 4. The spacing between adjacent vibrational energy levels decreases, with the separation eventually decreasing to zero when the molecule photodissociates into a continuum of states, as shown in Figure 2.5. For absorption spectra, the vibrational coarse structure for a given electronic transition forms a single progression or a series of transitions with a common level, often the lower level which is the zero-point energy of the bond. Similarly, vibrational and rotational excitations are also often coupled, giving rise to ro-vibrational transitions, which involve changes in both vibrational and rotational energy states of the molecule, resulting in IR and Raman spectra of molecules in the gas phase. These spectra often exhibit sharp and evenly spaced peaks centred around a transition energy corresponding to the difference in energy between the two vibrational energy levels or states. Since changes in rotational energy levels are much smaller than changes in vibrational energy levels, changes in rotational state tend to

give fine structure to the vibrational spectrum. Typically, ro-vibrational transitions occur between low-lying vibrational states, and are not dissociative at 298 K.

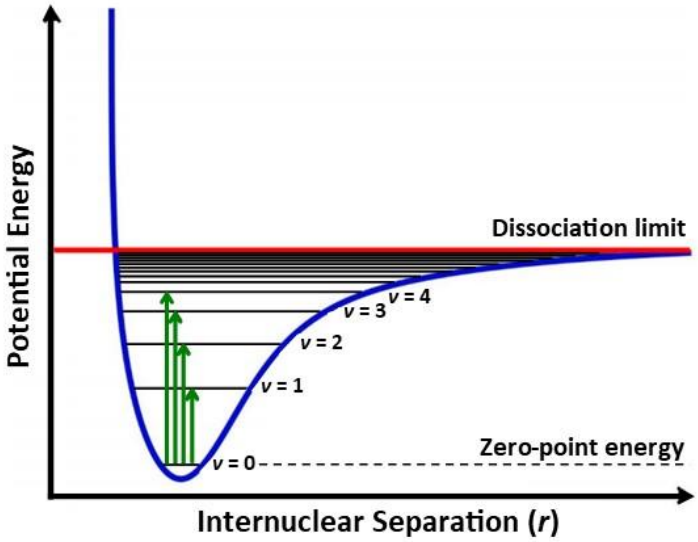

Figure 2.5: Schematic diagram of a morse potential curve, which is a convenient interatomic interaction model for the potential energy of molecules and illustrates an approximation for the vibrational structure of the molecule, showing the first four transitions from the vibrational ground state to the first four vibrational energy levels in green. The number of vibrational energy levels is finite, and energy levels become closer together until they become a continuum at the dissociation limit, shown in red. Note the excited states v = 1-4 are below the dissociation limit, and will not lead to bond cleavage in this example.

When a molecule undergoes electronic excitation from the ground state *via* the absorption of a photon, an electronically excited upper state is formed, with the fate of the excited state depending on its structure, i.e. whether it is a bound or an unbound state. A bound state is one where the molecule is confined to a potential well with quantised energies such that the molecule has a tendency to remain localised in this region of space whereas an unbound state, also known as a repulsive state, has no discrete values for allowed energies, i.e. all energies are allowed, hence represents a continuum of energies with no quantisation.

In the case of electronic transitions consisting of excitation of a ground state gas phase molecule to a bound upper state, the transition involves a simultaneous change in electronic, vibrational and rotational energy states of the molecule, called a ro-vibronic tranisition.[18] The structure of allowed ro-vibronic transitions exhibit one

or more sharp peaks, the intensities of which are governed by the Franck-Condon principle, which states that during an electronic transition, the probability of a transition between vibrational energy levels in the lower or ground state and the upper or excited state increases as the degree of overlap of the two vibrational wavefunctions increases, as illustrated in Figure 2.6. Above the dissociation limit, instead of discrete lines, a continuum of states is found since translational motion is no longer quantised. An electronically excited molecule with a bound excited state will relax down to the stable ground electronic state *via* one of many possible energy transfer processes, which are discussed further below.

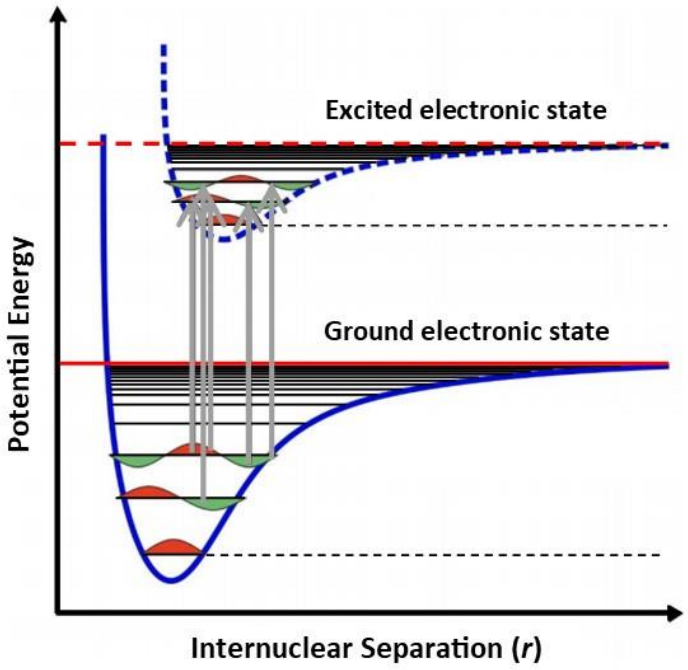

Figure 2.6: Schematic diagram showing the probability of transitions from vibrational levels in the ground electronic state to those in the upper electronic state increases with increasing degree of overlap between the phases of the wavefunctions, as governed by the Franck-Condon principle.

When the absorption of photons excites a ground state molecule to an unbound repulsive excited state, the molecule will rapidly travel along the PES of the excited state and proceed along the reaction coordinate to the formation of products, for which a schematic is shown in Figure 2.7. For an electronically excited molecule with an unbound or repulsive upper state, broad, smooth, continuous and featureless spectra are observed. Following excitation, the rapid proceeding of the system along the

reaction coordinate leads to a change in the structure of the molecule, often resulting in dissociation to two or more atoms or molecules.

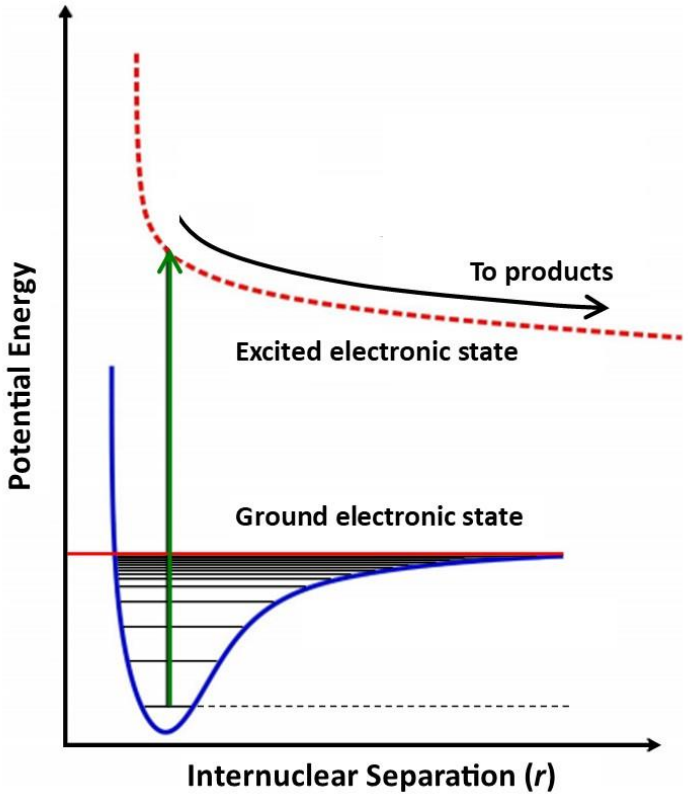

Figure 2.7: Schematic diagram showing the absorption of photons from the ground electronic state to an unbound upper electronic state which results in a broad featureless absorption band in the observed spectrum. Following excitation to the repulsive excited state PES, the reaction proceeds along the reaction coordinate to the formation of products.

In some spectra, the line structure is observed to disappear at energies below the dissociation limit and instead a strong continuous feature is observed, however reappears again at higher energies. This observation is explained by a phenomenon known as predissociation, which is a process in which a molecule excited to particular vibration levels of a bound excited state can be transferred onto an unbound or repulsive excited state of the same energy where the potential curves of the two states cross.[18] From the rovibronic state on the excited electronic state surface, the molecule can either relax down to a lower or ground electronic state by spontaneous emission of radiation or be transferred to the dissociative state by internally or externally induced coupling, as shown in Figure 2.8. Predissociation is often connected with an

internal conversion from the bound excited electronic state towards the unbound and hence dissociative excited electronic state. Sometimes, predissociation is introduced by additional external factors, such as collisions with other molecules pushing a molecule from the bound to the unbound state, or alternatively, for a molecule under the influence of an external field, selection rules may be overridden. Such instances are known as collision- or field-induced predissociation.

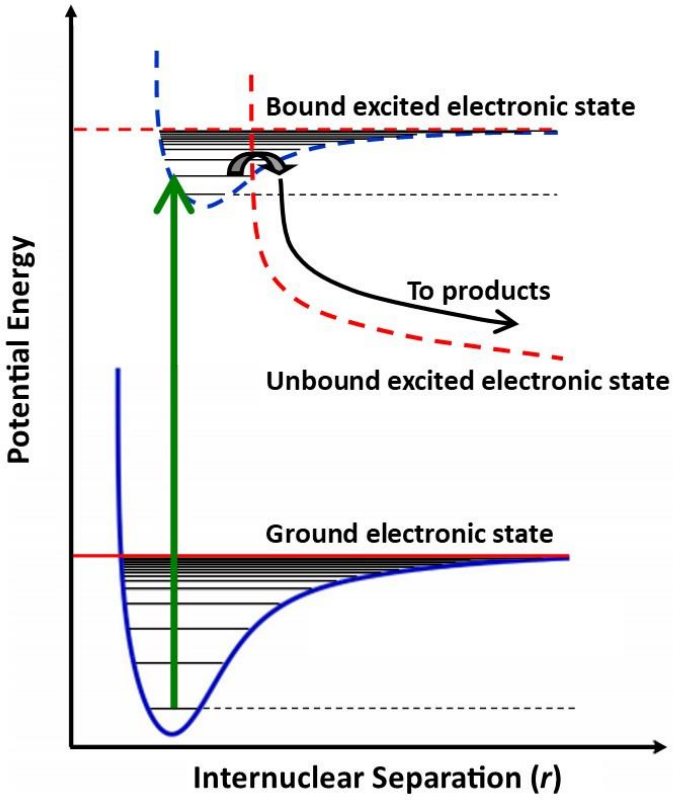

Figure 2.8: Schematic diagram showing the absorption of photons from the ground electronic state to a bound upper electronic state which intersects an unbound upper electronic state, allowing for dissociation of molecules which cross from the bound to the unbound excited state surface at energies corresponding to where the crossing takes place but lower than the dissociation limit of the bound excited state. This phenomena, called predissociation, results in a strong continuous feature in the observed spectrum, above and below which discrete line structure is observed.

It is assumed that there is some level of relatedness between the vibrational state(s) at the level of intersection and the translational motion during dissociation. Such circumstances allow separation of the molecule *via* the unbound and dissociative excited state without supplying the energy required for dissociation on the bound

excited state. Interpretation for observation of discrete lines in the range beyond the continuum caused by predissociation is that for higher vibrational states on the bound excited state surface, a conversion towards the unbound dissociative excited state is excluded again.

2.3.3 Fates of Electronically Excited Molecules

A number of possible fates exist for electronically excited molecules following absorption of a photon of light,[7, 19] which are summarised in Figure 2.9.

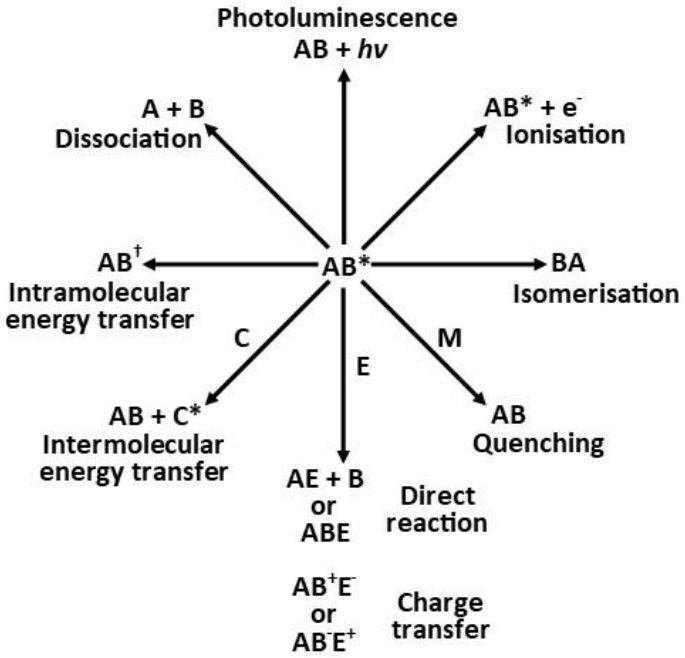

Figure 2.9: Schematic diagram showing some of the possible fates of the electronically excited molecule AB*. Reproduced and adapted from references 7 and 19.[7, 19]

The dissociation pathway:

$$AB + h\nu \rightarrow AB^* \quad \text{(R2.15)}$$

$$\rightarrow A + B \quad \text{(R2.16)}$$

is of particular importance in the atmosphere since the photolytically produced fragments A and B are often highly energetic and hence intrinsically reactive. The effective rate coefficient for solar photodissociation of a molecule at wavelength λ, J_λ, is given by:

$$J_\lambda = \int_{\lambda_2}^{\lambda_1} I_\lambda \ \sigma_\lambda \ \Phi_\lambda \ d\lambda \qquad \text{(Equation 2.56)}$$

where I_λ is the solar intensity at wavelength λ, σ_λ is the absorption cross-section of the molecule at wavelength λ (which can be temperature dependent) and Φ_λ is the quantum yield for dissociation of the molecule at wavelength λ (which can be both temperature and pressure dependent). Values for σ_λ and Φ_λ are provided by experimental laboratory measurements while radiative transfer models, such as the one discussed in Chapter 4 used to calculate the photodissociation rate of CH_2OO, are used to compute I_λ, taking into account the actinic flux at the top of the atmosphere, the absorption of solar radiation by other species in the atmosphere, such as O_2 and O_3, and factors such as scattering and surface albedo.

Following excitation of a molecule from a ground state to a bound upper state, the excited electronic singlet state S_1 or S_2 can undergo a variety of different processes or paths to dissipate the extra energy and relax back down to the ground state S_0. The excited state exists for a finite time (typically 1 – 10 nanoseconds) during which time the molecules are subject to a multitude of possible interactions with their molecular environment. First, the energy of the excited electronic singlet state is partially dissipated via intramolecular vibrational relaxation to lower lying vibrational levels of the same excited state yielding a relaxed singlet excited state, e.g. $S_1' \rightarrow S_1$. Molecules initially excited by absorption can return to the ground state and thereby depopulate the excited state *via* internal conversion to a lower lying singlet excited state e.g. $S_2 \rightarrow S_1$, intersystem crossing to a nearby triplet excited state e.g. T_1, emission of a photon *via* fluorescence from excited singlet states or phosphorescence from excited triplet states, and collisional energy transfer also known as quenching. The phosphorescence transition $T_1 \rightarrow S_0$ is in fact spin forbidden and so occurs on a slower timescale than the other processes. These processes can be summarised in what is known as a Jablonski diagram,[7] shown in Figure 2.10, which depicts each process which can occur upon excitation of an electron.

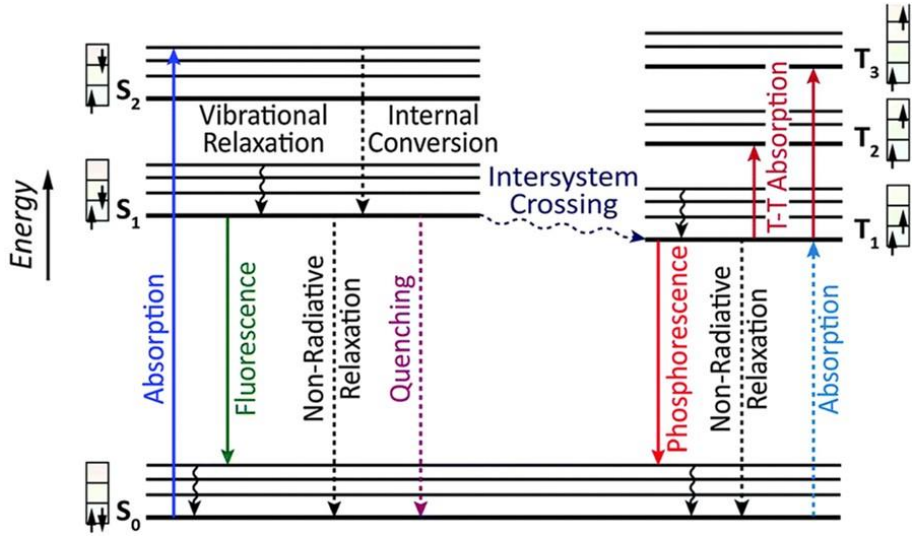

Figure 2.10: Schematic of a Jablonski energy level diagram showing the principle fates of electronically excited states in a molecule, with the left panel depicting a singlet manifold and the right panel depicting a triplet manifold, and with the full arrows representing radiative processes and the dashed arrows representing non-radiative processes. Adapted from reference 20.[20]

The Jablonski diagram shows the types of transitions which can occur in a molecule and each of these possibilities is dependent on the time scale of each transition. Table 2.1 summarises the time scales of these processes.

Transition	Time Scale	Radiative?
Absorption	10^{-15} s	yes
Internal Conversion	10^{-14} – 10^{-11} s	no
Vibrational Relaxation	10^{-14} – 10^{-11} s	no
Fluorescence	10^{-9} – 10^{-7} s	yes
Quenching	10^{-10} s	no
Non-radiative Relaxation	10^{-10} s	no
Intersystem Crossing	10^{-8} – 10^{-3} s	no
Phosphorescence	10^{-4} – 10^{-1} s	yes

Table 2.1. A summary of the possible transitions/processes which can occur in a molecule and their time scales.

The faster the transition, the more likely it is to occur as determined by selection rules therefore it is important to understand the time scale of each process to ascertain whether the process can occur. Some photochemical reactions are several orders of magnitude faster than thermal reactions, with reactions as fast as 10^{-9} seconds and associated processes as fast as 10^{-15} seconds often observed. Additionally, different processes can be both radiative (emit a photon of light) or non-radiative (do not emit a photon of light). The time a molecule spends in the excited state is determined by the sum of the kinetic constants of all de-excitation processes.[7]

2.3.4 Broadening of Spectral Lines

A spectral line is a bright or dark line in an otherwise uniform and continuous spectrum resulting from emission or absorption of light in a narrow frequency range compared with nearby frequencies. An important detail to note is that a spectral line does not occur at a single frequency but rather extends over a range of frequencies, i.e. it has a non-zero linewidth. The shape of a spectral line is described as the form of a feature corresponding to an energy change in a species such as an atom or molecule, with the width of the spectral line being the frequency range over which this change in energy occurs, both of which are controlled by a number of effects.

Absorption lines of molecules are of finite width since the lifetime of excited states, i.e. time for photon emission or absorption, is finite and results in natural broadening, also known as lifetime broadening, which is the same at all frequencies. The Heisenberg uncertainty principle, which explains why both the precise position and momentum of a particle cannot be determined simultaneously, relates the lifetime of an excited state with the inherent uncertainty in quantising the energy levels between which the transition occurred. However, this natural broadening is often inconsequential in comparison to the broadening attributable to the motions and collisions of the gas molecules.[18] Such line broadening is the phenomena whereby the spectral lines of molecules appear to spread over a greater frequency range, and is often evident in IR or vibrational spectroscopy.

The shape of spectral lines due to molecular collisions is referred to as pressure or collisional broadening and is associated with the presence of nearby atoms or

molecules which affect the radiation of an individual molecular entity. Collisions of other molecules with the molecule of interest interrupt the radiation process since they can supply or remove small amounts of energy during the radiative transition, thereby allowing photons with a broader range of frequencies to produce a particular transition of a molecule and shortening the characteristic time of the radiation, hence increasing the uncertainty in the energy, as in natural broadening. The duration of the collision is much shorter than the lifetime of the radiation process. This is the primary broadening mechanism in the troposphere.

Line shape due to the movement of molecules is referred to as thermal or Doppler broadening and is associated with the Doppler-shifting of frequencies at which the molecules experience the incident radiation by virtue of their random motions towards or away from the source of the radiation. This again allows a broader range of frequencies of radiation to affect a particular molecular transition. Furthermore, the molecules undergoing radiation have a distribution of velocities, with this distribution becoming wider with increasing temperature of the molecules. Since the spectral line is a combination of all the absorbed or emitted radiation, the higher the temperature of the molecules, the broader the spectral line. Doppler broadening becomes the dominant broadening mechanism at low pressures, i.e high altitudes, where collisions are less frequent.

Natural broadening and pressure or collisional broadening are both homogeneous effects meaning they affect all molecules equally hence result in Lorentzian profiles of spectral lines whereas Doppler or thermal broadening is an inhomogeneous effect meaning it affects only certain classes of molecules and hence results in Gaussian profiles of spectral lines.

2.4 Concluding Remarks

In general, theories enable knowledge to be gained, predictions to be made and conclusions to be drawn. As such, theoretical explanations of gas phase kinetics and photochemistry developed over the years have enabled and continue to enable good approximations of molecular behaviour. Theories such as those discussed in this chapter provide valuable insights, knowledge and understanding of fundamental

chemical and physical processes occurring in the atmosphere. While theories are useful in the information they provide, they require experimental verification, which not only demonstrates their accuracy but also facilitates their development allowing for required modifications to be made, and the theory of reaction kinetics is no exception. Experimental principles and techniques used to study gas phase reaction kinetics are discussed in the following chapter.

2.5 References

1. Prather, M. J., Lifetimes and time scales in atmospheric chemistry. *Philosophical Transactions of the Royal Society A* **2007,** *365* (1856), 1705-1726.

2. Vallance, C., *An introduction to chemical kinetics*. Morgan & Claypool Publishers: California, USA, 2017.

3. Zewail, A. H., Femtochemistry: Atomic-scale dynamics of the chemical bond. *The Journal of Physical Chemistry A* **2000,** *104* (24), 5660–5694.

4. Seinfeld, J. H.; Pandis, S. N., *Atmospheric chemistry and physics: from air pollution to climate change*. Third ed.; John Wiley & Sons, Incorporated: New Jersey, USA, 2016.

5. Arrhenius, S., Über die Reaktionsgeschwindigkeit bei der Inversion von Rohrzucker durch Säuren. *Zeitschrift für Physikalische Chemie* **1889,** *4U* (1), 226-248.

6. Sims, I. R., Low-temperature reactions: Tunnelling in space. *Nature Chemistry* **2013,** *5* (9), 734-736.

7. Pilling, M. J.; Seakins, P. W., *Reaction kinetics*. Oxford University Press: Oxford, 1995.

8. Shannon, R. J.; Taylor, S.; Goddard, A.; Blitz, M. A.; Heard, D. E., Observation of a large negative temperature dependence for rate coefficients of reactions of OH with oxygenated volatile organic compounds studied at 86–112 K. *Physical Chemistry Chemical Physics* **2010,** *12* (41), 13511-13514.

9. Lindemann, F. A.; Arrhenius, S.; Langmuir, I.; Dhar, N. R.; Perrin, J.; Lewis, W. C. M., Discussion on "the radiation theory of chemical action". *Transactions of the Faraday Society* **1922,** *17* (0), 598-606.

10. Carr, R. W., *Modeling of chemical reactions*. Elsevier Science: 2007; Vol. 42.

11. Hinshelwood, C. N., On the theory of unimolecular reactions. *Proceedings of the Royal Society of London* **1926,** *113* (763), 230-233.

12. Rice, O. K.; Ramsperger, H. C., Theories of unimolecular gas reactions at low pressures. *Journal of the American Chemical Society* **1927,** *49* (7), 1617–1629.

13. Kassel, L. S., Studies in homogeneous gas reactions. I. *The Journal of Physical Chemistry* **1928,** *32* (2), 225-242.

14. Marcus, R. A., Unimolecular dissociations and free radical recombination reactions. *The Journal of Chemical Physics* **1952,** *20* (3), 359-364.

15. Troe, J., Theory of thermal unimolecular reactions at low pressures. I. Solutions of the master equation. *The Journal of Chemical Physics* **1977,** *66* (11), 4745- 4757.

16. Sander, S. P.; Friedl, R. R.; Golden, D. M.; Kurylo, M. J.; Huie, R. E.; Orkin, V. L.; Moortgat, G. K.; Ravishankara, A. R.; Kolb, C. E.; Molina, M. J.; J.Finlayson-Pitts, B. *Chemical kinetics and photochemical data for use in atmospheric studies - Evaluation number 14*; Jet Propulsion Laboratory: Pasadena, California, USA, 2003.

17. Banwell, C. N.; McCash, E. M., *Fundamentals of molecular spectroscopy*. Fourth ed.; McGraw-Hill: London, England, 1994.

18. Hollas, J. M., *Modern spectroscopy*. Fourth ed.; John Wiley & Sons, Ltd: West Sussex, England, 2003.

19. Wayne, C. E.; Wayne, R. P., *Photochemistry*. Oxford University Press: 1996.

20. Xu, H.; Chen, R.; Sun, Q.; Lai, W.; Su, Q.; Huang, W.; Liu, X., Recent progress in metal–organic complexes for optoelectronic applications. *Chemical Society Reviews* **2014,** *43* (10), 3259-3302.

Chapter 3

Experimental Techniques for the Investigation of Gas Phase Kinetics

In order to carry out kinetic investigations on gas phase reactions, whether this is to determine the magnitude of the rate coefficient of a reaction or to establish the order of a reaction, it is necessary to measure the change in concentration, or a property related to concentration, of one or more of the reactants and/or products in the reaction as a function of time. Kinetic experiments must therefore bring together and mix reactants and initiate the reaction on a timescale that is well defined and negligible compared to that of the reaction, detect and measure the concentration of reactants or products with a system which has a suitable time resolution to respond to rapidly changing concentrations after initiation, and accurately measure and control the conditions under which the reaction occurs such as temperature and pressure. For the study of elementary reactions, which occur on very short timescales on the order of 10^{-2} seconds or less, various kinetic and analytical techniques can be used to fulfil these sometimes difficult but required criteria. The rates of such fast reactions are not only of practical interest, for example in modelling atmospheric chemistry, but also provide information about the mechanisms of the molecular interactions by which the reactions occur, i.e. molecular dynamics.

Gas phase reactions predominantly control both atmospheric and combustion systems, hence understanding the fundamental processes taking place during these reactions is of great importance to gain insight into the past, present and future state of the Earth's atmosphere, how and why changes in the atmosphere occur, and the environment in which we live. Significant progress has been made in the measurements of gas phase reaction kinetics over recent years, particularly in the identification of product yields from multichannel reactions. Both the development of laser flash photolysis and the advancement in many time-resolved detection techniques have made it possible to probe the reaction kinetics of short-lived species, such as radicals. Despite these advances in experimental methods and developments in computational methods leading to improvements in the accuracy of simulations used to model atmospheric systems, there are still many gas phase reactions about which little is known.

Furthermore, the accuracy of chemical models is only as good as the data which is put into the models, and calculations made by these chemical models still require validation. This means that more experimental work needs to be carried out and accurate measurements need to be acquired, both in the laboratory and in the field, to both verify and support computational work, and further our knowledge and understanding of the chemical processes occurring in the atmosphere.

Kinetics are associated with rates of change, so it is beneficial to consider the range of timescales within which the study of chemical processes takes place. Prior to 1945 the practical limit for kinetic investigations was on the order of seconds, with reactions faster than this being difficult to measure. Development of flash photolysis and flow methods, both of which are discussed below, in the mid-1940s, extended the lower time limit of kinetic experiments down to the millisecond range (10^{-3} s). However, it was in the 1970s that the most dramatic changes in kinetic measurements began to occur, as the availability of lasers capable of very short-lived pulses and fast electronics gradually opened up the study of reactions occurring beyond the order of microseconds (10^{-6} s) to those which are completed in nanoseconds (10^{-9} s), picoseconds (10^{-12} s), and even femtoseconds (10^{-15} s).

This chapter outlines the experimental methods used to study rapid gas phase reaction kinetics and discusses the principles, advantages and disadvantages of each. The relative rate method is described, along with two basic and widely used techniques for the mixing and initiation of reactions with fast kinetics, known generally as flow methods and perturbation or pump-probe methods, followed by an overview of some of the common detection techniques which can be employed to monitor the reaction *via* monitoring of reactant(s) and/or product(s) concentrations. A detailed description of the pulsed laser flash photolysis (PLFP) kinetic technique is also provided in this chapter, with a particular focus on its coupling with the absorption spectroscopy analytical technique, since these were the experimental methods used for the work described in this thesis. Two different absorption spectroscopy techniques were employed in experiments described in this thesis, ultraviolet absorption spectroscopy, for which the details on specific methodology used for data collection and analysis are provided in the final section of this chapter, and infrared absorption spectroscopy, which is the focus of Chapter 6 of this thesis.

3.1 Kinetics Techniques

Experimental techniques used to investigate rates of reaction can be either relative, in which the kinetics of the reaction are measured in relation to those of well-known and characterised reactions, or absolute, in which the kinetics of the reaction are measured independently of any other reaction. A description of the relative rate method is provided here. Two absolute kinetic methods commonly used for mixing and initiation of rapid experimental reactions are also discussed, termed flow methods, with a particular focus on discharge flow, and pump-probe methods, with a particular focus on laser flash photolysis.

3.1.1 Relative Rate Method

In certain cases, direct isolation of an elementary reaction for real time analysis, hence direct determination of the reaction rate coefficient, can be challenging, particularly in cases where the concentration of a reactant is difficult to measure. Under such circumstances, an alternative technique is required for the measurement of such reactions, and instead of a direct measurement, indirect determination of the rate coefficient may be possible *via* the relative rate method, made popular by Atkinson[1] in the atmospheric sciences. This method measures the loss of a reactant relative to that of a reference compound in the presence of a single reactive species, where the rate coefficient of the reaction of the reactive species with the reference compound is known while the rate coefficient of the reaction of the same reactive species with the reactant compound is to be determined.

Known concentrations of the reference and reactant compounds are introduced to a reaction vessel, such as a chamber, and allowed to mix with (precursor(s) of) the reactive species. A small but essentially constant concentration of the reactive species is generated, for example *via* use of photolysis lamps, and the concentrations of the reference compound and the reactant compound are determined as a function of time by taking samples from the reaction vessel at certain times throughout the reaction and analysing them using an appropriate detection method. The ratio of $k_{\text{reactant}}/k_{\text{reference}}$ is determined from the concentrations of the reactant compound and the reference compound and their rates of disappearance, i.e. the rate of change of concentration of each compound. Commonly used detection techniques to measure relative reactant

concentrations and monitor the reactions include gas chromatography (GC) and Fourier transform infrared spectroscopy (FTIR), both of which are discussed in further detail below. A specific detail to note is that the absolute concentration of the reactive species does not need to be known since the decay of one compound is measured relative to that of another with a known rate coefficient.[2]

When R_1 and R_2, the reactant compound and reference compound respectively, are present in the same reaction mixture in the presence of a reactive species, for example OH, for the reactions:

$$OH + R_1 \xrightarrow{k_{R_1}} \text{products} \qquad \text{(R3.1)}$$

$$OH + R_2 \xrightarrow{k_{R_2}} \text{products} \qquad \text{(R3.2)}$$

the consumption of the reactant compound R_1 and reference compound R_2 due to reaction with the reactive species OH are dictated by the rate equations:

$$-\frac{d[R_1]}{dt} = k_{R_1}[OH][R_1] \qquad \text{(Equation 3.1)}$$

$$-\frac{d[R_2]}{dt} = k_{R_2}[OH][R_2] \qquad \text{(Equation 3.2)}$$

and assuming that the only loss process occurring for each compound is the reaction with the reactive species, integrating the rate equations over time gives:

$$[R_1]_t = -k_{R_1}\int_0^t [OH].dt + [R_1]_0 \qquad \text{(Equation 3.3)}$$

$$[R_2]_t = -k_{R_2}\int_0^t [OH].dt + [R_2]_0 \qquad \text{(Equation 3.4)}$$

which, upon rearranging, gives:

$$\ln\left(\frac{[R_1]_0}{[R_1]_t}\right) = -k_{R_1}\int_0^t [OH].dt \qquad \text{(Equation 3.5)}$$

$$\ln\left(\frac{[R_2]_0}{[R_2]_t}\right) = -k_{R_2}\int_0^t [OH].dt \qquad \text{(Equation 3.6)}$$

which can be combined to describe the relationship between the rate coefficients k_{R_1} and k_{R_2} for the competing reactions and equated to:

$$\ln\left(\frac{[R_1]_0}{[R_1]_t}\right) = \frac{k_{R_1}}{k_{R_2}} \ln\left(\frac{[R_2]_0}{[R_2]_t}\right) \qquad \text{(Equation 3.7)}$$

Thus, a plot of $\ln([R_1]_0/[R_1]_t)$ vs $\ln([R_2]_0/[R_2]_t)$ should be linear with a gradient of k_{R_1}/k_{R_2} and an intercept of zero.[3, 4] Knowledge of the absolute rate coefficient k_{R_2} allows the relative rate coefficient k_{R_1} to be converted into an absolute one, thereby enabling determination of the rate coefficient of the reaction between the reactant compound and the reactive species. In practice, it is more often the case that if the absolute rate coefficient is known accurately for one member of a group of reactions for which the relative rate coefficients have been determined, the relative rate coefficients can all be converted into absolute ones.

An advantage of the relative rate method is that measurement of the concentrations of reactive species, which are often present in very low concentrations and have short lifetimes, is not required. Although, by using these low concentrations, the reactions often occur over minutes to tens of minutes and so experiments are performed over these timescales, which allows for the use of detection techniques with relatively poor time resolution.

Compared with the relative rate method, absolute methods are performed over faster timescales, with numerous techniques available to investigate chemistry occurring on varying timescales and under differing temperature and pressure conditions. Furthermore, in contrast to relative rate methods, absolute techniques do not require previous knowledge of the kinetics of a reference compound. Each of the rapid kinetic techniques discussed in the next section can be coupled to a range of detection techniques, which will also be discussed.

3.1.2 Flow Methods

In the use of flow methods to study the kinetics of gas phase reactions, the ability to achieve rapid linear gas flow velocities enables the controlled interaction of gases on short timescales. Often, microwave discharge is used to generate the reactant species, separately and continuously, and immediately prior to injection into the reaction

vessel, typically a flow tube, where it mixes into the main flow.[2] Production of reactant species A, from the precursor AB, using microwave discharge, which subsequently reacts with the co-reactant C can be written as:

$$AB \xrightarrow{\mu\text{-wave}} A + B \qquad \text{(R3.3)}$$

$$A + C \rightarrow AC \qquad \text{(R3.4)}$$

The common practice of employing microwave discharges in experiments with flow methods has coined the term discharge flow (DF) to describe this technique. The typical setup for a discharge flow experiment, as shown in Figure 3.1, consists of a main flow tube through which the bath gas flows directly, along with the reactive species flows, with a moveable injector through which the co-reactant is added to the main flow tube.

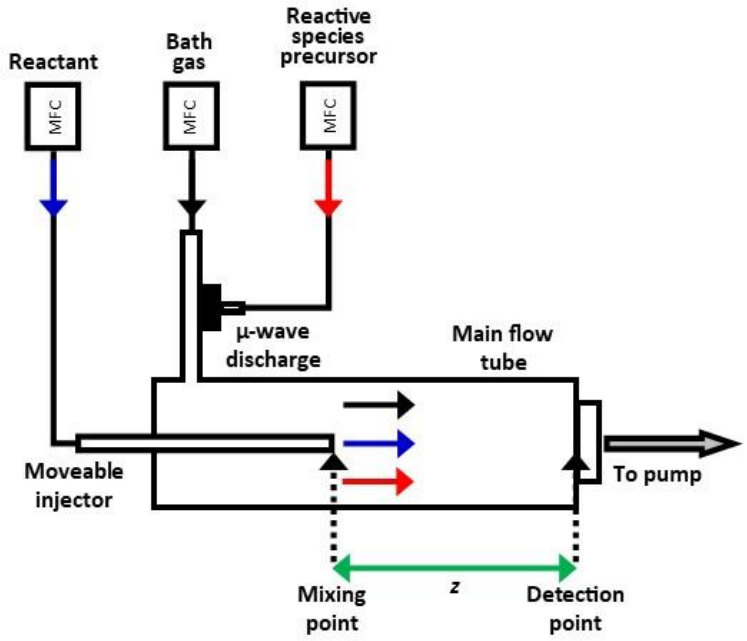

Figure 3.1: Schematic diagram of a typical discharge flow experimental setup, where *z* is the distance between reaction initiation or mixing point and detection point, and MFC denotes mass flow controllers.

Initiation of the reaction occurs at the tip of the moveable injector, which is where the reactant species are allowed to mix, with the timescale of the reaction being limited by the distance between the tip of the injector and the detector, i.e. the distance over which the reactants mix. Detection of reactant and/or products species occurs

downstream from this mixing point at the detection point, where the relative concentrations of reactants and/or products are monitored, with the flow characteristics enabling determination of the elapsed time between mixing and detection.

Knowledge of the velocity of the gas mixture in the flow tube allows for the reaction time, i.e. the time between initiation of the reaction due to mixing and detection of reactants and/or products, to be calculated via the relationship:

$$t = z/v \qquad \text{(Equation 3.8)}$$

where t is the reaction time, z is the distance between the initiation or mixing and detection points and v is the linear flow velocity of the gas mixture in the reaction vessel.

The detection of reactant or product species concentration is thereby carried out at this time point and can be plotted as the appropriate point on a concentration *vs* time (or distance) graph. Varying the position of the reactant injector along the flow tube, i.e. the distance between mixing and detection points, and measuring the signal associated with the relevant species concentration at each point whilst the flow rate is held constant then provides a series of reactant and/or product concentrations recorded at various times after the initiation of the reaction. In this way, a concentration *vs* time profile of the species concentration as a function of injector position, and hence reaction time, is gradually assembled, the analysis of which enables kinetic parameters such as the reaction rate coefficient to be determined. If one of the reacting species is suitably unreactive and can be kept present in a constant excess, with the added reactant typically being in excess of the reactive species concentration, the DF experiment can be conducted under pseudo-first-order conditions, meaning the kinetic parameters can be determined without knowledge of absolute concentrations for the minor reactant species.[1, 2, 5]

Certain limitations and restrictions apply for the experimental conditions under which the DF technique can be applied.[5] The first of these is that a uniform concentration of reactants is needed, which requires rapid and homogeneous reactant mixing with a well characterised gas flow, however in reality, mixing of gases takes a finite time. While this is insignificant if the timescale of mixing is short compared to that of the reaction, for fast reactions a significant portion of the reaction will already be

complete before a uniform concentration is achieved. For this reason, timescales of reactions studied by DF are limited to the millisecond time range. The second is the need to retain a uniform flow velocity along the length of the flow tube which can only be attained at low pressures. This means that DF experiments are generally limited to pressures below 10^3 Pa. High pressure experiments are further restricted since reactant mixing will also be slower at higher pressures and such systems would require large pumping capacities, however, there have been developments of high pressure flow systems in which these flow effects are accounted for, since these systems would enhance the range of experimental conditions that can be investigated.[6, 7] Further complications can arise from the use of low reaction pressures due to diffusion of reactants and heterogeneous processes occurring on the walls of the reaction vessel, both of which contribute to unwanted removal of reactant species. Heterogeneous chemistry can be somewhat reduced by coating the walls of the flow tube with materials such as halocarbon wax or Teflon, which remove the reactant species from the wall surfaces.[2, 5]

Despite these disadvantages, the DF technique has played an important role in gas phase kinetics over the years. Since reaction gas flows in DF experiments are in the steady state, signals can be accumulated over long periods of time to improve the signal-to-noise ratio, *S/N*, and as time resolution is achieved by variation of the distance between mixing and detection points, detection techniques do not need to have rapid response times. Consequently, a wide variety of sensitive detection techniques, including resonance fluorescence (RF), laser-induced fluorescence (LIF), laser magnetic resonance (LMR) and mass spectrometry (MS), can be coupled to DF experiments.[2, 5]

3.1.3 Pump-Probe Methods

Measurement of not only rapid chemical reactions but also ultrafast chemical phenomena, such as movements of atoms or electron excitations, has been enabled owing to what are known pump-probe techniques. Such methods, otherwise known as perturbation methods, work on the principle that when a system at equilibrium is subjected to a sudden perturbation, the effects of this disturbance can be monitored in real time as a new equilibrium is established. The most commonly used pump-probe

method employed to study kinetics of gas phase reactions is flash photolysis (FP) where photolysis refers to the use of light to dissociate a molecular species into smaller and simpler units, often ions or free radicals, meaning the possibility of side reactions, which can often lead to complex kinetics and mixtures of products, is minimised.

In laser flash photolysis, a short duration laser pulse of high intensity light, constituting the pump, is used to initiate a reaction *via* generation of the desired reactive species. Production of these reactive species may either be directly by photolysis, for example through excitation, or as a result of further rapid chemistry initiated through photodissociation of a suitable precursor species. Subsequently, reactant(s) and/or product(s) are measured as they decay and/or are formed respectively, using various detection techniques constituting the probe, to monitor the progress of the reaction of the generated reactive species with other species. The probe source may be pulsed, for example a second and weaker laser pulse, in which case varying the time delay or interval between the first and second pulses can be used to construct the evolution of the concentration-time behaviour of the reaction over its course, or continuous, for example a light source or a laser operated in continuous mode, in which case a complete concentration-time trace over the entire timescale of the reaction can be acquired per photolysis pulse, from which kinetic information can be obtained.[2] Similar to the discharge flow method, flash photolysis experiments are often conducted under pseudo-first-order conditions, by creating a situation where the concentration of the co-reactant is in large excess of the initial concentration of the reactive species produced by photolysis, in which case a bimolecular rate coefficient can be obtained from the pseudo-first-order rates of decay of reactants or formation of products.[1] Until the discovery and development of this kinetic technique of flash photolysis, there was no practical way of studying the kinetics of reactions involving highly reactive species. The idea was pioneered by Norrish and Porter in 1949, for which they were awarded the Nobel Prize in Chemistry in 1967.[8, 9]

Both the major disadvantages of flow systems such as discharge flow, mixing time and pressure limitations, are overcome by flash photolysis. Since reactant and precursor species are premixed and flowed into the reaction cell at the required temperature and pressure as a reaction mixture, meaning one or more of the reactive

species is generated *in situ*, this allows a homogeneous concentration of reactants to be obtained across the reaction cell if the photolysis beam used is of a uniform intensity, hence there is no mixing time. One requirement of the technique, however, is that production of the reactive species must occur on a timescale shorter than that of the reaction being investigated, necessitating that precursor gas mixtures be designed carefully to ensure that this is the case. Typically, reactants and precursor premixed samples are flowed into the photolysis cell at pressures in the range 0.001-10 atmospheres (1×10^{2} -1×10^{-6} Pa), although the technique can be used to investigate reactions at pressures of up to several hundred atmospheres if required, giving flash photolysis a much more versatile pressure range for the measurement of reaction kinetics than discharge flow.[2] In terms of pressure restrictions, the only one applicable to flash photolysis is that when subjected to the photolysis pulse, gases at low pressures may undergo adiabatic shock due to their typically low heat capacity.

Furthermore, probe light is often directed into the centre of the cell, with this probe region also being the location where the reactant species are generated and hence the reaction is monitored. This, combined with the pressure ranges employed in flash photolysis, results in complications from heterogeneous chemistry occurring on the walls of the cell, such as interferences from wall loss and wall catalysed reactions, being minimised and hence usually being rendered insignificant, which is a further advantage of flash photolysis over flow techniques. Limitation of flash photolysis in terms of the timescale of reactions which can be studied originates from the duration of the light pulse which produces the photolysis flash. In conventional flash photolysis where the source of the first flash was from a gas flash lamp, this duration could be several milliseconds, permitting measurement of processes with lifetimes on the microsecond timescale, however these light sources have since been generally replaced due to the advent of fast and high powered lasers in laser flash photolysis, with laser pulse durations being sufficiently short enough to last on the order of nanoseconds or less, gradually extending the range of timescales which could be experimentally followed to picoseconds and even femtoseconds. In flash photolysis, the rapid production of reactants following the photolysis of precursors decouples the kinetics of reactant production from the kinetics of the subsequent reaction processes, enabling the analysis of fast reactions on a wide array of timescales from milliseconds to femtoseconds depending on the nature of the photolysis source.[1, 2, 10]

An additional property of lasers making their use for photolysis advantageous over the use of flash lamps is that lasers have high specificity since, unlike flash lamps which have a broadband output, lasers have the ability of being tuned to specific wavelengths, offering control over which species are photolysed. Secondary chemistry may occur in the event that not only the precursor but also a co-reactant is photolysed at the wavelength of the flash, although this can be minimised, if not avoided, by using laser photolysis since the wavelength of the light which triggers the reaction can be adjusted to activate one particular kind of molecule without affecting others that might be present. Moreover, the fact that lasers are highly directional, can produce high energy pulses and do not suffer much from power degradation also means that lower precursor concentrations can be used since a significant quantity of reactant species can be produced from very low precursor concentrations, further minimising the occurrence of unwanted reactions, and simplifying the overall kinetics of the system. Despite this, the selection of a suitable precursor for the experiment is important, such that secondary reactions between the reactive species and the precursor are negligible.[11] A disadvantage of the flash photolysis technique is the need and availability of a suitable photolytic precursor since the discharge flow method does not have this requirement, making it more versatile. Fast and swift collection of data is enabled by the fact that lasers can be operated at high pulse repetition rates, with the rate of data collection only limited by the rate at which fresh reactants can be added to the cell between each laser pulse in order to again avoid secondary chemistry.

Because of the real time nature of flash photolysis experiments, a prerequisite of any detection technique which may be applied to follow the reaction is that it must have a rapid response time in order to respond to rapidly changing concentrations and achieve the necessary time resolution. Species produced after the flash can be monitored as a function of time using a range of detection techniques, with spectroscopic methods often being employed, such as absorption or fluorescence,[2] both of which are discussed in more detail below. Subsequent analysis of the concentration-time profiles of reactant and/or product species provides kinetic parameters for the reaction being studied.

3.1.3.1 Light Sources for Flash Photolysis

As described above, conventional flash photolysis used flash lamps to generate the transient species within the reaction,[12] and whilst lamps are still employed in some experiments, the majority of flash photolysis experiments are now conducted with lasers, which have the advantage of short pulse duration, high repetition rate, a narrow and precisely defined wavelength range, and a well-defined spatial profile. For lasing to commence in any laser employed in flash photolysis experiments two criteria must first be met. These are population inversion in the laser medium, which is a gas, liquid or solid where stimulated emission may take place, and the existence of an optical cavity within which amplification of the emitted light may occur.[13] These criteria are embedded in the word laser, which is an acronym for light amplification by stimulated emission of radiation. The mechanism by which lasers operate is centred on three basic radiative processes which can link any two energy levels, and are shown in Figure 3.2. Absorption of a photon by a lower state, spontaneous emission of a photon by the upper state, for example *via* fluorescence, as it returns to the lower state, and stimulated emission of a second photon from the upper state to the ground state by the first photon, i.e. two photons are produced, where the stimulated photon is coherent in direction and phase with the stimulating photon.[2, 11, 13] Different lasers can be employed in experiments to photolyse the precursor and initiate reactions, including excimer lasers, Nd:YAG lasers, both of which were employed in experiments detailed in this thesis in Chapters 4 and 5 and Chapter 6 respectively, and dye lasers. The principles involved in the operation of each type of laser are briefly discussed here.

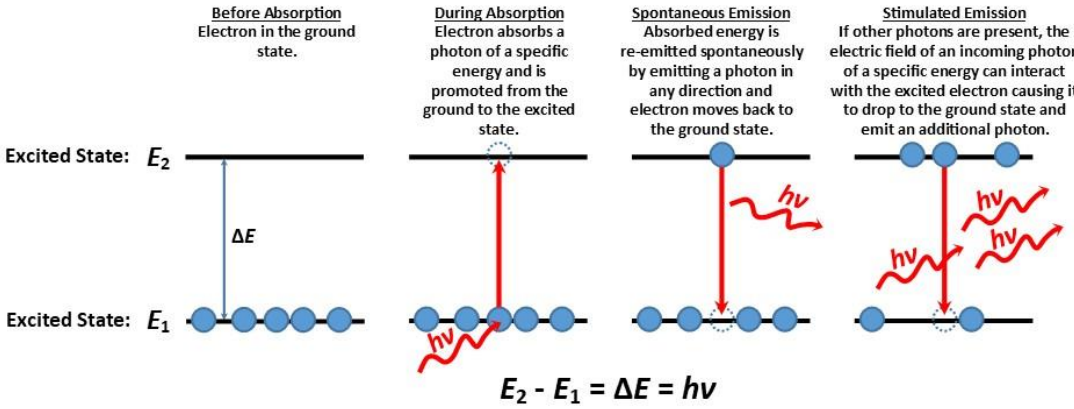

Figure 3.2: Schematic diagram to explain the absorption and emission of light in quantum theory. Reproduced and adapted from reference 11.[11]

3.1.3.1.1 Excimer Laser

One particular type of laser which is widely used in flash photolysis experiments is the excimer, or exciplex, laser, so called due to the formation of the active laser medium known as an excited dimer or excited diatomic complex which is electronically excited to produce the laser light.[11, 13] Excimer lasers are pulsed gas lasers which operate in the near ultraviolet region of the electromagnetic spectrum, and have pulse durations in the range 10-20 ns, repetition rates of up to 500 Hz, and high pulse energies of up to ~250 mJ pulse^{-1}. Laser radiation is produced in excimer lasers by passing a pulsed electric discharge through a noble halide gas mixture containing a buffer (helium), a noble gas (Ar, Kr, or Xe), and a halogen (either F_2 or HCl), to promote the active medium to an excited state by forming ions which combine to give the electronically excited species, or the exciplex, which then undergoes stimulated emission as it returns to the ground state. Exciplex compounds have bound upper electronic states and dissociative ground electronic states, between which the lasing action occurs.[2, 14] Since a population inversion, whereby the population of an excited state exceeds that of a lower state, is required to obtain laser action, this property of exciplexes is exploited in excimer lasers as a repulsive ground state means the ground state never becomes significantly occupied since its population is immediately removed by dissociation, hence creating a population inversion between the bound excited state and the dissociative ground state.[2, 11, 13] When light of the correct wavelength passes through the laser cavity consisting of the active medium where the population inversion is maintained, it is amplified because the rate of stimulated emission exceeds that of absorption. This inversion is generated and bounded in this laser cavity *via* the use of mirrors which reflect the light back and forth through the active medium, with one mirror made partially reflecting to allow some of the light out.[2]

The wavelength of the laser light depends on the composition of the exciplex formed and hence the gas mixture chosen, since the energy separation between the excited and ground states is different for each exciplex, with some of the major excimer wavelengths being 308 nm, 248 nm and 193 nm,[15] from the gas mixtures Xe/HCl/He, Kr/F_2/He and Ar/F_2/He respectively, corresponding to the exciplexes XeCl, KrF and ArF respectively. These wavelengths are particularly useful since the photon energies provided are comparable to bond dissociation energies (300-500 kJ mol^{-1}) and hence

absorption of such a UV photon often results in the cleavage of one or more bonds.[2, 11] The combination of these short wavelengths and with high power make excimer lasers ideal for generating significant quantities of radicals or reactive species. Experiments detailed in this thesis in Chapters 4 and 5 utilised a KrF excimer laser at a wavelength of λ = 248 nm, for which a $Kr/F_2/He$ gas mixture was used, creating excited Kr^+ and F^- ions which form the KrF exciplex, where He acts as a third body in the reaction.

3.1.3.1.2 Nd:YAG Laser

An Nd:YAG laser is a solid-state laser which utilises a crystalline lattice of neodymium-doped yttrium aluminium garnet ($Nd:Y_3Al_5O_{12}$) as the lasing medium. An important factor in the lasing action which occurs in Nd:YAG lasers is that in the host YAG crystal, ~1 % of the yttrium ions are replaced by Nd^{3+} ions, with the stimulated emission required for lasing occurring from electronic excitation of these Nd^{3+} ions.[16, 17] A high-power xenon flashlamp is fired, constituting the pump and producing broadband light across the near-UV, visible and near-IR range of the electromagnetic spectrum, and if the pumping from the flashlamp is sufficiently strong enough, it initiates a population inversion within the energy levels of the Nd^{3+} ions. When the light enters the cavity containing the active medium, a small percentage of the pumping light is absorbed by the Nd^{3+} ions in the YAG crystal lattice, promoting excitation from the ground state into a higher energy state which rapidly relaxes to a lower electronic state. Stimulated emission occurs between this lower electronic state and another even lower state when a photon passing through the lasing medium at the same frequency as the lasing transition is amplified by an induction decay of some of the Nd^{3+} ions from the upper to the lower state, with the resultant state of this stimulated emission then rapidly relaxing back to the ground state of the Nd^{3+} ions. Mirrors on either side of the active laser medium within the cavity reflect the amplified light back in resulting in significant amplification of the light at the wavelength of the lasing transition. A partially reflective surface is present on one of the two mirrors, allowing most light to pass through. The primary emission of light from this particular atomic transition within the Nd^{3+} ions in Nd:YAG lasers is at a fundamental wavelength of 1064 nm in the near-IR, although different

wavelengths of light can be produced from a phenomena known as frequency mixing, with the second, third and fourth harmonics of Nd:YAG lasers emitting 532nm, 355nm and 266 nm light respectively.[13, 18]

Operation of Nd:YAG lasers is often in the pulsed mode, which typically requires Q-switching to optimise the energy output from the laser.[19] During pumping or excitation of the active medium, the population inversion slowly reaches a steady-state, alongside the light intensity within the active medium being amplified but reaching a saturation intensity due to spontaneous emission. However, the time taken to reach this saturation intensity is significantly less than that to attain the maximum population inversion, hence Q-switching is introduced in order to synchronise these two events and thereby gain the maximum output from the laser. An optical switch or shutter is inserted into the laser cavity which, when closed, limits the light intensity within the active medium and waits for a maximum population inversion in the Nd^{3+} ions to be reached (~250 μs), at which point the switch opens, releasing the full power of the laser into the cavity and active medium, hence allowing stimulated emission. Since the active medium is already largely excited, the intensity of light in the cavity increases rapidly, leading to the output of a short pulse of high energy photons.[16] Experiments detailed in this thesis in Chapter 6 employed the fourth harmonic of an Nd:YAG laser giving a wavelength of λ = 266 nm, and the laser was used in the pulsed mode with a Q-switch.

3.1.3.1.3 Dye Laser

Dye lasers use solutions of organic dyes as the active laser medium, enabling them to have a tuneable output of many different wavelengths of light compared to lasers which use solid or gaseous active media.[11, 20] For efficient lasing to occur, the organic dye used in the laser must absorb strongly at the excitation wavelength of the pump laser and have a broad fluorescence spectrum, with the wavelength of light emitted always being greater, i.e. lower in energy, than the wavelength of light absorbed. Since the dye is dissolved in solution, the multitude of available energy levels within the dye molecules is broadened due to enhanced intermolecular interactions within the solution, giving the emission spectra of laser dyes their characteristic broadness, due to which the laser can be tuned to a selected output wavelength.[21]

In a dye laser, a short pulse of monochromatic light from a flash lamp or another laser e.g. an Nd:YAG laser is used to excite the dye to a singlet state.[13] Rapid vibrational relaxation ensues, and the molecule emits a photon *via* fluorescence to relax back down to the ground state, with the speed of this fluorescence process creating a population inversion between the ground vibrational level of the upper electronic state and the excited vibrational level of the ground electronic state (see Chapter 2 for further details on photochemistry). With each instance of light passing through the excited dye solution contained in the cavity, it gains intensity through spontaneous emission. The mirrors in the cavity reflect a number of photons of the fluorescent light back into the dye solution, or laser medium, and stimulate emission if the photons are of the correct frequency, resulting in this stimulated emission dominating over spontaneous fluorescence. In order for the wavelength of light directed back into the cavity to be monochromatic, a diffraction grating must be used within the optical cavity of the dye laser. This grating only resonates light of a certain wavelength, hence only allows this wavelength of light back into the cavity where it can stimulate further emission, and therefore only amplifies light at this single wavelength.[22] Since one of the two mirrors consists of a partially reflective surface, this enables some light to pass through and escape the cavity, resulting in a monochromatic laser light output beam. Like in the case of an Nd:YAG laser, this beam can undergo frequency doubling to generate the second-harmonic of the dye laser, where a crystal is used to double the optical frequency i.e. half the vacuum wavelength, of the input beam, with the output beam produced propagating in the same direction as the input beam.[23]

3.1.4 Summary of Kinetic Techniques in Atmospheric Chemistry

Over the 40 years since its introduction, the flash photolysis method became more powerful and sophisticated owing to developments in both optics and lasers, with interest in the technique growing considerably as the practical applications expanded from chemistry, facilitating research into a whole host of other areas including but not limited to biology, biochemistry, material sciences and environmental sciences. Flash photolysis revolutionised the study of photochemistry, particularly that relating to the chemistry of highly reactive species, such as free radicals, which cannot be isolated or stored but can be easily produced from photolysis of an appropriate precursor. It

has been and continues to be used extensively in investigations of extremely fast reactions down to the femtosecond timescale as the technique can isolate even very low concentrations of otherwise unobservable portions of chemical reactions and has proven invaluable for understanding the complicated kinetics relating to atmospheric chemistry.

Whilst flow and perturbation methods comprise the two main categories of kinetic experiments carried out, particularly in research pertaining to atmospheric science, other techniques do exist and have been developed and applied to this field of study, such as shock tubes and relaxation methods, however a detailed discussion of these is outside the scope of this work. Nevertheless, in all cases, the basic requirements of specificity, sensitivity and ease of reactive species generation are present and fulfilled, along with the ability to conduct experiments under the desired pressure and temperature conditions, making these techniques ideal for implementation in atmospheric research. The kinetic technique employed in this work, along with the selected analytical techniques, are discussed later in this chapter.

3.2 Analytical Techniques

Once a reactive species of interest has been generated, a variety of different techniques exist which can be used for detection. A range of experimental techniques have been utilised to monitor short-lived species in gas phase kinetics, with a selection of the most commonly employed analytical techniques, along with their merits and shortcomings, are described here. These techniques are mass spectrometry (MS), laser-induced fluorescence (LIF), and absorption spectroscopy which is further divided into ultraviolet absorption spectroscopy, cavity ring-down spectroscopy (CRDS), and infrared absorption spectroscopy, all of which can be and are typically used with both flow and flash photolysis methods. Alternative analytical techniques, such as resonance fluorescence (RF), laser magnetic resonance (LMR) and gas chromatography (GC), all of which are mentioned in this chapter as detection techniques often used in conjunction with one or more of the kinetic techniques discussed in this chapter, are also frequently employed, however a detailed discussion of these methods is outside the scope of this thesis.

3.2.1 Mass Spectrometry

The general principle behind mass spectrometry (MS) is that different atoms and molecules can be separated due to their differing masses, and MS operates on the basis that a charged species, such as an ion, in motion can be deflected by a magnetic field. The magnitude of the force experienced by the charged species is directly proportional to the mass-to-charge ratio, *m/z*, of that particular charged species, with ions of the same *m/z* ratio undergoing the same amount of deflection. Hence, MS identifies charged or ionic species based on their *m/z* ratio and their abundance.[2, 24] Although there are many different types of mass spectrometers, they all share the same four basic key stages, ionisation, acceleration, separation, and detection, which are coupled together in the MS analytical technique.[25] Mass spectrometers frequently employed in gas phase kinetics are the quadrupole and time-of-flight (ToF) mass spectrometers.

Only charged particles can be deflected in a mass spectrometer, meaning that before entering the spectrometer the species of interest must be ionised. Several suitable methods exist through which the gas sample may be ionised, including by thermal means, by applying an electric field or by impacting the sample with energetic electrons, ions or photons, with the ionisation method chosen dependent on the nature of the sample.[26] Ionisation methods are often classified as either soft ionisation methods or hard ionisation methods, which refer to processes which impart little or high quantities of residual energy onto the subject species respectively, therefore resulting in little fragmentation or invoking large degrees of fragmentation respectively. Examples of soft ionisation techniques include electrospray ionisation (ES), fast atom bombardment (FAB), matrix-assisted laser desorption/ionisation (MALDI), field ionisation (FI), thermal ionisation (TI), chemical impact ionisation (CI), secondary ion mass spectrometry (SIMS) and photoionisation mass spectrometry (PIMS), and the most common example of a hard ionisation method is electron impact ionisation (EI). Samples containing complex mixtures of gaseous species often demand soft ionisation techniques to reduce fragmentation of the parent molecule and limit complications in detection and analysis.

The PIMS system in particular, which uses a high energy photon to dissociate the gaseous molecule, is very effective, with the distinct advantage of photoionisation over other methods of ionisation being its high specificity. The wavelength of light

used in photoionisation can be tuneable, which means that the vacuum UV (VUV) radiation used to ionise different species can be specifically selected such that only one isomer is ionised. As such, PIMS can be used in investigations which seek to use MS as a means of resolving chemical kinetics mechanisms and isomeric product branching. It can be considered the ideal soft ionisation technique since the tuneability of the photoionisation energy results in reduced fragmentation as the molecule is supplied with just enough energy to ionise meaning there is not enough excess energy available to induce fragmentation. In instances where a synchrotron light source is utilised, such as the experiments resulting in the first direct detection of Criegee intermediates[27, 28] (see Chapter 1 for further details), tuneable photon energies for ionisation can be scanned to acquire a photoionisation spectrum in conjunction with the mass spectrum obtained from MS. A pulsed laser flash photolysis-photoionisation mass spectrometry (PLFP-PIMS) system was designed and built at the University of Leeds in collaboration with Kore technology,[29] and has been used to measure Criegee intermediate reaction kinetics.[30]

Upon ionisation, the energetically unstable molecular ion, $M^{\bullet+}$, is formed:

$$M + e^- \rightarrow M^{\bullet+} + 2e^- \qquad \text{(R3.5)}$$

which may further fragment into smaller ions and free radicals. After ionisation, the newly formed ions must then be accelerated towards the spectrometer, which is achieved by having a large potential difference between the gas sample inlet and the mass spectrometer.

A mass analyser within the spectrometer is used to separate the charged particles according to their *m/z* ratio, with the ions then detected proportionally to their abundance. A number of different mass analysers are utilised in MS, however the two most common ones are the quadrupole mass analyser and the time-of-flight (ToF) mass analyser.[25] The quadrupole mass analyser selects ions with a specific *m/z* ratio so that only a certain mass is detected.[2] A quadrupole achieves this by filtering ions as they move between four parallel metal rods, with the transverse rods coupled together giving two pairs of rods, across which opposing radio frequency voltages are applied, such that only ions of a certain *m/z* ratio have the correct trajectory to pass through the quadrupole and reach the detector while ions which do not have the required *m/z* ratio collide with the rods and are lost.[31] The range of *m/z* ratios detected

can be tuned by varying the voltages across the rods. The quadrupole mass analyser is a popular technique for separating ions and a low-cost method for detection. However, is limited since only one species can be detected at once.

The other main method to differentiate between ions in MS experiments is to use the ToF mass analyser. Ions are initially accelerated from the ionisation region into the mass spectrometer by using high voltages to accelerate the charged species towards the detector. By accelerating the ions through a such a constant electric field, the resultant kinetic energy of all the ions is identical, however the velocities at which they accelerate are dependent on their individual *m/z* ratios, meaning the time taken to reach the detector will depend on the *m/z* ratio of the ion, and consequently the lightest ions will arrive at the detector first.[24, 26] Ions are often detected using an electron multiplier, with results of MS experiments typically presented as a mass spectrum, which is a plot of intensity as a function of the *m/z* ratio. Despite quadrupole MS instruments being simpler to operate since complete time-resolved traces can be taken per pulse, unlike with ToF-MS where the delay time between the pump and probe pulses require scanning, the latter has one major and very important advantage. It allows observation of all the ion species generated at once, therefore theoretically, both the decay of reactants and growth of products can be measured simultaneously, with ToF-MS being capable of monitoring species on the millisecond timescale.[29] Also, because it can detect multiple species at once, it is possible to measure different products formed in multichannel reactions and determine product yields.

3.2.2 Laser-Induced Fluorescence

Laser-induced fluorescence (LIF) spectroscopy is a fluorescence technique in which the target species is electronically excited from its ground state using a laser as a light source, with a dye laser commonly being used, meaning the output from the laser is tuneable such that it is selected to match and hence probe a specific transition within the species of interest. Following this excitation of the species to an upper electronic state, several processes can occur, which can be represented on a Jablonski diagram and are discussed in detail in Chapter 2, however the process analysed in LIF is the corresponding fluorescence, in which an excited species relaxes back down to the ground electronic state by emitting a photon, the signal of which is detected using a

photomultiplier tube (PMT).[2] Before the excited species returns to the ground state, it can undergo a loss in vibrational energy *via* relaxation to the lowest lying vibrational energy level in this upper electronic state, and as a result the emitted photon can be either at a lower frequency, and hence longer wavelength, than the excitation photon, termed off-resonance fluorescence, or at the same frequency and hence same wavelength, called on-resonance fluorescence. Competition between all the processes the excited species can undergo, as summarised in Chapter 2, means that often LIF experiments are performed at low pressures to avoid quenching.[32] As the fluorescence signal is proportional to the number of ground state molecules present in the reaction mixture, the fluorescence intensity provides a relative measure of the concentration of the species of interest, allowing a concentration profile of this species to be built up as a function of time by varying the delay time between initiation of the reaction, for example through laser flash photolysis, and the light source inducing fluorescence, i.e. the probe laser pulse.

An advantage of LIF is that the range of commercial dyes available offers a wavelength output range of 320 nm-1 μm, providing the probe light required to monitor a variety of atmospheric species. Currently, the most common technique used to detect the OH radical, an important species in the field of atmospheric chemistry, is LIF, at an excitation wavelength of either ~282.5 nm or 308 nm. On-resonance fluorescence detection is employed for excitation at 308 nm, where the fluorescence also occurs at 308 nm, while excitation at ~282.5 nm typically involves off-resonance detection at 308 nm.[32] LIF is a highly sensitive technique particularly useful for detection of species during field campaigns since interferences can occur due to the presence of other species and atmospheric concentrations can be low, for example OH detection can be conducted using LIF and atmospheric OH concentrations are on the order of [OH] $\approx 10^6$ cm^{-3}. Moreover, time-resolved monitoring of low species concentrations, e.g. radicals, on the order of $<10^{12}$ cm^{-3}, often required during kinetic studies to simplify the chemistry occurring, maintain pseudo-first-order conditions and avoid unwanted secondary chemistry, necessitates the use of sensitive detection techniques. Exploitation of the well-defined spatial profile of light generated by a laser enables improved sensitivity of species detection using the LIF technique. To optimise the technique, in most LIF configurations, detection occurs perpendicular to the direction of probe laser propagation, since fluorescence emission occurs in random

directions and this orthogonal arrangement helps distinguish the fluorescence signal from the background scattered probe laser light.[2] Monitoring the off-resonance fluorescence through an optical interference filter and averaging the signal over several photolysis laser pulses can further increase the signal-to-noise ratio, *S/N*, of the LIF technique since this allows the signal to be measured relative to a zero background.

However disadvantages of the LIF technique do exist, such as the fact that it does not provide an absolute measurement of the concentration of the species of interest, rather a relative concentration is given meaning calibration is required before conversion to an absolute concentration of the species can be determined.[2] Furthermore, as stated above, LIF studies are generally limited to low pressures of <100 Torr due to collisional quenching, hence restricting the range of conditions under which experiments can be conducted, however recent developments in the sampling and detection methods employed have enabled high pressure measurements to be made.[33] Finally, despite the ability to tune the dye laser emission of LIF systems offering high selectivity to probe a wavelength corresponding to a transition between specific rovibrational states within the electronic bands of a particular species, this technique is not universal, since it can only be used to monitor certain species, namely those that have a bound and accessible upper electronic state and hence fluoresce.[2] This means that LIF is not suitable for larger molecules or radicals due to the increased difficulty in monitoring of such species because of the competition between fluorescence and other processes, since larger molecules have more vibrational modes which are more likely to undergo intersystem crossing and radiationless transitions than fluorescence.

3.2.3 Absorption Spectroscopy

Absorption spectroscopy is another important detection technique commonly used to monitor fast reactions and detect short-lived species, and operates on the basis of measuring the absorbance of light by the species of interest at a particular wavelength or within a wavelength range due to interactions of the radiation with the species. The intensity of this absorption varies as a function of wavelength, or frequency, with this variation being referred to as the absorption spectrum. Absorption spectroscopy is complementary to fluorescence spectroscopy, such as the LIF process described

above, in that fluorescence deals with transitions from the excited state to the ground state while absorption measures transitions from the ground state to the excited state. In theory, absorption spectroscopy can be employed as a universal technique in gas phase kinetics since all species, i.e. molecules/atoms/radicals, absorb light of certain wavelengths specific to that particular species, often in the UV/visible and/or IR regions of the electromagnetic spectrum. The fraction of light absorbed by the target species at certain characteristic wavelengths is proportional to the concentration of the species in the reaction mixture, as defined by the Beer-Lambert law (refer to Chapter 2 for further details):

$$A_\lambda = \ln\left(\frac{I_{0,\lambda}}{I_\lambda}\right) = \sum_{i=1}^{i=\mathrm{n}} \sigma_{i,\lambda}\,[C]_i\,l \qquad \text{(Equation 3.9)}$$

where A_λ is the absorbance at wavelength λ, $I_{0,\lambda}$ is the incident light intensity at wavelength λ, I_λ is measured change in light intensity at wavelength λ, $\sigma_{i,\lambda}$ is the wavelength specific absorption cross-section of species i, $[C]i$ is the concentration of species i and l is the optical path length.

One of the major advantages of absorption spectroscopy, which is highlighted in the Beer-Lambert law, is that since the absolute concentration of the target species is directly proportional to absorbance, it can be determined from measurement of the absorbance provided the cross-sections of the target species and path length of the sample are known.[2] Typically, during absorption spectroscopy, a broadband light source, such as an arc lamp, is used to generate light at a frequency absorbed by the reactant species. The light is passed through the reaction cell containing the reaction mixture, and a monochromator is used to select and direct only light of frequency pertinent to species absorption towards a detector. Laser radiation can also be used as the probe light source during absorption experiments, with the output of a dye laser able to be tuned to a specific absorption line without the need for a monochromator, or a quantum cascade laser (QCL) operated at a selected single wavelength, or wavenumber, able to provide a stable light source, as is used in experiments reported in Chapter 6. Alternatively, the entire range of wavelengths supplied by a broadband source can be utilised, as is the case in experiments reported in Chapters 4 and 5 of this thesis, in which a laser driven light source (LDLS) was used, for which experimental details are also provided further in this chapter.

As is often the case with the other analytical techniques described here, absorption spectroscopy experiments are also usually initiated using laser flash photolysis to generate reactant species in the cell, and the ratio of the incident to transmitted light intensity, $I_{0,\lambda}/I_{\lambda}$ can be measured as a function of time to give the change in concentration of the reactant and/or product species throughout the reaction.[34] This allows a complete concentration-time profile to be recorded, using absolute species concentrations in real time, each time the photolysis laser is fired, making data acquisition during absorption detection more efficient than by fluorescent means.

Absorption techniques require accurate measurement of the light intensity passing through the reaction cell both prior to and following the onset of absorption due to the production of reactive species, which, under typical experimental conditions where reactive species are generated in low concentrations to minimise the contribution of secondary chemistry to the observed kinetics, generally corresponds to only a small perturbation in light intensity. Such small changes in I_{λ} compared to $I_{0,\lambda}$ mean that experiments in which absorption detection methods are used often result in poor signal-to-noise ratio, *S/N*, hence poor sensitivity, especially when compared to fluorescent detection methods which monitor the reactive species signal relative to a zero background level of light, making it much easier to detect small variations. As a result, absorption techniques often require relatively high concentrations of reactive species, typically on the order of 10^{12} to 10^{13} cm^{-3} depending on the cross-section and optical path length, in order to detect appreciable intensity changes in the analysis light. Signal averaging can be used to improve the *S/N* ratio, which works on the concept that since the absorption signal is reproducible from one photolysis pulse to another whilst the contribution of noise from a variety of sources to the observed signal is random, adding together a series of data points averages out the noise leaving behind the absorption profile with a significantly enhanced *S/N* ratio.[2]

According to the Beer-Lambert law, provided in Equation 3.9, the amount of light absorbed is directly related to the product of the reactive species concentration and the path length of the light passing through the reaction cell. Consequently, the issue of noise described above can be overcome, and sensitivity of the technique improved, by the strategic placement of highly reflective mirrors at either side the reaction cell allowing the probe light to pass multiple times through the absorption region prior to

detection. Such an arrangement is commonly referred to as a multipass cell or instrument and increases the path length of the system which in turn increases the absorbance. The White[35] and Herriot[36] cell designs, with three and two spherical mirrors of identical radius of curvature respectively, represent the optical arrangements most often used in experiments which utilise multipassing of probe light. Both the experimental designs employed in work described in this thesis in Chapters 4 and 5 and Chapter 6 respectively included multipass alignments.

The main disadvantage of absorption spectroscopy is that many different species can absorb at the same or similar wavelengths, resulting in overlapping spectra if species in the reaction mixture, whether reactant(s) or product(s), other than the species of interest absorb at the wavelength(s) being monitored.[34] This can be particularly problematic when measuring in the UV region of the spectrum as many species have unstructured spectra in this region so may be difficult to identify and distinguish between. However, such interferences can be minimised by resolving time profiles of absorbance at all wavelengths such that absorbance due to each individual species within a mixture may be observed at each relevant wavelength.[37]

3.2.3.1 Ultraviolet and Infrared Absorption Spectroscopy

For many species of interest, absorption occurs in the UV, visible and/or infrared (IR) regions of the electromagnetic spectrum, and UV absorption cross-sections in particular are well known for many species which may be encountered in the atmosphere and/or in reaction systems studied in the laboratory. As a result, the most commonly employed spectroscopic methods are UV/visible absorption spectroscopy and IR absorption spectroscopy. In recent years, the development of tuneable UV, visible and IR lasers has also greatly enhanced the selectivity and sensitivity of these absorption spectroscopy techniques, making them highly influential detection methods for the determination of kinetic and mechanistic information relating to rapid gas phase reactions.

Since applications for each spectral region of the electromagnetic spectrum have developed independently of each other, each spectral region has acquired its own preferred units, with the UV region conventionally given in units of nm (10^{-9} m) and referred to in terms of wavelength, λ, and the IR region, which can be further

characterised into three sub-regions, near-IR (NIR), mid-IR (MIR) and far-IR (FIR), is given in units of μm (10^{-6} m) when in terms of wavelength. However, infrared measurements are almost exclusively reported in terms of wavenumber, $\tilde{\nu}$, which is the reciprocal of wavelength and is conveyed in units of cm^{-1}. It is worth noting that most IR studies investigating reactions of atmospheric relevance tend to focus on the 1-16 μm, or 10,000-625 cm^{-1}, spectral range.[32]

Many species which play an important role in atmospheric chemistry absorb radiation in the UV/vis region of the electromagnetic spectrum, making UV absorption spectroscopy ideal for use in investigations of atmospheric reactions.[32] In the UV region of the electromagnetic spectrum, which extends over the wavelength range 10-400 nm, species undergo electronic and vibrational transitions between vibrational levels of the lower and upper electronic states, therefore UV absorption spectroscopy utilises the properties of absorption from such transitions and the associated vibronic structure, with UV absorption spectra exhibiting a combination of broad, featureless spectra and discrete, sharp lines (see Chapter 2 for further details). It is worth noting that O_2 absorbs strongly below 190 nm which places a limit on the UV experiments which can be performed in air, and requires the use of vacuum UV experiments for detection below 190 nm since any O_2 in the system needs to be removed or an oxygen-free atmosphere needs to be used, commonly pure nitrogen. UV absorption spectroscopy benefits from wide applicability and high accuracy, however, can be influenced by stray light and is not very selective since several species can absorb at the same wavelengths. Additionally, UV spectra tend to be broad and structureless meaning it can sometimes be difficult to distinguish spectra for different species.

Nearly all atmospheric species exhibit moderate to strong absorptions in the IR region, making IR absorption spectroscopy an extremely versatile tool in atmospheric studies.[32] The IR region spans the wavelength range 0.7-1,000 μm, approximately equivalent to the wavenumber range ~14,000 cm^{-1}-10 cm^{-1}, with the NIR, MIR and FIR ranges being 0.7-2.5 μm or 14,000-4,000 cm^{-1}, 2.5-25 μm or 4,000-400 cm^{-1}, and 25-1,000 μm or 400-10 cm^{-1} respectively. Absorption of radiation in the IR region involves interactions with molecular vibrations and rotations resulting in transitions between rotational levels of the ground and excited vibrational states in the ground electronic state, with IR absorption spectra consisting of a series of vibrational bands,

from fundamental molecular vibrations corresponding to normal vibrational modes (e.g. stretching and bending) and the associated ro-vibrational structure, and from overtones and combination bands of molecular vibrations, each with a series of closely spaced rotational absorption lines at high resolution (see Chapter 2 for further details on photochemistry). For a vibrational mode of a species to be IR active, hence appear in the IR spectrum, it must be associated with a change in the dipole moment of the species, rendering some modes IR inactive. High resolution IR can avoid by-product interferences due to the distinct structure of ro-vibrationally resolved spectra, giving high selectivity and allowing unambiguous identification of species especially desirable when more than one species which absorbs in the same region is present in the mixture. However, infrared absorption can lead to complicated looking spectra which can be difficult to interpret.

3.2.3.2 Cavity Ring-Down and Cavity Enhanced Spectroscopy

Cavity ring-down spectroscopy (CRDS) is a technique utilised in measuring absorption for various applications, including kinetic determination of reactions. Light is introduced into an optical cavity consisting of two highly reflective mirrors and reflected thousands of times inside the cavity giving an effective path length on the order of kilometres. A small fraction of the light, typically $<10^{-5}$ % per reflection depending on the mirrors, leaks out of the other side of the cavity and is measured by a detector. The rate of, or time taken for, the light intensity exiting the optical cavity to decay to 1/*e* of its initial intensity, referred to as the ring-down time, is measured in the presence and absence of the absorbing species, and can be used to calculate the concentration of the absorbing species in the gas mixture in the cavity *via*:[38]

$$\alpha = \sigma_\lambda [C] = \frac{R_l}{c}\left(\frac{1}{\tau} - \frac{1}{\tau_0}\right) \qquad \text{(Equation 3.10)}$$

where α is the absorption coefficient specific to the absorbing species at the resonance wavelength of the cavity, λ, and is equivalent to the wavelength dependent absorbance A_λ divided by the path length l from the Beer-Lambert law provided above in Equation 3.9, σ_λ is the absorption cross-section of the species at wavelength λ, [C] is the concentration of the species, c is the speed of light, τ and τ_0 are the ring-down times in the presence and absence of the absorbing species respectively, and R_l is the ratio

between the cavity length (the distance between the two mirrors) and the absorption path length, *l* (the overlap region of the photolysis and probe laser beams).

CRDS experiments often use laser flash photolysis to initiate reactions within the cavity, and can utilise various probe light sources, hence be coupled with multiple absorption spectroscopic techniques, including UV and IR absorption spectroscopy. CRDS is a highly sensitive technique given its long path length due to the multipass nature of the system, and is not affected by fluctuations in probe light intensity since the ring-down time is independent of this intensity. Conventional CDRS operates at single wavelength or over a very small wavelength range, with optics typically being highly reflective (>99.99 %) at ± 5 % of the centre wavelength, however outside of this range the mirrors lack reflectivity to enable broadband multipass absorption spectroscopy measurements, making it unsuitable for applications where multipass absorption over a wide range of wavelengths is desired.[39] Furthermore, overlap of the photolysis laser with the cavity region can be challenging in CRDS experiments.

Cavity enhanced absorption spectroscopy (CEAS) is a modification of the CRDS technique based on an off-axis arrangement of the optical cavity and allows the radiation absorption of species within the cavity to be determined.[38] Since light intensities are directly measured in CEAS, unlike CRDS, this technique is not immune to fluctuations in probe light intensity.[39] CEAS is also often coupled with incoherent broadband light sources such as a xenon arc lamp, a light-emitting diode (LED) or a super continuum (SC) laser, meaning while dichroic mirrors are used in CRDS, CEAS uses highly reflective broadband optical cavity mirrors to multipass the probe radiation through the cavity and increase the effective path length of the absorption.[40] This path length in CEAS experiments is wavelength dependent as a result of the dependence of the number of passes on the reflectivity of the cavity mirrors, and can vary significantly for broadband light sources requiring calibration of the path length as a function of wavelength.

Despite absorption techniques employing the cavity enhanced technique having a greatly increased path length of the probe light, the sensitivity of such techniques is impeded by the fact that the probe intensity which reaches the detector is low. Whilst it is beneficial to extend the path length of the absorption, sufficient probe light intensity (number of counts) is required to detect small changes in absorbance.

3.3 Experimental Details and Procedure of This Work

The following section outlines the specific apparatus used during this work, with details of the photolysis and probe lasers used to initiate and monitor reactions within the reaction cell respectively, the spectroscopic technique used to detect species and follow reactions, and the way in which data was collected, processed, and analysed to determine both spectroscopic and kinetic parameters.

UV absorption cross-sections of the CH_2OO Criegee intermediate (described in Chapter 4), along with kinetics of the CH_2OO self-reaction and the reaction between CH_2OO and I (described in Chapter 5), were studied using laser flash photolysis of $CH_2I_2/O_2/N_2$ gas mixtures, coupled with broadband time-resolved UV absorption spectroscopy. The development and characterisation of the experimental apparatus has been described in detail elsewhere,[37, 41] briefly described in Chapters 4 and 5, and is summarised here. Figure 3.3 shows a schematic of the experimental setup used to carry out the work described in Chapters 4 and 5 of this thesis. Note that the IR experimental setup and work carried out using this setup are described in Chapter 6.

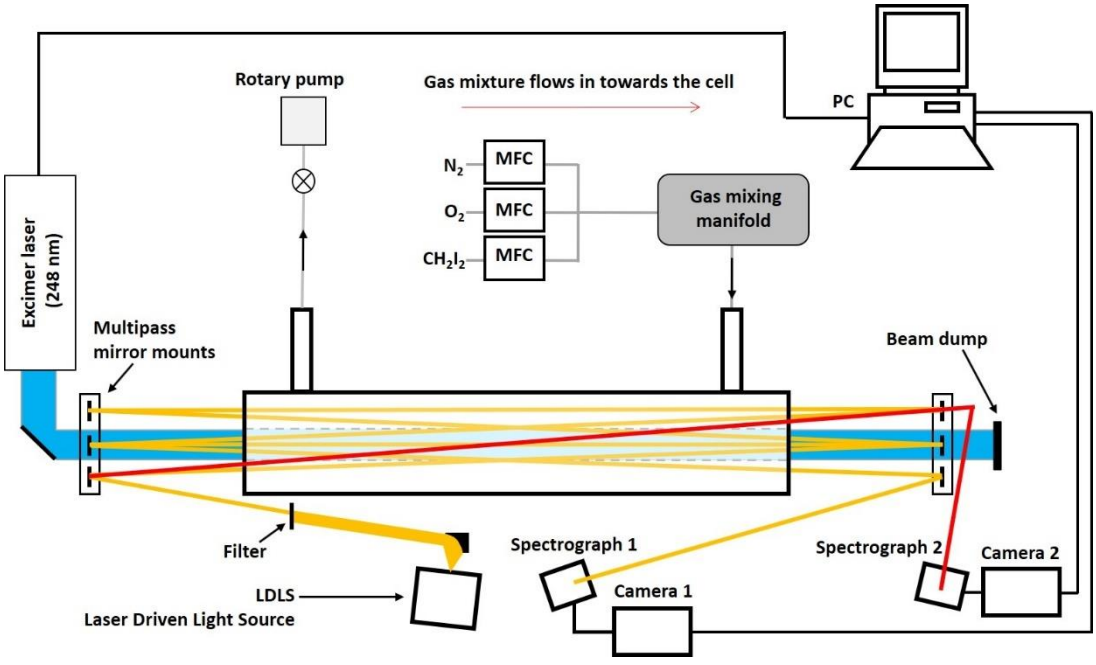

Figure 3.3: Schematic diagram of the experimental setup used in this work, with the red line showing the path of the single pass probe beam, the orange line showing the path of the multipass probe beam and the dashed grey lines combined with the light blue section within showing the overlap region of the photolysis beam, used to generate the reactive species, with the multipassed probe beam, used to monitor the reaction.

3.3.1 Gas Handling and Initiation of Chemistry

Precursor gases were mixed in a gas manifold at known flow rates determined by calibrated mass flow controllers (MKS Instruments), for which details are provided in Appendix 1, with CH_2I_2 introduced into the gas flow by passing a known slow flow of N_2 through a bubbler containing liquid CH_2I_2 at room temperature, and passed into a 1.5 m long glass reaction cell. The reaction cell was 54 mm inner diameter, and sealed with fused silica windows at both ends. The total flow rate was maintained at 4000 standard cm^3 per minute (sccm) at 100 Torr and adjusted accordingly with pressure to maintain constant number densities for reactant gases and a constant residence time in the cell of ~6 s. Total pressure in the cell was determined by a capacitance manometer (MKS Instruments) and controlled by a rotary pump (EM2, Edwards) by throttling the exit to the reaction cell. The pressure gauge operates by measuring the change in electrical capacitance between a metal diaphragm and an adjacent, fixed powered electrode within the gauge. All experiments were performed at T = (298 ± 2) K in N_2 (BOC oxygen free, 99.998 %) at pressures between 6 and 300 Torr. CH_2I_2 (Alfa Aesar 99 %) concentrations were in the range $1 \times 10^{12} – 4 \times 10^{13}$ cm^{-3} and O_2 (BOC, 99.5 %) concentrations were varied between 1×10^{16} and 4×10^{17} cm^{-3}. Gases and chemicals were used as supplied.

Reactions R3.6-R3.10 were initiated in the reaction cell by an excimer laser (KrF, Lambda-Physik CompEx 210), operating at a wavelength of λ = 248 nm, for which details of the working procedure are provided above. This KrF excimer laser was aligned along the length of the reaction cell using a dichroic turning mirror (Edmund Optics). The timing of the photolysis laser was controlled by a delay generator (SRS DG535) with a pulse repetition rate of 0.15 Hz such that a fresh gas mixture was photolysed on each pulse. The typical laser fluence was measured to be ~25 mJ cm^{-2}, giving $[CH_2OO]_{t=0}$ on the order of ~10^{11} cm^{-3}. The timescale for production of such concentrations of CH_2OO from $CH_2I + O_2$ (R3.7a) and subsequent loss *via* multiple pathways (R3.8-R3.10) was observed to be on the order of 10s ms, typically 50 ms.

$$CH_2I_2 + h\nu\ (\lambda{=}248\ \text{nm}) \rightarrow CH_2I + I \qquad \text{(R3.6)}$$

$$CH_2I + O_2 \rightarrow CH_2OO + I \qquad \text{(R3.7a)}$$

$$CH_2I + O_2 \xrightarrow{+M} CH_2IO_2 \qquad \text{(R3.7b)}$$

$CH_2OO + CH_2OO \rightarrow$ products (R3.8)

$CH_2OO + I \rightarrow$ products (R3.9)

$CH_2OO \rightarrow$ products (R3.10)

3.3.2 Monitoring Species and Reactions

Absorption of UV/visible radiation by species within the cell was monitored using a laser-driven light source (LDLS, Energetiq EQ-99X), which provides ~10 mW cm^{-2} of light at wavelengths between 185 and 850 nm. When compared to a standard Xenon arc lamp, the LDLS is more suitable for this application since the output is more stable leading to an improved *S/N* ratio and hence requiring shorter averaging/integration times, and the temperature of the spectral output is much higher (~11,000 K vs 3,000 K) resulting in more UV radiation. Furthermore, the light source is derived from a much smaller point (100-200 μm vs ~2-3 mm), making the beam from the LDLS much easier to collimate over the long distances (up to ~20 m) required for such an application than that from a standard Xenon arc lamp. Output from the LDLS was directed onto an off-axis parabolic mirror (ThorLabs) to collimate the beam. Approximately 10 % of the light was aligned along the length of the cell to give a single pass through the cell overlapping completely with the photolysis beam, with the remaining light aligned in the multipass arrangement described in detail in previous work,[41] for which a brief description is provided here.

The multipass optical arrangement features up to fourteen 12 mm diameter mirrors, each of which are spherically curved with a 2.4 m radius of curvature, and are UV enhanced such that their reflectivity is ~85 % in the UV region (custom made by Knight Optical). Mounts were used for the mirrors, consisting of 2 back plates and 8 individual threaded mounting disks, all made from aluminium, with these threaded mounting disks held in place with L-shaped brackets which are slotted to allow vertical, horizontal and transverse translation of the mounting disk assembly (designed in SolidWorks 2013 and custom built in-house). Mirrors were adhered to the threaded mounting disks, with the disks separated from the back plate using small silicone O-rings. M3 screws were fed through the back plate, through the O-rings and screwed into the threaded mounting disks, allowing the angle of each mirror to be

adjusted as required such that the probe beam can be arranged in a multipass configuration as shown in Figure 3.3.

The number of passes between the mirrors can be altered for different applications and desired path lengths, with 7 passes typically being sufficient for measuring cross-sections in the UV region (250-400 nm), however a maximum of 13 passes can be achieved, particularly useful for measuring small cross-sections in the UV/visible region. The fact that each mirror was able to be adjusted allowing for translational motion meant that the overlap between the photolysis and probe beams could be maximised. Probe intensity of the LDLS was recorded at wavelengths between 185 and 600 nm for the single pass arrangement, and 250 and 850 nm for the multipass arrangement, with near constant radiance across the spectral range. The UV/vis wavelength range 280-450 nm is an important spectral region as many molecules absorb strongly within this range.

Of the two most common types of multipass absorption experiment systems, the White[35] and Herriott[36] cells, the mutipass arrangement employed in this work most closely resembles the Herriott cell, however with the added component of possessing fully translatable mirrors for each pass of the probe beam. This ability to translate each mirror independently is an important feature of this experimental instrument since, unlike the Herriott cell which is constrained by the required geometry dictated by the distance between and the radius of curvature of the two mirrors, the multipass setup within the reaction cell employed in this work allows each pass of the probe light to cut through the path of the photolysis laser, in this case an excimer laser, optimally, thereby optimising the overlap between the photolysis and probe beams and hence maximising the path length. Determination of this path length of multipass arrangement is described in detail in the Appendix 2.

3.3.3 Data Acquisition

Transient absorption spectra of the reactant gas mixture were recorded before, during and after photolysis. The output beams from both the single and multipass arrangements were each passed through sharp cut-off filters (248 nm RazorEdge ultasteep long-pass edge filter, Semrock) to minimise the impacts of scattered excimer light and focused onto fibre optics via fibre launchers (Elliot Scientific). Outputs from

the fibre optics were directed onto spectrographs (CP140-103 Imaging Spectrograph, Horiba) and imaged onto line-scan charge-coupled device (CCD) detectors (S7030-1006 FFT, Hamamatsu), giving spectral resolution of 1.5 nm FWHM and time resolution of 1 ms. Wavelength calibration was performed via measurements of the well-known Hg emission spectrum from a low pressure Hg pen-ray lamp (Oriel), for which further information, along with details of the CCDs used and how they work, are provided below. Timing of the cameras was controlled by the same delay generator used to control the firing of the excimer laser. Intensity data recorded by the cameras were typically averaged for 100 to 400 photolysis shots and were transferred to a PC for analysis.

3.3.4 Principles of CCD Operation

Measuring multipassed broadband absorption requires a detector with multiple channels, the most common of which is the charge-coupled device (CCD) and has been used by numerous groups in spectroscopic and kinetic studies.[42, 43] CCDs comprise an array of photosensitive metal oxide semiconductor pixels which allow conversion of incident light to photocharge, which is stored in a potential well within each pixel, with the number of photons incident on each pixel within a given exposure time upon absorption of radiation being proportional to the accumulated charge of that pixel. Thus, situating a CCD in the dispersive plane of a spectrograph enables wavelength resolved intensities to be recorded, since the broadband probe light is separated into a frequency spectrum and wavelength resolved using the spectrograph, which projects a narrow wavelength range (~0.1-1 nm) onto each pixel.

The spectrographs used in the experimental setup described here included gratings with 285 grooves / mm and had a range of ~650 nm, with the camera collecting the multipassed light measuring between 250 and 850 nm and the single pass camera recording in the range 185-600 nm. The high light throughput of the spectrographs meant that despite short exposure times of 1 ms, sufficient light and hence charge was accumulated on the CCD pixels to see adequate signal for absorption measurements. Light entered the spectrographs through narrow slits (25 μm and 50 μm) illuminating the diffraction gratings causing the light to be wavelength dispersed, and was imaged onto the CCDs using 70 mm off-axis parabolic mirrors.

The cameras used were 1D line-array CCD detectors comprising an array of 1024 by 64 pixels. The wavelength dispersed light illuminated the CCD during exposure, after which the charge accumulated in each of the pixels in the 64 rows was summed vertically and binned into the readout register as 1 line of 1024 pixels, giving a wavelength resolved intensity spectrum, as shown in the schematic in Figure 3.4. Data was read off the CCD at a speed of > 1000 Hz (780 μs minimum read time), acquiring time resolved absorption data at a time resolution of 1 ms. Typically, such high data acquisition read rates would be associated with and achieved by using a 2D CCD array, in which each time slice is shifted into a masked area of the array and at the end of each photolysis pulse the entire 2D array is read. Shifting and masking CCD signals in this way can intrinsically introduce charge accumulation due to processes within the CCD itself, termed dark noise, however the fast expose-bin-read cycle of the line CCD described here avoids this effect without the requirement of expensive cooling systems. Although faster 1D CCDs exist, they tend to be less efficient at collecting light since faster read rates necessarily result in shorter exposure times and therefore less charge accumulation, which results in a reduction of the instrument sensitivity. Experiments to determine the UV absorption cross sections of CH_2OO and the rate coefficient of the CH_2OO self-reaction, described in Chapters 4 and 5 respectively, were performed using this 1D line-array CCD.

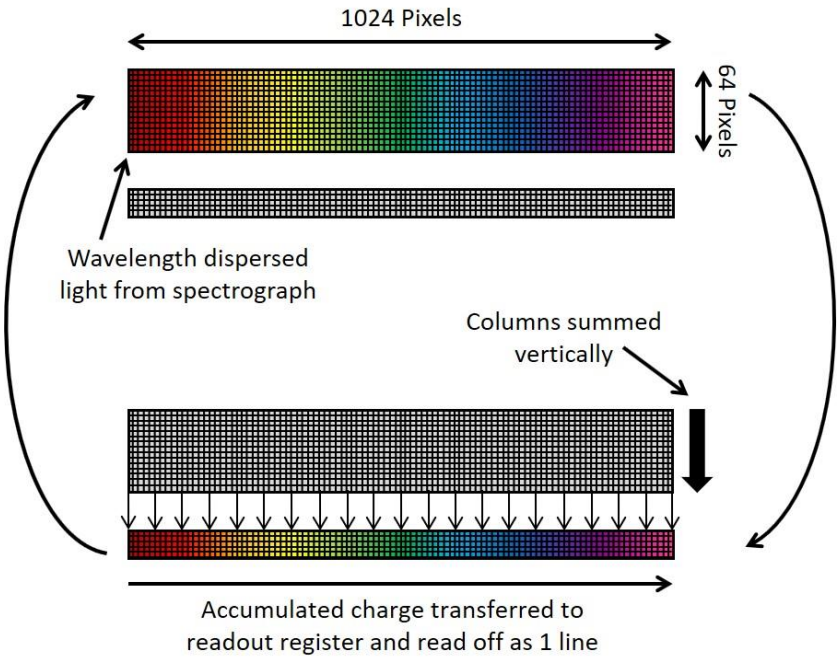

Figure 3.4: A schematic of the acquisition process of the 1D line-array CCD, showing the wavelength dispersed light illuminating the line CCD array during exposure, after which the charge accumulated in each row of the 64 pixels within the array is summed and transferred to the readout register before being transferred to the computer, and the cycle restarts (curly arrows).

All wavelength calibrations were performed via measurements of the well-known Hg emission spectrum from a low pressure Hg pen-ray lamp. Each peak from the Hg spectrum is associated with an emission line of a particular wavelength, which is assigned to the pixel number at which the line is observed. Plotting λ / nm against pixel number gives a linear relationship, the gradient and intercept of which are used to calibrate the wavelength, as shown in Figure 3.5.

$$\text{Wavelength} = (\text{Gradient} \times \text{Pixel Number}) + \text{Intercept} \qquad \text{(Equation 3.11)}$$

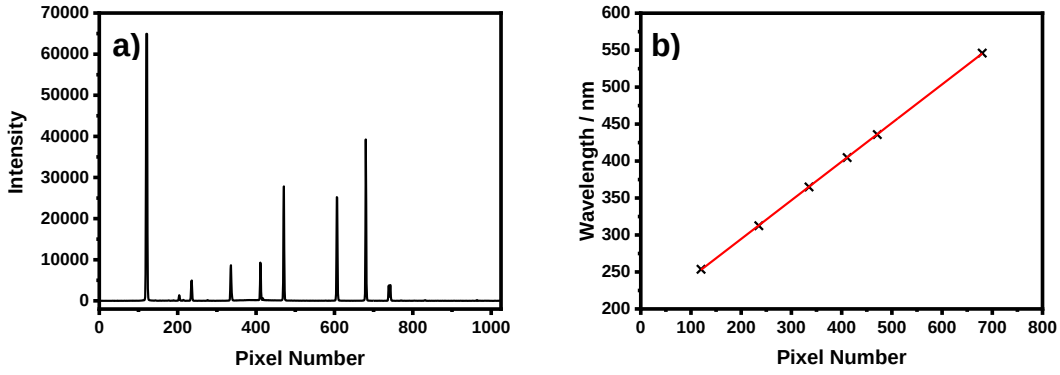

Figure 3.5: Wavelength calibration graphs showing a) Hg pen-ray lamp emission lines as measured by the spectrograph in the multipass arrangement, with each peak corresponding to an emission line and pixel number on the CCD and b) a plot of pixel number vs wavelength (nm) of the corresponding peak, and a fit of Equation 3.11 (red line), to give gradient = 0.52248 and intercept = 190.19481.

3.3.5 Data Processing and Analysis

The raw data from the CCD was output as a 2D array of pixel number *vs* time which was converted into wavelength *vs* time using the wavelength calibration, where the magnitude of the intensity recorded represents the amount of charge accumulated by each pixel during exposure and effectively constitutes the *z* axis. This array gave information on intensity for each of the 2000 time points in 1 millisecond intervals over the 2 second timescale of the run and each of the 1024 wavelength points in ~0.6 nm intervals over the wavelength range λ = 250-850 nm. The intensity of the light prior to the photolysis laser pulse at time t_0 was averaged at each wavelength and represents $I_{0,\lambda}$, and the intensity of light after the photolysis laser pulse at every recorded time subsequent to t_0 represents $I_{\lambda,t>0}$. A cut of the 2D array through the time axis provides a view of the spectrum at any given time delay, which have *x* and *y* assignments of wavelength and intensity respectively. Alternatively, for kinetic applications, a cut can be taken through the wavelength axis to give the time evolution of the intensity for any given wavelength. Only a description of the data processing prior to or during analysis is given here, and a detailed description of the data analysis in which absorbance was calculated from the recorded intensities according to the Beer-Lambert law, and the analytical procedures carried out to determine the transient

absorbance spectra, the identity and contributions from each absorbing species, species concentrations and kinetic parameters, is provided in Chapters 4 and 5.

A baseline correction was applied to the data to correct the absorbance signals in the region of interest for fluctuations in probe lamp output intensity. Correction based on the average apparent absorbance between 500 and 600 nm, where it is expected that there are no absorbing species, has been implemented in this analysis. Fixing the absorbance, *A*, to zero in a wavelength region where no absorption occurs in this way reduces the noise due to lamp fluctuations, thereby increasing the *S/N* ratio and decreasing the number of excimer laser pulses required to obtain the desired quality of signal.

There was also evidence for probe lamp fluctuations affecting $I_{0,\lambda}$, the light intensity in the 1 second timescale prior to photolysis, resulting in apparent non-zero absorbance signals once chemistry is complete and thus absorbance is expected to be zero. The photolysis laser was fired 1000 ms after the camera was initiated, over which timescale there can be significant variation in $I_{0,\lambda}$. Given that the processes under investigation occur in the first 50 ms post-photolysis, the period of time used to determine $I_{0,\lambda}$ was also selected to be the 50 ms prior to photolysis, hence giving CH_2OO decay profiles which return to the baseline at long times, i.e. give the expected zero concentration once the chemistry has occurred.

A description of only the experimental details of the more established UV setup used for experiments described in this thesis is provided here. Details of the IR setup used for much of the remainder of the experiments described in this thesis are provided in Chapter 6. Fundamental concepts of gas flow, generation of reactive species and monitoring the reaction by absorption spectroscopy are the same for UV and IR experiments, however the IR system is discussed in detail in Chapter 6 in terms of design, characterisation and initial results.

3.4 References

1. Atkinson, R., Kinetics and mechanisms of the gas-phase reactions of the hydroxyl radical with organic compounds under atmospheric conditions. *Chemical Reviews* **1986,** *86* (1), 69-201.

2. Pilling, M. J.; Seakins, P. W., *Reaction kinetics*. Oxford University Press: Oxford, 1995.

3. King, M. *The relative-rate technique for determining rate constants (ECG Environmental Brief No 13)*; 2016.

4. Barnes, I.; Bastian, V.; Becker, K. H.; Fink, E. H.; Zabel, F., Reactivity studies of organic substances towards hydroxyl radicals under atmospheric conditions. *Atmospheric Environment* **1982,** *16* (3), 545-550.

5. Howard, C. J., Kinetic measurements using flow tubes. *The Journal of Physical Chemistry* **1979,** *83* (1), 3-9.

6. Seeley, J. V.; Jayne, J. T.; Molina, M. J., Kinetic studies of chlorine atom reactions using the turbulent flow tube technique. *The Journal of Physical Chemistry* **1996,** *100* (10), 4019–4025.

7. Percival, C. J.; Shallcross, D. E.; Canosa-Mas, C. E.; Dyke, J. M., Recent advances in the application of discharge-flow to the determination of gas-phase rate coefficients at pressures and temperatures of relevance to the Earth's atmosphere. *Journal of Photochemistry and Photobiology A: Chemistry* **2005,** *176* (1-3), 250-259.

8. Norrish, R. G. W.; Porter, G., Chemical reactions produced by very high light intensities. *Nature* **1949,** *164*, 658.

9. Porter, G., Flash photolysis and spectroscopy- A new method for the study of free radical reactions. *Proceedings of the Royal Society of London. Series A, Mathematical and Physical Sciences* **1950,** *200* (1061), 284-300.

10. Wayne, R. P., *Principles and applications of photochemistry*. Oxford University Press: Oxford, UK, 1988.

11. Lackner, M., *Lasers in chemistry: probing matter*. Wiley-VCH Verlag GmbH & co: Weinheim 2008; Vol. 1.

12. Nelson, L. S.; Ramsay, D. A., Flash photolysis experiments with a sapphire flash lamp. *The Journal of Chemical Physics* **1956,** *25* (2), 372.

13. Andrews, D. L., *Lasers in chemistry*. Third ed.; Springer-Verlag: Berlin, Germany, 1997.

14. Basting, D.; Marowsky, G., *Excimer laser technology*. Springer-Verlag: Germany, 2005.

15. Delmdahl, R.; Pätzel, R., Excimer laser technology trends. *Journal of Physics D: Applied Physics* **2013,** *47* (3), 034004.

16. Koechner, W.; Bass, M., *Solid-state lasers: A graduate text*. Springer-Verlag: New York, USA, 2003.

17. Thomason, L. P., *Nd:YAG lasers: Technology and applications*. Nova Science Publishers Inc: New York, USA, 2019.

18. Cremers, D. A.; Radziemski, L. J., *Handbook of Laser-Induced Breakdown Spectroscopy*. John Wiley & Sons: Hoboken, New Jersey, 2013.

19. Golik, S. S.; Bukin, O. A.; Ilyin, A. A. e.; Tsarev, V. I.; Saluk, P. A.; Shmirko, K., Application of high-power Nd:YAG lasers for environmental monitoring. *Proceedings of SPIE* **2005,** *5627*, 350-356.

20. Schäfer, F. P., Dye lasers and laser dyes in physical chemistry. In *Dye lasers: 25 years*, Springer-Verlag: Berlin, Germany, 1992.

21. Nemkovich, N. A.; Rubinov, A. N.; Tomin, V. I., Kinetics of luminescence spectra of rigid dye solutions due to directed electronic energy transfer. *Journal of Luminescence* **1981,** *23* (3-4), 349-361.

22. Loewen, E. G.; Popov, E., *Diffraction gratings and applications*. Marcel Dekker, Inc: New York, USA, 1997.

23. Franken, P. A.; Hill, A. E.; Peters, C. W.; Weinreich, G., Generation of optical harmonics. *Physical Review Letters* **1961,** *7* (4), 118-119.

24. Hoffmann, E. d.; Stroobant, V., *Mass spectrometry: Principles and applications*. Third ed.; John Wiley & Sons, Ltd: West Sussex, England, 2007.

25. Harris, D. C., *Quantitative chemical analysis*. Eighth ed.; W. H. Freeman and Company: New York, USA, 2010.

26. Gross, J. H., *Mass spectrometry: A textbook*. Third ed.; Springer International Publishing AG: Switzerland, 2017.

27. Taatjes, C. A.; Meloni, G.; Selby, T. M.; Trevitt, A. J.; Osborn, D. L.; Percival, C. J.; Shallcross, D. E., Direct observation of the gas-phase Criegee intermediate (CH_2OO). *Journal of the American Chemical Society* **2008,** *130* (36), 11883–11885.

28. Welz, O.; Savee, J. D.; Osborn, D. L.; Vasu, S. S.; Percival, C. J.; Shallcross, D. E.; Taatjes, C. A., Direct kinetic measurements of Criegee intermediate (CH_2OO) formed by reaction of CH_2I with O_2. *Science* **2012,** *335* (6065), 204-207.

29. Blitz, M. A.; Goddard, A.; Ingham, T.; Pilling, M. J., Time-of-flight mass spectrometry for time-resolved measurements. *Review of Scientific Instruments* **2007,** *78* (3), 034103.

30. Howes, N. U. M.; Mir, Z. S.; Blitz, M. A.; Hardman, S.; Lewis, T. R.; Stone, D.; Seakins, P. W., Kinetic studies of C_1 and C_2 Criegee intermediates with SO_2 using laser flash photolysis coupled with photoionization mass spectrometry and time resolved UV absorption spectroscopy. *Physical Chemistry Chemical Physics* **2018,** *20* (34), 22218-22227.

31. Dawson, P. H., *Quadrupole mass spectrometry and its applications*. Elsevier Scientific Publishing Company: Amsterdam, The Netherlands, 1976.

32. Heard, D., *Analytical techniques for atmospheric measurement*. Blackwell Publishing: Oxford, UK, 2006.

33. Stone, D.; Blitz, M.; Ingham, T.; Onel, L.; Medeiros, D. J.; Seakins, P. W., An instrument to measure fast gas phase radical kinetics at high temperatures and pressures. *Review of Scientific Instruments* **2016,** *87* (5), 054102.

34. Pilling, M. J.; Smith, I. W. M., *Modern gas kinetics: Theory, experiment and application*. Blackwell Scientific Publications: Oxford, UK, 1987.

35. White, J. U., Long optical paths of large aperture. *Journal of the Optical Society of America* **1942,** *32* (5), 285-288.

36. Herriott, D. R.; Schulte, H. J., Folded optical delay lines. *Applied Optics* **1965,** *4* (8), 883-889.

37. Lewis, T. R.; Blitz, M. A.; Heard, D. E.; Seakins, P. W., Direct evidence for a substantive reaction between the Criegee intermediate, CH_2OO, and the water vapour dimer. *Physical Chemistry Chemical Physics* **2015,** *17* (7), 4859-4863.

38. Nowakowski, M.; Wojtas, J.; Bielecki, Z.; Mikołajczyk, J., Cavity enhanced absorption spectroscopy sensor. *Acta Physica Polonica A* **2009,** *116* (3), 363-367.

39. Paldus, B.; Kachanov, A., Spectroscopic techniques: Cavity-enhanced methods. In *Springer handbook of atomic, molecular, and optical physics*, Drake, G. W. F., Ed. Springer: New York, USA, 2006.

40. Gagliardi, G.; Loock, H.-P., *Cavity-enhanced spectroscopy and sensing*. Springer: Berlin, Germany, 2014.

41. Lewis, T.; Heard, D. E.; Blitz, M. A., A novel multiplex absorption spectrometer for time-resolved studies. *Review of Scientific Instruments* **2018,** *89* (2), 024101.

42. Rowley, D. M.; Harwood, M. H.; Freshwater, R. A.; Jones, R. L., A novel flash photolysis/UV absorption system employing charge-coupled device (CCD) detection: A study of the BrO + BrO reaction at 298 K. *The Journal of Physical Chemistry* **1996,** *100* (8), 3020–3029.

43. Sheps, L.; Chandler, D. W. *Time-resolved broadband cavity-enhanced absorption spectroscopy for chemical kinetics*; California, USA, 2013.

Chapter 4

CH_2OO UV Absorption Cross-Sections

Ozonolysis reactions, resulting in the production of reactive Criegee intermediates, make significant contributions to the tropospheric oxidising capacity, particularly at night and in winter when photochemistry is limited by the low intensity of solar radiation.[1, 2] These Criegee intermediates play important roles in many aspects of atmospheric chemistry. Not only does Criegee intermediate formation involve ozone and alkene destruction (through production *via* ozonolysis), their reactions also involve OH formation (through chemical decomposition of the highly internally energised product of ozonolysis reactions), and stabilised Criegee intermediates can undergo bimolecular reactions with other trace atmospheric species and hence contribute to pollutant removal, aerosol formation (global cooling), acid rain formation and the global H_2SO_4 budget, which is described in further detail in Chapter 1.

Direct detection of reactive Criegee intermediates is thus important for determination of reaction kinetics, products and mechanisms, and their relative significance in the atmosphere. The recent availability of the photolytic method for producing Criegee intermediates proposed by Welz *et al*.[3] has enabled them to be produced at relatively high concentrations under laboratory conditions in relative isolation, thereby making them easier to detect directly in the laboratory using various different spectroscopic detection methods, including ultraviolet (UV) absorption, infrared (IR) absorption, microwave spectroscopy, laser induced fluorescence (LIF) spectroscopy (of reaction products), and mass spectroscopy (MS). These spectroscopic detection methods have facilitated characterisation of the structures and spectral parameters of Criegee intermediates, for which further detail is provided in Chapter 1.

UV absorption spectroscopy is a widely employed detection method in atmospheric chemistry. Utilisation of this detection method to study the kinetics of Criegee intermediate reactions and obtain accurate kinetic parameters is only possible if accurate UV absorption cross-sections for the Criegee intermediate of interest are available. Measurements of the UV absorption cross-sections of CH_2OO have indicated that the absorption cross-sections are relatively large, on the order of $\sim 10^{-17}$

cm^2,[4-7] thus making UV absorption spectroscopy a highly useful tool for the measurement of atmospherically relevant Criegee intermediate reaction kinetics. UV absorption cross-sections of CH_2OO have been reported by several groups, however there are significant discrepancies in the absolute cross-sections reported, and in the shape and peak of the spectrum, as is shown in Figure 4.1.

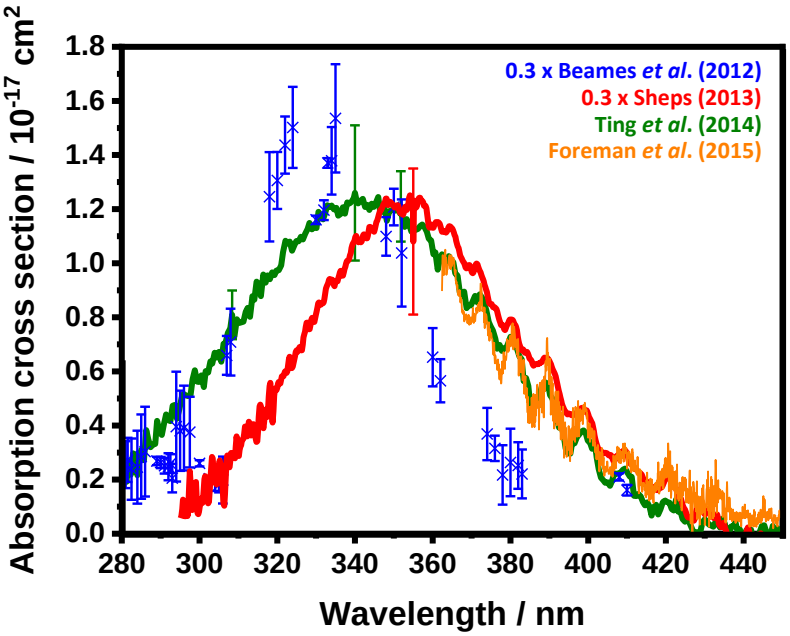

Figure 4.1: Comparison of absolute CH_2OO cross-sections determined in previous work. Note that the results of Beames *et al.*[4] and Sheps[5] are scaled by a factor of 0.3.

4.1 Directly Observed CH_2OO UV Spectrum

The first measurements of the UV spectrum of CH_2OO were reported by Beames *et al.*[4] in 2012, in which an action spectrum was observed by monitoring the change in the CH_2OO photoionisation signal on irradiation with UV light generated by a tunable Nd:YAG pumped dye laser at wavelengths between 280 and 420 nm. A pulsed valve system was used to produce jet cooled CH_2OO following photolysis of CH_2I_2 at λ = 248 nm in the presence of O_2 in Ar at ~1300 Torr, with CH_2OO monitored following single photon photoionisation in a time-of-flight mass spectrometer at λ = 118 nm, a VUV radiation equivalent to 10.5 eV, so that only the CH_2OO Criegee isomer was photoionised and detected. Excitation of CH_2OO from the ground $\tilde{X}^1A'$ electronic state on irradiation with UV light resulted in depletion of the photoionisation signal

at *m/z* = 46, with the extent of depletion combined with knowledge of the UV photon flux used to determine the cross-sections.

The spectrum was observed to be broad in the wavelength region 300 – 370 nm, with a maximum cross-section of (5.0 ± 0.7) × 10^{-17} cm^2 at λ ~335 nm, indicating an atmospheric lifetime of CH_2OO of ~1 s at midday with respect to photodissociation by solar photolysis.[4] This lifetime was concluded to be comparable to that for key bimolecular reactions of CH_2OO with SO_2 and NO_2 in the troposphere, expected to occur at a rate of ~2 s^{-1}, thus making UV absorption photolysis a potentially significant decay path for CH_2OO under daytime conditions in the troposphere. In a subsequent paper by the same group investigating the UV absorption spectrum of the alkyl-substituted Criegee intermediate CH_3CHOO using the same experimental technique, it was determined that experimental factors, such as homogeneity of the laser beam and laser-molecular beam overlap, suggested an uncertainty in absolute cross-section measurements on the order of a factor of 2.[8]

The large UV induced depletion observed, approaching 100 % near the peak of the profile at ~335 nm, indicated rapid dissociation of CH_2OO promoted to the $\tilde{B}^1A'$ state, consistent with the theoretically computed fully repulsive excited $\tilde{B}^1A'$ potential along the O-O coordinate as shown in the potential energy surface (PES) in Figure 4.2. Products of this repulsion have been reported as formaldehyde and excited atomic oxygen.[9]

$$CH_2OO\ (\tilde{B}^1A') \rightarrow HCHO\ (X^1A_1) + O(^1D) \qquad (R4.1)$$

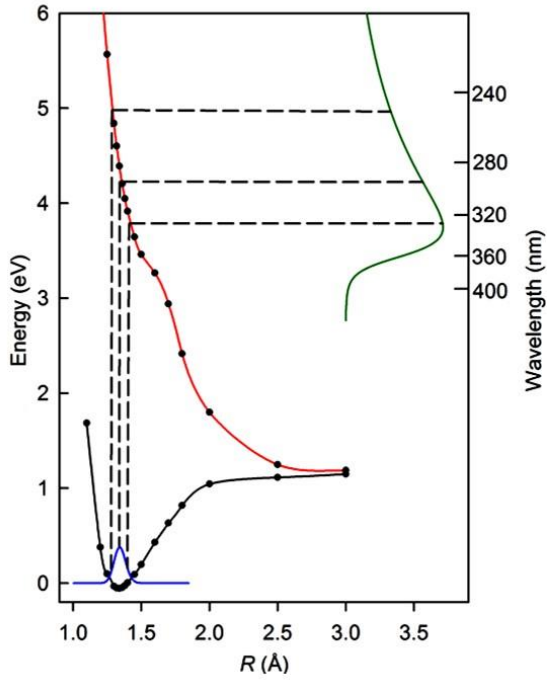

Figure 4.2: Prediction by Beames *et al.*[4] of the UV absorption spectrum of CH_2OO (green) using the ground $\tilde{X}^1A'$ (black) and excited $\tilde{B}^1A'$ (red) electronic state potential energy curves along the O-O radial coordinate R obtained from CASSCF calculations.

A broad UV spectrum was also reported by Sheps[5] in 2013 at ~0.2 nm intervals using time-resolved broadband cavity-enhanced absorption spectroscopy with a Xe arc lamp operating in the wavelength range 300-450 nm. This work had a spectral resolution of 2 nm, and was conducted at a temperature of 295 K and a pressure of 5.1 Torr, with the improved wavelength resolution of the technique revealing the significant vibronic structure at longer wavelengths predicted previously.[10] However, the direct absorption measurements demonstrated a wider absorption spectrum than observed for the action spectrum,[4] with a lower peak absorption cross-section of (3.6 ± 0.9) × 10^{-17} cm^2 occurring at a longer wavelength of ~355 nm. The cavity-enhanced measurements used photolysis of CH_2I_2/O_2/He mixtures at λ = 266 nm, leading to the total observed absorbance containing overlapping contributions from CH_2OO, the depletion of CH_2I_2, and the production of IO radicals from unavoidable secondary chemistry occurring in the reaction system.

Separation of the spectral contributions was achieved by the addition of SO_2 to the reaction system to aid identification of the contribution from CH_2OO.[5] Scaling of the

total absorbance observed following complete removal of CH_2OO by SO_2, as shown in Figure 4.3, to the time dependence of the absorbance signal in a region of the spectrum dominated by IO absorption, and subtraction of the scaled spectrum from the total absorbance observed at each time point in the experiment enabled identification of the CH_2OO absorbance, assuming that the time dependence of CH_2I_2 is negligible, i.e. that the CH_2I_2 concentration, determined from the observed CH_2I_2 precursor depletion signal, remains constant following photolysis. Fitting the kinetics of the time dependence of the CH_2OO signal gave a bimolecular rate coefficient for the reaction of CH_2OO with SO_2 of $(4.1 \pm 0.3) \times 10^{-11}$ cm^3 s^{-1}, a value in agreement with that reported previously by Welz *et al.*[3] of $(3.9 \pm 0.7) \times 10^{-11}$ cm^3 s^{-1}, and also enabled determination of the CH_2OO absorbance immediately following photolysis (i.e. at $t = 0$). Separate experiments to measure the CH_2I absorbance, and hence concentration, combined with knowledge of the CH_2OO yields from $CH_2I + O_2$[11-13] gave the absolute CH_2OO concentration produced in the system ($\sim 5 \times 10^{11}$ cm^{-3}). Absolute absorption cross-sections for CH_2OO could then be ascertained from the Beer-Lambert law using the total absorption path length, which varied with the probe wavelength and was measured to be 40-56 m across the spectral range, by measuring the well-characterised absorbance spectra of known concentrations of NO_2 and CH_2I_2.

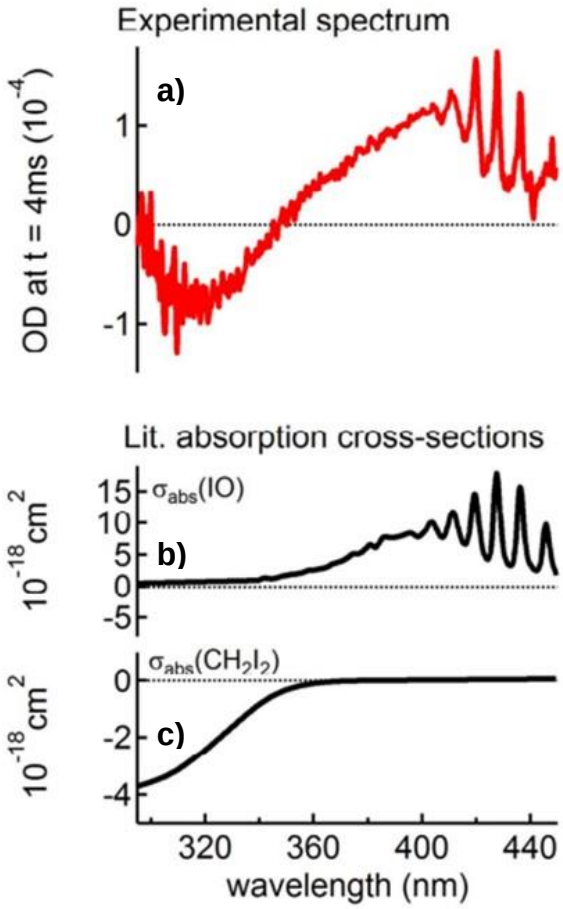

Figure 4.3: Absorption spectra a) of contributions other than CH_2OO in the experimental spectra measured by Sheps[5] of overlapping spectral interferences due to IO formation and CH_2I_2 depletion taken in the presence of SO_2 and averaged between t = 4-4.4 ms which are time points after photolysis at which CH_2OO had reacted away completely; used in the data analysis carried out by Sheps[5] for b) IO; c) CH_2I_2 (negative due to its depletion by the photolysis laser pulse).

The UV absorption cross-sections of CH_2OO were also reported by Ting *et al.*[6] in 2014, using photolysis of $CH_2I_2/O_2/N_2$ at λ = 248 nm to generate CH_2OO at total pressures between 8 and 760 Torr at a temperature of 295 K. Broadband transient absorption spectroscopy with a 2 nm spectral resolution was used in a single pass cell in the spectral range of 280-480 nm to obtain the total absorbance in the reaction system, which, similarly to the work of Sheps,[5] contained significant contributions from CH_2I_2 and IO, as shown in Figure 4.4. Separation of the contribution from IO to the total absorbance was achieved by using the characteristic vibronic structure in the IO spectrum to identify and subtract the contribution from IO at each time point. The

CH_2I_2 contribution was determined by subtracting the IO-corrected absorbance at a time point following complete reaction of CH_2OO, when only CH_2I_2 contributes to the IO-corrected absorbance, from an earlier time point, when both CH_2I_2 and CH_2OO contribute. Experiments were performed in which CH_2OO removal was dominated by CH_2OO self-reaction, and in which SO_2 was added to increase the removal rate *via* $CH_2OO + SO_2$, as shown in Figure 4.4.

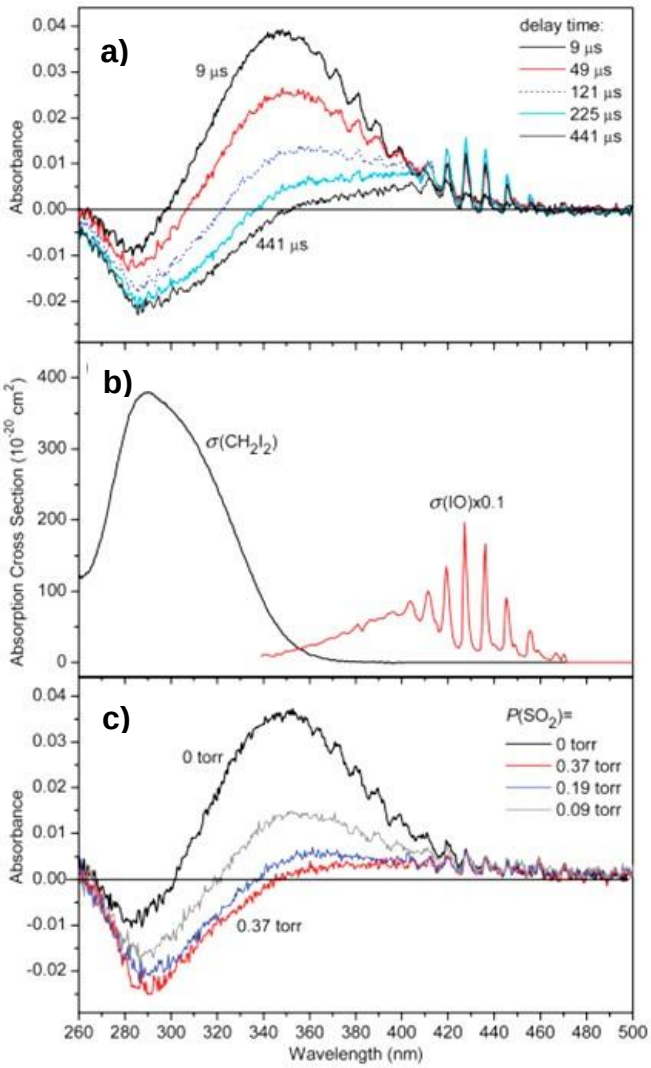

Figure 4.4: Absorption spectra a) measured by Ting *et al.*[6] at various delay times showing the depletion of CH_2I_2 resulting in negative absorbance peaked at ~290 nm, the broad and strong absorption band peaked at ~340 nm most likely due to the short-lived CH_2OO and at longer delay times, the formation of IO giving sharp peaks in the 410-460 nm range; b) used in the data analysis carried out by Ting *et al.*[6] for CH_2I_2 and IO; c) measured by Ting *et al.*[6] at t = 10.6 µs and different SO_2 concentrations showing that the intensity of the band peaked at ~340 nm decreases at higher SO_2 concentrations.

Initial concentrations of CH_2OO were determined to be ~10^{13} cm^{-3} by measurements of CH_2I absorbance and the known yield of CH_2OO from $CH_2I + O_2$, and were used to obtain a peak CH_2OO absorption cross-section of $(1.26 \pm 0.25) \times 10^{-17}$ cm^2 at λ = 340 nm, a maximum near that reported by Beames *et al.*[4] of ~335 nm. The spectral shape observed by Ting *et al.*[6] at 0.5-0.6 nm intervals was similar to that reported by Sheps,[5] with significant vibronic structure at $\lambda > 340$ nm, in agreement with the results of Sheps.[5] Cross-sections at λ = 308.4 nm and at λ = 351.8 nm were also measured independently by Ting *et al.*[6] in a molecular beam experiment to monitor the effects of UV laser irradiation on CH_2OO ion signals, obtained by electron impact ionisation and quadrupole mass spectrometry, with similarities to the experiments performed by Beames *et al.*[4] The molecular beam experiments gave photodissociation cross-sections of $\sigma = (8.09 \pm 0.90) \times 10^{-18}$ cm^2 at λ = 308.4 nm and $\sigma \leq (1.21 \pm 0.13) \times 10^{-17}$ cm^2 at λ = 351.8 nm, which scale to a peak cross-section of $(1.23 \pm 0.18) \times 10^{-17}$ cm^2 at λ ~340 nm.

Subsequent experiments by Foreman *et al.*[7] in 2015 using photolysis of $CH_2I_2/O_2/N_2$ at λ = 355 nm with single-pass broadband absorption spectroscopy at a total pressure of 50 Torr over the temperature range 276-357 K with a spectral resolution of 0.12 nm, and cavity ringdown spectroscopy at a total pressure of 70 Torr and room temperature with a spectral resolution of 0.0014 nm, were carried out to determine high resolution absorption cross-sections of CH_2OO at wavelengths between 362 and 476 nm. Contributions to the total absorbance from CH_2I_2 were negligible over the wavelength range under consideration, while those from IO were subtracted in a similar method to that employed by Ting *et al.*[6]

Measurements of the initial CH_2I_2 concentration and photolysis laser fluence were used to estimate the initial CH_2I concentration, and thus the initial CH_2OO concentration (~1.5×10^{13} cm^{-3} for broadband absorption measurements and ~5×10^{12} cm^{-3} for cavity ringdown measurements, with an estimated uncertainty of ~28 % for both types of measurement) from the measured yields of $CH_2I + O_2$. The results of both the absorption measurements and the cavity ringdown experiments showed good agreement with both the spectral shape and absolute cross-sections reported by Ting *et al.*,[6] and indicated no significant temperature dependence of the cross-sections as shown in Figure 4.5 and no resolvable rotational fine structure in any of the vibronic

features in the spectrum. An average separation between the vibronic features of ~9.5 nm (~610 cm^{-1}) was reported with absolute cross-sections given at 0.06 nm intervals.

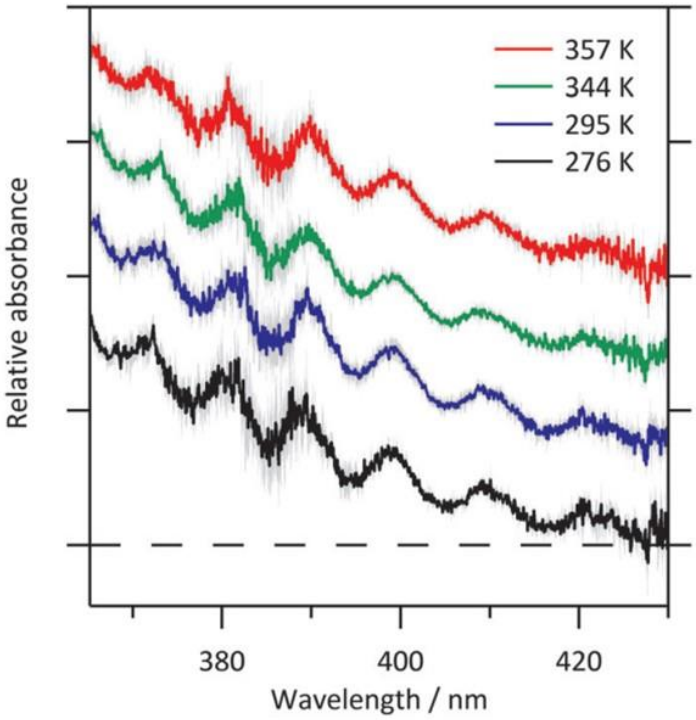

Figure 4.5: Temperature dependence of the CH_2OO absorption spectrum measured by Foreman *et al.*[7] over the range 276-357 K. Spectra are offset for clarity with the grey shading representing the 1σ uncertainty.

4.2 Theoretically Calculated CH_2OO UV Spectrum

The first theoretical prediction of the electronic spectrum of CH_2OO was reported by Lee *et al.*[10] in 2012, prior to the availability of the directly observed spectra discussed above.[4-7] Several groups have since attempted to simulate the CH_2OO UV spectrum using theoretical calculations considering the electronic states of CH_2OO and their decomposition dynamics and hence rationalise the observed UV spectra reported in the literature.[14-17]

A combination of electronic structure and Franck-Condon factor calculations were used by Lee *et al.* to predict the features of the CH_2OO UV spectrum, indicating the presence of a broad but intense absorption band in the region 250-450 nm owing to the $\tilde{B}^1A' \leftarrow \tilde{X}^1A'$ transition, with a computed band maximum of (318 ± 8) nm for this

transition of CH_2OO.[10] The calculations also suggested that the spectrum would exhibit extensive vibronic structure, owing to excitation of O-O stretching modes and C-O-O bending modes, and that there were hints of CH_2OO absorption in previous measurements of the UV spectrum assigned to CH_2IO_2 by Gravestock *et al.*[18] Both the predicted UV spectrum of CH_2OO reported by Lee *et al.* and the measured UV spectrum assigned to CH_2IO_2 by Gravestock *et al.* are shown in Figure 4.6.

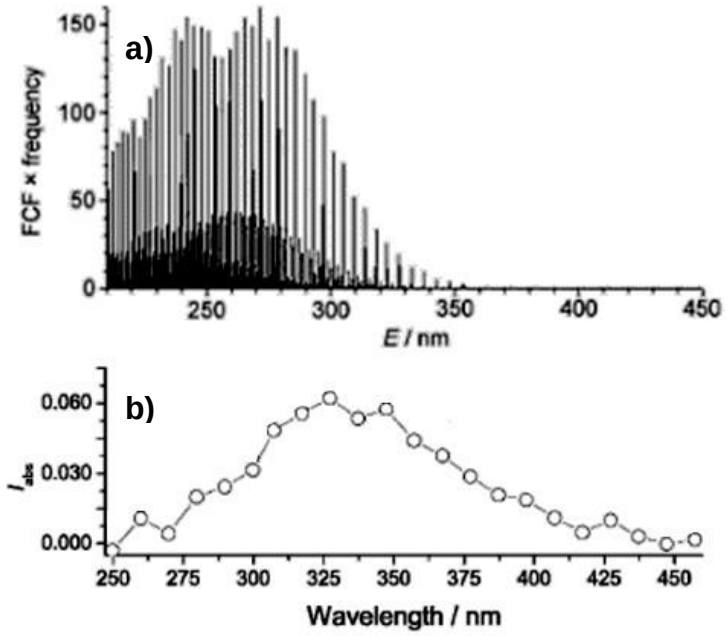

Figure 4.6: UV absorption spectrum of CH_2OO a) computed by Lee *et al.*[10] at a Boltzmann vibrational temperature of 0 K; b) measured by Gravestock *et al.*[18] following 193 nm photolysis of a $CH_2I_2/O_2/N_2$ reaction mixture once corrected for absorption by IO and CH_2I and assigned to CH_2IO_2.

Time-resolved UV absorption spectroscopy was employed by Gravestock *et al.*[18] to monitor IO at an analysis wavelength of 427.2 nm following photolysis of $CH_2I_2/O_2/N_2$ at wavelengths of 193 nm or 248 nm at room temperature and atmospheric pressure. Dependence of the production rate and yield of IO on the concentrations of CH_2I_2 and O_2 was observed, indicating that IO is not a direct photolysis product of the $CH_2I_2 + O_2$ reaction but is produced *via* secondary radical processes, and leading to the suggestion that the production of IO was dominated by the reaction between CH_2IO_2 and I. Absorption spectra recorded between 250 and 450 nm at approximately 10 nm intervals and corrected for absorption by IO and CH_2I

showed a broad absorption of an unknown species 'X' in the reaction mixture. Time-resolved absorption traces recorded at 337.2 nm (where strong absorption of species 'X' was observed) and 427.2 nm (where absorption is dominated by IO) showed a correlation between the removal of the 337.2 nm absorber 'X' and the formation of IO at 427.2 nm, suggesting that they are formed consecutively and that species 'X' is a direct precursor to IO in the reaction system.

By comparison of the absorption spectrum obtained (once corrected for absorption by IO and CH_2I) with the known spectra of CH_2ClO_2 and CH_2BrO_2 and the spectrum reported in the literature for CH_2IO_2, the broad absorption of the unknown species 'X' in the reaction mixture, observed in the wavelength range 250-450 nm with a maximum at 327.2 nm determined to have an absorption cross-section of $\sigma \geq 1.7 \times 10^{-18}$ cm^2, was assigned as being most probably but not unambiguously due to the CH_2IO_2 peroxy radical. It has since been reported by Stone *et al.*[13] that under the experimental conditions employed by Gravestock *et al.*,[18] the production of CH_2IO_2 dominates over that of CH_2OO owing to the pressure dependent branching ratios for the $CH_2I + O_2$ reaction (R4.3), with a yield of ~18 % CH_2OO at atmospheric pressure. From the typical CH_2I_2 concentrations employed in experiments conducted by Gravestock *et al.*[18] of 10^{14}-10^{15} cm^{-3}, the laser fluence of the excimer laser and the absorption cross-section of CH_2I_2 at 248 nm, it was calculated that approximately 19 % of the initial CH_2I_2 concentration was photolysed. Combining this with the reported yield of CH_2OO at atmospheric pressure by Stone *et al.*[13] (for which more details are provided in section 4.4) suggests an estimated CH_2OO concentration of 10^{12}-10^{13} cm^{-3} in experiments carried out by Gravestock *et al.*,[18] which has been shown to be sufficient for absorption measurements of CH_2OO.[4-7]

$$CH_2I_2 + h\nu\ (\lambda{=}248\ \text{nm}) \rightarrow CH_2I + I \qquad \text{(R4.2)}$$

$$CH_2I + O_2 \rightarrow CH_2OO + I \qquad \text{(R4.3a)}$$

$$CH_2I + O_2 \xrightarrow{+M} CH_2IO_2 \qquad \text{(R4.3b)}$$

Contrary to the findings of Lee *et al.*,[10] results reported in 2014 by Samanta *et al.*,[14] who computed the CH_2OO absorption spectrum at 0 K by performing one-dimensional and two-dimensional calculations along the O-O bond length and the C-O-O bond angle using the dynamically-weighted state-averaged complete active

space self-consistent field (DW-SA-CASSCF(14,10)) method, indicated the simulated electronic absorption spectrum to be broad and structureless, lacking any vibrational features due to the dissociative nature of the excited $\tilde{B}^1A'$ vibrational state, as shown in Figure 4.7. Such a spectrum devoid of vibrational structure is in agreement with the experimental results of Beames *et al.*[4] for jet cooled CH_2OO (~10 K), but not with those of Sheps[5] and Ting *et al.*[6] at room temperature, and those of Foreman *et al.*[7] at 276-357 K, all displaying vibronic structure on the long-wavelength side of the observed spectra. However, results showed the maximum absorption to be near ~245 nm,[14] a much lower wavelength than obtained in any of the experimental spectra.[4-7]

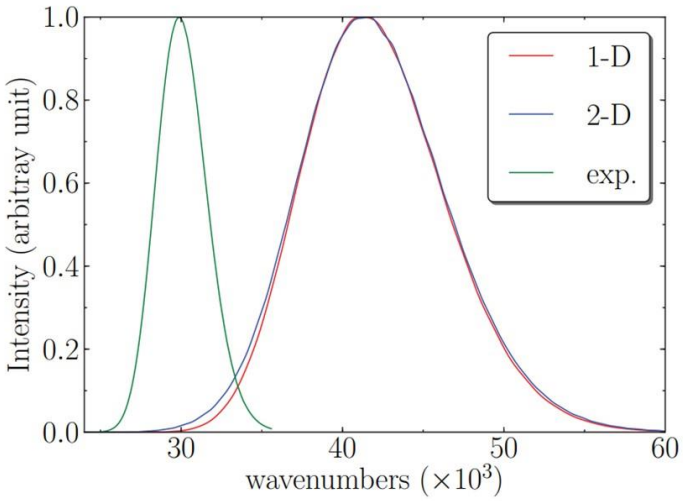

Figure 4.7: Absorption spectra for CH_2OO with the theoretical spectra labelled '1-D' and '2-D' showing the results calculated at 0 K by Samanta *et al.*[14] based on the one-dimensional cut of the diabatic surfaces along the O-O bond length at C-O-O bond angle = 120° and on the two-dimensional diabatic surfaces respectively, and the experimental spectrum labelled 'exp' showing a Gaussian fit to the data reported by Beames *et al.*[4] Note that all the spectra are scaled so that the maximum intensity is equal to unity.

Conversely, the UV absorption spectrum of Meng and Meyer[15] reported in 2014, also predicted at 0 K but by performing full-dimensional calculations using the multilayer multiconfigurational time-dependent Hartree (ML-MCTDH) approach with the multireference configuration interaction (MRCI(8,8)) treatment of electronic structure, indicated a maximum at ~334 nm, much closer to those of experimental measurements, but with a spectral width much narrower than observed

experimentally, as shown in Figure 4.8.[4-7] Furthermore, the strong oscillations observed did not match any of those in experimental results, particularly on the low-energy side of the spectrum where vibrational structure was observed experimentally, but the computed spectrum displayed a more diffuse spectral shape.[15]

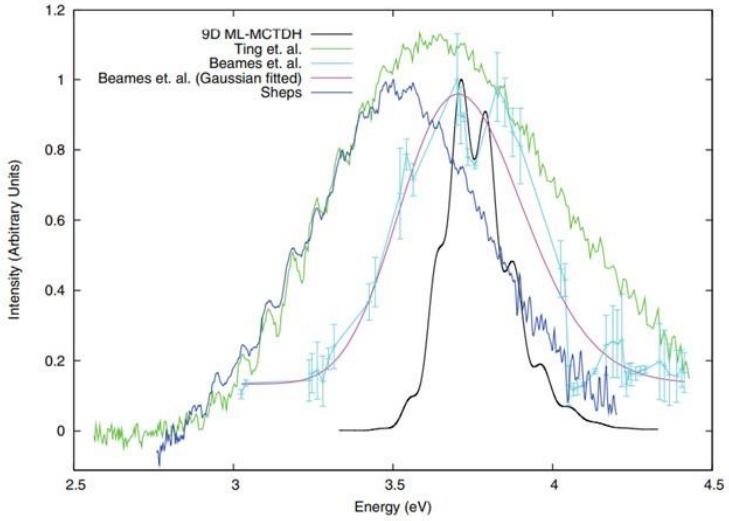

Figure 4.8: Absorption spectra for CH_2OO with the theoretical spectrum labelled '9D ML-MCTDH' showing the results calculated by Meng and Meyer[15] obtained *via* a Fourier-transform of the auto-correlation function followed by a broadening of the spectrum by convoluting it with a Gaussian, and the experimental spectra of Ting *et al.*,[6] Beames *et al.*,[4] Beames *et al.*[4] with a Gaussian fit to the data and Sheps[5] labelled in the figure.

It was stated by Dawes *et al.*[16] in 2015 that neither of these theoretical models using quantum dynamics is adequate to accurately describe the electronic structure and/or dynamics of CH_2OO, as high-level treatment of dynamic electron-correlation is required to accurately describe its electronic states. Using a one-dimensional simulation based on the high-level explicitly correlated multireference configuration interaction (MRCI-F12) electronic structure level of theory and large active spaces, a potential energy well was identified in the excited $\tilde{B}^1A'$ vibrational state with an equilibrium geometry differing substantially from that of the ground $\tilde{X}^1A'$ state mainly in three coordinates,[16] presumed to be responsible for the structure observed in the experimental UV spectra of Sheps,[5] Ting *et al.*[6] and Foreman *et al.*[7]

The O-O and C-O bond distances in CH_2OO were both reported to be significantly longer, and the ∠COO angle significantly smaller, in the excited state than the ground

state counterpart, by Dawes *et al.*[16] Although large differences in these coordinates was also reported by Lee *et al.*,[10] their simulated absorption spectrum was centred at ~318 nm, a shorter wavelength than observed experimentally,[4-7] unlike the vertical excitation energy to the $\tilde{B}^1A'$ state predicted by Dawes *et al.*[16] of 3.751 eV, an energy equating to ~331 nm, close to those obtained experimentally by Beames *et al.*[4] and Ting *et al.*[6] of 335 nm and 340 nm respectively, as shown in Figure 4.9. Despite the limitations of this model, the calculated UV absorption spectrum using a one-dimensional model and a potential energy surface (PES)[16] was found to be in good agreement with experimental observations.[4-7] However, although this simulation by Dawes *et al.*[16] was able to replicate the position and width quite well, it did not fully reproduce the long-wavelength side of the experimentally observed spectra[4-7] and it only signalled the emergence of a vibrational structure.

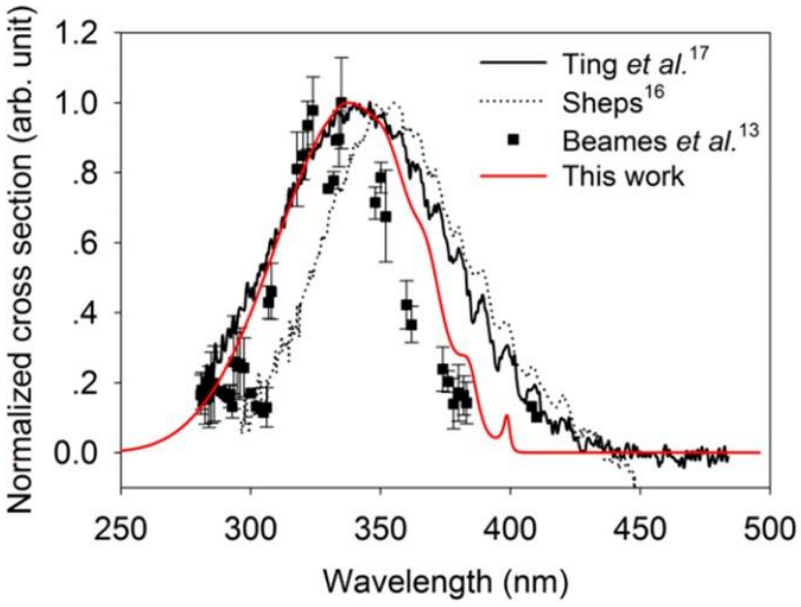

Figure 4.9: Absorption spectra for CH_2OO with the theoretical spectrum labelled 'This work' showing the results calculated by Dawes *et al.*[16] using a 1D model and PESs at the MRCI-F12 level of theory for geometries relaxed along the ground vibrational state, and the experimental spectra reported by Ting *et al.*,[6] Sheps[5] and Beames *et al.*[4] labelled in the figure.

The quality of any calculated spectrum should be judged on all its parameters i.e. the position(s) of the peak(s), the width(s) of the peak(s) and the absolute cross-sections.[17] A consistently lacking feature of these theoretical studies of the CH_2OO absorption

spectrum,[10, 14-16] highlighted by Sršeň *et al.*[17] in 2018 as being essential in the atmospheric context yet absent in all of these simulations, is absolute intensities. In an assessment of whether theory and quantum chemical methods available in the present day can provide UV absorption cross-sections accurate enough to be used (e.g. in atmospheric models), Sršeň *et al.*[17] showed that high quality data can be obtained at a reasonable computational price. The development and application of a new composite computational scheme applicable for systems larger than CH_2OO (i.e. up to ~15 atoms) was concluded to enable prediction of absorption spectra for Criegee intermediates not yet determined experimentally,

Calculation of absorption cross-sections was done by Sršeň *et al.*[17] using the semiclassical reflection principle approach coupled with an efficient implementation of the path integral molecular dynamics and the UV spectrum was processed using the kernel density estimation method.[17] New composite approaches were formulated in which the effect of triple excitations on excited state energies and oscillator strengths was estimated from calculations utilising a smaller basis set, combining the equation-of-motion coupled-cluster singles and doubles (EOM-CCSD) and the equation-of-motion coupled-cluster singles, doubles and triples (EOM-CCSDT) methods, and the coupled cluster theory of the second (CC2) and third (CC3) orders, denoted equation-of-motion coupled-cluster singles, doubles/triples (EOM-CCSD/T) theory and coupled cluster theory of the second/third order (CC2/3), providing excellent absorption cross-sections for CH_2OO at an acceptable computational cost. The modelled absolute CH_2OO UV absorption cross-sections[17] closely resembled the experimental data of Ting *et al.*[6] with the position and width of the spectra being almost identical, however the theoretical peak, at ~$(1.5 – 1.8) \times 10^{-17}$ cm^2,[17] appeared to be a little more intense than the experimental spectrum,[6] and the vibrational structure in the experimental data[6] was not recovered in the computed spectrum, as shown in Figure 4.10.[17] Simulations of the spectrum were found to be complicated due to the difficult electronic structure of the Criegee intermediate with the biradical component in the structure setting limitations for computational methods.[17]

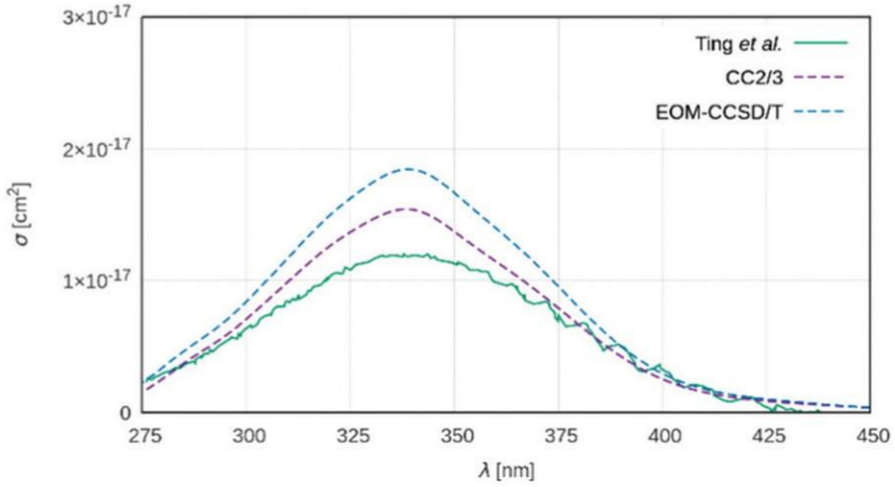

Figure 4.10: Absorption cross-sections for CH_2OO with the theoretical spectra labelled 'CC2/3' and 'EOM-CCSD/T' showing the results calculated by Sršeň *et al.*[17] obtained with the composite methods based on the coupled cluster theory and equation-of-motion coupled-cluster theory respectively, both using the aug-cc-pVDZ basis set, and the experimental spectrum reported by Ting *et al.*[6] labelled in the figure.

Although there is some discrepancy in reported absolute CH_2OO absorption cross-sections as well as the shape and peak of the spectrum, all previous studies have demonstrated that Criegee UV absorption cross-sections are relatively large, on the order of $\sim 10^{-17}$ cm^2.[4-7] Qualitatively, the absorption measurements recorded have similar spectra, displaying distinct vibronic band structure[5-7] superimposed on an underlying continuum[4-7] (described in further detail in Chapter 2), yet quantitatively, the absolute absorption cross-sections vary by approximately a factor of three. Spectra of CH_2OO reported in the literature highlight the challenges associated with measuring absorption cross-sections for a species which is reacting on the timescale of the experimental measurements. In order to utilise UV absorption spectroscopy in the study of Criegee intermediates and their reaction kinetics, it is important to eliminate discrepancies arising in the current literature. Accurate measurements of the absolute absorption cross-sections of CH_2OO in the UV region are also necessary to predict the true fate of CH_2OO in the troposphere. In this work, the absolute CH_2OO UV absorption cross-sections have been determined at 298 K as a function of pressure in the range 6 to 300 Torr using flash photolysis coupled with time-resolved broadband UV absorption spectroscopy.

4.3 Experimental

Experiments were carried out as described in Chapter 3 therefore only a brief description is given here.

The UV absorption cross-sections of the CH_2OO Criegee intermediate were studied using laser flash photolysis of $CH_2I_2/O_2/N_2$ gas mixtures, coupled with broadband time-resolved UV absorption spectroscopy. The development and characterisation of the experimental apparatus has been described elsewhere,[19, 20] and is summarised in Chapter 3.

Precursor gases were mixed in a gas manifold at known flow rates determined by calibrated mass flow controllers (MFCs, MKS Instruments), with CH_2I_2 introduced into the gas flow by passing a known slow flow of N_2 through a bubbler containing liquid CH_2I_2 at room temperature. The total flow rate was maintained at 4000 standard cm^3 per minute (sccm) at 100 Torr and adjusted accordingly with pressure to maintain constant number densities for reactant gases and a constant residence time in the cell of ~6 s. All experiments were performed at T = (298 ± 2) K in N_2 (BOC oxygen free, 99.998 %) at pressures between 6 and 300 Torr. CH_2I_2 (Alfa Aesar 99 %) concentrations were in the range $1 \times 10^{12} – 4 \times 10^{13}$ cm^{-3} and O_2 (BOC, 99.5 %) concentrations were varied between 1×10^{16} and 4×10^{17} cm^{-3}. Gases and chemicals were used as supplied.

Reactions R4.2-R4.6 were initiated in the reaction cell by an excimer laser operating at a wavelength of λ = 248 nm. The typical laser fluence was measured to be ~25 mJ cm^{-2}, giving $[CH_2OO]_{t=0}$ on the order of ~10^{11} cm^{-3}.

$CH_2I_2 + h\nu$ (λ=248 nm)	→	$CH_2I + I$	(R4.2)
$CH_2I + O_2$	→	$CH_2OO + I$	(R4.3a)
$CH_2I + O_2$	$\xrightarrow{+M}$	CH_2IO_2	(R4.3b)
$CH_2OO + CH_2OO$	→	products	(R4.4)
$CH_2OO + I$	→	products	(R4.5)
CH_2OO	→	products	(R4.6)

Absorption of UV/visible radiation by species within the cell was monitored between 250 and 850 nm over an effective path length of (443 ± 21) cm and (1136 ± 143) cm for 7 and 13 multipass arrangements of the probe beam respectively (further information is provided in Appendix 2). A spectral resolution of 1.5 nm full width at half maximum (FWHM) and time resolution of 1 ms was determined for data obtained using this experimental setup, with intensity data recorded typically averaged for 100 to 400 photolysis shots.

4.4 Analysis

The raw data was output as a 2D array of intensity vs time for each of the 2000 time points in 1 millisecond intervals over the 2 second timescale of the run vs wavelength for the range λ = 250-850 nm in 1024 wavelength points.

Using the Beer-Lambert law the total observed absorbance, $A_{t,\lambda}$, can be calculated at a given wavelength, λ, and time point, t, throughout the run:

$$A_{t,\lambda} = \ln(I_{0,\lambda}/I_{t,\lambda}) = \Sigma\, \sigma_{i,\lambda}\, [\mathrm{C}]_{i,t}\, l \qquad \text{(Equation 4.1)}$$

where $I_{0,\lambda}$ is the average light intensity at wavelength λ prior to photolysis and $I_{t,\lambda}$ is the light intensity at wavelength λ and time t following photolysis; and where $\sigma_{i,\lambda}$ is the absorption cross-section of each individually absorbing species i in the system at wavelength λ, $[C]_{i,t}$, is the concentration of each individually absorbing species i in the system at time point t, and l is the total path length of the light being absorbed by all individually absorbing species through the system.

The total absorbance observed, i.e. the transient absorption spectrum, was found to contain contributions from the absorbance of CH_2I_2 ($A_{CH2I2,t,\lambda}$), CH_2OO ($A_{CH2OO,t,\lambda}$) and IO ($A_{IO,t,\lambda}$):

$$A_{t,\lambda} = A_{CH2I2,t,\lambda} + A_{CH2OO,t,\lambda} + A_{IO,t,\lambda} \qquad \text{(Equation 4.2)}$$

This is because the spectra of these three contributing species, CH_2I_2, CH_2OO and IO, overlap in the wavelength region of interest as shown in Figure 4.11.

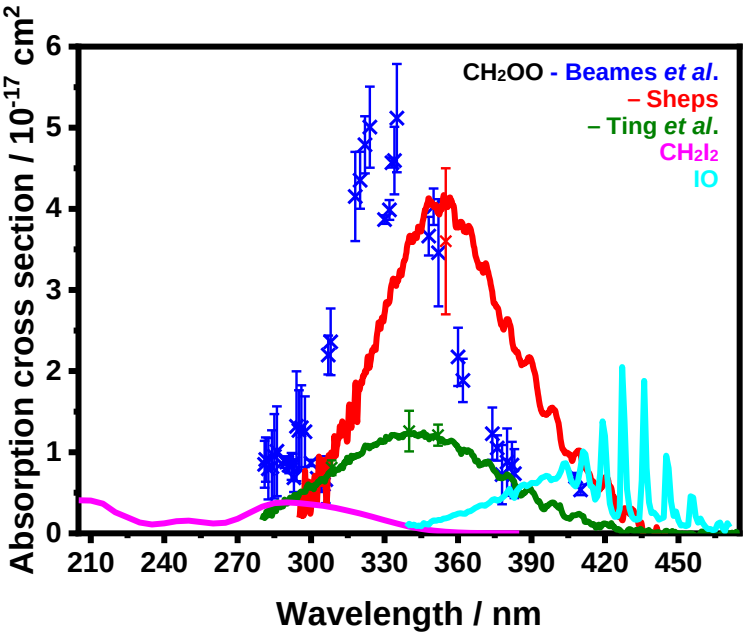

Figure 4.11: The overlapping spectral contributions from CH_2I_2,[21, 22] IO[21, 23] and CH_2OO[4-6] absorbance observed in the experimental transient absorption spectra.

Substituting in the absorption cross-section, concentration and path length terms for each absorbing species gives:

$$A_{t,\lambda} = \sigma_{CH2I2,\lambda}\,\Delta[CH_2I_2]_t\,l + \sigma_{CH2OO,\lambda}\,[CH_2OO]_t\,l + \sigma_{IO,\lambda}\,[IO]_t\,l$$

(Equation 4.3)

where $\sigma_{CH2I2,\lambda}$ is the CH_2I_2 absorption cross-section at wavelength λ, $\Delta[CH_2I_2]_t$ is the change in CH_2I_2 concentration at time t following photolysis, $\sigma_{CH2OO,\lambda}$ is the CH_2OO absorption cross-section at wavelength λ, $[CH_2OO]_t$ is the concentration of CH_2OO at time t, $\sigma_{IO,\lambda}$ is the IO absorption cross-section at wavelength λ, $[IO]_t$ is the concentration of IO at time t, and l is the effective path length of the light.

The contribution from IO is readily distinguished by the strong vibronic structure in the region 400-450 nm as shown in Figure 4.12, and a fit of the IO reference spectrum[21, 23] over this wavelength range was performed to remove the contribution from IO, giving $A'_{t,\lambda}$:

$$A'_{t,\lambda} = A_{t,\lambda} - A_{IO,t,\lambda} = A_{CH2I2,t,\lambda} + A_{CH2OO,t,\lambda}$$

$$= \sigma_{CH2I2,\lambda}\,\Delta[CH_2I_2]_t\,l + \sigma_{CH2OO,\lambda}\,[CH_2OO]_t\,l \qquad \text{(Equation 4.4)}$$

The CH_2I_2 spectrum is observed as a negative absorption due to its depletion upon photolysis, as shown in Figure 4.12. As described in previous work,[5, 6] it is assumed that following photolysis, the change in the concentration of CH_2I_2 at time t, $\Delta[CH_2I_2]_t$, is constant with respect to time, hence $\Delta[CH_2I_2]$ at any time t after photolysis ($t > 0$) is the same, and so the value determined for $\Delta[CH_2I_2]$ at a late time point can also be used during analysis at early time points. Since the CH_2I_2 concentration remains constant after photolysis, the absorbance owing to CH_2OO can be determined by subtraction of the absorbance $A'_{t,\lambda}$ at a late time point following photolysis (typically 50 ms after photolysis, when CH_2OO has reacted and $A'_{t,\lambda} = \sigma_{CH2I2,\lambda}\ \Delta[CH_2I_2]\ l$) from the absorbance $A'_{t,\lambda}$ at an earlier time point following photolysis (where $A'_{t,\lambda} = \sigma_{CH2I2,\lambda}\ \Delta[CH_2I_2]\ l + \sigma_{CH2OO,\lambda}\ [CH_2OO]t\ l$).

$$
\begin{aligned}
A'_{t=\text{early},\lambda} - A'_{t=\text{late},\lambda} &= (A_{CH2I2,t,\lambda} + A_{CH2OO,t,\lambda}) - (A_{CH2I2,t,\lambda}) \\
&= (\sigma_{CH2I2,\lambda}\ \Delta[CH_2I_2]\ l + \sigma_{CH2OO,\lambda}\ [CH_2OO]_t\ l) \\
&\quad - (\sigma_{CH2I2,\lambda}\ \Delta[CH_2I_2]\ l) \\
&= \sigma_{CH2OO,\lambda}\ [CH_2OO]_t\ l \qquad \text{(Equation 4.5)}
\end{aligned}
$$

The average CH_2OO absorbance spectrum in the first 50 ms following photolysis was thus determined and normalised to the maximum absorbance to determine the overall shape and position of the CH_2OO spectrum. This combination of CH_2OO absorbance from several time points within the first 50 ms after photolysis, such as those shown in Figure 4.12, allows for the shape of the CH_2OO spectrum to be determined with an improved signal-to-noise ratio, however requires that the spectrum be normalised by dividing the average absorbance spectrum for all time points considered by the maximum absorbance in the averaged spectrum, resulting in a determination of the ratio of the CH_2OO UV absorption cross-section at wavelength λ to the maximum CH_2OO UV absorption cross-section at the wavelength corresponding to the peak of the spectrum, λ_{peak}, $\sigma_{CH2OO,\lambda} / \sigma_{maximum,CH2OO,\lambda peak}$. The normalised CH_2OO spectrum, $\sigma_{CH2OO,\lambda} / \sigma_{maximum,CH2OO,\lambda peak}$, is shown in Figure 4.13.

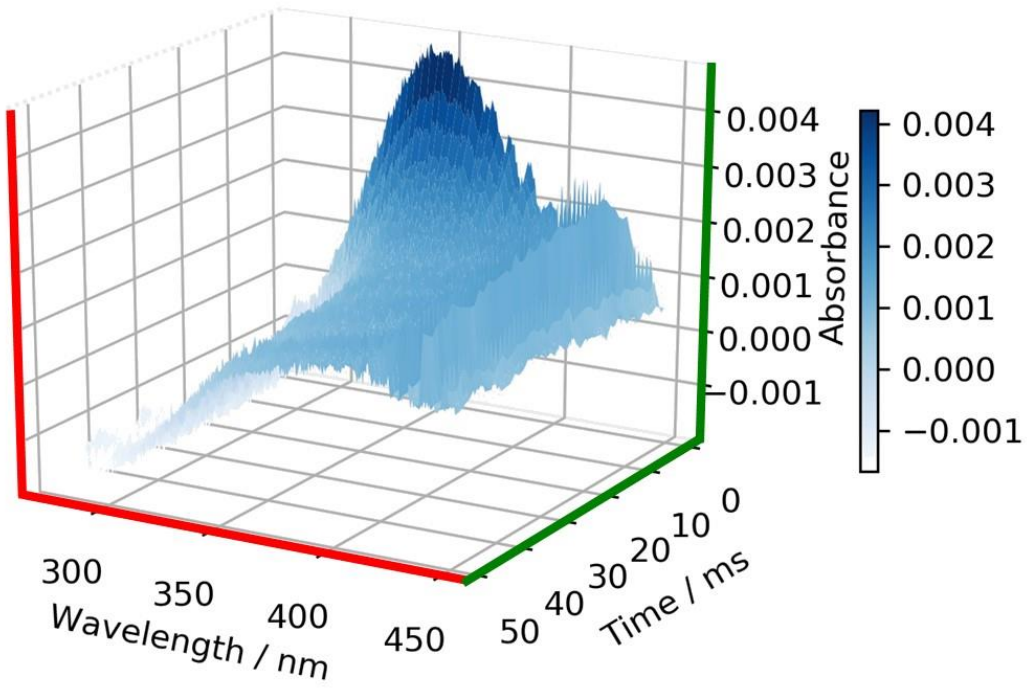

Figure 4.12: A 3-D representation of experimental transient absorption spectra at various time points and wavelengths, displaying the overlapping spectral contributions from IO (strong vibronic structure in the 400-450 nm region), CH_2I_2 (constant negative absorption due to depletion following photolysis in the 280-360 nm region), and CH_2OO (strong broad absorption in the 280-450 nm region with a peak at ~340 nm and vibronic structure at wavelengths above 360 nm) from which the normalised CH_2OO spectrum was determined.

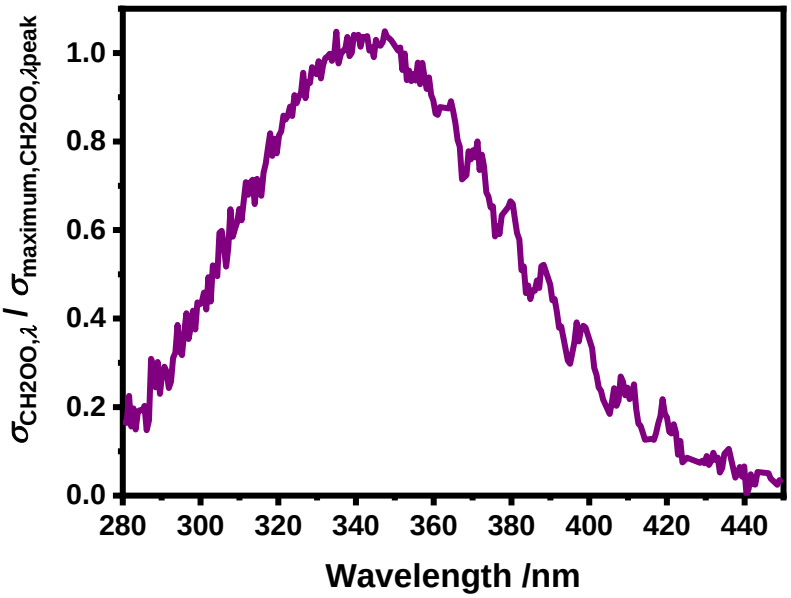

Figure 4.13: Normalised CH_2OO spectrum, $\sigma_{CH2OO,\lambda}$ / $\sigma_{maximum,CH2OO,\lambda peak}$, determined from CH_2OO absorbance at time points within the first 50 ms after photolysis of $CH_2I_2/O_2/N_2$. For these data, p = 70 Torr, $[O_2] = 2.19 \times 10^{17}$ cm^{-3}, $[CH_2I_2] = 9.72 \times 10^{12}$ cm^{-3}, $\Delta[CH_2I_2]\ l = 6.06 \times 10^{14}$ cm^{-2}.

Substituting this determination of $\sigma_{CH2OO,\lambda}$ / $\sigma_{maximum,CH2OO,\lambda peak}$ into $A'_{t,\lambda}$ means that $A'_{t,\lambda}$ thus becomes:

$$A'_{t,\lambda} = \sigma_{CH2I2,\lambda}\ \Delta[CH_2I_2]\ l + \frac{\sigma_{CH2OO,\lambda}}{\sigma_{maximum,CH2OO,\lambda peak}}\ \sigma_{maximum,CH2OO,\lambda peak}\ [CH_2OO]_t\ l$$

(Equation 4.6)

Absorption cross-sections for the reference CH_2I_2 spectrum,[21, 22] $\sigma_{CH2I2,\lambda}$, and the normalised CH_2OO spectrum, $\sigma_{CH2OO,\lambda}$ / $\sigma_{maximum,CH2OO,\lambda peak}$, were subsequently fit to $A'_{t,\lambda}$ at each post-photolysis time point and wavelength in the region 280 – 450 nm, to determine $\Delta[CH_2I_2]\ l$, and the product of the maximum CH_2OO cross-section, $\sigma_{maximum,CH2OO,\lambda peak}$, and $[CH_2OO]_t\ l$. Figure 4.14 shows typical fits of reference spectra IO and CH_2I_2[21-23] and of the normalised CH_2OO spectrum to the total absorbance observed at various time points including immediately following photolysis.

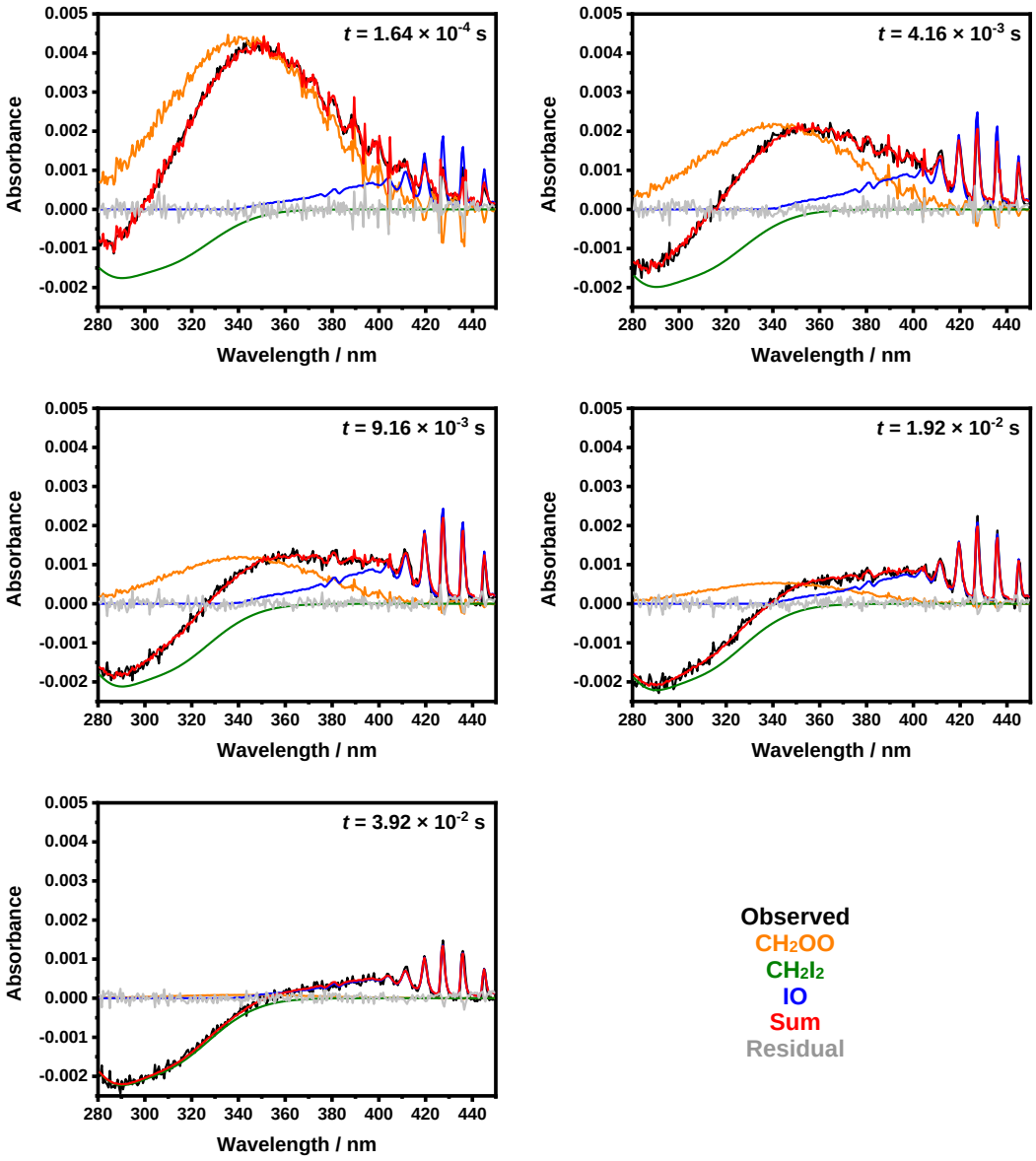

Figure 4.14: Total observed absorbance (A, black) at the first post-photolysis time point, $t = 1.64 \times 10^{-4}$ s following photolysis of $CH_2I_2/O_2/N_2$, and various other time points after photolysis throughout the reaction at $t = 4.16 \times 10^{-3}$ s, $t = 9.16 \times 10^{-3}$ s, $t = 1.92 \times 10^{-2}$ s and $t = 3.92 \times 10^{-2}$ s respectively. Contributions from CH_2I_2, IO and CH_2OO determined by fitting reference spectra to the observed absorbance, and the fit residual, are also shown. It can be seen that the CH_2I_2 depletion signal remains approximately constant over time following photolysis and that CH_2OO completely reacts within 50 ms following photolysis. For these data, $p = 70$ Torr, $[O_2] = 2.19 \times 10^{17}$ cm^{-3}, $[CH_2I_2] = 9.72 \times 10^{12}$ cm^{-3}, $\Delta[CH_2I_2]\ l = 6.06 \times 10^{14}$ cm^{-2}, $[CH_2OO]_{t=0} = 7.27 \times 10^{11}$ cm^{-3}, $[CH_2OO]_{t=1.64\times10^{-4}\text{ s}} = 7.06 \times 10^{11}$ cm^{-3}, $[IO] = 1.96 \times 10^{11}$ cm^{-3}.

Absolute CH_2OO cross-section values can be determined from the normalised CH_2OO spectrum if $\sigma_{maximum,CH2OO,\lambda peak}$ $[CH_2OO]_t$ l and $[CH_2OO]_t$ l are known for a given time point, allowing for determination of $\sigma_{maximum,CH2OO,\lambda peak}$. However, while the fit of the reference CH_2I_2 spectrum[21, 22] and the normalised CH_2OO spectrum to $A'_{t,\lambda}$ gives $\sigma_{maximum,CH2OO,\lambda peak}$ $[CH_2OO]_t$ l for all time points after photolysis ($t > 0$), $[CH_2OO]_t$ l can only be determined for $t = 0$.

The yields of CH_2OO and CH_2IO_2 from the reaction of CH_2I radicals with O_2 as a function of total pressure have been measured previously in this laboratory by Stone *et al.*[13] at 295 K and pressures between 25 and 450 Torr using three complementary methods, with the yield of CH_2OO decreasing with increasing pressure and an 18 % CH_2OO yield being reported at atmospheric pressure. This pressure dependent yield of CH_2OO following photolysis of CH_2I_2 in the presence of O_2 reported by Stone *et al.*[13] was used to determine the product of the initial concentration of CH_2OO and the path length, $[CH_2OO]_{t=0}$ l, from the observed product of the depletion of CH_2I_2 and the path length, $\Delta[CH_2I_2]$ l, which is equivalent to the product of the initial concentration of CH_2I radicals and the path length, $[CH_2I]_{t=0}$ l. Although the path length, l, was experimentally determined for the 7 and 13 multipass configurations of the probe beam, for which a more detailed description is given in Appendix 2, it should be noted that an advantage of this data analysis is that the determination of $\sigma_{maximum,CH2OO,\lambda peak}$ is independent of the path length, hence the value of l does not need to be known.

Two further methods were used to determine $\Delta[CH_2I_2]$ and therefore $[CH_2I]_{t=0}$ and $[CH_2OO]_{t=0}$. The first one of these methods was *via* measurement of the spectrum of CH_2I_2 before each run with the photolysis laser turned off, combined with the measured laser energy and the pressure dependent CH_2OO yield from the reaction of $CH_2I + O_2$ (R4.3a) as determined by Stone *et al.*[13] The absorbance was given *via* measurement of the intensity of light without, I_0, and with, I, the absorbing species present, which were measured with N_2/O_2 and $N_2/O_2/CH_2I_2$ respectively. The literature spectrum of CH_2I_2 is well defined,[21, 22] hence a fit of this reference spectrum to the observed absorbance in the experimental spectrum gave the concentration of CH_2I_2 in the reaction cell *via* the Beer-Lambert Law, $A_{CH2I2,t,\lambda} = \sigma_{CH2I2,\lambda}$ $[CH_2I_2]_t$ l, where $A_{CH2I2,t,\lambda}$ is the total observed absorbance due to CH_2I_2 at time t and wavelength

λ, $\sigma_{CH2I2,\lambda}$ is the absorption cross-section of CH_2I_2 at wavelength λ, $[CH_2I_2]$ is the concentration of CH_2I_2 at time t, and l is the path length over which absorbance is observed and equals 1050 cm (the length of the cell, 150 cm, multiplied by the number of passes of the probe beam, 7).

The excimer laser energy was measured and $[CH_2I]$ was calculated *via* the following equations. First, the energy of a single photon was calculated at the photolysis wavelength, 248 nm:

$$E_{photon} = \frac{h\,c}{\lambda\,(248\text{ nm})} = 8.01 \times 10^{-19}\text{ J} \qquad \text{(Equation 4.7)}$$

The laser fluence was measured for each experiment and taking a typical laser fluence value of E_{total} = 25 mJ cm^{-2} gives the number of photons:

$$\text{No. of photons } (cm^{-2}) = \frac{E_{total}}{E_{photon}} = 3.12 \times 10^{16}\text{ photons } cm^{-2} \qquad \text{(Equation 4.8)}$$

The fraction of CH_2I_2 photolysed is dependent on the absorption cross-section of CH_2I_2 at 248 nm, $\sigma_{CH2I2,\,248\text{ nm}}$, *via* the equation:

$$\text{Fraction } CH_2I_2 \text{ photolysed} = \text{No. of photons} \times \sigma_{CH2I2,\,248\text{ nm}} \qquad \text{(Equation 4.9)}$$

$\sigma_{CH2I2,\,248\text{ nm}}$ was taken as 1.56×10^{-18} cm^2,[21, 22] giving the fraction of CH_2I_2 photolysed as 4.87×10^{-2}. $[CH_2I]_{t=0}$ was then calculated *via*:

$$[CH_2I]_{t=0} = \text{Fraction } CH_2I_2 \text{ photolysed} \times [CH_2I_2] \qquad \text{(Equation 4.10)}$$

The pressure dependent CH_2OO yield from the reaction of CH_2I radicals and O_2 has been reported in the literature,[13] *via* the relationship:

$$\frac{1}{CH_2OO\text{ yield}} = \left(\left((1.90 \pm 0.22) \times 10^{-19}\right) \times \text{total pressure } (cm^{-3})\right) + (1.10 \pm 0.23) \qquad \text{(Equation 4.11)}$$

From this $[CH_2OO]_{t=0}$ could be deduced *via*:

$$[CH_2OO]_{t=0} = [CH_2I]_{t=0} \times CH_2OO\text{ yield} \qquad \text{(Equation 4.12)}$$

Taking a typical value of CH_2I_2 to be 8×10^{12} cm^{-3} and a pressure of 70 Torr, this gives a value for $[CH_2OO]_{t=0}$ of 2.54×10^{11} cm^{-3} i.e. on the order of $10^{11} - 10^{12}$ cm^{-3}.

A comparison of the results from the above two methods for calculating $\Delta[CH_2I_2]$, and hence $[CH_2I]_{t=0}$ and the initial concentration of CH_2OO, $[CH_2OO]_{t=0}$, is shown in Figure 4.15. Method 1 refers to the depletion in the CH_2I_2 precursor concentration from fits to $A'_{t,\lambda}$ to determine $[CH_2OO]_{t=0}$, and Method 2 refers to the measured spectrum of CH_2I_2 along with the measured laser fluence to determine $[CH_2OO]_{t=0}$. The comparison shows the ratio of the initial CH_2OO concentration calculated *via* the two methods *via* a direct comparison between the value of $[CH_2I]_{t=0}$ l determined from Method 1 and the value of the product of $[CH_2I]_{t=0}$ determined from Method 2 and the independently measured path length, l, for the 7 pass arrangement of the probe beam, (443 ± 21) cm.

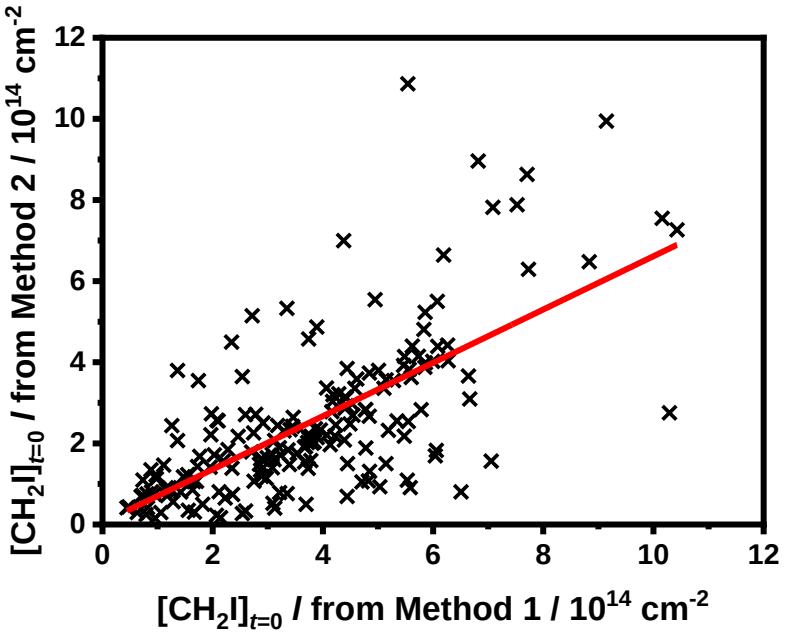

Figure 4.15: Comparison between two different methods for determining $\Delta[CH_2I_2]$, and hence $[CH_2I]_{t=0}$ and $[CH_2OO]_{t=0}$, *via* the ratio of the value for $[CH_2I]_{t=0}$ l determined using Method 1, which refers to fitting the CH_2I_2 depletion signal in experimental transient absorption spectra, to that determined using Method 2, which refers to measuring the spectrum of CH_2I_2. The slope of the graph is 0.66 ± 0.05 and the intercept is 0.05 ± 0.22.

From the comparison, it can be seen that there is a correlation between the two methods, with the results showing the value of $[CH_2I]_{t=0}$ l determined *via* Method 2 to be 66 % of that determined *via* Method 1. For both methods, it is assumed that the time dependence of the CH_2I_2 concentration is negligible and hence that $[CH_2I_2]$ is

constant throughout the timescale of the reaction, which is a valid assumption to make since the observed absorption spectra show the CH_2I_2 depletion signal to be steady over time and hence time profiles for $[CH_2I_2]$ show a constant negative absorption. Thus, the difference observed in results from these two methods of determining $[CH_2I_2]$, and hence $[CH_2I]_{t=0}$ and $[CH_2OO]_{t=0}$ is thought to be due to a combination of experimental factors such as the inherent error associated with measurement of the path length required for Method 2 and the stability in the excimer laser fluence. Since Method 1 does not require the path length to be known and relies on measurements taken simultaneously with those for CH_2OO, it is likely that this is the more accurate method, and hence the method that was selected as the one to be used in the analysis of the experimental data.

A third method for determination of $\Delta[CH_2I_2]$ in the reaction cell was also recorded, *via* use of the calibrated MFC through which CH_2I_2 entered the reaction mixture, the vapour pressure of CH_2I_2 at 298 K, 1.2 Torr,[24] and the back pressure on the regulator for the supply of N_2 passed through the bubbler containing liquid CH_2I_2, varied between 0.25 and 1 bar above atmospheric pressure. However, this method was limited in that it assumes complete saturation of the MFC with the gas flowing through it, which was not always the case, especially for compounds with low volatility such as CH_2I_2. The concentration of CH_2I_2 determined *via* measurement of the CH_2I_2 spectrum (Method 2) was on average 30-50 % that calculated from the vapour pressure and calibrated MFC.

Thus, $[CH_2OO]_{t=0}\ l$ is determined from the observed product of the depletion of CH_2I_2 and the pressure dependent yield of CH_2OO from the $CH_2I + O_2$ reaction,[13] however, $\sigma_{maximum,CH2OO,\lambda peak}\ [CH_2OO]_{t=0}\ l$, which is required to determine $\sigma_{maximum,CH2OO,\lambda peak}$ and hence $\sigma_{CH2OO,\lambda}$, remains unknown. In order to determine $\sigma_{maximum,CH2OO,\lambda peak}\ [CH_2OO]_{t=0}\ l$, an extrapolation of the time profile of $\sigma_{maximum,CH2OO,\lambda peak}\ [CH_2OO]_t\ l$ back to $t = 0$ is required, therefore it was necessary to fit the time profile for the absorbance at the wavelength at which the maximum CH_2OO cross-section is observed, $A_{CH2OO,t,\lambda peak} = \sigma_{maximum,CH2OO,\lambda peak}\ [CH_2OO]_t\ l$, determined from the fit of the CH_2I_2 cross-sections[21, 22] and normalised CH_2OO cross-sections to the observed absorbance, to a mixed first- and second-order analytical kinetic loss equation.

The fit of a mixed first- and second-order analytical kinetic loss equation to the data includes a first-order loss component for CH_2OO, primarily resulting from diffusion out of the probe beam, and a second-order loss component for CH_2OO, owing to bimolecular reaction processes of CH_2OO in the system, namely the CH_2OO self-reaction and the CH_2OO + I reaction, on the timescale of the experiment, for which further details are provided in Chapter 5. The rate of change in $[CH_2OO]$ for such a mixed-order process is[25, 26]:

$$-\frac{d[CH_2OO]}{dt} = k_{1st}[CH_2OO] + 2k_{2nd}[CH_2OO]^2 \qquad \text{(Equation 4.13)}$$

where k_{1st} is the rate coefficient for the first-order loss of CH_2OO and k_{2nd} is the rate coefficient for the second-order loss of CH_2OO in the system. The mixed-order integrated rate equation is[25, 26]:

$$[CH_2OO]_t = \frac{k_{1st}[CH_2OO]_{t=0}}{k_{1st}\,e^{k_{1st}t} - 2\,k_{2nd}[CH_2OO]_{t=0} + 2\,k_{2nd}[CH_2OO]_{t=0}\,e^{k_{1st}t}}$$

(Equation 4.14)

The time-profile for the absorbance at the wavelength at which the maximum CH_2OO cross-section is observed is in the Beer-Lambert law form of $A_{CH2OO,t,\lambda peak} = \sigma_{maximum,CH2OO,\lambda peak}[CH_2OO]_t\,l$, which, when substituted into the integrated rate equation, gives:

$$\frac{A_{CH2OO,t,\lambda peak}}{\sigma_{maximum,CH2OO,\lambda peak}\,l} = \frac{k_{1st}\left(\frac{A_{CH2OO,t=0,\lambda peak}}{\sigma_{maximum,CH2OO,\lambda peak}\,l}\right)}{k_{1st}\,e^{k_{1st}t} - 2\,k_{2nd}\left(\frac{A_{CH2OO,t=0,\lambda peak}}{\sigma_{maximum,CH2OO,\lambda peak}\,l}\right) + 2\,k_{2nd}\left(\frac{A_{CH2OO,t=0,\lambda peak}}{\sigma_{maximum,CH2OO,\lambda peak}\,l}\right)e^{k_{1st}t}}$$

(Equation 4.15)

The mixed first- and second-order analytical kinetic loss equation to which the time-profile of the product $A_{CH2OO,t,\lambda peak} = \sigma_{maximum,CH2OO,\lambda peak}[CH_2OO]_t\,l$ was fit, to determine $A_{CH2OO,t=0,\lambda peak} = \sigma_{maximum,CH2OO,\lambda peak}[CH_2OO]_{t=0}\,l$ and hence $\sigma_{maximum,CH2OO,\lambda peak}$, can then be obtained by rearranging the substituted integrated rate equation:

$$A_{CH2OO,t,\lambda peak} = \frac{k_{1st} A_{CH2OO,t=0,\lambda peak}}{k_{1st} e^{k_{1st}t} - 2\left(\frac{k_{2nd}}{\sigma_{maximum,CH2OO,\lambda peak} l}\right) A_{CH2OO,t=0,\lambda peak} + 2\left(\frac{k_{2nd}}{\sigma_{maximum,CH2OO,\lambda peak} l}\right) A_{CH2OO,t=0,\lambda peak} e^{k_{1st}t}}$$

(Equation 4.16)

where $A_{CH2OO,t=0,\lambda peak} = \sigma_{maximum,CH2OO,\lambda peak} [CH_2OO]_{t=0} l$ (the value of $[CH_2OO]_{t=0} l$ is determined from the observed product of the depletion of CH_2I_2 and path length, $\Delta[CH_2I_2] l$, and the pressure dependent CH_2OO yield from $CH_2I + O_2$[13]), k_{1st} is the first-order loss component for CH_2OO, primarily resulting from diffusion out of the probe beam, and k_{2nd} is the second-order loss component for CH_2OO owing to both the CH_2OO self-reaction and the reaction of CH_2OO + I. Figure 4.16 shows the fit result.

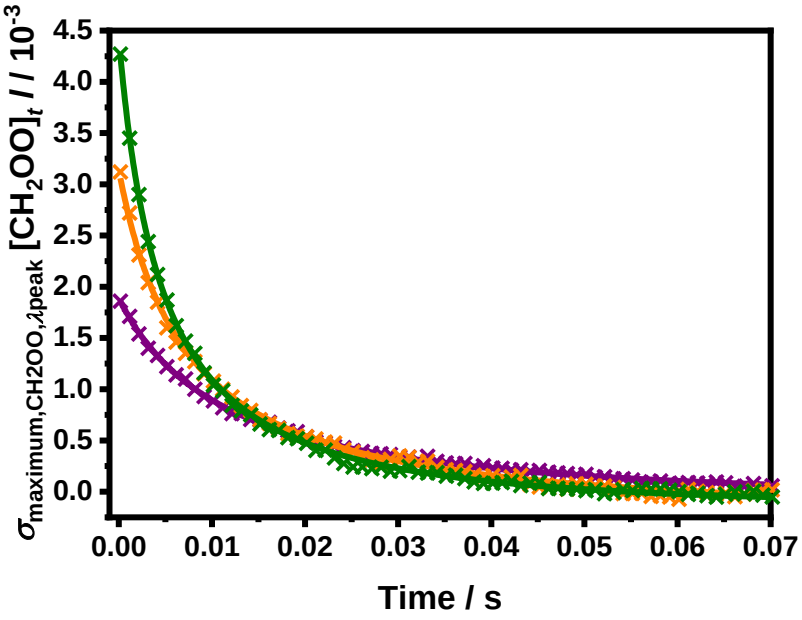

Figure 4.16: Temporal profile of the product $\sigma_{maximum,CH2OO,\lambda peak}$ $[CH_2OO]_t$ l = $A_{CH2OO,t,\lambda peak}$ (green, orange and purple points) determined from the observed absorbance at each time point and the respective fit of the mixed-order equation (Equation 4.16, green, orange and purple lines) to the data. For all these data p = 70 Torr; for the data shown in green $[O_2] = 2.19 \times 10^{17}$ cm^{-3}, and $[CH_2I_2] = 9.72 \times 10^{12}$ cm^{-3}, and the fit to the data gives $A_{CH2OO,t=0,\lambda peak} = \sigma_{maximum,CH2OO,\lambda peak}$ $[CH_2OO]_{t=0}$ l = (4.55 ± 0.03) × 10^{-3}, k_{1st} = (34.3 ± 1.3) s^{-1} and k_{2nd} / $\sigma_{maximum,CH2OO,\lambda peak}$ l = (21614 ± 309) s^{-1}; for the data shown in orange $[O_2] = 1.49 \times 10^{17}$ cm^{-3}, and $[CH_2I_2] = 1.91 \times 10^{13}$ cm^{-3}, and the fit to the data gives $A_{CH2OO,t=0,\lambda peak} = \sigma_{maximum,CH2OO,\lambda peak}$ $[CH_2OO]_{t=0}$ l = (3.31 ± 0.03) × 10^{-3}, k_{1st} = (20.6 ± 2.6) s^{-1} and k_{2nd} / $\sigma_{maximum,CH2OO,\lambda peak}$ l = (19048 ± 559) s^{-1}; and for the data shown in purple $[O_2] = 1.50 \times 10^{17}$ cm^{-3}, and $[CH_2I_2] = 7.25 \times 10^{12}$ cm^{-3}, and the fit to the data gives $A_{CH2OO,t=0,\lambda peak} = \sigma_{maximum,CH2OO,\lambda peak}$ $[CH_2OO]_{t=0}$ l = (1.94 ± 0.02) × 10^{-3}, k_{1st} = (20.6 ± 2.6) s^{-1} and k_{2nd} / $\sigma_{maximum,CH2OO,\lambda peak}$ l = (19048 ± 559) s^{-1}. From the product of the CH_2I_2 depletion and path length, for the data shown in green $\Delta[CH_2I_2]$ l = 6.06×10^{14} cm^{-2}, for the data shown in orange $\Delta[CH_2I_2]$ l = 3.89×10^{14} cm^{-2}, and for the data shown in purple $\Delta[CH_2I_2]$ l = 2.28×10^{14} cm^{-2}, and pressure dependent CH_2OO yield, $Y_{CH2OO,\ p=70\ Torr}$ = 0.65, the product of the initial concentration of CH_2OO and path length was calculated to be $[CH_2OO]_{t=0}$ l = 3.96×10^{14} cm^{-2} for the data shown in green, $[CH_2OO]_{t=0}$ l = 2.54×10^{14} cm^{-2} for the data shown in orange, and $[CH_2OO]_{t=0}$ l = 1.49×10^{14} cm^{-2} for the data shown in purple. $\sigma_{maximum,CH2OO,\lambda peak}$ is then calculated from $\sigma_{maximum,CH2OO,\lambda peak}$ $[CH_2OO]_{t=0}$ l / $[CH_2OO]_{t=0}$ l.

From the value obtained for $A_{CH2OO,t=0,\lambda peak}$ = $\sigma_{maximum,CH2OO,\lambda peak}$ $[CH_2OO]_{t=0}$ l from the mixed-order fit to the $A_{CH2OO,t,\lambda peak}$, and knowledge of $[CH_2OO]_{t=0}$ l, the parameter

$\sigma_{maximum,CH2OO,\lambda peak}$ was determined. Absolute absorption cross-sections for CH_2OO, $\sigma_{CH2OO,\lambda}$, were thus determined from the normalised CH_2OO cross-sections and the value of $\sigma_{maximum,CH2OO,\lambda peak}$. While the kinetic fits performed to determine $\sigma_{maximum,CH2OO,\lambda peak}$ do provide some information regarding the kinetics of CH_2OO loss in the system, a more detailed analysis, described in Chapter 5, was performed to determine the CH_2OO self-reaction kinetics to enable investigation of secondary chemistry within the system.

4.5 Results and Discussion

The absorption cross-sections for CH_2OO determined in this work are shown in Figure 4.17 and provided in tabulated form in Appendix 3. Results from this work indicate a maximum absorption cross-section of $(1.37 \pm 0.29) \times 10^{-17}$ cm^2 at a wavelength of ~340 nm. Results of the average value determined for $\sigma_{maximum,CH2OO,\lambda peak}$ at each pressure under which experiments were carried out are shown in Figure 4.18, indicating that there is no significant dependence of the CH_2OO UV absorption cross-sections on pressure in the range 6 to 300 Torr.

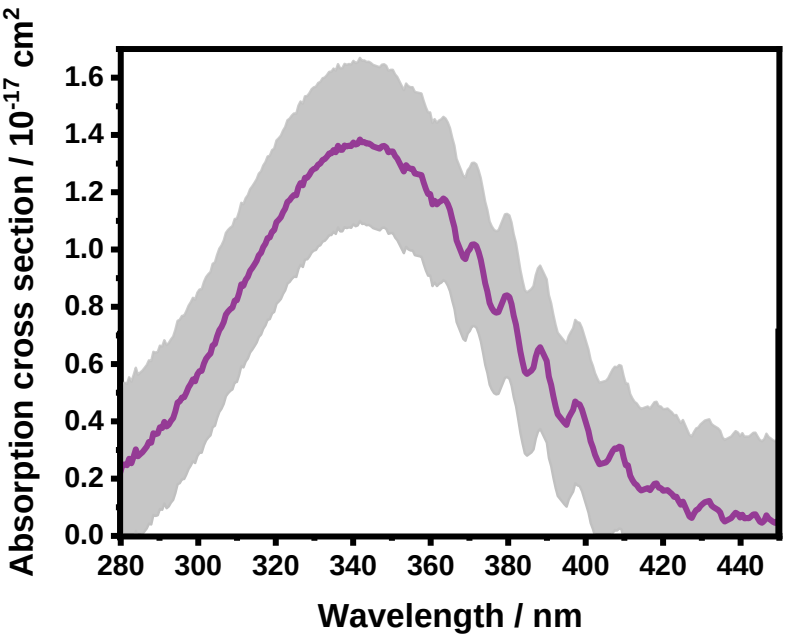

Figure 4.17: Absolute CH_2OO cross-sections determined in this work (purple line), with the 1σ standard deviation (grey shading).

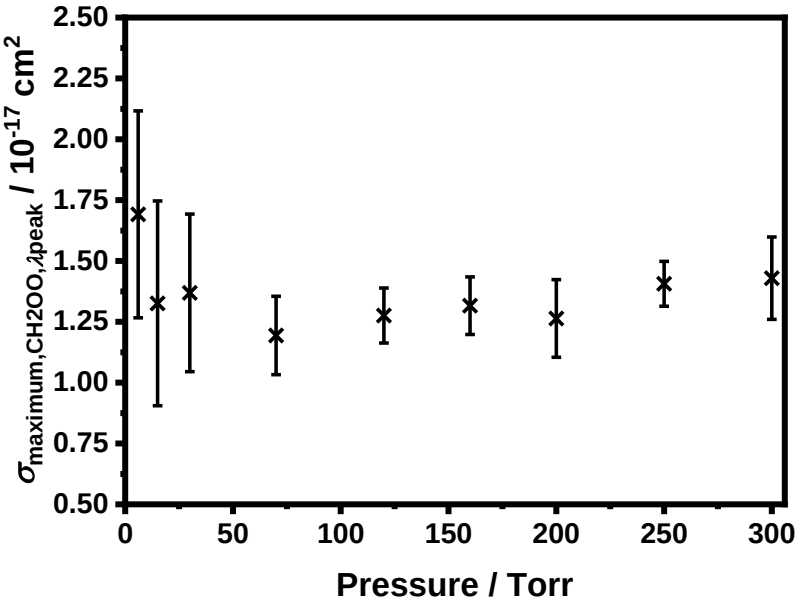

Figure 4.18: Dependence of $\sigma_{maximum,CH2OO,\lambda peak}$ on pressure. Results are displayed as the mean value at each pressure, with errors given by the standard deviation of all values at each pressure.

The maximum CH_2OO absorption cross-section determined in this work is in agreement with previous work by Ting *et al.*[6] which reports a maximum cross-section of $(1.23 \pm 0.18) \times 10^{-17}$ cm^2 at a wavelength of ~340 nm. A comparison of the CH_2OO UV absorption cross-sections determined in this work with those reported in previous work is shown in Figure 4.19, and a comparison of the maximum CH_2OO cross-section reported and the wavelength corresponding to this peak is given in Table 4.1.

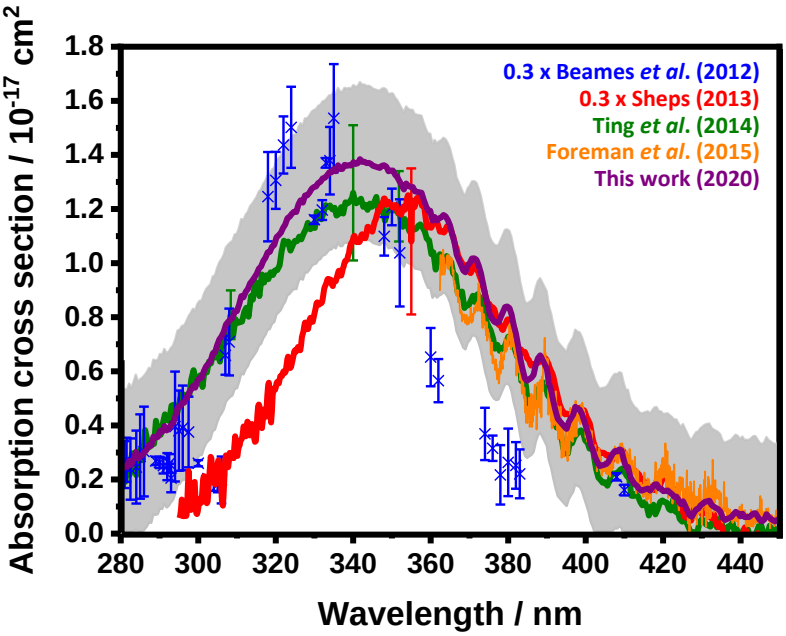

Figure 4.19: Comparison of absolute CH_2OO cross-sections determined in this work (purple line), with the 1σ standard deviation (grey shading), and results from previous work. Note that the results of Beames *et al.*[4] and Sheps[5] are scaled by a factor of 0.3.

Study	Temperature / K	Pressure / Torr	Photolysis λ / nm	Detection Technique	$\sigma_{maximum}$ / 10^{-17} cm^2	$\lambda_{maximum}$ / nm
Beames *et al.*[4]	~10 K	1300	248	PIMS	5	335
Sheps[5]	295	5.1	266	CE-UVA	3.6 ± 0.9	355
Ting *et al.*[6]	295	8-760	248	UVA/PIMS	1.23 ± 0.18	340
Foreman *et al.*[7]	276-357	50	355	UVA/CRDS	-	-
This work	298	6-300	248	UVA	1.37 ± 0.29	340

Table 4.1: Summary of results for the maximum CH_2OO UV absorption cross-section and the wavelength corresponding to this maximum cross-section obtained in this work and reported in the literature. PIMS = photoionisation mass spectrometry; CE-UVA = cavity-enhanced UV absorption; UVA = UV absorption; CRDS = cavity ringdown spectroscopy

Vibronic structure is evident at wavelengths above 360 nm in the CH_2OO spectrum observed in this work, with eight bands observable, in agreement with previous work by Sheps,[5] Ting *et al.*[6] and Foreman *et al.*[7] The physical processes taking place which give rise to this observed vibronic structure are described in detail in Chapter 2. Band centres for the vibronic features observed in the CH_2OO spectrum are listed in Table 4.2, indicating good agreement between the results obtained in this work and those reported by Ting *et al.*[6] and Foreman *et al.*[7]

Band centre / nm (This work)	FWHM / nm	Band centre / nm Ting *et al.*[6]	Band centre / nm Foreman *et al.*[7]
364.3	17.5	363.6	364.272
372.0	13.3	372.0	371.955
380.2	10.6	380.7	380.040
388.4	10.3	389.3	388.863
399.0	8.9	399.0	397.915
408.6	10.9	409.3	408.680
420.2	11.7	420.5	419.305
431.5	7.9	-	431.109

Table 4.2: Band centres and widths of the vibronic features observed in the CH_2OO spectrum. Ting *et al.*[6] report only seven of the features observed in this work and in the work of Foreman *et al.*[7] The weak feature centred at ~431 nm has been tentatively assigned as the band origin by Foreman *et al.*[7]

To investigate the agreement between the CH_2OO absorption spectrum determined in this work and in the work of Ting *et al.*[6] and Foreman *et al.*,[7] differential absorption spectra, the difference between a maximum and an adjacent minimum, were calculated for each study. This was done by fitting a Gaussian function (Equation 4.17) to the absorption cross-sections, as shown in Figures 4.20, and then subtracting the smooth part of the Gaussian from the absolute CH_2OO cross-sections to find the differential CH_2OO cross-sections, as shown in Figure 4.21.

$$\sigma_{CH2OO,Gaussian,\lambda} = \sigma_{CH2OO,maximum,Gaussian} \exp - \frac{(\lambda_{CH2OO,Gaussian} - \lambda_{CH2OO,maximum,Gaussian})^2}{2W^2}$$

(Equation 4.17)

where $\sigma_{CH2OO,maximum,Gaussian}$ is the fitted Gaussian parameter for the maximum absorption cross-section of CH_2OO (i.e. the height of the Gaussian curve's peak), $\lambda_{CH2OO,maximum,Gaussian}$ is the fitted Gaussian parameter for the wavelength corresponding to the maximum absorption cross-section of CH_2OO (i.e. the position of the centre of the peak of the Gaussian curve) and W is the fitted Gaussian parameter for the width of the Gaussian (i.e. controls the width).

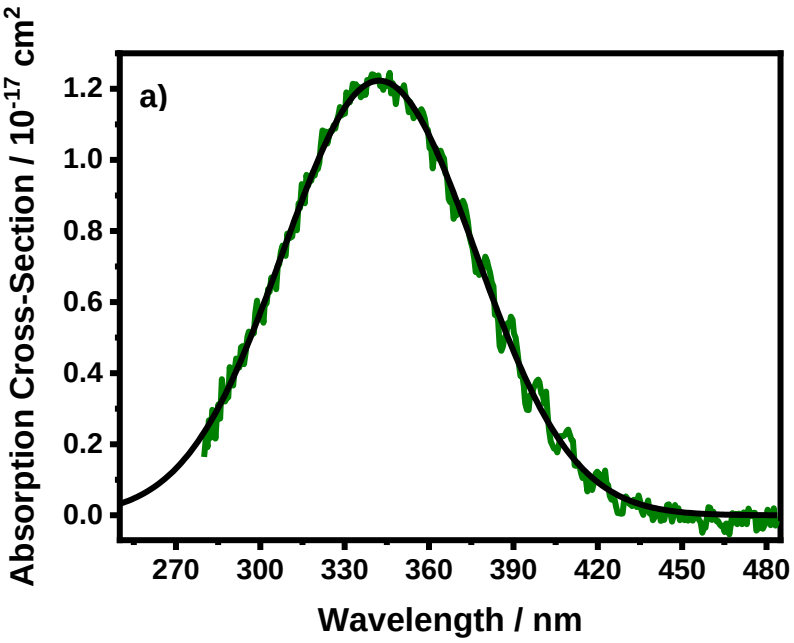

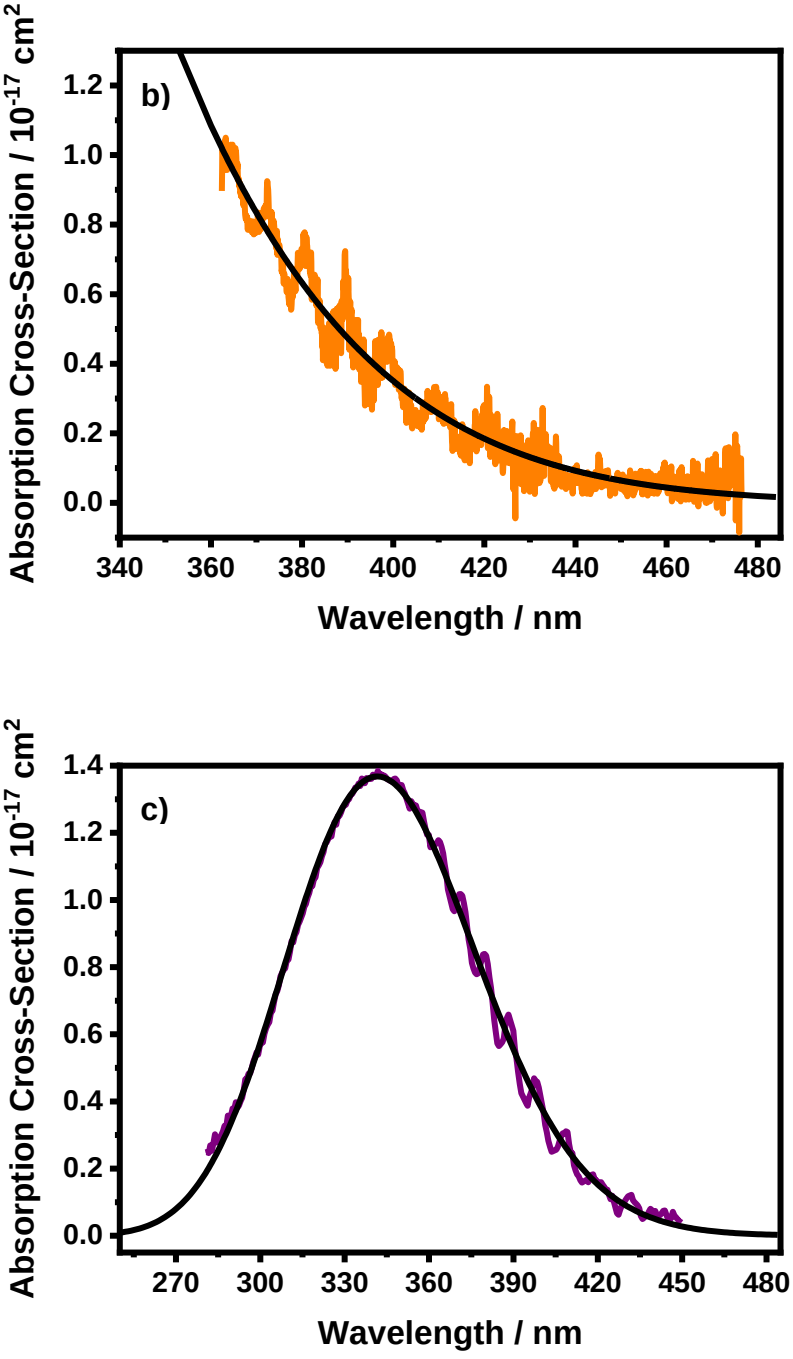

Figure 4.20: Absolute CH_2OO cross-sections for a) the work of Ting *et al.*[6] (green) and the Gaussian fit of Equation 4.17 to this data (black); b) the work of Foreman *et al.*[7] (orange) and the Gaussian fit of Equation 4.17 to this data (black); c) this work (purple) and the Gaussian fit of Equation 4.17 to this data (black).

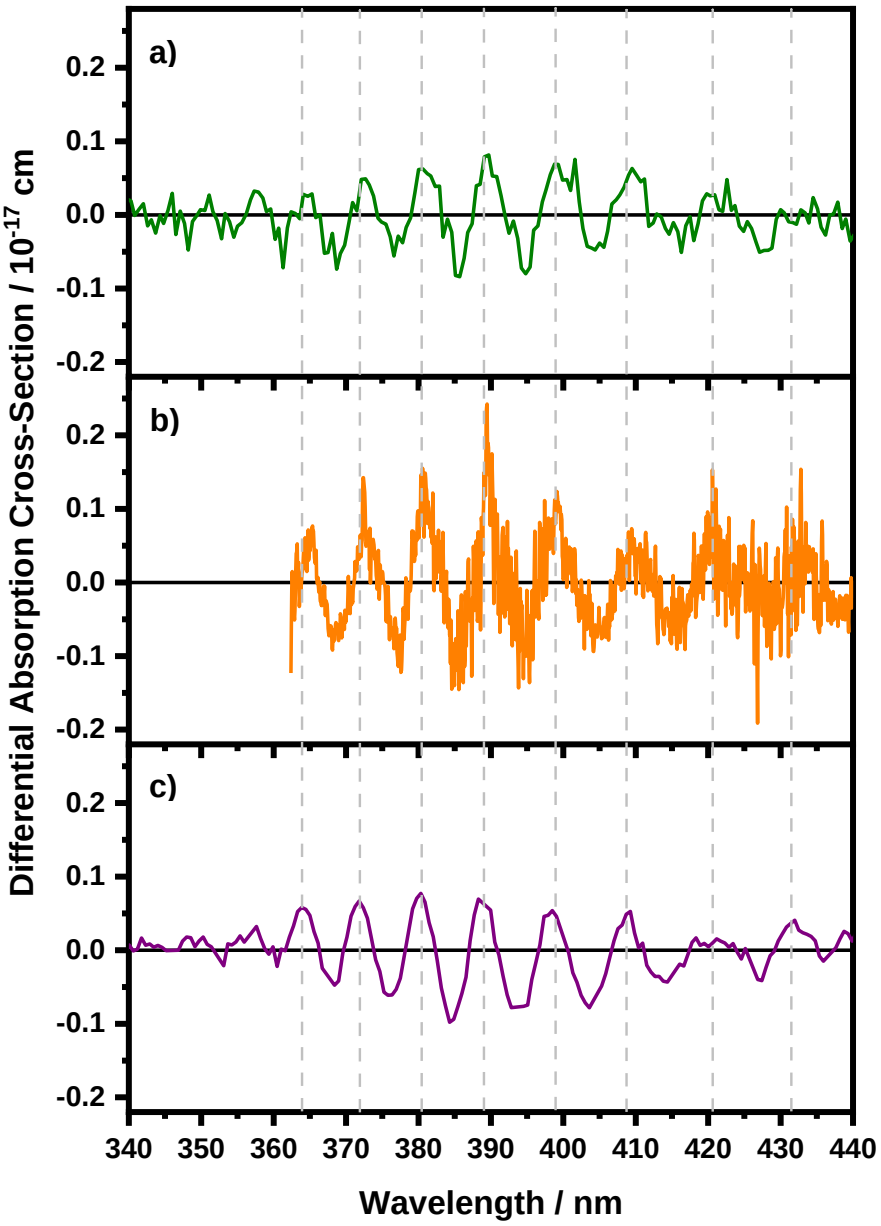

Figure 4.21: Differential CH_2OO cross-sections for a) the work of Ting *et al.*[6] (green), b) the work of Foreman *et al.*[7] (orange) and c) this work (purple), each calculated by subtracting the Gaussian function fitted to the absolute CH_2OO cross-section from the absolute CH_2OO cross-sections. The graphs shows the agreement between the shapes and positions of the vibronic features in the spectrum for all 3 studies and also displays the increased signal to noise in this work compared to Ting *et al.*[6] and Foreman *et al.*[7]

The differential spectra for results obtained in this work and those reported by Ting *et al.*[6] and Foreman *et al.*[7] are shown in Figure 4.21, displaying the agreement between

the shapes and positions of the vibronic features in the spectrum. These differential spectra also demonstrate the increased signal-to-noise ratio of data and results from this work compared to those previously reported.[6, 7]

Discrepancies in the shape of the CH_2OO spectrum, and position and absolute value of the maximum cross-section, between the experimental spectra reported in the literature have been discussed in detail in previous work.[4-7, 17] The shape of the absorption spectrum reported by Sheps[5] was in good agreement with that of the action spectrum reported by Beames *et al*.[4] on the high-energy side of the peak. However the observation of vibronic structure by Sheps[5] led to the conclusion that the difference between spectra reported by Beames *et al*.[4] could have arisen from excitation to long-lived $\tilde{B}^1A'$ vibrational states, as a sufficiently long-lived upper or excited state would be able to support vibrational and rotational structure, which arise upon simultaneous changes in vibrational and electronic energy states in a molecule, known as vibronic coupling. Such vibronic transitions can also be accompanied by changes in rotational energy in the gas phase, as described in Chapter 2.

On the contrary, for a repulsive or unbound state with no minimum in the potential energy there would be no discrete vibrational energy levels, rather a continuum of levels would be formed instead, as is formed at energies above the dissociation limit for a bound state. If the potential curve of a repulsive state crosses that of a bound state, a phenomenon known as predissociation occurs, where excitation to particular vibrational levels in the bound state allows the electrons in the molecule to rearrange and cross onto the unbound repulsive state (internal conversion) to dissociate without supplying sufficient energy for dissociation on the bound state. Such a state is easily identifiable in electronic absorption spectroscopy as it often appears as a strong continuous feature in the spectrum in the spectral range corresponding to the energies at which this crossing takes place, above and below which discrete line structure is observed.

Since vibronic transitions were not observed in experiments by Beames *et al*.,[4] it was determined by Sheps[5] that their photodissociation quantum yield must have been < 1, meaning the bound states relax to lower electronic states by fluorescence or non-radiative processes such as intersystem crossing rather than by photodissociation. If the quantum yield for photodissociation of CH_2OO is unity at all UV wavelengths

measured, the action spectrum reported by Beames *et al*.[4] would have the same shape and absolute cross-sections as the absorption spectrum, whereas quantum yields of < 1 for dissociation would lead to different shapes and magnitudes of the action and absorption spectra. It should be noted that given the resolution of the experiments conducted by Beames *et al*.[4] it is highly unlikely that vibronic transitions would have been evident in the measurements since the band centres of the vibronic features in the spectrum are separated by approximately 10 nm.

It was stated by Ting *et al*.[6] that there is discrepancy in the argument used by Sheps[5] as there is no theoretical evidence for the non-radiative process, and photodissociation is actually faster than rotation, which is on the picosecond timescale, as indicated by the measurement of the photoproduct anisotropy,[9] hence the slower fluorescence process cannot compete with rapid dissociation. The complete depletion of CH_2OO observed in the molecular beam experiments carried out by Ting *et al*.[6] indicated a dissociation quantum yield of unity at both 308.4 and 351.8 nm, hence the photodissociation cross-section obtained at these wavelengths is equal to the absorption cross-section.

Differences between their results and the results of Beames *et al*.[4] were rationalised by Ting *et al*.[6] by arguing that Beames *et al*.[4] only estimated laser fluence from their dye laser pulse energy and spot size. Since the spot size of a dye laser is prone to being non-uniform, it is difficult to quantify the actual laser fluence without a laser beam profiler, leading to a possible underestimation in laser fluence and thus an overestimation in CH_2OO photodissociation cross-sections. For this reason, Ting *et al*.[6] concluded that as a reference molecule (Cl_2) was used in their work to effectively calibrate the laser fluence and cancel the effect of a non-uniform laser spot, their results should be more accurate. It has also been postulated by Ting *et al*.[6] that temperature effects, as in the case of the Huggins or Hartley bands of O_3 where smaller cross-sections are obtained at lower temperatures, may give rise to varying spectral shapes and hence cross-sections of CH_2OO, possibly explaining why a weaker spectrum is observed by Beames *et al*.[4] at $\lambda > 360$ nm, for which $T = \sim 10$ K, than in the other observed spectra, which were recorded at $T = 298$ K. The much faster decay on the short-wavelength side of the experimental spectrum observed by Sheps,[5] as well as the higher reported peak position and absolute absorption cross-section than

that of Ting *et al.*[6] was attributed to the complexity of the cavity-enhanced measurements.

The observed lack of temperature dependence in the range 276-357 K in the absorption cross-sections observed by Foreman *et al.*[7] indicated that the vibrational structure was not due to hot bands, but rather the excitation to bound levels of the $\tilde{B}^1A'$ state. While the peak progression was found to be dominated by a component with a wavenumber of ~610 cm^{-1} (wavelengths of 7.5-11.5 nm), it was concluded that the variation in the band contours was strongly suggestive of other modes leading to significant vibrational congestion in the spectrum, as suggested originally by Sheps,[5] who claimed that excitation to relatively long-lived $\tilde{B}^1A'$ vibrational states was responsible for the structure in the spectrum. It was further stated by Foreman *et al.*[7] that the argument used by Ting *et al.*[6] against the existence of long-lived states on the basis that angular anisotropy of $O(^1D)$ photofragments indicates sub-picosecond excited state lifetimes neglects the fact that the longest photolysis wavelength used in the ion imaging study was 360 nm,[9] which is the short wavelength onset of the structured region of the CH_2OO spectrum. Dissociation photoproducts have not been detected following excitation in the structured region of the CH_2OO spectrum at wavelengths larger than 360 nm.

It was expected by Foreman *et al.*[7] that the lower lying bound levels of CH_2OO would have a slower dissociation rate than the repulsive excited $\tilde{B}^1A'$ state which may lead to resolvable rotational fine structure in the absorption spectrum superimposed on the vibrational coarse structure, however none was observed. Broad widths of the individual vibrational bands coupled with the absence of vibrational peak progression in the VUV depletion measurements by Beames *et al.*,[4] indicating a photodissociation quantum yield in this region of < 1, led to the conclusion that the rapid excited state dynamics evidenced by broad bandwidths must be attributed to non-dissociative population transfer.

While the results determined in this work are in agreement with those reported by Ting *et al.* and Foreman *et al.*, discrepancy remains when compared to results reported by Beames *et al.* and Sheps. The complexity of cavity-enhanced measurements, with mirrors having differing reflectivities at different wavelengths, and the errors associated with a wavelength dependent path length, may explain the larger absolute

absorption cross-sections and quicker fall off on the short-wavelength side of the CH_2OO spectrum observed by Sheps[5] than that observed in this work, while the CH_2OO action spectrum recorded under jet cooled conditions by Beames *et al*.[4] may be subject to temperature effects.

4.6 Atmospheric Photolysis Rate

Since the UV absorption cross-sections of CH_2OO have been measured beyond 280 nm where solar flux also increases sharply, this means that CH_2OO UV absorption overlaps with the UV radiation penetrating the upper atmosphere to reach the troposphere, which can potentially result in daytime photolysis of this Criegee intermediate. Atmospheric excitation of CH_2OO from the ground $\tilde{X}^1A'$ state *via* absorption of a photon upon irradiation from solar light may result in photolysis of the molecule *via* the dissociative excited $\tilde{B}^1A'$ vibrational state. It is important to quantify the potential rate of solar photolysis of CH_2OO in the atmosphere as it could be a significant atmospheric sink of CH_2OO. A solar photolysis lifetime of ~1 s at midday was calculated by Beames *et al*.[4] for CH_2OO from which it was concluded that photochemical loss may be a significant decay path for CH_2OO under daytime conditions in the troposphere. In light of the more recent measurements of the absorption cross-sections for CH_2OO[5, 6] in which significantly smaller cross-sections are reported, this value of solar photolysis lifetime needs recalculating in order to obtain an accurate result.

Since absorption of solar radiation by molecules provides the energy required to break bonds and hence form radicals, this can also initiate oxidation of both biogenic (natural e.g. from plants) and anthropogenic (human made e.g. from vehicle exhausts) emissions in the Earth's atmosphere. Using the absolute absorption cross-sections for CH_2OO determined in this work, the photochemical loss rate of CH_2OO *via* solar irradiation, J_{CH2OO}, can be estimated:

$$J_{CH2OO} = \int_{\lambda=0}^{\lambda=\infty} \Phi_{CH2OO,\lambda}\ \sigma_{CH2OO,\lambda}\ F_\lambda\ d\lambda \qquad \text{(Equation 4.18)}$$

where $\Phi_{CH2OO,\lambda}$ is the photodissociation quantum yield of CH_2OO at wavelength λ, and is assumed to be unity at all wavelengths, $\sigma_{CH2OO,\lambda}$ is the absolute CH_2OO

absorption cross-section at wavelength λ, and F_λ is the solar actinic flux for a 0° zenith angle at the Earth's surface.

The tropospheric ultraviolet and visible (TUV) radiation model[27] calculates the diurnal variation in atmospheric photolysis rates of species which absorb in the actinic window based on absorption cross-sections, quantum yields, solar actinic flux and wavelength at a given latitude, longitude, altitude, date and time. Solar actinic flux varies across the Earth's atmosphere and as a function of wavelength, and is described in detail in Chapter 1. This variation in actinic flux at a certain point in the Earth's troposphere, i.e. as a function of longitude, latitude and altitude, across the wavelength region in the actinic window, is coded into the model with consideration towards atmospheric inputs such as the vertical profiles of N_2, O_2, O_3, SO_2, clouds and aerosols, all of which attenuate electromagnetic radiation at given wavelengths of light *via* absorption and/or scattering.

The annual mean photolysis rate, J_{CH2OO}, at the Earth's surface (ground level) under clear sky conditions was calculated using the TUV radiation model as a function of latitude and longitude using absorption cross-sections reported in this work, and is shown in Figure 4.22.

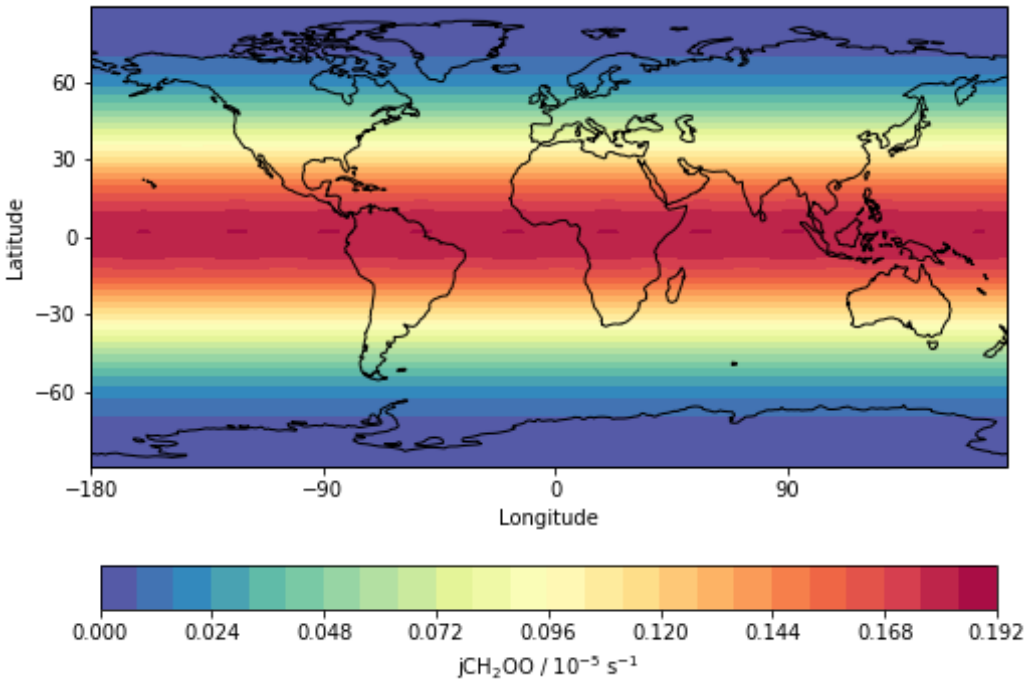

Figure 4.22: Annual mean photolysis rate, J_{CH2OO}, at the Earth's surface calculated using the TUV radiation model with CH_2OO UV absorption cross-sections observed in this work.

The value determined for J_{CH2OO} using this method at 0° longitude and 0° longitude is 1.9×10^{-6} s^{-1}, as shown in Figure 4.22, which, when converted to the corresponding solar photolysis lifetime using the relationship $\tau = (J_{CH2OO})^{-1}$ s, gives a value of 5.3×10^5 s (~147 hours or ~6 days). This result is significantly different to the solar photolysis lifetime calculated by Beames *et al.*[4] of ~1 s at midday, and indicates that photochemical loss of CH_2OO does not play a significant role in the overall atmospheric lifetime of this Criegee intermediate during the daytime. For comparison with photolysis rates of other important atmospheric molecules which absorb in the actinic window, the photolysis rate of O_3 with respect to $O(^1D)$ formation is typically one order of magnitude higher (1×10^{-5} s^{-1} giving a photolysis lifetime of ~1 day)[28] and that of NO_2 with respect to NO and $O(^3P)$ formation is typically two to three orders of magnitude higher (on the order of 1×10^{-4} s^{-1} to 1×10^{-3} s^{-1} giving a photolysis lifetime between ~3 hours and ~15 minutes).

The global photolysis rate of CH_2OO was also calculated using absorption cross-sections observed by Beames *et al.*,[4] Sheps[5] and Ting *et al.*[6] using the TUV radiation model, and the ratios of the annual mean J_{CH2OO} at the Earth's surface for each of these studies relative to the absorption cross-sections reported in this work are shown in Figure 4.23.

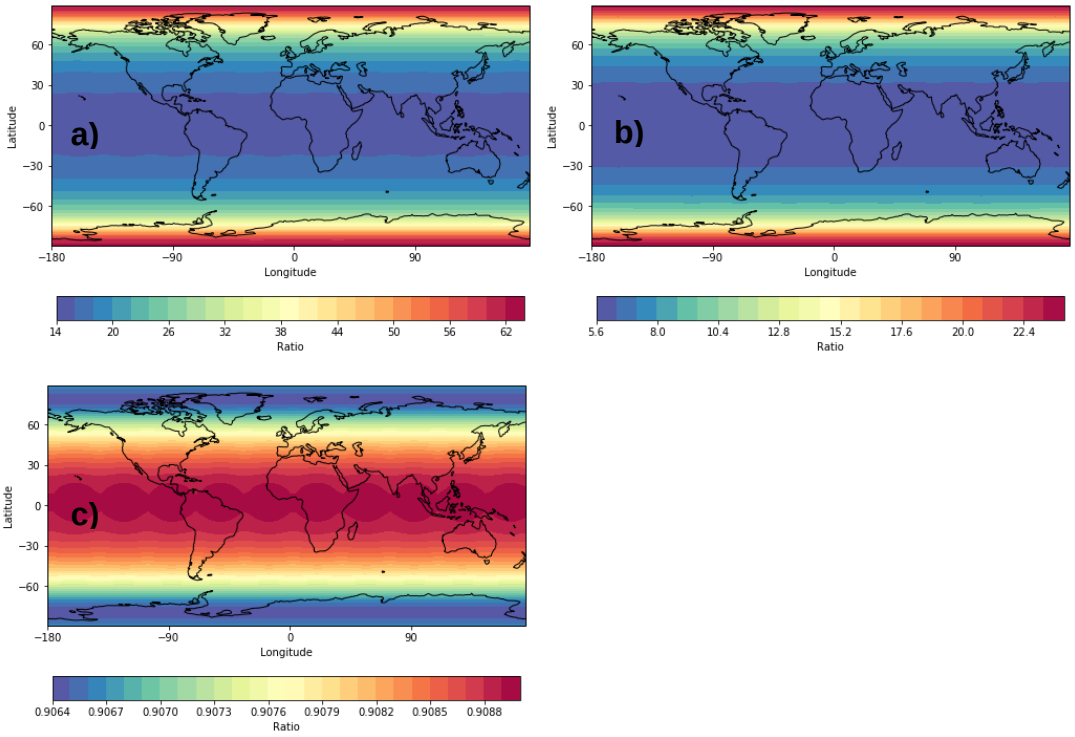

Figure 4.23: Ratios for the annual mean photolysis rate, J_{CH2OO}, at the Earth's surface calculated using the TUV radiation model with CH_2OO UV absorption cross-sections observed in the work of a) Beames *et al.*,[4] b) Sheps[5] and c) Ting *et al.*[6] relative to the CH_2OO absorption cross-sections reported in this work i.e. CH_2OO absorption cross-sections reported by Beames *et al.*, Sheps and Ting *et al.* / CH_2OO absorption cross-sections reported in this work respectively. Note that the scales vary in each plot.

It can be seen from Figure 4.23 that the ratios of the CH_2OO photolysis rate calculated using CH_2OO absorption cross-sections reported by Beames *et al.*,[4] Sheps[5] and Ting *et al.*[6] relative to the absorption cross-sections reported in this work at 0° longitude and 0° longitude are 14, 5.6 and 0.9 respectively, which equates to absolute photolysis rates of 2.7×10^{-5} s^{-1}, 1.1×10^{-5} s^{-1} and 1.7×10^{-6} s^{-1} respectively. These results indicate good agreement between the photolysis rate calculated using the CH_2OO absorption spectrum observed in this work of 1.9×10^{-6} s^{-1} and that calculated using the CH_2OO absorption spectrum observed in the work of Ting *et al.*[6] of 1.7×10^{-6} s^{-1}, which are both significantly slower (one order of magnitude) than the photolysis rates calculated according to the CH_2OO absorption spectra observed by both Beames *et al.*[4] and Sheps.[5]

It should be noted that the photolysis rate calculated here using CH_2OO absorption cross-sections reported by Beames *et al*.[4] equates to a solar photolysis lifetime of 3.7 × 10^4 s (~10 hours), which is significantly different to the CH_2OO solar photolysis lifetime calculated by Beames *et al*.[4] of ~1 s at midday. This value reported by Beames *et al*.[4] should be regarded with uncertainty since it is not known exactly how this value was calculated and it is difficult to reconcile this result with the details of the calculation provided. For comparison, using the same TUV radiation model[27] used here to calculate the photolysis rate of CH_2OO, the photolysis rates of other atmospheric species was calculated at the same longitude and latitude. The photolysis rates calculated were, for O_3 to make O_2 and $O(^1D)$, 3.9 × 10^{-5} s^{-1}, for NO_2 to make NO and $O(^3P)$, 1.0 × 10^{-2} s^{-1}, and for IO (which exhibits an absorption spectrum in a similar wavelength region to CH_2OO but further into visible range and has absorption cross-section values on the order of 10^{-17} cm^2 like CH_2OO) to make I and O atoms, 1.2 × 10^{-1} s^{-1}, which equate to solar photolysis lifetimes of 2.6 × 10^4 s (~7 hours), 100 s and 8 s for O_3, NO_2 and IO respectively.

Oxidation reactions of CH_2OO with key atmospheric species, such as $(H_2O)_2$, SO_2, NO_2 and carboxylic acids, have been found to be atmospherically significant in terms of both reaction kinetics and products, however the reaction with water dimer is considered to be the dominant chemical sink of stabilised Criegee intermediates in the troposphere due to its relative abundance. Typical atmospheric concentrations of $(H_2O)_2$, SO_2, NO_2 and carboxylic acids are at ≥ 36 % relative humidity (H_R), 50 ppb, 50 ppb and 5 ppb respectively, which, when multiplied by the second-order rate coefficients of their reactions with CH_2OO, give estimations of effective pseudo- first-order rate coefficients of ≥ 1000 s^{-1}, 50 s^{-1}, 9 s^{-1} and 12 s^{-1} respectively.[29] Comparing these rate coefficients to that calculated for the photolysis rate of CH_2OO using CH_2OO absorption cross-sections reported in this work of 1.9 × 10^{-6} s^{-1} signifies that the fractional atmospheric loss of CH_2OO through photolysis is negligible when compared to losses through these bimolecular reaction channels, thus solar photolysis is not an important loss mechanism for CH_2OO in the atmosphere.

4.7 Conclusions

The UV absorption cross-sections of the Criegee intermediate CH_2OO have been investigated at a temperature of 298 K and pressures between 6 and 300 Torr using pulsed laser flash photolysis of $CH_2I_2/O_2/N_2$ gas mixtures coupled with time-resolved broadband UV absorption spectroscopy.[20] Results indicate a broad UV absorption spectrum for CH_2OO, with a peak absorption cross-section of $(1.37 \pm 0.29) \times 10^{-17}$ cm^2 at λ ~340 nm showing no significant pressure dependence, and vibronic structure at wavelengths greater than the maximum of the spectrum, in good agreement with results by Ting *et al.*[6] and Foreman *et al.*[7] Eight resolvable vibronic bands have been observed, the positions and shapes of which are in good agreement with the work of Ting *et al.*[6] and Foreman *et al.*,[7] with results from this work exhibiting an increased signal-to-noise ratio than those of Ting *et al.*[6] and Foreman *et al.*,[7] suggesting increased data quality for the determination of absolute CH_2OO UV absorption cross-sections. The photolysis rate of CH_2OO was calculated to be $J_{CH2OO} = 1.9 \times 10^{-6}$ s^{-1} using the tropospheric ultraviolet and visible (TUV) radiation model[27] and UV absorption cross-sections for CH_2OO reported in this work, which, in contrast to the findings of Beames *et al.*,[4] indicates solar photolysis to be an insignificant atmospheric sink for CH_2OO.

The most fundamental aspect of investigating reactive Criegee intermediate chemistry is to have direct and definitive identification of the Criegee, enabling it to be detected and monitored throughout a reaction. The high reactivity of Criegee intermediates inevitably leads to relatively short lifetimes, making measurements *via* direct detection challenging as it necessitates *in situ* preparation of the Criegee intermediate with rapid and sensitive monitoring. Since the UV absorption cross-sections of Criegee intermediates have been shown to be relatively large, this method of detection is ideal for measuring the kinetics of Criegee intermediate reactions, including those which are important under atmospheric conditions. However, in order to take advantage of this property of Criegee intermediates and determine accurate reaction kinetics, accurate absorption cross-sections are first required. Results presented here for the UV absorption cross-sections of the simplest Criegee intermediate, CH_2OO, will thus be useful for future studies of CH_2OO reaction kinetics employing UV absorption spectroscopy as the detection method.

4.8 References

1. Heard, D. E.; Carpenter, L. J.; Creasey, D. J.; Hopkins, J. R.; Lee, J. D.; Lewis, A. C.; Pilling, M. J.; Seakins, P. W.; Carslaw, N.; Emmerson, K. M., High levels of the hydroxyl radical in the winter urban troposphere. *Geophysical Research Letters* **2004,** *31* (18), L18112.

2. Harrison, R. M.; J.Yin; Tilling, R. M.; Cai, X.; Seakins, P. W.; Hopkins, J. R.; Lansley, D. L.; Lewis, A. C.; Hunter, M. C.; Heard, D. E.; Carpenter, L. J.; Creasey, D. J.; Lee, J. D.; Pilling, M. J.; Carslaw, N.; Emmerson, K. M.; Redington, A.; Derwent, R. G.; Ryall, D.; Mills, G.; Penkett, S. A., Measurement and modelling of air pollution and atmospheric chemistry in the U.K. West Midlands conurbation: Overview of the PUMA Consortium project. *Science of the Total Environment* **2006,** *360* (1-3), 2-25.

3. Welz, O.; Savee, J. D.; Osborn, D. L.; Vasu, S. S.; Percival, C. J.; Shallcross, D. E.; Taatjes, C. A., Direct kinetic measurements of Criegee intermediate (CH_2OO) formed by reaction of CH_2I with O_2. *Science* **2012,** *335* (6065), 204-207.

4. Beames, J. M.; Liu, F.; Lu, L.; Lester, M. I., Ultraviolet spectrum and photochemistry of the simplest Criegee intermediate CH_2OO. *Journal of the American Chemical Society* **2012,** *134* (49), 20045-20048.

5. Sheps, L., Absolute ultraviolet absorption spectrum of a Criegee intermediate CH_2OO. *The Journal of Physical Chemistry Letters* **2013,** *4* (24), 4201-4205.

6. Ting, W.-L.; Chen, Y.-H.; Chao, W.; Smith, M. C.; Lin, J. J.-M., The UV absorption spectrum of the simplest Criegee intermediate CH_2OO. *Physical Chemistry Chemical Physics* **2014,** *16* (22), 10438-10443

7. Foreman, E. S.; Kapnas, K. M.; Jou, Y.; Kalinowski, J.; Feng, D.; Gerber, R. B.; Murray, C., High resolution absolute absorption cross sections of the B^1A'–X^1A' transition of the CH_2OO biradical. *Physical Chemistry Chemical Physics* **2015,** *17* (48), 32539-32546.

8. Beames, J. M.; Liu, F.; Lu, L.; Lester, M. I., UV spectroscopic characterization of an alkyl substituted Criegee intermediate CH_3CHOO. *The Journal of Chemical Physics* **2013,** *138* (24), 244307.

9. Lehman, J. H.; Li, H.; Beames, J. M.; Lester, M. I., Communication: Ultraviolet photodissociation dynamics of the simplest Criegee intermediate CH_2OO. *Journal of Chemical Physics* **2013,** *139* (14), 141103.

10. Lee, E. P. F.; Mok, D. K. W.; Shallcross, D. E.; Percival, C. J.; Osborn, D. L.; Taatjes, C. A.; Dyke, J. M., Spectroscopy of the simplest Criegee intermediate CH_2OO: Simulation of the first bands in its electronic and photoelectron spectra. *Chemistry - A European Journal* **2012,** *18* (39), 12411-12423.

11. Huang, H.; Eskola, A. J.; Taatjes, C. A., Pressure-dependent I-atom yield in the reaction of CH_2I with O_2 shows a remarkable apparent third-body efficiency for O_2. *The Journal of Physical Chemistry Letters* **2012,** *3* (22), 3399-3403.

12. Huang, H.; Rotavera, B.; Eskola, A. J.; Taatjes, C. A., Correction to "Pressure-dependent I atom yield in the reaction of CH_2I with O_2 shows a remarkable apparent third-body efficiency for O_2". *The Journal of Physical Chemistry Letters* **2013,** *4* (22), 3824.

13. Stone, D.; Blitz, M.; Daubney, L.; Ingham, T.; Seakins, P., CH_2OO Criegee biradical yields following photolysis of CH_2I_2 in O_2. *Physical Chemistry Chemical Physics* **2013,** *15* (44), 19119-19124

14. Samanta, K.; Beames, J. M.; Lester, M. I.; Subotnik, J. E., Quantum dynamical investigation of the simplest Criegee intermediate CH_2OO and its O–O photodissociation channels. *The Journal of Chemical Physics* **2014,** *141* (13), 134303.

15. Meng, Q.; Meyer, H.-D., A full-dimensional multilayer multiconfiguration time-dependent Hartree study on the ultraviolet absorption spectrum of formaldehyde oxide. *The Journal of Chemical Physics* **2014,** *141* (12), 124309.

16. Dawes, R.; Jiang, B.; Guo, H., UV absorption spectrum and photodissociation channels of the simplest Criegee intermediate (CH_2OO). *Journal of the American Chemical Society* **2015,** *137* (1), 50-53.

17. Sršeň, Š.; Hollas, D.; Slavíček, P., UV absorption of Criegee intermediates: quantitative cross sections from high-level *ab initio* theory. *Physical Chemistry Chemical Physics* **2018,** *20* (9), 6421-6430.

18. Gravestock, T. J.; Blitz, M. A.; Bloss, W. J.; Heard, D. E., A multidimensional study of the reaction $CH_2I + O_2$: products and atmospheric implications. *ChemPhysChem* **2010,** *11* (18), 3928-3941.

19. Lewis, T. R.; Blitz, M. A.; Heard, D. E.; Seakins, P. W., Direct evidence for a substantive reaction between the Criegee intermediate, CH_2OO, and the water vapour dimer. *Physical Chemistry Chemical Physics* **2015,** *17* (7), 4859-4863.

20. Lewis, T.; Heard, D. E.; Blitz, M. A., A novel multiplex absorption spectrometer for time-resolved studies. *Review of Scientific Instruments* **2018,** *89* (2), 024101.

21. Keller-Rudek, H.; Moortgat, G. K.; Sander, R.; Sörensen, R., The MPI-Mainz UV/VIS spectral atlas of gaseous molecules of atmospheric interest. *Earth System Science Data* **2013,** *5*, 365–373.

22. Sander, S. P.; Abbatt, J. P. D.; Barker, J. R.; Burkholder, J. B.; Friedl, R. R.; Golden, D. M.; Huie, R. E.; Kolb, C. E.; Kurylo, M. J.; Moortgat, G. K.; Orkin, V. L.; Wine, P. H., Chemical kinetics and photochemical data for use in atmospheric studies - Evaluation number 17. In *JPL Publication 10-6*, Jet Propulsion Laboratory: Pasadena, California, 2011.

23. Harwood, M. H.; Burkholder, J. B.; Hunter, M.; Fox, R. W.; Ravishankara, A. R., Absorption cross sections and self-reaction kinetics of the IO radical. *The Journal of Physical Chemistry A* **1997,** *101* (5), 853-863.

24. Yaws, C. L., *Chemical properties handbook: Physical, thermodynamic, environmental, transport, safety, and health related properties for organic and inorganic chemicals*. McGraw--Hill: New York, 1999.

25. Chhantyal-Pun, R.; Davey, A.; Shallcross, D. E.; Percival, C. J.; Orr-Ewing, A. J., A kinetic study of the CH_2OO Criegee intermediate self-reaction, reaction with SO_2 and unimolecular reaction using cavity ring-down spectroscopy. *Physical Chemistry Chemical Physics* **2015,** *17* (5), 3617-3626.

26. Espenson, J. H., *Chemical kinetics and reaction mechanisms*. The McGraw-Hill Companies, Inc: USA, 1995.

27. Tropospheric ultraviolet and visible (TUV) radiation model. https://www2.acom.ucar.edu/modeling/tropospheric-ultraviolet-and-visible-tuv-radiation-model (accessed 21st September).

28. King, M. *Calculating photolysis rates and estimating photolysis lifetimes (ECG Environmental Brief No 1)*; 2013.

29. Chao, W.; Hsieh, J.-T.; Chang, C.-H.; Lin, J. J.-M., Direct kinetic measurement of the reaction of the simplest Criegee intermediate with water vapor. *Science* **2015,** *347* (6223), 751-754.

Chapter 5

CH_2OO Self-Reaction Kinetics

Experiments have shown a rapid CH_2OO + CH_2OO self-reaction,[1-4] the kinetics of which can be closely coupled to the measurement of the absorption cross-sections, including those in the UV (Chapter 4) and IR (Chapter 6) regions, since significant changes in concentration can occur on the timescale of the absorption measurements. However, there are notable discrepancies in previous measurements of CH_2OO self-reaction kinetics, with rate coefficients reported differing by almost one order of magnitude,[1-4] as is shown in Figure 5.1.

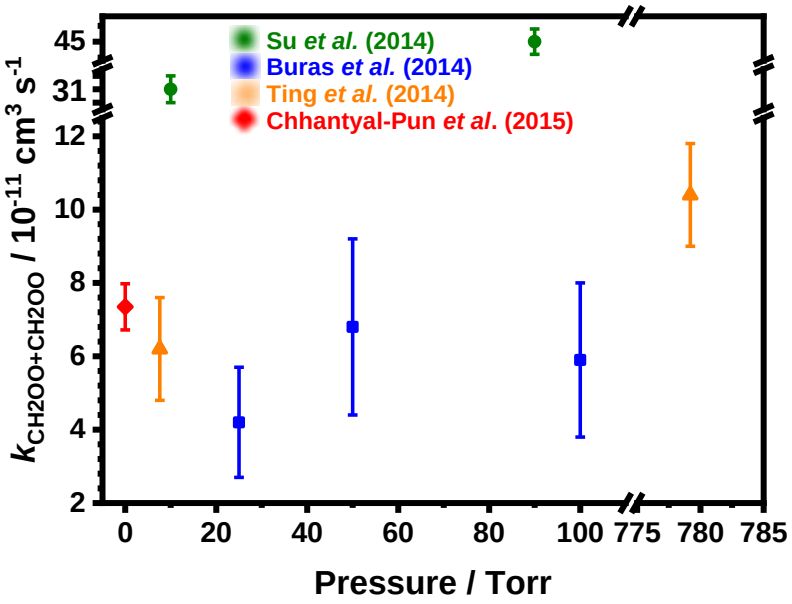

Figure 5.1: Comparison of directly measured rate coefficients for the CH2OO self-reaction, CH2OO + CH2OO, in previous work.

In the atmosphere, the steady state concentration of Criegee intermediates produced from atmospheric ozonolysis of alkenes is relatively small, with estimated atmospheric concentrations reported to be on the order of 10^2 to 10^5 cm^{-3}.[5-13] Under these typical atmospheric conditions, this rapid CH_2OO self-reaction is not likely to play a significant role as it is unlikely to compete with processes of trace reactive species at higher atmospheric concentrations. However, it can potentially impact

determination of kinetic parameters for all experiments carried out under laboratory conditions, where the concentration of Criegee intermediates is relatively high, owing to the photolytic production method of Criegees first proposed by Welz *et al*.[14] in 2012, whereby a diidoalkane precursor is photolysed in excess oxygen. Under these conditions, potential impacts of the CH_2OO self-reaction must be taken into account. CH_2OO self-reaction kinetics are important for further studies of CH_2OO chemistry and the determination of other CH_2OO reaction kinetics, including those which are of atmospheric relevance such as the reactions with $(H_2O)_2$,[15-18] SO_2[4, 14, 19-26] and organic acids,[27, 28] among others. The reaction between CH_2OO and I is also potentially important in laboratory experiments using CH_2I_2 photolysis to generate CH_2OO.

5.1 Theoretical Studies of CH_2OO + CH_2OO and CH_2OO + I

Prior to the availability and introduction of a method allowing direct measurements of experimentally determined rate coefficients for the kinetics of the CH_2OO self-reaction, theoretical analysis played an important role in the understanding of Criegee intermediates and their chemistry. Vereecken *et al*.[29] used a combination of quantum chemical calculations with theoretical kinetic methodologies, at the spin-restricted open-shell coupled-cluster singles, doubles (triples) with a meta hybrid functional (ROCCSD(T)//M06-2X) level of theory, to predict the potential energy surfaces (PES), reaction mechanisms and kinetics of reactions between CH_2OO and various co-reactants, including itself. The CH_2OO self-reaction was found to be barrierless with a rate coefficient of approximately 4×10^{-11} cm^3 s^{-1} at room temperature, with an estimated uncertainty of a factor of 5 and constant within 20 % over the temperature range 250-350 K. This fast CH_2OO self-reaction nearing the collision limit was reported to be driven by the zwitterionic character of the Criegee intermediates, however, it was concluded that the low atmospheric concentration of Criegee intermediates limits the impact of their self-reactions to experimental conditions where the concentration is much higher.

The CH_2OO self-reaction energy profile of the simultaneous double head-to-tail cycloaddition to form two new C-O bonds in a six-membered cyclic biperoxide was found to be purely attractive with no evidence of a pre-reactive complex, well-defined

transition state or energy barrier, and the reaction was reported to be highly exothermic, ~ -420.5 kJ mol^{-1},[29] as shown in Figure 5.2. Subsequent chemistry was found to involve chemically activated breakage of the weaker O-O bonds forming a singlet peroxide bisalkoxy radical, OCH_2OOCH_2O, the dominant reaction channel of which was expected to be elimination of HCHO forming singlet $OOCH_2O$, which in turn dissociates to HCHO + $O_2(^1\Delta)$, with an overall exothermicity of -310.0 kJ mol^{-1}. Several higher energy pathways were also found to be accessible in chemically activated reactions leading to the formation of acids, peroxy acids and carbonyl compounds.

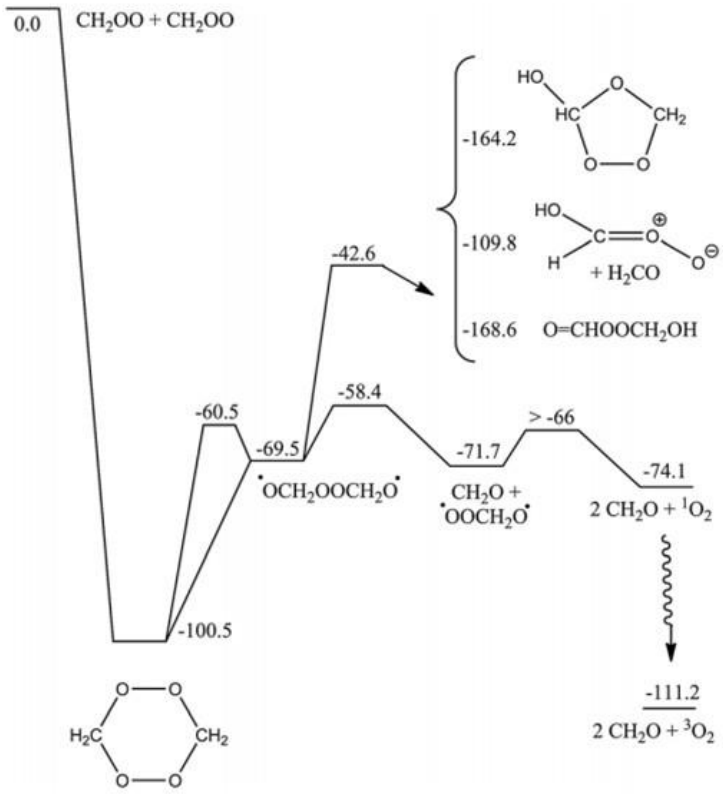

Figure 5.2: Zero-point energy (ZPE) corrected potential energy surface (PES) of the CH_2OO + CH_2OO head-to-tail cycloaddition reaction and subsequent chemistry, in units of kcal mol^{-1}, at the M06-2X level of theory, calculated by Vereecken *et al.*[29]

Alongside the first experimental measurements of the CH_2OO self-reaction, Su *et al.*[1] performed high-level theoretical calculations, using the coupled-cluster singles, doubles (triples) method with the Becke 3-parameter, Lee-Yang-Parr hybrid functional and an augmented version of the correlation-consistent polarised valence

only triple-zeta pseudopotential basis set (CCSD(T)//B3LYP/aug-cc-pVTZ-pp) to investigate the energies of possible reaction channels in the system, including the CH_2OO self-reaction and the reaction between CH_2OO and I. Similar to Vereecken *et al.*,[29] the PES calculated by Su *et al.*,[1] shown in Figure 5.3, demonstrated the dominant channel (minimal energy path) of the formation of a $(CH_2OO)_2$ cyclic dimer to have no barrier and a large exothermicity, calculated to be -386.6 kJ mol^{-1}, before further decomposition to products (2 HCHO + O_2 ($^1\Delta_g$) (electronically excited)). The rapid CH_2OO self-reaction was reported to be a result of this barrierless entrance channel, the large exothermicity for the formation of a cyclic dimeric intermediate due to the strong head-to-tail zwitterionic interaction, and the small barrier to decomposition of the dimer via a transition state. However, Su *et al.*[1] predicted a much faster rate coefficient for the CH_2OO self-reaction of 2.2×10^{-10} cm^3 s^{-1} at 343 K independent of pressure in the range 20-100 Torr, and a value of 2.4×10^{-10} cm^3 s^{-1} at 298 K.

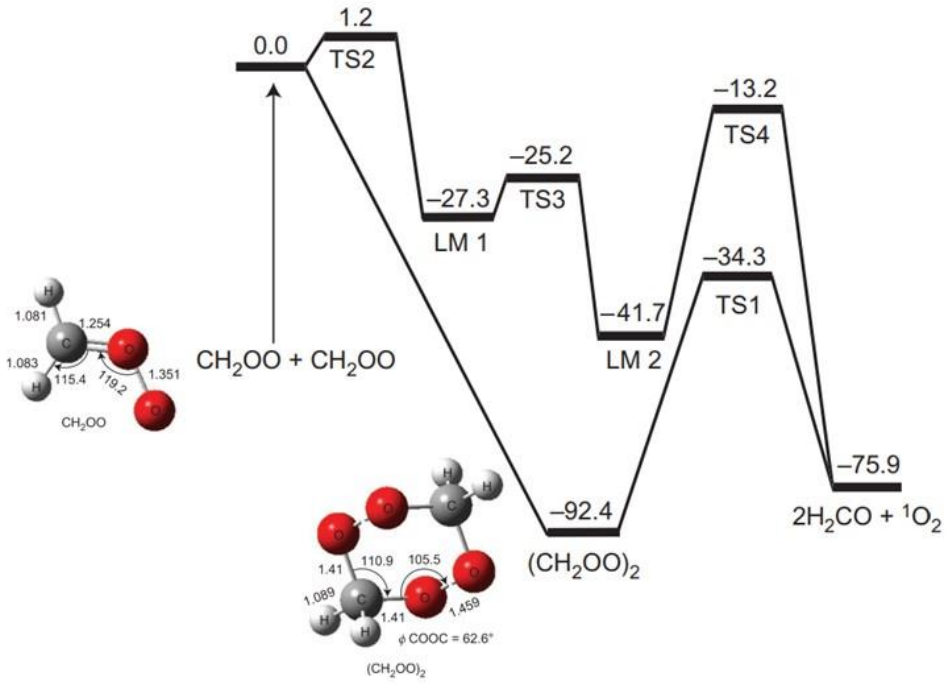

Figure 5.3: Potential energy surface (PES) for the CH_2OO + CH_2OO reaction, with pathways computed by Su *et al.*[1] at the CCSD(T)//B3LYP/aug-cc-pVTZ-pp level with corrections for vibrational zero-point energy (ZPE). Relative energies at 0 K are given in units of kcal mol^{-1} with transition states and reaction intermediates labelled TS and LM respectively. The reaction proceeds via $(CH_2OO)_2$ and TS1 whereas the path via TS2 is unimportant due to the higher barrier involved. Computed optimised geometries for CH_2OO and $(CH_2OO)_2$ are shown (lengths are in Ångströms (Å), angles are in degrees (°) and ϕ is the dihedral angle).

Calculations carried out by Su *et al.*[1] investigating the reaction of CH_2OO + I were shown to have three product channels, with the formation of CH_2I + O_2 via decomposition of internally excited CH_2IO_2 reported as the dominant product channel at both 298 K and 343 K with a rate coefficient of (8.1-7.6) × 10^{-11} cm^3 s^{-1} and (9.3-8.9) × 10^{-11} cm^3 s^{-1} respectively over the pressure range 20-100 Torr, despite the lowest energy pathways of the PES leading to formation of CH_2IO_2 and HCHO + IO, as shown in Figure 5.4. The computed pathways showed formation of CH_2IO_2 to be either by direct attack of the I atom at the C atom of CH_2OO with no barrier or via an intermediate with the I atom attached to the terminal O atom followed by rearrangement to CH_2IO_2 via a transition state, and formation of HCHO + IO to proceed from decomposition of the same intermediate with the I atom attached to the terminal O atom via a different transition state followed by abstraction of the terminal O atom of CH_2OO by the I atom.

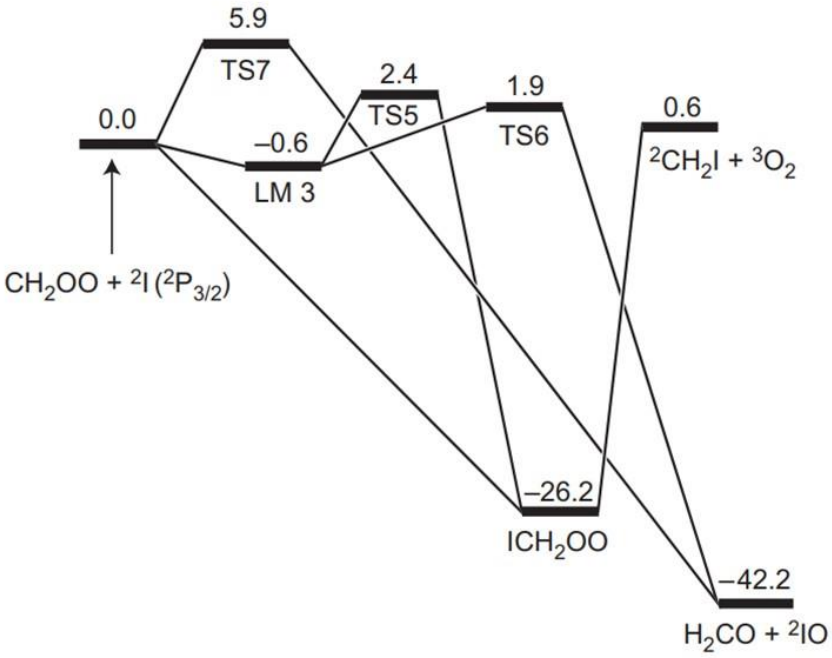

Figure 5.4: Potential energy surface (PES) for the CH_2OO + I reaction, with pathways computed by Su *et al.*[1] at the CCSD(T)//B3LYP/aug-cc-pVTZ-pp level with corrections for vibrational zero-point energy (ZPE). Relative energies at 0 K are given in units of kcal mol^{-1} with transition states and reaction intermediates labelled TS and LM respectively.

5.2 Experimental Studies of CH_2OO Self-Reaction and CH_2OO + I Kinetics

Self-reaction kinetics of CH_2OO were first reported by Su *et al.*[1] using flash photolysis of $CH_2I_2/O_2/N_2$ at λ = 355 nm with step-scan Fourier-transform infrared spectroscopy to monitor CH_2OO, generated in a multipass White cell, throughout the reaction. Observed decays of CH_2OO were analysed considering potential loss of CH_2OO through reaction with I atoms and CH_2I radicals as well as loss through the CH_2OO self-reaction, with results indicating a CH_2OO self-reaction rate coefficient of $(4 \pm 2) \times 10^{-10}$ cm^3 s^{-1} at 343 K at total pressures between 20 and 100 Torr, as shown in Figure 5.5. Such a rapid self-reaction was attributed to the zwitterionic nature of CH_2OO, but theory by Vereecken *et al.*[29] (details of which are provided above) predicted a significantly lower rate coefficient of ~4×10^{-11} cm^3 s^{-1} over the temperature range 250-350 K.

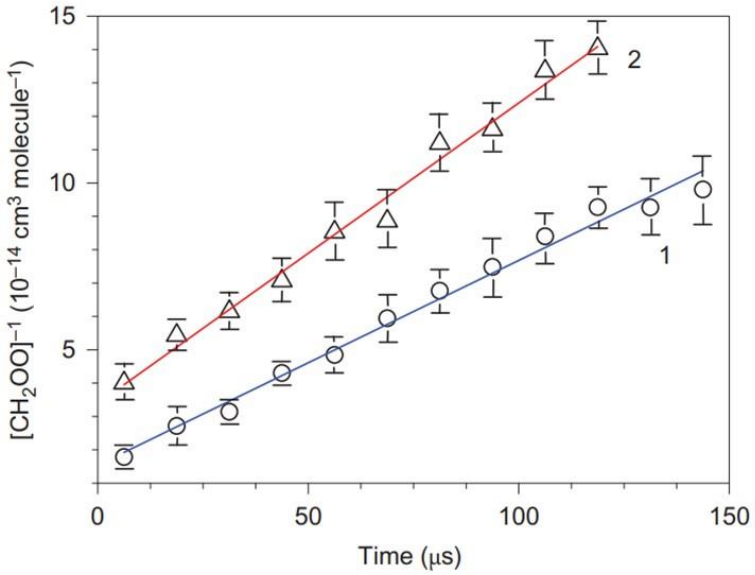

Figure 5.5: Two representative plots of the inverse of the CH_2OO concentration, $[CH_2OO]^{-1}$, versus reaction time, *t*, measured by Su *et al.*,[1] with data shown as circles and triangles representing experiments carried out under different conditions, the fitted rate coefficients shown as solid lines, and error bars reflecting only one standard deviation in the fitting. Experiments were recorded at 343 K, and for traces labelled '1' and '2', 10 Torr and 90 Torr respectively. Both plots exhibit a linear relationship between $[CH_2OO]^{-1}$ and *t*, which indicates second-order behaviour, for which results of the effective second-order rate coefficients for traces labelled '1' and '2' were $(3.1 \pm 0.1) \times 10^{-10}$ cm^3 s^{-1} (blue) and $(4.5 \pm 0.2) \times 10^{-10}$ cm^3 s^{-1} (red) respectively, approaching the gas kinetic collision value.

According to the quantum-chemical calculations carried out by Su *et al.*,[1] the bimolecular association of two CH_2OO molecules produces a cyclic dimeric intermediate, $(CH_2OO)_2$, with the terminal O atom (with a partial negative charge) of one CH_2OO molecule bonded to the C atom (with a partial positive charge) of the other CH_2OO molecule in a barrierless reaction with large exothermicity. A rate coefficient of $(4 \pm 2) \times 10^{-11}$ cm^3 s^{-1} was also reported for the reaction of CH_2OO + I, with the dominant product channel determined to be the reformation of reactants CH_2I and O_2 at 343 K.[1]

Buras *et al.*[2] observed a CH_2OO self-reaction rate coefficient of $(6.0 \pm 2.1) \times 10^{-11}$ cm^3 s^{-1} at 297 K using flash photolysis of CH_2I_2/O_2 at λ = 266 nm in N_2 and He in a Herriot cell at total pressures between 25 and 100 Torr. CH_2OO was monitored by UV absorption spectroscopy at λ = 375 nm with simultaneous near-infrared absorption measurements of I atoms at 1315.246 nm to quantify the initial CH_2OO concentration and investigate the role of CH_2OO + I. The estimated uncertainty for the initial CH_2OO concentration was reported to be ± 35 %. These measurements also enabled determination of the CH_2OO absorption cross-section at 375 nm, which was found to be in agreement with the results of Ting *et al.*[30]

While CH_2OO decays were observed to become faster with increasing initial CH_2OO concentration as expected and as shown in Figure 5.6, I atom decays were found to be completely insensitive to the initial concentrations of both CH_2OO and I, and to the concentration of CH_2I_2 in the system, indicating a negligible reaction between CH_2OO and I. As a result, the reaction was reported to have no significant impact on the observed CH_2OO decays, and an upper limit of 1.0×10^{-11} cm^3 s^{-1} was reported for the rate coefficient of CH_2OO + I. Both the CH_2OO self-reaction rate coefficient and the upper limit for the CH_2OO + I rate coefficient reported by Buras *et al.*[2] were at least a factor of 5 smaller than those reported by Su *et al.*[1]

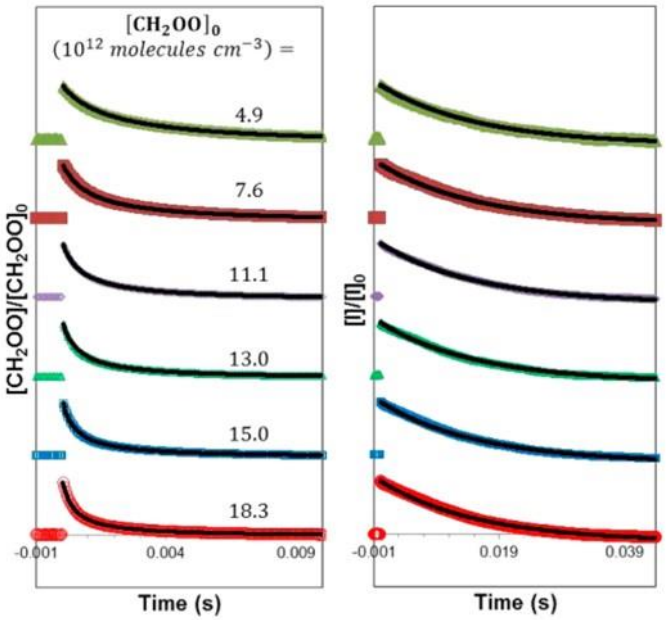

Figure 5.6: Decays of simultaneously recorded CH_2OO (left) UV and I atom (right) IR absorbance measured by Buras *et al.*[2] at 297 K and 50 Torr He over a range of initial CH_2OO concentration, $[CH_2OO]_{t=0}$, values. Solid black lines are fits of a 'complex' kinetic model requiring numerical integration. Only every 100th data point is shown for clarity.

Further experiments by Ting *et al.*,[3] using flash photolysis of $CH_2I_2/O_2/N_2$ at λ = 248 nm with broadband transient UV spectroscopy, were performed to investigate the kinetics of the CH_2OO self-reaction at 295 K at pressures between 7.6 and 779 Torr. Temporal profiles of CH_2OO and IO, obtained by deconvoluting the total observed absorbances through knowledge of the CH_2OO and IO absorption cross-sections, were fitted to a detailed chemical mechanism using numerical integration, as shown in Figure 5.7, to determine a rate coefficient for the CH_2OO self-reaction of $(8 \pm 4) \times 10^{-11}$ cm^3 s^{-1}.

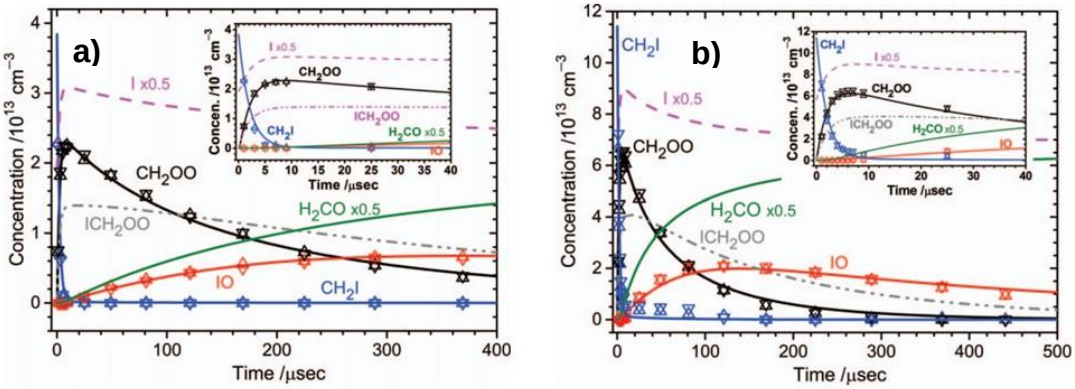

Figure 5.7: Representative temporal profiles of concentrations of CH_2I, CH_2OO and IO recorded by Ting *et al.*[3] upon photolysis of a flowing mixture of $CH_2I_2/O_2/N_2$ at 295 K in two experiments near 100 Torr with differing initial CH_2OO concentrations, i.e. a) with small $[CH_2OO]_{t=0}$, where $[CH_2OO]$ decreased and [IO] increased slowly, and b) with high $[CH_2OO]_{t=0}$, where $[CH_2OO]$ decreased and [IO] increased rapidly, indicating the second-order nature of the decay of CH_2OO, and that some IO was produced from subsequent reactions of CH_2OO. The decrease in concentration of CH_2I_2 upon laser irradiation gave the initial CH_2I concentration, i.e. $-[CH_2I_2] = [CH_2I]_{t=0}$. Concentrations of CH_2I (blue), CH_2OO (black), IO (red), ICH_2OO (grey), I (magenta, scaled by 0.5), and HCHO (green, scaled by 0.5) simulated with a kinetic model using numerical integration are shown as lines. The inset shows a more detailed view in the 0-40 μs region.

However, the results were observed to be sensitive to the kinetics of the reaction between CH_2OO and I, in contrast to the observations of Buras *et al.*,[2] with the best fit to the data giving a rate coefficient of $\sim 8 \times 10^{-11}$ cm^3 s^{-1} for CH_2OO + I.[3] The yield of CH_2OO from $CH_2I + O_2$ was found to have a pressure dependence smaller than that reported previously by Stone *et al.*,[31] with a yield of approximately 30 % at atmospheric pressure[3] compared to the previously reported value of 18 %.

Cavity ringdown spectroscopy has also been used by Chhantyal-Pun *et al.*[4] to monitor CH_2OO at λ = 355 nm to determine the self-reaction kinetics of CH_2OO, using flash photolysis of $CH_2I_2/O_2/N_2$ at λ = 355 nm at 293 K over the pressure range 7-30 Torr. Initially, the observed decays were fit to an analytical solution describing a mixed first- and second-order loss of CH_2OO (the equation for which is provided in Chapter 4) to find the first-order component to the loss. However, the second-order component to the loss was found to depend on the total pressure in the system, as shown in Figure 5.8, with an observed rate coefficient of $(1.61 \pm 0.03) \times 10^{-10}$ cm^3 s^{-1} at the highest

pressure measured of 30 Torr, indicating the presence of second-order losses other than CH_2OO self-reaction. Fits to the data obtained at 7 Torr using numerical integration and considering losses through CH_2OO self-reaction and CH_2OO + I, as shown in Figure 5.8, showed no significant contribution from CH_2OO + I, in agreement with the results of Buras *et al.*,[2] and gave a rate coefficient of (7.35 ± 0.63) × 10^{-11} cm^3 s^{-1} for the CH_2OO self-reaction. A conservative upper limit estimate of 1 × 10^{-11} cm^3 s^{-1} was used for the reaction of CH_2OO + I.[4]

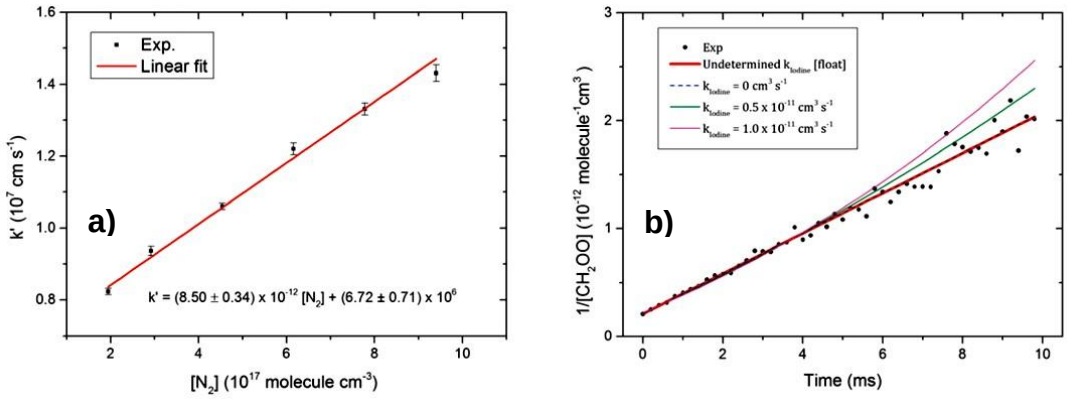

Figure 5.8: Results reported by Chhantyal-Pun *et al.*[4] showing a) the CH_2OO overall scaled second order decay rate coefficient, *k*', obtained from fitting the kinetic decay traces to a second-order decay equation, as a function of total pressure or N_2 concentration, and depicts a positive relationship between the two, with error bars representing the 1σ uncertainties from the fits of the kinetic decay traces, and b) numerical kinetic fits to the CH_2OO decay trace at 7 Torr using various values for the rate coefficient of the CH_2OO + I reaction, referred to as k_{iodine}, with the CH_2OO concentration obtained using the absorption cross-section of CH_2OO at the probe wavelength of 355 nm reported by Ting *et al.*[30] and the change in ring-down rate, and indicates no significant contribution from the reaction between CH_2OO and I at this pressure.

Although the results at 7 Torr were not significantly affected by CH_2OO + I,[4] it is likely that the results obtained at higher pressures were impacted by CH_2OO + I which is evident from the increase in the rate of CH_2OO loss as the pressure is increased. However, this clear secondary chemistry observed to impact the loss of CH_2OO in experiments by Chhantyal-Pun *et al.*[4] at pressures above 7 Torr was attributed to changes in the CH_2IO_2 yield from CH_2I + O_2 as a function of pressure and a potential reaction between CH_2OO and CH_2IO_2 rather than the reaction between CH_2OO and I.

Discrepancies in the kinetics for the CH_2OO self-reaction and the reaction between CH_2OO and I have consequences for understanding of CH_2OO chemistry under both laboratory and atmospheric conditions and hence impact the accuracy of atmospheric modelling. The reaction of CH_2OO + I has eluded detailed investigation with no systematic study of this reaction in the literature despite the discrepancies between rate coefficients reported by previous studies. In this work, the kinetics of the CH_2OO self-reaction and the reaction of CH_2OO and I have been determined at 298 K as a function of pressure in the range 6 to 300 Torr using time-resolved broadband UV spectroscopy.

5.3 Experimental

Kinetics of the CH_2OO Criegee intermediate self-reaction and the reaction between CH_2OO and I were investigated using laser flash photolysis of $CH_2I_2/O_2/N_2$ gas mixtures, coupled with broadband time-resolved UV absorption spectroscopy. All experiments were performed at T = (298 ± 2) K in N_2 (BOC oxygen free, 99.998 %) at pressures between 6 and 300 Torr. CH_2I_2 (Alfa Aesar 99 %) concentrations were in the range $1 \times 10^{12} – 4 \times 10^{13}$ cm^{-3} and O_2 (BOC, 99.5 %) concentrations were varied between 1×10^{16} and 4×10^{17} cm^{-3}. Gases and chemicals were used as supplied. More details of the experimental procedure are given in Chapters 3 and 4. Reactions R5.1-R5.5 were initiated in the reaction cell as described in Chapter 3.

$CH_2I_2 + h\nu$ (λ=248 nm)	→	$CH_2I + I$	(R5.1)
$CH_2I + O_2$	→	$CH_2OO + I$	(R5.2a)
$CH_2I + O_2$	$\xrightarrow{+M}$	CH_2IO_2	(R5.2b)
$CH_2OO + CH_2OO$	→	products	(R5.3)
$CH_2OO + I$	→	products	(R5.4)
CH_2OO	→	products	(R5.5)

5.4 Analysis, Results and Discussion

Experiments carried out in this work to determine the rate coefficient for the CH_2OO self-reaction were analysed first by fitting analytical kinetic loss equations to the data, and subsequently by using numerical integration to account for secondary chemistry in the system, specifically the reaction between CH_2OO and I. A detailed description of each analysis is provided here along with results and a discussion of the implications of these results.

5.4.1 Analytical Kinetic Loss Equation

Where the data has been analysed using an analytical kinetic loss equation, the analysis carried out in this chapter to determine the kinetics of the CH_2OO loss in the system is linked to that carried out in the previous chapter to determine CH_2OO UV absorption cross-sections. As described in Chapter 4, the time-profile of the product $A_{CH2OO,t,\lambda peak} = \sigma_{maximum,CH2OO,\lambda peak}\,[CH_2OO]_t\,l$, where $A_{CH2OO,t,\lambda peak}$ is the absorbance at the wavelength at which the maximum CH_2OO cross-section is observed, $\sigma_{maximum,CH2OO,\lambda peak}$ is the maximum CH_2OO UV absorption cross-section at the wavelength λ corresponding to the peak of the spectrum, $[CH_2OO]_t$ is the concentration of CH_2OO at time t, and l is the effective path length of the light, was determined from the fit of the reference CH_2I_2 cross-sections[32, 33] and the normalised CH_2OO cross-sections to the observed absorbance.

Conventionally, kinetic analysis is performed in terms of concentration of one or more species. As described in Chapter 2, rates of reaction and integrated rate equations include terms for rate coefficients and concentrations, regardless of the order of the reaction e.g. zero-, first-, second-, pseudo-first-, mixed-, n^{th} order. In these experiments, as explained in Chapters 3 and 4, simultaneous detection of spectral and kinetic parameters was achieved, hence the analysis also inherently contains simultaneous determination of both types of parameters, i.e. absolute absorption cross-sections for CH_2OO cannot be determined without kinetic analysis and, equally, rate coefficients for reactions/processes by which the concentration of CH_2OO decays over time cannot be determined without spectral analysis.

Consequently, the analysis carried out to determine results reported in Chapter 4, for the UV absorption cross-sections of CH_2OO, and to determine results reported in this chapter, Chapter 5, for the rate coefficients and kinetics of CH_2OO loss in the system (as established solely from fitting an analytical equation to the data and not from numerical integration), was executed simultaneously. For this reason, the concentration term for CH_2OO was used in the Beer-Lambert Law form in this analysis, which means that rather than fitting a CH_2OO concentration vs time profile to the integrated rate equation, a time-profile of the product, $\sigma_{\text{maximum,CH2OO,}\lambda\text{peak}}$ $[CH_2OO]_t$ l, which is equal to $A_{\text{CH2OO,}t,\lambda\text{peak}}$, was fit to a substituted integrated rate equation.

5.4.1.1 Second-Order Kinetics

It might be expected that the decay profile of $A_{\text{CH2OO,}t,\lambda\text{peak}}$ would exhibit second-order kinetics owing to the dominant loss of CH_2OO occurring via self-reaction, for which the rate of reaction is given by:

$$-\frac{d[CH_2OO]}{dt} = k_{2\text{nd}}\,[CH_2OO]^2 \qquad \text{(Equation 5.1)}$$

where $k_{2\text{nd}}$ is the rate coefficient for the overall second-order loss of CH_2OO in the system. The second-order integrated rate equation is therefore:

$$\frac{1}{[CH_2OO]_t} = \frac{1}{[CH_2OO]_{t=0}} + k_{2\text{nd}}\,t \qquad \text{(Equation 5.2)}$$

The time-profile for the absorbance at the wavelength at which the maximum CH_2OO cross-section is observed is in the Beer-Lambert law form of $A_{\text{CH2OO,}t,\lambda\text{peak}} = \sigma_{\text{maximum,CH2OO,}\lambda\text{peak}}$ $[CH_2OO]_t$ l, which, when substituted into the integrated rate equation, gives:

$$\frac{1}{\left(\frac{A_{\text{CH2OO,}t,\lambda\text{peak}}}{\sigma_{\text{maximum,CH2OO,}\lambda\text{peak}}\,l}\right)} = \frac{1}{\left(\frac{A_{\text{CH2OO,}t=0,\lambda\text{peak}}}{\sigma_{\text{maximum,CH2OO,}\lambda\text{peak}}\,l}\right)} + k_{2\text{nd}}\,t \qquad \text{(Equation 5.3)}$$

The second-order analytical kinetic loss equation to which the time-profile of the product $A_{\text{CH2OO,}t,\lambda\text{peak}} = \sigma_{\text{maximum,CH2OO,}\lambda\text{peak}}$ $[CH_2OO]_t$ l was fit can then be obtained by rearranging the substituted integrated rate equation:

$$A_{CH2OO,t,\lambda peak} = \frac{1}{\left(\left(\frac{1}{A_{CH2OO,t=0,\lambda peak}}\right) + \left(\left(\frac{k_{2nd}}{\sigma_{maximum,CH2OO,\lambda peak}\, l}\right) t\right)\right)}$$

(Equation 5.4)

where $A_{CH2OO,t=0,\lambda peak} = \sigma_{maximum,CH2OO,\lambda peak}\, [CH_2OO]_{t=0}\, l$ (the value of $[CH_2OO]_{t=0}\, l$ is determined from the observed product of the depletion of CH_2I_2 and path length, $\Delta[CH_2I_2]\, l$, and the pressure dependent CH_2OO yield from $CH_2I + O_2$[31]), and k_{2nd} is the second-order loss component for CH_2OO owing to both the CH_2OO self-reaction and the reaction of CH_2OO + I. Figure 5.9 shows the fit result, and illustrates that second-order kinetics were not adequate to describe the system accurately since the equation fit does not agree with the fast part of the CH_2OO decay (the initial, fast exponential decay) or with the slower CH_2OO decay show in the tail (the region where the concentration of CH_2OO starts to level off as the CH_2OO loss within the system comes to an end). Instead, the kinetics observed in the experimental decays describing the loss of CH_2OO were found to be representative of a mixed-order reaction.

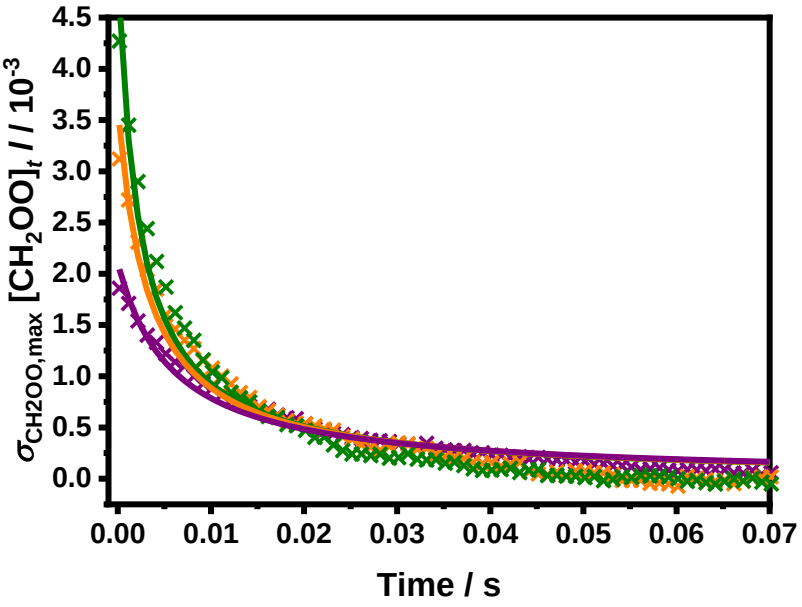

Figure 5.9: Temporal profile of the product $\sigma_{maximum,CH2OO,\lambda peak}$ $[CH_2OO]_t$ $l = A_{CH2OO,t,\lambda peak}$ (green, orange and purple points) determined from the observed absorbance at each time point and the respective fit of the second-order equation (Equation 5.4, green, orange and purple lines) to the data. For all these data p = 70 Torr; for the data shown in green $[O_2] = 2.19 \times 10^{17}$ cm^{-3}, and $[CH_2I_2] = 9.72 \times 10^{12}$ cm^{-3}, and the fit to the data gives $A_{CH2OO,t=0,\lambda peak} = \sigma_{maximum,CH2OO,\lambda peak}$ $[CH_2OO]_{t=0}$ $l = (4.98 \pm 0.20) \times 10^{-3}$ and $k_{2nd} / \sigma_{maximum,CH2OO,\lambda peak}$ $l = (87612 \pm 4482)$ s^{-1}; for the data shown in orange $[O_2] = 1.49 \times 10^{17}$ cm^{-3}, and $[CH_2I_2] = 1.91 \times 10^{13}$ cm^{-3}, and the fit to the data gives $A_{CH2OO,t=0,\lambda peak} = \sigma_{maximum,CH2OO,\lambda peak}$ $[CH_2OO]_{t=0}$ $l = (3.63 \pm 0.16) \times 10^{-3}$ and $k_{2nd} / \sigma_{maximum,CH2OO,\lambda peak}$ $l = (85292 \pm 4461)$ s^{-1}; and for the data shown in purple $[O_2] = 1.50 \times 10^{17}$ cm^{-3}, and $[CH_2I_2] = 7.25 \times 10^{12}$ cm^{-3}, and the fit to the data gives $A_{CH2OO,t=0,\lambda peak} = \sigma_{maximum,CH2OO,\lambda peak}$ $[CH_2OO]_{t=0}$ $l = (2.10 \pm 0.06) \times 10^{-3}$ and $k_{2nd} / \sigma_{maximum,CH2OO,\lambda peak}$ $l = (79570 \pm 2894)$ s^{-1}. The fit of a second-order equation does not sufficiently describe the kinetics observed in the system.

5.4.1.2 Mixed-Order Kinetics

The fit of a mixed first- and second-order analytical kinetic loss equation to the data includes a first-order loss component for CH_2OO, primarily resulting from diffusion out of the probe beam, and a second-order loss component for CH_2OO, owing to bimolecular reaction processes of CH_2OO in the system, namely the CH_2OO self-reaction and the CH_2OO + I reaction, on the timescale of the experiment. The rate of change in $[CH_2OO]$ for such a mixed-order process is[4, 34]:

$$-\frac{d[CH_2OO]}{dt} = k_{1st}[CH_2OO] + 2k_{2nd}[CH_2OO]^2 \qquad \text{(Equation 5.5)}$$

where k_{1st} is the rate coefficient for the first-order loss of CH_2OO and k_{2nd} is the rate coefficient for the second-order loss of CH_2OO in the system. The mixed-order integrated rate equation is thus[4, 34]:

$$[CH_2OO]_t = \frac{k_{1st}[CH_2OO]_{t=0}}{k_{1st}\,e^{k_{1st}t} - 2\,k_{2nd}[CH_2OO]_{t=0} + 2\,k_{2nd}[CH_2OO]_{t=0}\,e^{k_{1st}t}}$$

(Equation 5.6)

The time-profile for the absorbance at the wavelength at which the maximum CH_2OO cross-section is observed, determined from the fit of the CH_2I_2 cross-sections[32, 33] and normalised CH_2OO cross-sections to the observed absorbance, is in the form $A_{CH2OO,t,\lambda peak} = \sigma_{maximum,CH2OO,\lambda peak}[CH_2OO]_t\,l$, which, when substituted into the integrated rate equation, gives:

$$\frac{A_{CH2OO,t,\lambda peak}}{\sigma_{maximum,CH2OO,\lambda peak}\,l} = \frac{k_{1st}\left(\frac{A_{CH2OO,t=0,\lambda peak}}{\sigma_{maximum,CH2OO,\lambda peak}\,l}\right)}{k_{1st}\,e^{k_{1st}t} - 2\,k_{2nd}\left(\frac{A_{CH2OO,t=0,\lambda peak}}{\sigma_{maximum,CH2OO,\lambda peak}\,l}\right) + 2\,k_{2nd}\left(\frac{A_{CH2OO,t=0,\lambda peak}}{\sigma_{maximum,CH2OO,\lambda peak}\,l}\right)e^{k_{1st}t}}$$

(Equation 5.7)

The mixed first- and second-order analytical kinetic loss equation to which the time-profile of the product $A_{CH2OO,t,\lambda peak} = \sigma_{maximum,CH2OO,\lambda peak}[CH_2OO]_t\,l$ was fit, to determine $A_{CH2OO,t=0,\lambda peak} = \sigma_{maximum,CH2OO,\lambda peak}[CH_2OO]_{t=0}\,l$ and hence $\sigma_{maximum,CH2OO,\lambda peak}$ as described in Chapter 4, can then be obtained by rearranging the substituted integrated rate equation:

$$A_{CH2OO,t,\lambda peak} = \frac{k_{1st}\,A_{CH2OO,t=0,\lambda peak}}{k_{1st}\,e^{k_{1st}t} - 2\left(\frac{k_{2nd}}{\sigma_{maximum,CH2OO,\lambda peak}\,l}\right)A_{CH2OO,t=0,\lambda peak} + 2\left(\frac{k_{2nd}}{\sigma_{maximum,CH2OO,\lambda peak}\,l}\right)A_{CH2OO,t=0,\lambda peak}\,e^{k_{1st}t}}$$

(Equation 5.8)

where $A_{CH2OO,t=0,\lambda peak} = \sigma_{maximum,CH2OO,\lambda peak}[CH_2OO]_{t=0}\,l$ (the value of $[CH_2OO]_{t=0}\,l$ is determined from the observed product of the depletion of CH_2I_2 and path length,

$\Delta[CH_2I_2]$ l, and the pressure dependent CH_2OO yield from $CH_2I + O_2$[31]), k_{1st} is the first-order loss component for CH_2OO, primarily resulting from diffusion out of the probe beam, and k_{2nd} is the second-order loss component for CH_2OO owing to both the CH_2OO self-reaction and the $CH_2OO + I$ reaction. Figure 5.10 shows the fit result.

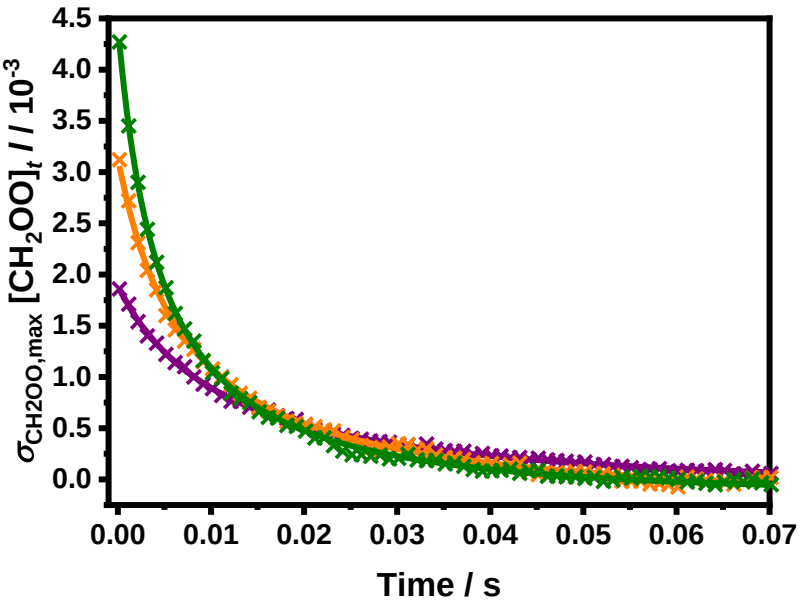

Figure 5.10: Temporal profile of the product $\sigma_{maximum,CH2OO,\lambda peak}$ $[CH_2OO]_t$ l = $A_{CH2OO,t,\lambda peak}$ (green, orange and purple points) determined from the observed absorbance at each time point and the respective fit of the mixed-order equation (Equation 5.8, green, orange and purple lines) to the data. For all these data p = 70 Torr; for the data shown in green $[O_2] = 2.19 \times 10^{17}$ cm^{-3}, and $[CH_2I_2] = 9.72 \times 10^{12}$ cm^{-3}, and the fit to the data gives $A_{CH2OO,t=0,\lambda peak} = \sigma_{maximum,CH2OO,\lambda peak}$ $[CH_2OO]_{t=0}$ $l = (4.55 \pm 0.03) \times 10^{-3}$, $k_{1st} = (34.3 \pm 1.3)$ s^{-1} and $k_{2nd} / \sigma_{maximum,CH2OO,\lambda peak}$ $l = (21614 \pm 309)$ s^{-1}; for the data shown in orange $[O_2] = 1.49 \times 10^{17}$ cm^{-3}, and $[CH_2I_2] = 1.91 \times 10^{13}$ cm^{-3}, and the fit to the data gives $A_{CH2OO,t=0,\lambda peak} = \sigma_{maximum,CH2OO,\lambda peak}$ $[CH_2OO]_{t=0}$ $l = (3.31 \pm 0.03) \times 10^{-3}$, $k_{1st} = (20.6 \pm 2.6)$ s^{-1} and $k_{2nd} / \sigma_{maximum,CH2OO,\lambda peak}$ $l = (19048 \pm 559)$ s^{-1}; and for the data shown in purple $[O_2] = 1.50 \times 10^{17}$ cm^{-3}, and $[CH_2I_2] = 7.25 \times 10^{12}$ cm^{-3}, and the fit to the data gives $A_{CH2OO,t=0,\lambda peak} = \sigma_{maximum,CH2OO,\lambda peak}$ $[CH_2OO]_{t=0}$ $l = (1.94 \pm 0.02) \times 10^{-3}$, $k_{1st} = (20.6 \pm 2.6)$ s^{-1} and $k_{2nd} / \sigma_{maximum,CH2OO,\lambda peak}$ $l = (19048 \pm 559)$ s^{-1}. From the product of the CH_2I_2 depletion and path length, for the data shown in green $\Delta[CH_2I_2]$ $l = 6.06 \times 10^{14}$ cm^{-2}, for the data shown in orange $\Delta[CH_2I_2]$ $l = 3.89 \times 10^{14}$ cm^{-2}, and for the data shown in purple $\Delta[CH_2I_2]$ $l = 2.28 \times 10^{14}$ cm^{-2}, and pressure dependent CH_2OO yield, $Y_{CH2OO,\ p=70\ Torr} = 0.65$, the product of the initial concentration of CH_2OO and path length was calculated to be $[CH_2OO]_{t=0}$ $l = 3.96 \times 10^{14}$ cm^{-2} for the data shown in green, $[CH_2OO]_{t=0}$ $l = 2.54 \times 10^{14}$ cm^{-2} for the data shown in orange, and $[CH_2OO]_{t=0}$ $l = 1.49 \times 10^{14}$ cm^{-2} for the data shown in purple. $\sigma_{maximum,CH2OO,\lambda peak}$ is then calculated from $\sigma_{maximum,CH2OO,\lambda peak}$ $[CH_2OO]_{t=0}$ l / $[CH_2OO]_{t=0}$ l.

While determination of $\sigma_{maximum,CH2OO,\lambda peak}$ was independent of the effective path length, l, determination of the kinetic parameter k_{2nd} requires knowledge of the path length. This was determined for a seven and thirteen multipass configuration of the probe beam from experiments in which the absorbance owing to IO from a single pass of the probe beam through the reaction cell, which overlapped completely with the photolysis laser and thus has a path length equal to the 1.5 m length of the reaction cell, was compared to the absorbance owing to IO measured simultaneously from the multipass arrangement. A more detailed description of these experiments and the subsequent analysis is given in Appendix 2. For seven passes of the probe beam through the cell, l was determined to be (443 ± 21) cm, and for thirteen passes of the probe beam through the cell, l was determined to be (1136 ± 143) cm.

The global fit of multiple time-profile traces of $A_{CH2OO,t,\lambda peak}$ at various $A_{CH2OO,t=0,\lambda peak}$ to the mixed-order analytical loss equation for CH_2OO gave the local parameter $A_{CH2OO,t=0,\lambda peak}$ for each time-profile and global parameters of k_{1st} and k_{2nd} / $\sigma_{maximum,CH2OO,\lambda peak}$ l. The value for the maximum CH_2OO absorption cross-section, $\sigma_{maximum,CH2OO,\lambda peak}$, was determined from $A_{CH2OO,t=0,\lambda peak}$ and the previously determined $[CH_2OO]_{t=0}$ l for each time-profile as described in Chapter 4. From this determination of $\sigma_{maximum,CH2OO,\lambda peak}$ along with knowledge of the path length, l, the rate coefficient for the second-order loss of CH_2OO, k_{2nd}, was determined from the parameter k_{2nd} / $\sigma_{maximum,CH2OO,\lambda peak}$ l.

$$k_{2nd} = \frac{k_{2nd}}{\sigma_{maximum,CH2OO,\lambda peak}\, l}\, \sigma_{maximum,CH2OO,\lambda peak}\, l \qquad \text{(Equation 5.9)}$$

The rate coefficient for this second-order loss component of CH_2OO in the system was observed to be independent of pressure over the range 6-300 Torr, as shown in Figure 5.11, with an average value of $k_{2nd} = (1.3 \pm 0.4) \times 10^{-10}$ cm^3 s^{-1} as determined by Equation 5.9. The uncertainty is the 1σ standard deviation of the mean value for all pressures. On comparison of this value with reported rate coefficients for the CH_2OO self-reaction in the literature, as shown in Figure 5.1, it is clear that in general, the value obtained in this work is greater than those quoted in the literature for studies conducted at the same temperature.[2-4] Measuring a higher reaction rate coefficient than previously reported values can indicate that other loss processes are contributing to the overall loss of CH_2OO, potentially due to secondary I atom chemistry.

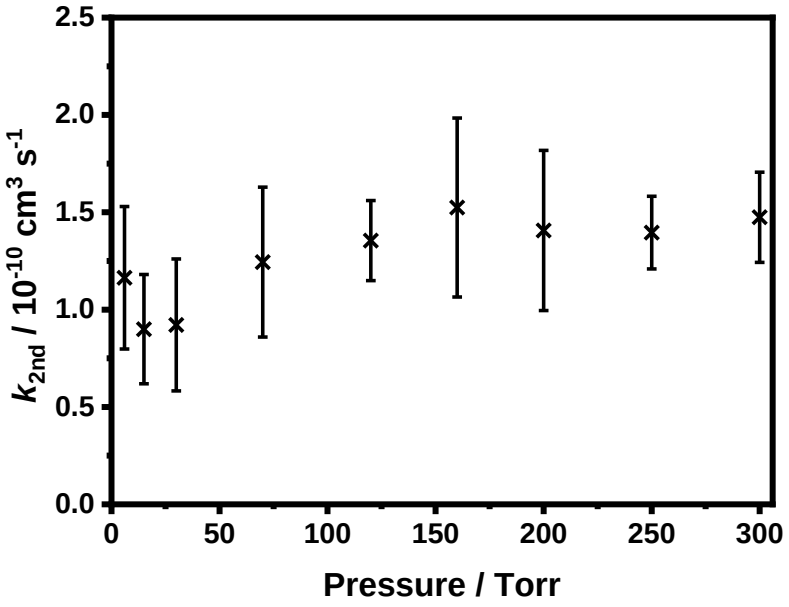

Figure 5.11: Rate coefficients for the second-order loss component CH_2OO in the system (k_{2nd}) as a function of pressure at 298 K determined in this work (black points) from the fit of the mixed-order equation (Equation 5.8) to the data. Uncertainties represent the 1σ standard deviation of the mean values at each pressure.

5.4.1.2.1 Secondary Chemistry

In this analysis is has been assumed that the system can be described as a mixed-order reaction with a simplified chemistry scheme involving only R5.1, R5.2a, R5.3 and R5.5, where R5.5 accounts for any other loss mechanism of CH_2OO which is not second-order.

$CH_2I_2 + h\nu$ (λ=248 nm)	→	$CH_2I + I$	(R5.1)
$CH_2I + O_2$	→	$CH_2OO + I$	(R5.2a)
$CH_2OO + CH_2OO$	→	products	(R5.3)
CH_2OO	→	products	(R5.5)

It is evident from R5.1 and R5.2a that I atoms are formed in the system in a 2:1 ratio of I:CH_2OO when the chemistry in the system is initiated, i.e. at time t = 0. It is the subsequent chemistry of these I atoms which leads to the observed IO absorption in

the experimental spectrum. However, it is unclear what the reactive species are, how IO is formed or what the ensuing chemistry of the IO radical is.

I + reactant	→	IO (+ products)	(R5.6)
IO + reactant	→	products	(R5.7)

Secondary chemistry may also influence the observed CH_2OO decay via the reaction between CH_2OO and I (R5.4), thereby potentially affecting the rate coefficient derived for the second-order loss component of CH_2OO, k_{2nd}.

CH_2OO + I	→	products	(R5.4)

Experiments conducted in this work were carried out at lower initial CH_2I_2 concentrations than previous work ($[CH_2I_2]$ on the order of 10^{12}-10^{13} cm^{-3} compared to approximately 10^{13}-10^{15} cm^{-3} respectively), hence lower initial CH_2OO concentration than previous work ($[CH_2OO]_{t=0}$ on the order of 10^{11}-10^{12} cm^{-3} in this work compared to approximately 10^{12}-10^{14} cm^{-3} in previous work), as summarised in Table 5.3. This lower initial concentration of CH_2OO indicates higher sensitivity to CH_2OO detection than previous work.

Since this initial analysis does not take into account any secondary I atom chemistry (which impacts the kinetics obtained but not the absorption cross-sections), but the analyses used in work conducted at the same temperature by Buras *et al.*,[2] Ting *et al.*[3] and Chhantyal-Pun *et al.*[4] do take this into account, this may be the origin of the differences in the rate coefficient determined from this mixed-order analysis in this work and those previously reported in the literature. However, it is important to note that of these studies in the literature which include the reaction CH_2OO + I in the analysis to determine the CH_2OO self-reaction rate coefficient, only Ting *et al.*[3] found this reaction to impact the kinetics in the system. It is worth noting that, as summarised in Table 5.3, Ting *et al.*[3] used a photolysis wavelength of 248 nm, as in this work, whereas Buras *et al.*[2] and Chhantyal-Pun *et al.*[4] used a photolysis wavelength of 355 nm.

While the mixed-order kinetic fits performed to determine $\sigma_{maximum,CH2OO,\lambda peak}$ do provide some information regarding the kinetics of CH_2OO loss in the system, a more detailed analysis was required to determine the CH_2OO self-reaction kinetics to enable investigation of secondary chemistry within the system.

5.4.2 Numerical Integration

Concentrations for CH_2OO were determined from the fits of $A'_{t,\lambda}$ as described in Chapter 4, which gave the product $\sigma_{maximum,CH2OO,\lambda peak}$ $[CH_2OO]_t$ l, using $\sigma_{maximum,CH2OO,\lambda peak} = (1.37 \pm 0.29) \times 10^{-17}$ cm^2 and knowledge of the path length (l = (443 ± 21) cm for 7 passes of the probe beam or l = (1136 ± 143) cm for 13 passes of the probe beam).

Kinetics describing the observed CH_2OO decays were fit with the numerical integration package FACSIMILE[35] using the mechanism shown in Table 5.1. Fits were performed globally at each pressure investigated to determine the rate coefficients for the CH_2OO self-reaction ($k_{5.3}$), CH_2OO + I ($k_{5.4}$) and the first-order rate coefficient ($k_{5.5}$) describing CH_2OO loss by diffusion out of the probe beam, with the initial CH_2OO concentration as a local parameter for each trace in the global fit. Initial concentrations of CH_2I, I and CH_2IO_2 were determined from their relationship to the initial CH_2OO concentrations using previous measurements of the yields of $CH_2I + O_2$ (R5.2) as a function of pressure from this laboratory,[31] as described in Chapter 1. At each pressure, a range of initial CH_2OO concentrations was used in order to provide greater sensitivity to the second-order components of the loss ($k_{5.3}$ and $k_{5.4}$) over the first-order components of the loss ($k_{5.5}$). A typical fit is shown in Figure 5.12. A summary of the conditions under which experiments were carried out and the fit results from these experiments at all pressures investigated is provided in Appendix 4.

Reaction Number	Reaction	Rate Coefficient, k / $cm^3\ s^{-1}$	Reference
R5.2a	$CH_2I + O_2 \rightarrow CH_2OO + I$	$Y \times (1.5 \times 10^{-12})$	31, 36, 37
R5.2b	$CH_2I + O_2 \xrightarrow{+M} CH_2IO_2$	$(1\text{-}Y) \times (1.5 \times 10^{-12})$	31, 36, 37
R5.3	$CH_2OO + CH_2OO \rightarrow 2\ HCHO + O_2$	$k_{5.3}$	Determined in fit
R5.4	$CH_2OO + I \rightarrow$ products	$k_{5.4}$	Determined in fit
R5.5	$CH_2OO \rightarrow$ loss	$k_{5.5}$ *	Determined in fit
R5.8	$CH_2IO_2 + CH_2IO_2 \rightarrow 2\ CH_2IO + O_2$	9.0×10^{-11}	38
R5.9	$CH_2IO_2 + I \rightarrow CH_2IO + IO$	3.5×10^{-11}	38
R5.10	$CH_2IO \rightarrow HCHO + I$	1.0×10^{5} *	38
R5.11	$IO + IO \rightarrow$ products	1.5×10^{-10}	3, 39

Table 5.1: Summary of the reactions and rate coefficients used in the model to fit to experimental observations of CH_2OO to determine the rate coefficients $k_{5.4}$, $k_{5.4}$ and $k_{5.5}$. Initial concentrations of CH_2OO were determined by fitting to the data, with initial concentrations of CH_2I, I and CH_2IO_2 determined from our previous measurements[31] of the yields of $CH_2I + O_2$, where Y indicates the yield of CH_2OO from $CH_2I + O_2$, and their relationship to the initial concentration of CH_2OO. *Units of s^{-1}.

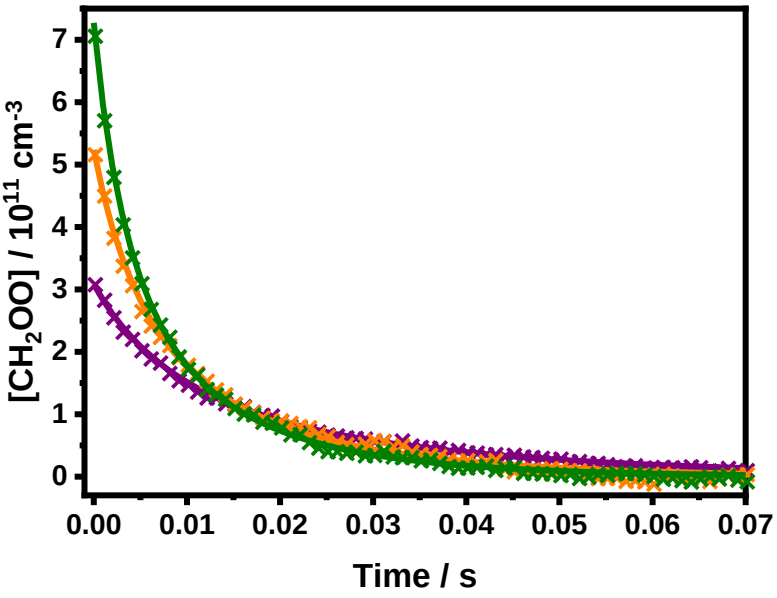

Figure 5.12: Temporal profile of the experimentally observed [CH_2OO] (green, orange and purple points) and the respective model fit (green, orange and purple lines) using the mechanism given in Table 5.1. For all these data p = 70 Torr; for the data shown in green [O_2] = 2.19 × 10^{17} cm^{-3}, and [CH_2I_2] = 9.72 × 10^{12} cm^{-3}, and the fit to the data gave [CH_2OO]$_{t=0}$ = (7.27 ± 0.12) × 10^{11} cm^{-3}, $k_{5.3}$ = (9.5 ± 0.9) × 10^{-11} cm^3 s^{-1}, $k_{5.4}$ = (4.4 ± 0.4) × 10^{-11} cm^3 s^{-1} and $k_{5.5}$ = 0.030 ± 0.002 s^{-1}; for the data shown in orange [O_2] = 1.49 × 10^{17} cm^{-3}, and [CH_2I_2] = 1.91 × 10^{13} cm^{-3}, and the fit to the data gave [CH_2OO]$_{t=0}$ = (5.24 ± 0.11) × 10^{11} cm^{-3}, $k_{5.3}$ = (7.9 ± 0.4) × 10^{-11} cm^3 s^{-1}, $k_{5.4}$ = (5.0 ± 0.2) × 10^{-11} cm^3 s^{-1} and $k_{5.5}$ = 1.00 ± 0.21 s^{-1}; and for the data shown in purple [O_2] = 1.50 × 10^{17} cm^{-3}, and [CH_2I_2] = 7.25 × 10^{12} cm^{-3}, and the fit to the data gave [CH_2OO]$_{t=0}$ = (3.08 ± 0.13) × 10^{11} cm^{-3}, $k_{5.3}$ = (8.1 ± 1.3) × 10^{-11} cm^3 s^{-1}, $k_{5.4}$ = (5.0 ± 0.5) × 10^{-11} cm^3 s^{-1} and $k_{5.5}$ = 0.15 ± 0.27 s^{-1}.

5.4.2.1 CH_2OO + CH_2OO and CH_2OO + I Reaction Kinetics

The rate coefficient for the CH_2OO self-reaction was not observed to display any significant dependence on pressure, as shown in Figure 5.13 and Table 5.2, with an average value of $k_{5.3}$ = (8.0 ± 1.1) × 10^{-11} cm^3 s^{-1} over all pressures. The uncertainty is the 1σ standard deviation of the mean value for all pressures combined with the uncertainties determined from the sensitivity analysis described below.

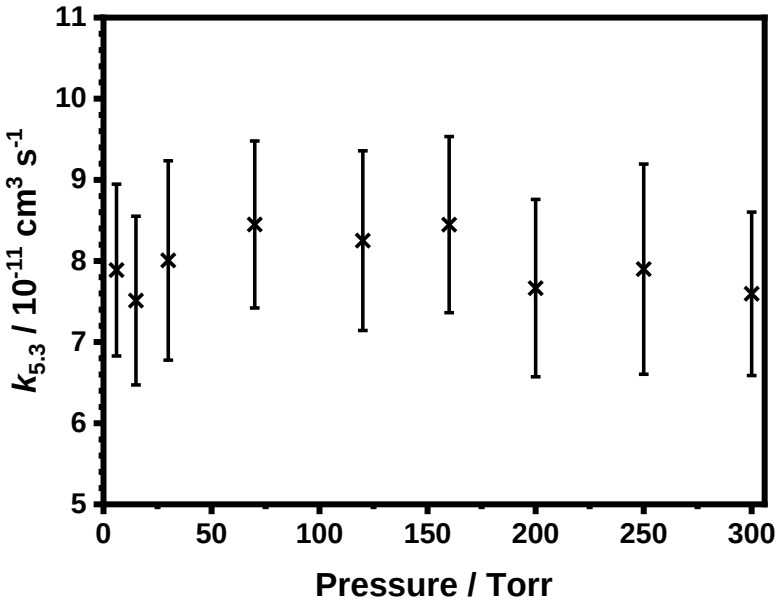

Figure 5.13: Rate coefficients for the CH_2OO self-reaction ($k_{5.3}$) as a function of pressure at 298 K determined in this work (black points) from the fit of a kinetic model (Table 5.1) to the data using numerical integration. Uncertainties include the 1σ standard deviation of the mean values and the uncertainties determined from the fit sensitivities to reactions R5.8-R5.11 and the branching ratios for reaction R5.4.

A comparison of results obtained for the rate coefficient of the CH_2OO self-reaction in this work with values previously reported in the literature is shown in Figure 5.14 and a summary of results reported in previous work is given in Table 5.3. Results from this work are in agreement with those reported by Ting *et al.*,[3] Buras *et al.*[2] and the results of Chhantyal-Pun *et al.*[4] at 7 Torr, which are all significantly lower than that reported by Su *et al.*[1] at a temperature of 343 K using infrared absorption spectroscopy.

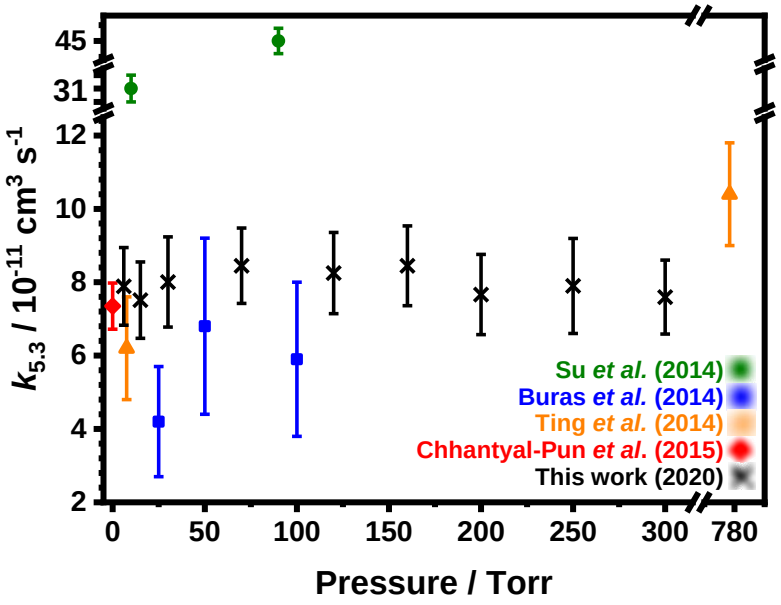

Figure 5.14: Comparison of rate coefficients for the CH_2OO self-reaction ($k_{5.3}$) as a function of pressure determined in this work at 298 K (black points), with uncertainties including the 1σ standard deviation of the mean values and the uncertainties determined from the fit sensitivities to reactions R5.8-R5.11 and the branching ratios for reaction R5.4, and results reported in previous work at 295 ± 2 K (blue, orange and red points) and 343 K (green points).

Figure 5.15 shows the rate coefficient obtained in this work for the reaction between CH_2OO and I as a function of pressure, with values at each pressure given in Table 5.2. This work shows significant pressure dependence in the kinetics for CH_2OO + I, with $k_{5.4}$ varying from $(1.1\ ^{+2.2}_{-1.1}) \times 10^{-12}$ cm^3 s^{-1} at 6 Torr to $(5.5 \pm 2.1) \times 10^{-11}$ cm^3 s^{-1} at 300 Torr. A Lindemann fit (Equation 5.10), for which more detail is provided in Chapter 2, to the observed kinetics as a function of pressure gives $k_{5.4,0} = (4.4 \pm 1.0) \times 10^{-29}$ cm^6 s^{-1} and $k_{5.4,\infty} = (6.7 \pm 0.6) \times 10^{-11}$ cm^3 s^{-1}, where the uncertainty if the 1σ standard deviation of the fit.

$$k_4 = k_{5.4,0}\,[\mathrm{M}]\,k_{5.4,\infty} \Big/ (k_{5.4,0}\,[\mathrm{M}] + k_{5.4,\infty}) \qquad \text{(Equation 5.10)}$$

where [M] is the total pressure in units of cm^{-3}, and $k_{5.4,0}$ and $k_{5.4,\infty}$ are the low and high pressure limits of the rate coefficient for reaction R5.4 respectively.

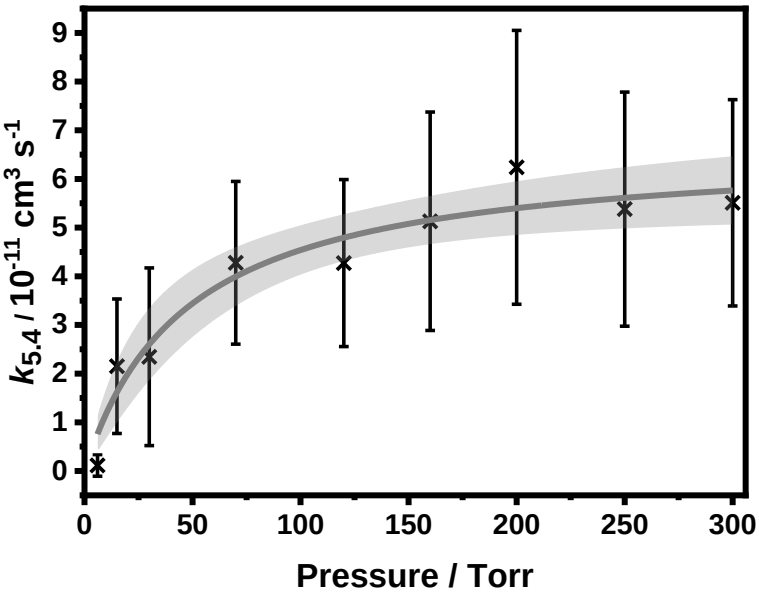

Figure 5.15: Rate coefficients for the CH_2OO + I reaction ($k_{5.4}$) as a function of pressure at 298 K determined in this work (black points) from the fit of a kinetic model (Table 5.1) to the data using numerical integration. Uncertainties include the 1σ standard deviation of the mean values and the uncertainties determined from the fit sensitivities to reactions R5.8-R5.11 and the branching ratios for reaction R5.4. The fit of this work to the Lindemann equation (Equation 5.10, shown by the grey line, with the 95 % confidence bands to the fit shown by the light grey shaded region) gives $k_{5.4,0} = (4.4 \pm 1.0) \times 10^{-29}$ cm^6 s^{-1} and $k_{5.4,\infty} = (6.7 \pm 0.6) \times 10^{-11}$ cm^3 s^{-1}.

Pressure / Torr	$k_{5.3}$ / 10^{-11} cm^3 s^{-1}	$k_{5.4}$ / 10^{-11} cm^3 s^{-1}
6	7.9 ± 1.1	$0.1^{+0.2}_{-0.1}$
15	7.5 ± 1.0	2.2 ± 1.4
30	8.0 ± 1.2	2.4 ± 1.8
70	8.5 ± 1.0	4.3 ± 1.7
120	8.3 ± 1.1	4.3 ± 1.7
160	8.5 ± 1.1	5.1 ± 2.2
200	7.7 ± 1.1	6.2 ± 2.8
250	7.9 ± 1.3	5.4 ± 2.4
300	7.6 ± 1.0	5.5 ± 2.1

Table 5.2: Summary of results for the rate coefficients for the CH_2OO self-reaction ($k_{5.3}$) and CH_2OO + I ($k_{5.4}$) as a function of pressure at 298 K. Values at each pressure are the mean values obtained over all experiments at that pressure. Uncertainties include the 1σ standard deviation of the mean values and the uncertainties determined from the fit sensitivities to reactions R5.8-R5.11 and the branching ratios for reaction R5.4.

A comparison of results obtained for the rate coefficient of the reaction between CH_2OO and I in this work with values previously reported in the literature is shown in Figure 5.16 and a summary of results reported in previous work is given in Table 5.3. Despite the discrepancies between values from previous studies, no systematic study of the CH_2OO + I reaction has been carried out in the literature to date. The extensive data set collected in this work over a range of pressures and initial radical concentrations has enabled a detailed investigation of the CH_2OO + I reaction.

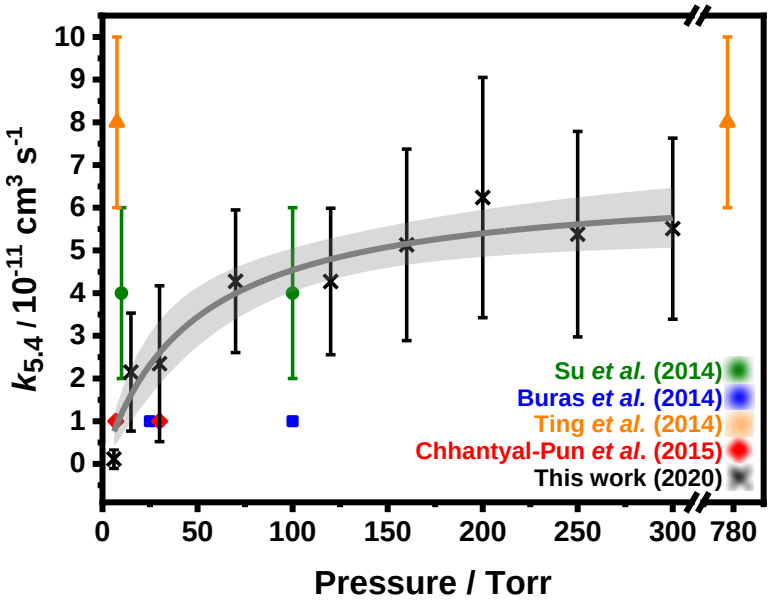

Figure 5.16: Comparison of the rate coefficients for the reaction between CH_2OO and I ($k_{5.4}$) as a function of pressure determined in this work at 298 K (black points), with uncertainties including the 1σ standard deviation of the mean values and the uncertainties determined from the fit sensitivities to reactions R5.8-R5.11 and the branching ratios for reaction R5.4, and results reported in previous work at 295 ± 2 K (blue, orange and red points) and 343 K (green points). The fit of this work to the Lindemann equation (Equation 5.10, shown by the grey line, with the 95 % confidence bands to the fit shown by the light grey shaded region) gives $k_{5.4,0}$ = (4.4 ± 1.0) × 10^{-29} cm^6 s^{-1} and $k_{5.4,\infty}$ = (6.7 ± 0.6) × 10^{-11} cm^3 s^{-1}.

Study	Temperature / K	Pressure / Torr	Photolysis λ / nm	Detection Technique	$[CH_2OO]_{t=0}$ / 10^{11} cm^{-3}	$k_{5.3}$ / 10^{-11} cm^3 s^{-1}	$k_{5.4}$
Su *et al.*, 2014 [1]	343	10 – 100	355	FTIR	100 - 800	40 ± 20	$(4 \pm 2) \times 10^{-11}$ cm^3 s^{-1}
Buras *et al.*, 2014 [2]	297	25 – 100	266	UVA	20 - 200	6.0 ± 2.1	$< 1 \times 10^{-11}$ cm^3 s^{-1}
Ting *et al.*, 2014 [3]	295	7.6 – 779	248	UVA	200 - 2000	8.2 ± 1.4	$(6 – 10) \times 10^{-11}$ cm^3 s^{-1}
Chhantyal-Pun *et al.*, 2015 [4]	293	7 – 30	355	CRDS	25 - 50	7.35 ± 0.63	$< 1 \times 10^{-11}$ cm^3 s^{-1}
This work	298	6 – 300	248	UVA	1 - 10	8.0 ± 1.1	$k_0 = (4.4 \pm 1.0) \times 10^{-29}$ cm^6 s^{-1} $k_\infty = (6.7 \pm 0.6) \times 10^{-11}$ cm^3 s^{-1}

Table 5.3: Summary of results for the rate coefficient for the CH_2OO self-reaction ($k_{5.3}$) and for the reaction between CH_2OO and I ($k_{5.4}$) obtained in this work and reported in the literature. FTIR = Fourier transform infrared; UVA = UV absorption; CRDS = cavity ringdown spectroscopy.

Previous studies of the CH_2OO self-reaction have indicated varying impacts of the reaction between CH_2OO and I. Table 5.3 summarises the range of values for $k_{5.4}$ that have been reported in the literature. Buras *et al.*[2] reported an upper limit for $k_{5.4}$ of 1×10^{-11} cm^3 s^{-1} on the basis of measurements of both CH_2OO and I atoms. These measurements, performed between 25 and 100 Torr at 297 K with initial concentrations on the order of 10^{12}-10^{13} cm^{-3}, indicated that the kinetics of I atoms loss were independent of the initial concentrations of CH_2OO or I, and were dominated by diffusion. Chhantyal-Pun *et al.*[4] also reported an upper limit of 1×10^{-11} cm^3 s^{-1} for $k_{5.4}$ for experiments at 7 Torr and 293 K, although clear secondary chemistry was observed to impact the loss of CH_2OO at pressures above 7 Torr. The pressure dependence observed in the kinetics describing the loss of CH_2OO in the experiments by Chhantyal-Pun *et al.* was attributed to changes in the CH_2IO_2 yield from $CH_2I + O_2$ as a function of pressure and a potential reaction between CH_2OO and CH_2IO_2.

The results of Su *et al.*[1] indicated $k_{5.4} = (4 \pm 2) \times 10^{-11}$ cm^3 s^{-1} between 10 and 100 Torr, in broad agreement with the results of this work but it should be noted that experiments were conducted at 343 K and gave a significantly higher value for $k_{5.3}$ than determined in this work and in other studies. It is also worth noting that for the analysis of these experiments carried out by Su *et al.*,[1] accurate IR absorption cross-sections of CH_2OO were required,[40] which are not available in the literature since values reported contain significant uncertainties given the reduced sensitivity of IR absorption measurements, hence kinetic data determined from these IR cross-sections also intrinsically contain large uncertainties. Experiments performed by Ting *et al.*[3] over a range of pressures (7.6 to 779 Torr) at 295 K also indicated significant impacts of $CH_2OO + I$ on the loss of CH_2OO across the entire pressure range investigated, with the best fits to the observed CH_2OO decays giving pressure independent $k_{5.4}$ values in the range $6\text{-}10 \times 10^{-11}$ cm^3 s^{-1}, in agreement with the high pressure limit obtained in this work. Thus, while there are significant discrepancies for $k_{5.4}$ reported in the literature, the pressure dependence observed in this work provides some insights as to the source of the discrepancies and reconciles the results of Chhantyal-Pun *et al.*[4] and Ting *et al.*,[3] with the results of Buras *et al.*[2] at low pressures within the experimental uncertainties of this work.

5.4.2.2 Sensitivity Analysis

In order to investigate the sensitivity of $k_{5.3}$ and $k_{5.4}$ to the parameters used in the model (Table 5.1) to fit to the observed CH_2OO decays, each of the rate coefficients used in the model were sequentially doubled and halved and the effects of the fitted values of $k_{5.3}$ and $k_{5.4}$ were determined. Results are provided in terms of a sensitivity factor which is defined as the fractional difference in the fit result for the rate coefficient, i.e. $k_{5.3}$ or $k_{5.4}$, compared to the fit result determined using rate coefficients as listed in Table 5.1, subtract 1, and is given by:

$$SF = \frac{k_{out}}{k_{base\_case}} - 1 \qquad \text{(Equation 5.11)}$$

where SF is the calculated sensitivity factor, k_{out} is the rate coefficient determined from the fit result for the sensitivity to whichever reaction is being considered/altered, k_{base_case} is the rate coefficient determined for whichever reaction is being considered/altered when it is unaltered i.e. as determined using the reaction model shown in Table 5.1.

Results from the sensitivity analysis are shown in Figure 5.17, and indicate no significant dependence of $k_{5.3}$ on the parameters used in the model. For $k_{5.4}$, the results indicate there is some sensitivity at low pressures to the rate coefficients used for R5.8-R5.11. The rate coefficients for R5.8-R5.10 used in the model shown in Table 5.1 are based on laser induced fluorescence measurements of IO and HCHO production following photolysis of $CH_2I_2/O_2/N_2$ at 100 Torr by Gravestock *et al.*,[38] and were obtained by fitting a model containing reactions R5.2b and R5.8-R5.10 to the experimentally observed HCHO, assuming that all CH_2IO produced in R5.8 rapidly decomposes to HCHO + I. For R5.11, the rate coefficient used in the analysis is that used by Ting *et al.*,[3] which is higher than the current IUPAC recommendation[39] but was required to adequately model the IO loss in the system, suggesting the presence of other loss processes for IO which could not be separated from IO + IO with any sensitivity. While there is some sensitivity of $k_{5.4}$ to R5.8-R5.11, uncertainties for $k_{5.4}$ reported in this work include uncertainties arising from sensitivity to the rate coefficients for R5.8-R5.11.

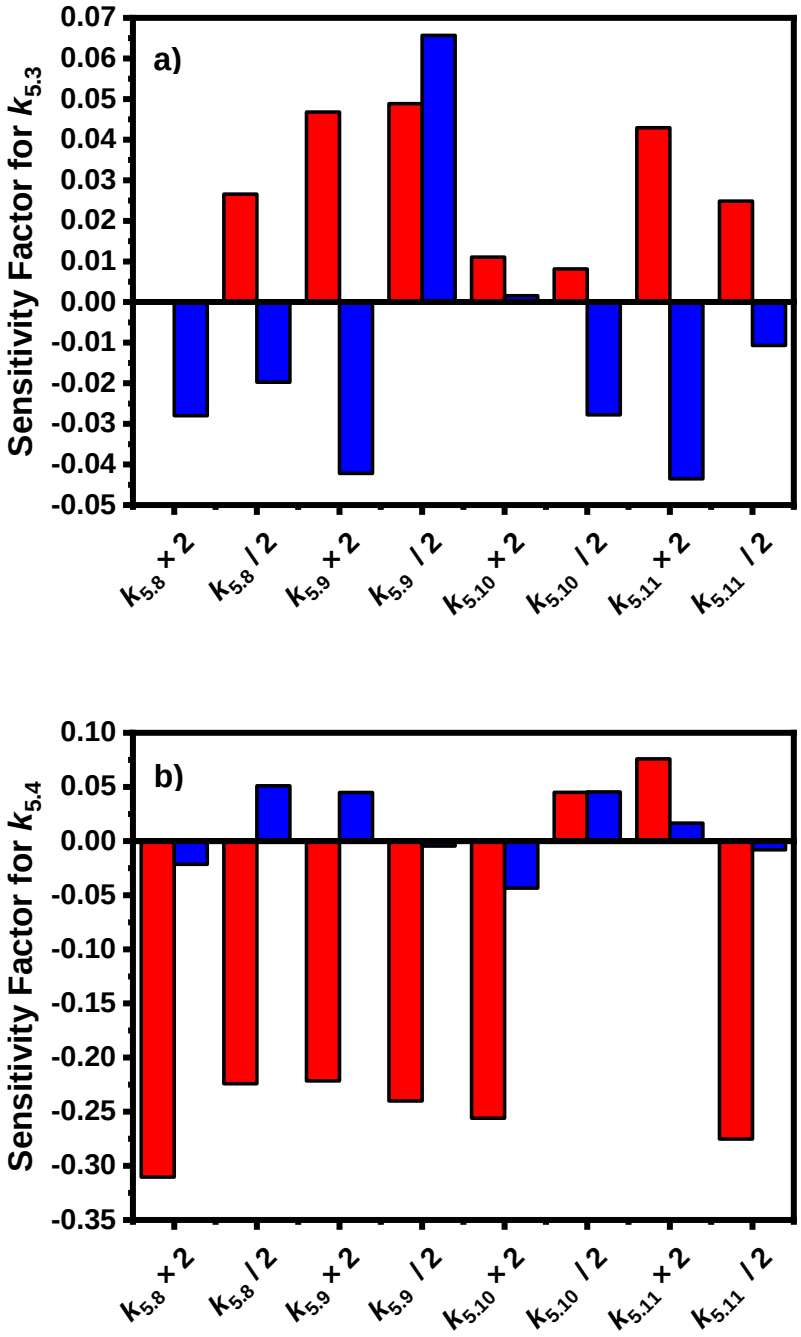

Figure 5.17: Sensitivity of a) $k_{5.3}$ and b) $k_{5.4}$ to the rate coefficients adopted in the model used to fit to experimental observations. Results are shown for analyses at 70 Torr (red) and 300 Torr (blue). The sensitivity factor is calculated using Equation 5.11 and defined as the fractional difference in the fit result subtract 1 for a) $k_{5.3}$ and b) $k_{5.4}$ compared to the fit result determined using the rate coefficients as given in Table 5.1.

The potential for reaction between CH_2OO and peroxy radicals (RO_2), such as CH_2IO_2, has been investigated in theoretical studies, with predicted rate coefficients for $CH_2OO + RO_2$ reactions between 3.74×10^{-12} cm^3 s^{-1} and 1×10^{-11} cm^3 s^{-1}.[5, 41, 42] The impact of any such reaction on the results reported in this work was investigated by incorporating a reaction between CH_2OO and CH_2IO_2 in the model at the upper limit of the predicted rate coefficients for $CH_2OO + RO_2$. Results at 70 Torr were affected by ~2 %, with those at 300 Torr affected by ~5 %.

Simulations were also performed to determine the sensitivity of the results for $k_{5.3}$ and $k_{5.4}$ on the products of $CH_2OO + I$ specified in the model. Since the products, and branching ratios, of $CH_2OO + I$ are uncertain, fits were performed in which the reaction was considered simply as a loss mechanism for CH_2OO and I (i.e. with no products specified, as shown in Table 5.1), and in which varying branching ratios were considered for production of $CH_2I + O_2$, CH_2IO_2, and HCHO + IO:

$$CH_2OO + I \rightarrow CH_2I + O_2 \quad \text{(R5.4a)}$$

$$CH_2OO + I \xrightarrow{+M} CH_2IO_2 \quad \text{(R5.4b)}$$

$$CH_2OO + I \rightarrow HCHO + IO \quad \text{(R5.4c)}$$

where branching ratios are defined as α, β and γ for reaction channels R5.4a, R5.4b and R5.4c respectively, forming $CH_2I + O_2$, CH_2IO_2 and HCHO + IO respectively.

The impacts on $k_{5.3}$ and $k_{5.4}$ of varying the branching ratios for channels R5.4a-c are shown in Figure 5.18. For $k_{5.3}$, there is little sensitivity of the results to the nature of the products or branching ratio for R5.4. For $k_{5.4}$, there is some sensitivity to the branching ratio adopted in the model, particularly at low pressures and if the reaction proceeds primarily via R4a to form $CH_2I + O_2$. Although Su *et al*. predicted that production of $CH_2I + O_2$ is the dominant reaction channel for R5.4, the kinetics of this reaction pathway are not expected to exhibit any significant pressure dependence, and the lowest energy pathways in the reaction result in production of CH_2IO_2 or HCHO + IO.[1] R5.4a is expected to be thermodynamically unfeasible due to the existence of an activation barrier to such a reaction given the reactants are lower in energy, i.e. more stable, than the products, hence an additional driving force is required for the reaction to occur, and since the forward reaction between CH_2I and O_2 has been shown to occur (R5.2a and R5.2b) and is fast, the reverse reaction between CH_2OO and I to

produce CH_2I and O_2 (R5.4a) is unlikely to occur. Previous measurements of the HCHO products of CH_2OO chemistry from this laboratory indicate that the CH_2OO self-reaction and CH_2OO + I ultimately produce HCHO in 100 % yield, either directly or via formation and subsequent chemistry of CH_2IO_2.[21, 31] Ting *et al.*[3] have also indicated that channels producing CH_2IO_2 and HCHO + IO are more significant than that producing CH_2I + O_2. The possibility that the reaction proceeds 100 % via R5.4a has therefore been excluded from further analysis. For all other combinations of branching ratios, the results for $k_{5.4}$ are within 20 % of the value given by the model in which the reaction is treated as a loss mechanism for CH_2OO and I but with products unspecified. Results reported for $k_{5.3}$ and $k_{5.4}$ in this work used the model as shown in Table 5.1 (i.e. with products for R5.4 not specified) and include uncertainties resulting from assumptions regarding the rate coefficients and branching ratios adopted in the model.

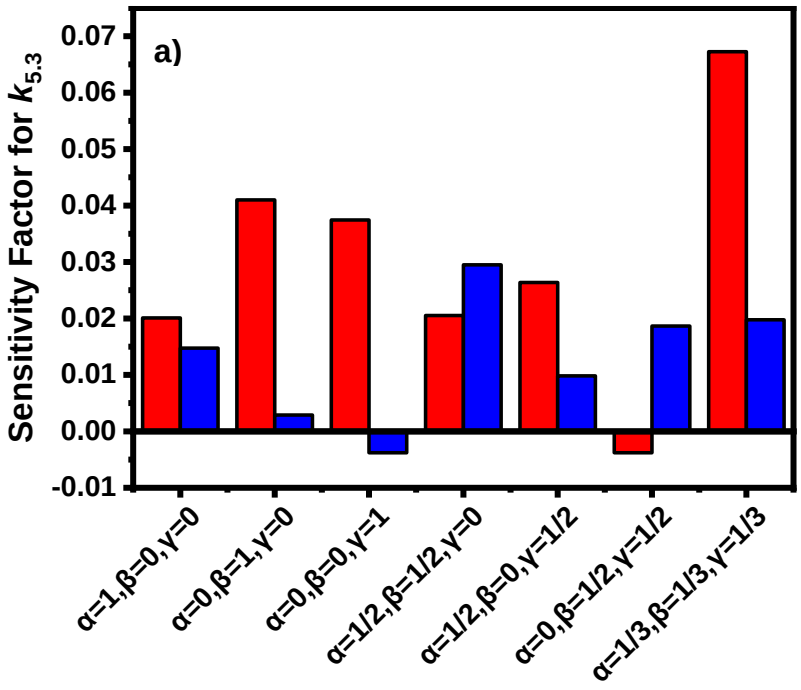

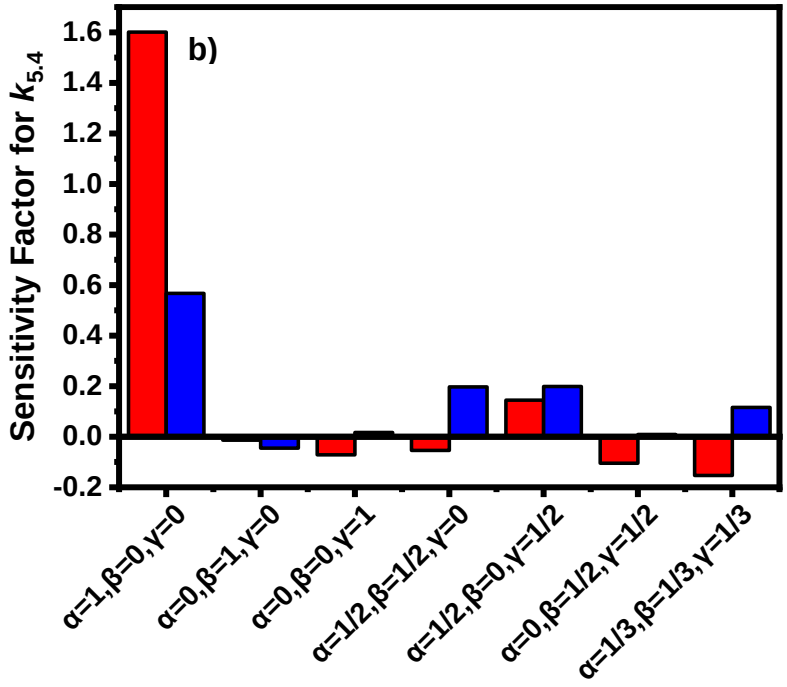

Figure 5.18: Sensitivity of a) $k_{5.3}$ and b) $k_{5.4}$ to the branching ratios adopted in the model for the reaction between CH_2OO and I (R5.4). Branching ratios are defined as α for channel R5.4a (producing $CH_2I + O_2$), β for channel R5.4b (producing CH_2IO_2), and γ for channel R5.4c (producing HCHO + IO). Results are shown for analyses at 70 Torr (red) and 300 Torr (blue). The sensitivity factor is calculated using Equation 5.11 and defined as the fractional difference in the fit result subtract 1 for a) $k_{5.3}$ and b) $k_{5.4}$ compared to the result determined for fits in which no products for R5.4 are specified.

5.4.2.3 Source of IO Radicals

The production of IO following photolysis of CH_2I_2/O_2 mixtures has long been an outstanding question in the literature and has been investigated in a number of previous studies, with several arguments proposed to explain the source of IO within the system. Early studies of the reaction between CH_2I and O_2 indicated that IO was produced directly from $CH_2I + O_2$.[36, 37, 43, 44] However, later studies have provided evidence that IO is not produced directly from the reaction between CH_2I and O_2, but is a product of secondary reactions involving I atoms.[3, 38, 45, 46] Dillon *et al.*[45] monitored the production of IO using laser-induced fluorescence (LIF) spectroscopy following photolysis of CH_2I_2/O_2 at a wavelength of 351 nm at pressures between 15 and 60 Torr, and observed a non-linear dependence of the IO yield on the fluence of

the photolysis laser and on the concentration of O_2, suggesting an indirect radical-radical mechanism. Subsequent work was carried out by Gravestock *et al.*,[38] in which IO was monitored via time-resolved broadband UV absorption spectroscopy following photolysis of CH_2I_2/O_2 at wavelengths of 193 nm or 248 nm at room temperature and atmospheric pressure, under which conditions the chemistry of CH_2IO_2 dominates over that of CH_2OO owing to the pressure dependent branching ratios for $CH_2I + O_2$. Gravestock *et al*. observed a dependence of the production rate and yield of IO on the concentrations of CH_2I_2 and O_2, indicating an indirect mechanism and leading to the suggestion that the production was dominated by the reaction between CH_2IO_2 and I. Ting *et al*.[3] have also indicated that production of IO at high pressures is dominated by CH_2IO_2 + I (R5.9), while production at lower pressures (p < 60 Torr) is dominated by CH_2OO + I (R5.4). Foreman and Murray[46] monitored the production of IO(v=0) and IO(v=1) using cavity ringdown spectroscopy following 355 nm photolysis of CH_2I_2/O_2 at 52 Torr and 295 K, with measurements indicating that the production of IO(v=0) was dominated by secondary chemistry, such as CH_2OO + I. Production of IO(v=1) was observed to occur with a rate coefficient five times larger than that for IO(v=0), but with a smaller yield, with results indicating direct production of IO(v=1) from the reaction of excited CH_2I^* with O_2 and a dependence of the mechanism on the degree of excitation of CH_2I.[46]

Typical IO concentration-time profiles observed in this work were found to be characterised by a rapid production of IO that occurs within 1 ms of photolysis, followed by a slower production and subsequent decay, as has been observed in previous studies.[38, 46] In this work, the initial IO concentration observed from the rapid production and the peak IO concentration were both observed to be dependent on the initial concentration of CH_2I radicals. The initial concentration of CH_2I in the system, $[CH_2I]_{t=0}$, was determined from the observed depletion in CH_2I_2 absorbance. The concentration of IO radicals produced in the initial rapid process and hence observed at the first post-photolysis time point, $[IO]_{t=1.64\times10^{-4}\ s}$, was observed to be directly proportional to $[CH_2I]_{t=0}$, as shown in Figure 5.19a, with a yield of rapid IO formation of (14.8 ± 0.5) % of the initial CH_2I concentration. Similarly, the maximum or peak IO concentration, $[IO]_{max}$, was also observed to be directly proportional to $[CH_2I]_{t=0}$, as shown in Figure 5.19b, with an IO yield of (17.2 ± 0.5) % of the initial CH_2I concentration.

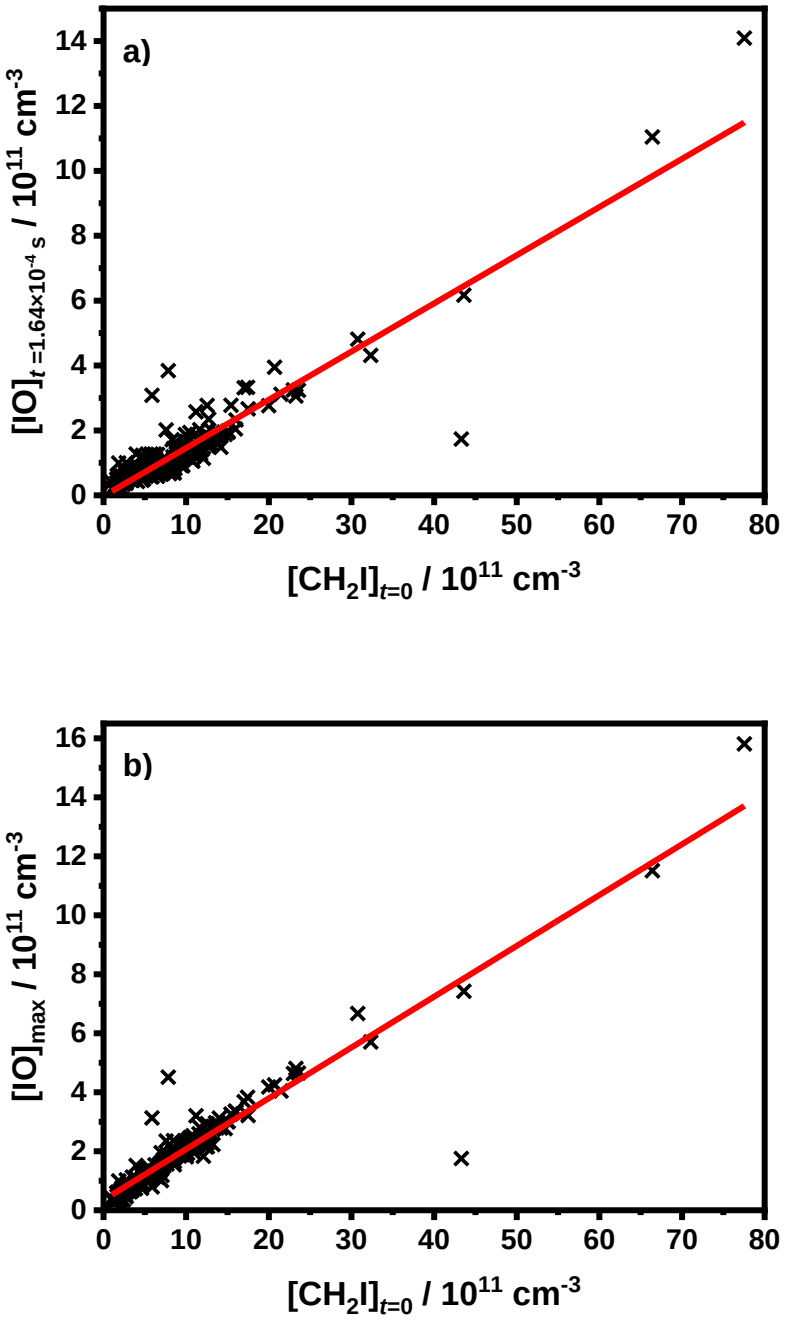

Figure 5.19: Relationships between a) the concentration of IO produced within 1 ms of photolysis, i.e. observed at the first post-photolysis time point, and the initial concentration of CH_2I, and b) the maximum concentration of IO and the initial concentration of CH_2I. Linear fits to the data (red lines) give a) gradient = (14.8 ± 0.5) and intercept = (-2.3 ± 6.1) × 10^9 cm^{-3} and b) gradient = (17.2 ± 0.5) and intercept = (3.5 ± 0.6) × 10^{10} cm^{-3}.

Gravestock *et al.*[38] observed similar behaviour in the dependence of the peak IO concentration on the initial CH_2I concentration, but with a higher yield of yield of 30-40 %, with results indicating that IO is not a direct photolysis product of CH_2I_2/O_2 but is produced via secondary radical processes. It was postulated that IO could be produced by a multi-photon process on photolysis of CH_2I_2 at 248 nm, leading to the production of CH_2 radicals which react rapidly with the excess O_2 to form HCHO + O, with subsequent production of IO through the reaction of $O + CH_2I_2 \rightarrow IO + CH_2I$. However, this mechanism could only account for ~5 % of the IO observed in the system.[38] Subsequent work by Foreman and Murray[46] monitored production of both IO(v=0) and IO(v=1) by cavity ringdown spectroscopy following CH_2I_2/O_2 photolysis at 355 nm, and found IO(v=0) to be predominantly formed through secondary chemistry involving formation of CH_2OO which reacts with I atoms, while IO(v=1) was formed exclusively via a direct mechanism of $CH_2I + O_2$ with a rate coefficient that was five times larger than that for IO (v=0), yet the maximum vibrationally excited population was observed to be significantly smaller than that of the ground state. This observed behaviour suggested production of excited CH_2I^* radicals is required for direct production of IO, which is generated on reaction with O_2. It was concluded that as collisions and reactions remove the photolytically produced internally excited CH_2I^* population, the direct reaction is quenched, and the slower sequential mechanism continues to result in predominantly IO(v=0). The impact of excited CH_2I^* on secondary production of HCHO and OH radicals has also been observed in other studies of CH_2OO chemistry.[21, 47]

In this work, the focus for IO radicals is on the IO production in the system which occurs following the initial rapid production. Figure 5.20 shows the ratio of the maximum observed IO concentration to the concentration of IO generated by the initial rapid production observed in this work, representing the yield of IO produced in the system following the initial rapid growth, as a function of pressure. The yield of IO was observed to increase with increasing pressure, with limited production of IO at low pressures. Model simulations constrained to the observed initial IO concentrations (i.e. the rapid IO production) were compared to the observed temporal behaviour of IO to investigate the impacts of $CH_2OO + I$ (R5.4) and $CH_2IO_2 + I$ (R5.9) on the subsequent production of IO using the mechanism given in Table 5.1. The rate coefficient used for R5.9 in the model shown in Table 5.1 is taken from the work of

Gravestock *et al.*,[38] in which laser-induced fluorescence was employed to monitor the formation of IO and HCHO following photolysis of CH_2I_2/O_2 at 100 Torr, with kinetics determined by fitting to the HCHO observations. A mechanism producing IO directly from $CH_2I + O_2$ was found to be inconsistent with their observations, which led to the conclusion that the formation and subsequent reactions of CH_2IO_2 are most likely to be responsible for IO production.

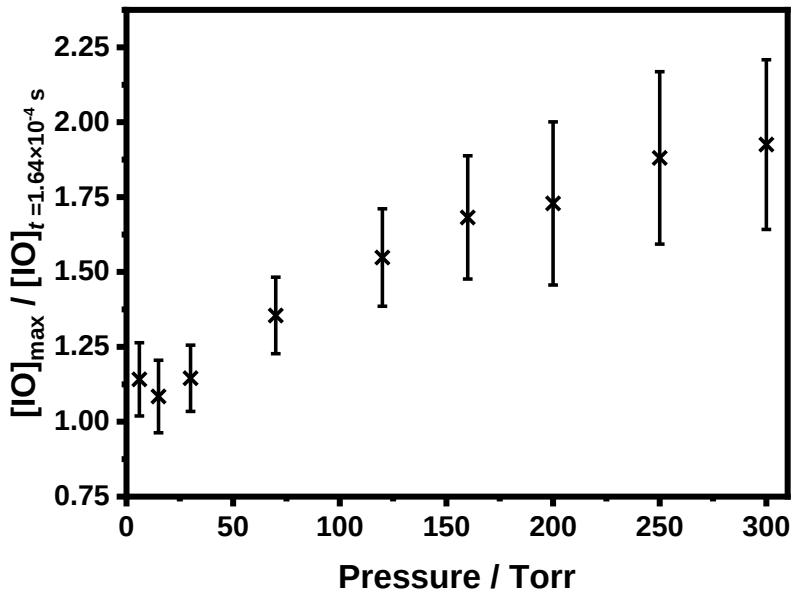

Figure 5.20: Ratio of the maximum observed IO concentration to the concentration of IO generated by the initial rapid production observed in this work, representing the yield of IO produced in the system following the initial rapid growth, as a function of pressure. Uncertainties are the 1σ standard deviation of the mean values at each pressure.

Production of IO in the system following the initial rapid production in this work potentially results from the chemistry of CH_2OO or CH_2IO_2, or a combination of the two. If produced through reactions of CH_2OO, IO can be produced either directly, via R5.4c, or indirectly, via R5.4b by way of production of CH_2IO_2 which then proceeds to generate IO through R5.9. Figures 5.15 and 5.16 indicate that R5.4b is the dominant channel of the $CH_2OO + I$ reaction and that R5.4c does not occur since association reactions, such as R5.4b, exhibit pressure dependence whereas bimolecular reactions, such as R5.4c, do not. As the fit of the Lindemann equation through the experimental data (Figure 5.15 and 5.16) shows that at zero pressure the overall rate coefficient of

R5.4 is zero or very small, this signifies that the contribution of R5.4c to the overall rate coefficient for R5.4 is not significant. Since R5.4a has already been excluded as a potential pathway for the reaction between CH_2OO and I at 298 K, this suggests that the only viable channel for this reaction is the production of the CH_2IO_2 peroxy radical. Figure 5.21 shows typical comparisons between observed and simulated IO profiles, constrained to the initial observed IO concentrations, in which R5.4 exclusively produces CH_2IO_2 (i.e. R5.4b is the only reaction pathway considered), at two different pressures. Simulations in which R5.4 produces 100 % CH_2IO_2 underpredict the observed IO at early times following photolysis where a growth is seen, and overpredict the observed IO at late time points following photolysis where the IO decay can be observed. This suggests that both the production and decay of IO in the system are underestimated in the model as listed in Table 5.1. This discrepancy between observed and simulated IO may be due to uncertainties in the chemistry of the CH_2IO_2 peroxy radical.

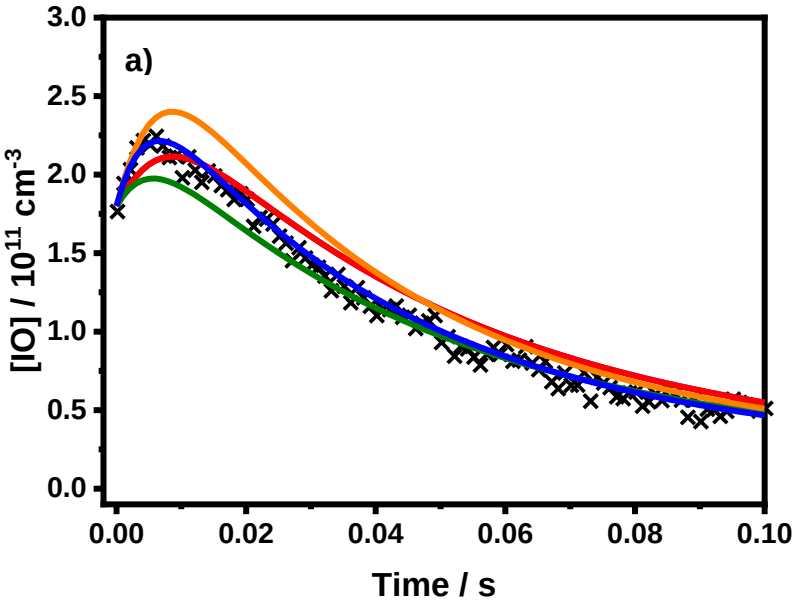

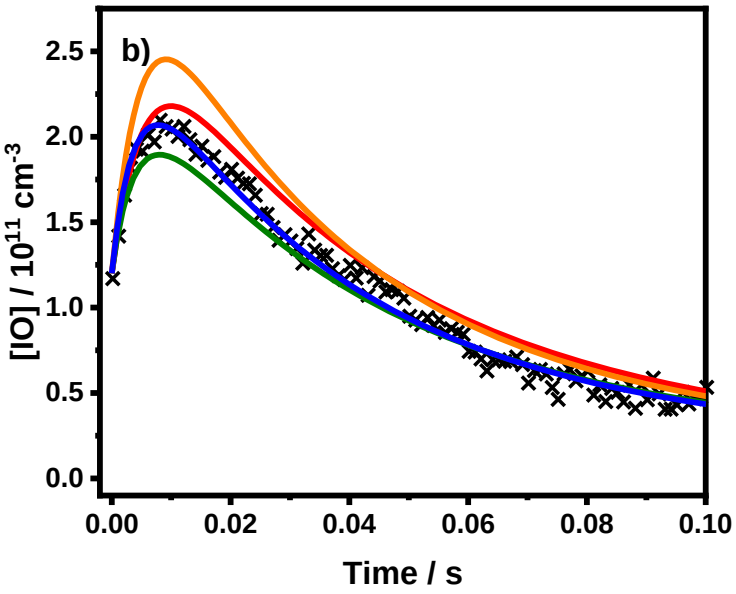

Figure 5.21: Experimentally observed IO concentrations (black points) and simulated IO profiles using the mechanism given in Table 5.1, except where specified otherwise, and constrained to the observed IO concentration at t = 1.64 × 10^{-4} s, at a) 70 Torr and b) 300 Torr. The reaction between CH_2OO and I (R5.4) was set to produce CH_2IO_2 with 100 % yield (red). Adjustments made to the rate coefficients of the CH_2IO_2 self-reaction (R5.8) and the CH_2IO_2 + I reaction (R5.9) to simulate IO profiles which better represented the IO observed in the system than using rate coefficients as given in Table 5.1 were a) 3 × $k_{5.8}$ (green), 1.5 × $k_{5.9}$ (orange) and a combination of both 3 × $k_{5.8}$ and 1.5 × $k_{5.9}$ (blue) for which p = 70 Torr, $[O_2]$ = 1.49 × 10^{17} cm^{-3}, $[CH_2I_2]$ = 1.57 × 10^{13} cm^{-3}, and $[CH_2OO]_{t=0}$ = 6.77 × 10^{11} cm^{-3} and b) 2.75 × $k_{5.8}$ (green), 1.25 × $k_{5.9}$ (orange) and a combination of both 2.75 × $k_{5.8}$ and 1.25 × $k_{5.9}$ (blue) for which p = 300 Torr, $[O_2]$ = 1.76 × 10^{17} cm^{-3}, $[CH_2I_2]$ = 1.30 × 10^{13} cm^{-3}, and $[CH_2OO]_{t=0}$ = 3.50 × 10^{11} cm^{-3}.

To investigate whether this is the case, simulations were performed in which the rate coefficients for reactions involving CH_2IO_2 (R5.8 and R5.9) were systematically increased and decreased, and the simulated IO profile was compared to the experimental data. Figure 5.21 shows that while increasing the rate coefficient for the CH_2IO_2 self-reaction ($k_{5.8}$) brings the simulated IO at late times into agreement with the observed IO, it is still underestimated at early times. It can also be seen that increasing the rate coefficient for the CH_2IO_2 + I reaction ($k_{5.9}$) increases the IO production such that the experimentally observed IO at early times is accounted for, but overestimates IO at later times. On average, an increase in the rate coefficient for

the CH_2IO_2 self-reaction of a factor of 3 was required in order to simulate an IO profile in agreement with the observed IO whereas the increase required for the rate coefficient of the CH_2IO_2 + I reaction is approximately a factor of 2. An example of the IO profiles simulated upon these adjustments to the rate coefficients for the CH_2IO_2 self-reaction and the reaction between CH_2IO_2 and I and their comparison to experimental data is given in Figure 5.21a for data at 70 Torr and in Figure 5.21b for data at 300 Torr. These results suggest that kinetics of CH_2IO_2 chemistry in the model, in particular that of the CH_2IO_2 self-reaction, need to be significantly altered in order to account for the observed IO in the system. It should be noted that these adjustments to the rate coefficients of R5.8 and R5.9 show that a combination of changes to both rate coefficients may be required, and demonstrate the magnitude of these changes, in order to produce an IO simulation which can account for the IO observed in the system. However, a quantitative analysis of CH_2IO_2 chemistry is outside the scope of this work. It is worth noting that an attempt was made to simultaneously fit the numerical integration model listed in Table 5.1 to both time-resolved CH_2OO and IO traces experimentally observed in this work, however the model showed little sensitivity to the experimental IO data. Results reported in this work for $k_{5.3}$ and $k_{5.4}$ include uncertainties arising from assumptions regarding rate coefficients and branching ratios used in the model given in Table 5.1.

5.4.2.3.1 CH_2OO + IO Sensitivity

Impacts of a potential reaction between CH_2OO and IO were also investigated in this work through model fits in which the reaction between CH_2OO and IO was included in the mechanism. A previous study in the literature has provided an estimated rate coefficient of this reaction of 1.5×10^{-10} cm^3 s^{-1}, where the main focus of the study was determination of the kinetics of the CH_2OO + O_3 reaction and no IO data was collected.[48] Work has also been carried out in this laboratory to determine the rate coefficient of the reaction between CH_2OO and O_3, in which both CH_2OO and IO were measured simultaneously and a fitting scheme along with numerical integration have been used to determine the rate coefficient of the CH_2OO + IO side reaction in this system, giving a value of $(7.6 \pm 1.4) \times 10^{-11}$ cm^3 s^{-1}.[49] It was reported that results for the rate coefficients determined for CH_2OO + O_3 and CH_2OO + IO were not

sensitive to the value of the rate coefficient for CH_2OO + I owing to the low concentration of I atoms in the system as a result of efficient titration of I to IO through reaction with O_3. Under such conditions of high [O_3], I atoms are rapidly converted to IO leading to a higher relative concentration of IO to I, and hence the dominant secondary chemistry reaction is shifted from CH_2OO + I, as in this work, to CH_2OO + IO.

$$CH_2OO + IO \rightarrow \text{products} \qquad \text{(R5.12)}$$

In this work, fits were performed with the rate coefficient for CH_2OO + IO fixed to a series of values between 1×10^{-11} and 1×10^{-10} cm^3 s^{-1}, with the mechanism otherwise as shown in Table 5.1. However, results for $k_{5.3}$ and $k_{5.4}$ obtained by fitting to the observed CH_2OO profiles showed low sensitivity to the inclusion of a reaction between CH_2OO and IO in the model with a rate coefficient below 1×10^{-10} cm^3 s^{-1}, regardless of whether the model was constrained or unconstrained to the observed initial IO concentrations. This confirms the expectation that the reactions of CH_2OO with itself and the I atom dominate the system considering the relative amounts of CH_2OO, I and IO ([I]>[CH_2OO]>[IO]), and hence sensitivity of the system to R5.12 is expected to be minimal. Figure 5.22 shows the impacts on the fit results for $k_{5.3}$ and $k_{5.4}$. For the largest rate coefficient adopted in the model for CH_2OO + IO, the fit results for $k_{5.3}$ and $k_{5.4}$ are within 15 % of the values obtained from model fits in which CH_2OO + IO is not considered, with the loss of IO dominated by the IO self-reaction. Results for $k_{5.3}$ and $k_{5.4}$ reported in this work are thus given from fits performed in which the reaction CH_2OO + IO is not considered.

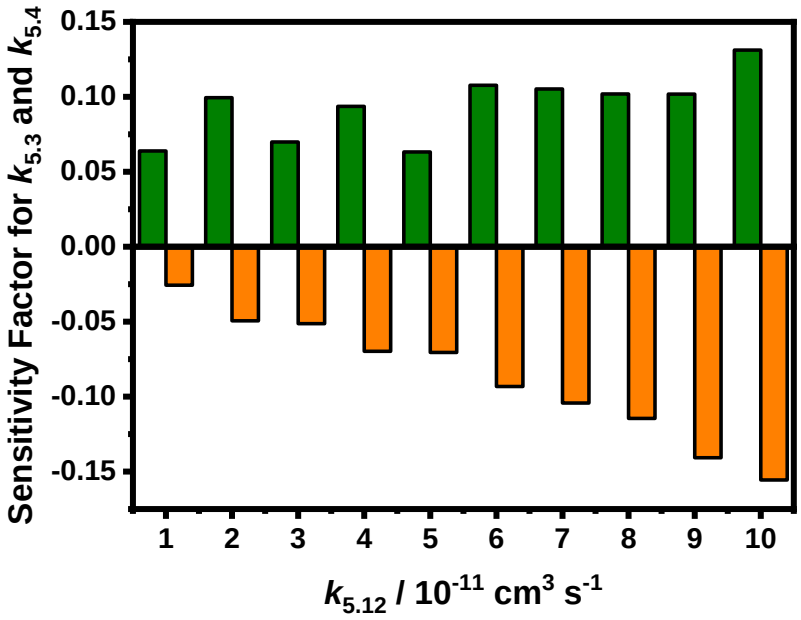

Figure 5.22: Sensitivity of $k_{5.3}$ (green) and $k_{5.4}$ (orange) to the rate coefficient for CH_2OO + IO, $k_{5.12}$, adopted in the model used to fit to experimental observations. Results are shown for model fits performed at p = 300 Torr, at which pressure the effects, if any, of a potential CH_2OO + IO reaction are expected to be most prevalent due to the high yield of IO in the system. The sensitivity factors are calculated using Equation 5.11 and defined as the fractional difference in the fit result for the rate coefficient compared to the result obtained for fits in which CH_2OO + IO is not considered subtract 1.

5.5 Conclusions

The kinetics of the CH_2OO self-reaction and the reaction of CH_2OO with I have been investigated at a temperature of 298 K and pressures between 6 and 300 Torr using pulsed laser flash photolysis of $CH_2I_2/O_2/N_2$ gas mixtures coupled with time-resolved broadband UV absorption spectroscopy.[50] Kinetics of the CH_2OO self-reaction have been shown to be independent of pressure over the range investigated, with a rate coefficient of $(8.0 \pm 1.1) \times 10^{-11}$ cm^3 s^{-1} over all pressures, in agreement with results reported by Ting *et al.*,[3] Buras *et al.*[2] and the results of Chhantyal-Pun *et al.*[4] at 7 Torr. The reaction between CH_2OO and I is significant in the reaction system, with a pressure-dependent total rate coefficient ranging from $(1.1\ ^{+2.2}_{-1.1}) \times 10^{-12}$ cm^3 s^{-1} at 6 Torr to $(5.5 \pm 2.1) \times 10^{-11}$ cm^3 s^{-1} at 300 Torr which can be parameterised by a Lindemann fit using $k_0 = (4.4 \pm 1.0) \times 10^{-29}$ cm^6 s^{-1} and $k_\infty = (6.7 \pm 0.6) \times 10^{-11}$ cm^3

s^{-1}. The pressure dependence observed in the rate coefficient of the CH_2OO + I reaction in this work, with an extensive dataset over a range of pressures and initial radical concentrations, offers some clarity as to the source of the discrepancies in previously reported measurements and reconciles the results of Ting *et al.*,[3] Chhantyal-Pun *et al.*[4] and Buras *et al.*[2] The production of IO in the system has also been investigated as a function of pressure. Results indicate that IO formation results from the chemistry of both CH_2OO and CH_2IO_2, with relative contributions from CH_2OO and CH_2IO_2 chemistry varying as a function of pressure owing to the pressure-dependent yields of CH_2OO and CH_2IO_2 from $CH_2I + O_2$ and the pressure dependence of the CH_2OO + I reaction.

5.6 References

1. Su, Y.-T.; Lin, H.-Y.; Putikam, R.; Matsui, H.; Lin, M. C.; Lee, Y.-P., Extremely rapid self-reaction of the simplest Criegee intermediate CH_2OO and its implications in atmospheric chemistry. *Nature Chemistry* **2014,** *6* (6), 477–483.

2. Buras, Z. J.; Elsamra, R. M. I.; Green, W. H., Direct determination of the simplest Criegee intermediate (CH_2OO) self reaction rate. *The Journal of Physical Chemistry Letters* **2014,** *5* (13), 2224-2228.

3. Ting, W.-L.; Chang, C.-H.; Lee, Y.-F.; Matsui, H.; Lee, Y.-P.; Lin, J. J.-M., Detailed mechanism of the $CH_2I + O_2$ reaction: Yield and self-reaction of the simplest Criegee intermediate CH_2OO. *The Journal of Chemical Physics* **2014,** *141* (10), 104308.

4. Chhantyal-Pun, R.; Davey, A.; Shallcross, D. E.; Percival, C. J.; Orr-Ewing, A. J., A kinetic study of the CH_2OO Criegee intermediate self-reaction, reaction with SO_2 and unimolecular reaction using cavity ring-down spectroscopy. *Physical Chemistry Chemical Physics* **2015,** *17* (5), 3617-3626.

5. Vereecken, L.; Hardera, H.; Novellia, A., The reaction of Criegee intermediates with NO, RO_2, and SO_2, and their fate in the atmosphere. *Physical Chemistry Chemical Physics* **2012,** *14* (42), 14682-14695.

6. Boy, M.; Mogensen, D.; Smolander, S.; Zhou, L.; Nieminen, T.; Paasonen, P.; Plass-Dülmer, C.; Sipilä, M.; Petäjä, T.; Mauldin, L.; Berresheim, H.; Kulmala, M., Oxidation of SO_2 by stabilized Criegee intermediate (sCI) radicals as a crucial source for atmospheric sulfuric acid concentrations. *Atmospheric Chemistry and Physics* **2013,** *13* (7), 3865–3879.

7. Percival, C. J.; Welz, O.; Eskola, A. J.; Savee, J. D.; Osborn, D. L.; Topping, D. O.; Lowe, D.; Utembe, S. R.; Bacak, A.; McFiggans, G.; Cooke, M. C.; Xiao, P.; Archibald, A. T.; Jenkin, M. E.; Derwent, R. G.; Riipinen, I.; Mok, D. W. K.; Lee, E. P. F.; Dyke, J. M.; Taatjes, C. A.; Shallcross, D. E., Regional and global impacts of Criegee intermediates on atmospheric sulphuric acid concentrations and first steps of aerosol formation. *Faraday Discussions* **2013,** *165*, 45-73.

8. Bonn, B.; Bourtsoukidis, E.; Sun, T. S.; Bingemer, H.; Rondo, L.; Javed, U.; Li, J.; Axinte, R.; Li, X.; Brauers, T.; Sonderfeld, H.; Koppmann, R.; Sogachev, A.; Jacobi, S.; Spracklen, D. V., The link between atmospheric radicals and newly formed particles at a spruce forest site in Germany. *Atmospheric Chemistry and Physics* **2014,** *14* (9), 10823–10843.

9. Kim, S.; Guenther, A.; Lefer, B.; Flynn, J.; Griffin, R.; Rutter, A. P.; Gong, L.; Cevik, B. K., Potential role of stabilized Criegee radicals in sulfuric acid production in a high biogenic VOC environment. *Environmental Science and Technology* **2015,** *49* (6), 3383-3391.

10. Novelli, A.; Hens, K.; Ernest, C. T.; Martinez, M.; Nölscher, A. C.; Sinha, V.; Paasonen, P.; Petäjä, T.; Sipilä, M.; Elste, T.; Plass-Dülmer, C.; Phillips, G. J.; Kubistin, D.; Williams, J.; Vereecken, L.; Lelieveld, J.; Harder, H., Estimating the atmospheric concentration of Criegee intermediates and their possible interference in a FAGE-LIF instrument. *Atmospheric Chemistry and Physics* **2017,** *17* (12), 7807-7826.

11. Vereecken, L.; Novelli, A.; Taraborrelli, D., Unimolecular decay strongly limits the atmospheric impact of Criegee intermediates. *Physical Chemistry Chemical Physics* **2017,** *19* (47), 31599-31612.

12. Khan, M. A. H.; Morris, W. C.; Galloway, M.; Shallcross, B. M. A.; Percival, C. J.; Shallcross, D. E., An estimation of the levels of stabilized Criegee

intermediates in the UK urban and rural atmosphere using the steady-state approximation and the potential effects of these intermediates on tropospheric oxidation cycles. *International Journal of Chemical Kinetics* **2017,** *49* (8), 611–621.

13. Khan, M. A. H.; Percival, C. J.; Caravan, R. L.; Taatjes, C. A.; Shallcross, D. E., Criegee intermediates and their impacts on the troposphere. *Environmental Science: Processes & Impacts* **2018,** *20* (3), 437-453.

14. Welz, O.; Savee, J. D.; Osborn, D. L.; Vasu, S. S.; Percival, C. J.; Shallcross, D. E.; Taatjes, C. A., Direct kinetic measurements of Criegee intermediate (CH_2OO) formed by reaction of CH_2I with O_2. *Science* **2012,** *335* (6065), 204-207.

15. Chao, W.; Hsieh, J.-T.; Chang, C.-H.; Lin, J. J.-M., Direct kinetic measurement of the reaction of the simplest Criegee intermediate with water vapor. *Science* **2015,** *347* (6223), 751-754.

16. Lewis, T. R.; Blitz, M. A.; Heard, D. E.; Seakins, P. W., Direct evidence for a substantive reaction between the Criegee intermediate, CH_2OO, and the water vapour dimer. *Physical Chemistry Chemical Physics* **2015,** *17* (7), 4859-4863.

17. Smith, M. C.; Chang, C.-H.; Chao, W.; Lin, L.-C.; Takahashi, K.; Boering, K. A.; Lin, J. J.-M., Strong negative temperature dependence of the simplest Criegee intermediate CH_2OO reaction with water dimer. *Journal of Physical Chemistry Letters* **2015,** *6* (14), 2708-2713.

18. Sheps, L.; Rotavera, B.; Eskola, A. J.; Osborn, D. L.; Taatjes, C. A.; Au, K.; Shallcross, D. E.; Khan, M. A. H.; Percival, C. J., The reaction of Criegee intermediate CH_2OO with water dimer: primary products and atmospheric impact. *Physical Chemistry Chemical Physics* **2017,** *19* (33), 21970-21979.

19. Sheps, L., Absolute ultraviolet absorption spectrum of a Criegee intermediate CH_2OO. *The Journal of Physical Chemistry Letters* **2013,** *4* (24), 4201-4205.

20. Liu, Y.; Bayes, K. D.; Sander, S. P., Measuring rate constants for reactions of the simplest Criegee intermediate (CH_2OO) by monitoring the OH radical. *Journal of Physical Chemistry A* **2014,** *118* (4), 741-747.

21. Stone, D.; Blitz, M.; Daubney, L.; Howes, N. U. M.; Seakins, P. W., Kinetics of CH_2OO reactions with SO_2, NO_2, NO, H_2O and CH_3CHO as a function of pressure. *Physical Chemistry Chemical Physics* **2014,** *16* (3), 1139-1149.

22. Taatjes, C. A.; Welz, O.; Eskola, A. J.; Savee, J. D.; Scheer, A. M.; Shallcross, D. E.; Rotavera, B.; Lee, E. P. F.; Dyke, J. M.; Mok, D. W. K.; Osborn, D. L.; Percival, C. J., Direct measurements of conformer-dependent reactivity of the Criegee intermediate CH_3CHOO. *Science* **2013,** *340* (6129), 177-180.

23. Sheps, L.; Scully, A. M.; Au, K., UV absorption probing of the conformer-dependent reactivity of a Criegee intermediate CH_3CHOO. *Physical Chemistry Chemical Physics* **2014,** *16* (48), 26701-26706.

24. Huang, H.-L.; Chao, W.; Lin, J. J.-M., Kinetics of a Criegee intermediate that would survive high humidity and may oxidize atmospheric SO_2. *Proceedings of the National Academy of Sciences* **2015,** *112* (35), 10857-10862.

25. Smith, M. C.; Chao, W.; Takahashi, K.; Boering, K. A.; Lin, J. J.-M., Unimolecular decomposition rate of the Criegee intermediate $(CH_3)_2COO$ measured directly with UV absorption spectroscopy. *Journal of Physical Chemistry A* **2016,** *120* (27), 4789-4798.

26. Chhantyal-Pun, R.; Welz, O.; Savee, J. D.; Eskola, A. J.; Lee, E. P. F.; Blacker, L.; Hill, H. R.; Ashcroft, M.; Khan, M. A. H.; Lloyd-Jones, G. C.; Evans, L.; Rotavera, B.; Huang, H.; Osborn, D. L.; Mok, D. K. W.; Dyke, J. M.; Shallcross, D. E.; Percival, C. J.; Orr-Ewing, A. J.; Taatjes, C. A., Direct measurements of unimolecular and bimolecular reaction kinetics of the Criegee intermediate $(CH_3)_2COO$. *Journal of Physical Chemistry A* **2017,** *121* (1), 4-15.

27. Welz, O.; Eskola, A. J.; Sheps, L.; Rotavera, B.; Savee, J. D.; Scheer, A. M.; Osborn, D. L.; Lowe, D.; Booth, M.; Xiao, P.; Khan, M. A. H.; Percival, C. J.; Shallcross, D. E.; Taatjes, C. A., Rate coefficients of C_1 and C_2 Criegee intermediate reaction with formic and acetic acid near the collision limit: Direct kinetics measurements and atmospheric implications. *Angewandte Chemie International Edition* **2014,** *53* (18), 4547-4550.

28. Chhantyal-Pun, R.; McGillen, M. R.; Beames, J. M.; Khan, M. A. H.; Percival, C. J.; Shallcross, D. E.; Orr-Ewing, A. J., Temperature-dependence of the

rates of reaction of trifluoroacetic acid with Criegee intermediates. *Angewandte Chemie International Edition* **2017,** *56* (31), 9044-9047.

29. Vereecken, L.; Harder, H.; Novelli, A., The reactions of Criegee intermediates with alkenes, ozone, and carbonyl oxides. *Physical Chemistry Chemical Physics* **2014,** *16* (9), 4039-4049.

30. Ting, W.-L.; Chen, Y.-H.; Chao, W.; Smith, M. C.; Lin, J. J.-M., The UV absorption spectrum of the simplest Criegee intermediate CH_2OO. *Physical Chemistry Chemical Physics* **2014,** *16* (22), 10438-10443

31. Stone, D.; Blitz, M.; Daubney, L.; Ingham, T.; Seakins, P., CH_2OO Criegee biradical yields following photolysis of CH_2I_2 in O_2. *Physical Chemistry Chemical Physics* **2013,** *15* (44), 19119-19124

32. Keller-Rudek, H.; Moortgat, G. K.; Sander, R.; Sörensen, R., The MPI-Mainz UV/VIS spectral atlas of gaseous molecules of atmospheric interest. *Earth System Science Data* **2013,** *5*, 365–373.

33. Sander, S. P.; Abbatt, J. P. D.; Barker, J. R.; Burkholder, J. B.; Friedl, R. R.; Golden, D. M.; Huie, R. E.; Kolb, C. E.; Kurylo, M. J.; Moortgat, G. K.; Orkin, V. L.; Wine, P. H., Chemical kinetics and photochemical data for use in atmospheric studies - Evaluation number 17. In *JPL Publication 10-6*, Jet Propulsion Laboratory: Pasadena, California, 2011.

34. Espenson, J. H., *Chemical kinetics and reaction mechanisms*. The McGraw-Hill Companies, Inc: USA, 1995.

35. *FACSIMILE Kinetic Modelling Software*, MCPA Software Ltd: 2014.

36. Masaki, A.; Tsunashima, S.; Washida, N., Rate constants for reactions of substituted methyl radicals (CH_2OCH_3, CH_2NH_2, CH_2I, and CH_2CN) with O_2. *The Journal of Physical Chemistry* **1995,** *99* (35), 13126-13131.

37. Eskola, A. J.; Wojcik-Pastuszka, D.; Ratajczak, E.; Timonen, R. S., Kinetics of the reactions of CH_2Br and CH_2I radicals with molecular oxygen at atmospheric temperatures. *Physical Chemistry Chemical Physics* **2006,** *8* (12), 1416-1424.

38. Gravestock, T. J.; Blitz, M. A.; Bloss, W. J.; Heard, D. E., A multidimensional study of the reaction $CH_2I + O_2$: products and atmospheric implications. *ChemPhysChem* **2010,** *11* (18), 3928-3941.

39. Atkinson, R.; Baulch, D. L.; Cox, R. A.; Crowley, J. N.; Hampson, R. F.; Hynes, R. G.; Jenkin, M. E.; Rossi, M. J.; Troe, J., Evaluated kinetic and photochemical data for atmospheric chemistry: Volume III – gas phase reactions of inorganic halogens. *Atmospheric Chemistry and Physics* **2007,** *7* (4), 981–1191.

40. Su, Y.-T.; Huang, Y.-H.; Witek, H. A.; Lee, Y.-P., Infrared absorption spectrum of the simplest Criegee intermediate CH_2OO. *Science* **2013,** *340* (6129), 174-176.

41. Anglada, J. M.; Olivella, S.; Solé, A., The reaction of formaldehyde carbonyl oxide with the methyl peroxy radical and its relevance in the chemistry of the atmosphere. *Physical Chemistry Chemical Physics* **2013,** *15* (43), 18921-18933.

42. Miliordos, E.; Xantheas, S. S., The origin of the reactivity of the Criegee intermediate: Implications for atmospheric particle growth. *Angewandte Chemie International Edition* **2016,** *55* (3), 1015 –1019.

43. Enami, S.; Ueda, J.; Goto, M.; Nakano, Y.; Aloisio, S.; Hashimoto, S.; Kawasaki, M., Formation of iodine monoxide radical from the reaction of CH_2I with O_2. *The Journal of Physical Chemistry A* **2004,** *108* (30), 6347-6350.

44. Enami, S.; Sakamoto, Y.; Yamanaka, T.; Hashimoto, S.; Kawasaki, M.; Tonokura, K.; Tachikawa, H., Reaction mechanisms of IO radical formation from the reaction of CH_3I with Cl atom in the presence of O_2. *Bulletin of the Chemical Society of Japan* **2008,** *81* (10), 1250-1257.

45. Dillon, T. J.; Tucceri, M. E.; Sander, R.; Crowley, J. N., LIF studies of iodine oxide chemistry. *Physical Chemistry Chemical Physics* **2008,** *10* (11), 1540-1554.

46. Foreman, E. S.; Murray, C., Kinetics of IO production in the $CH_2I + O_2$ reaction studied by cavity ring-down spectroscopy. *The Journal of Physical Chemistry A* **2015,** *119* (34), 8981-8990.

47. Stone, D.; Au, K.; Sime, S.; Medeiros, D. J.; Blitz, M.; Seakins, P. W.; Decker, Z.; Sheps, L., Unimolecular decomposition kinetics of the stabilised Criegee

intermediates CH_2OO and CD_2OO. *Physical Chemistry Chemical Physics* **2018,** *20* (38), 24940-24954.

48. Chang, Y.-P.; Chang, H.-H.; Lin, J. J.-M., Kinetics of the simplest Criegee intermediate reaction with ozone studied using a mid-infrared quantum cascade laser spectrometer. *Physical Chemistry Chemical Physics* **2018,** *20* (1), 97-102.

49. Lavinia Onel; Mark Blitz; Paul Seakins; Dwayne Heard; Stone, D., Kinetics of the gas phase reactions of the Criegee intermediate CH_2OO with O_3 and IO. *Journal of Physical Chemistry A* **2020,** *124* (31), 6287-6293.

50. Lewis, T.; Heard, D. E.; Blitz, M. A., A novel multiplex absorption spectrometer for time-resolved studies. *Review of Scientific Instruments* **2018,** *89* (2), 024101.

Chapter 6

Identification, Monitoring, and Reaction Kinetics of Reactive Trace Species Using Time-Resolved Mid-Infrared Quantum Cascade Laser Absorption Spectroscopy: Development, Characterisation, and Initial results

The behaviour of reactive intermediates is critical to understanding the chemistry of complex systems. In the gas phase, reactive intermediates govern the chemistry and composition of planetary atmospheres,[1] the interstellar medium and star-forming regions,[2] as well as controlling combustion processes and autoignition.[3, 4] In the Earth's atmosphere, the chemistry of reactive intermediates determines the rate at which compounds emitted into the atmosphere are removed and transformed into other species, and thus drives changes to air quality and climate (refer to Chapter 1 for further details).[5, 6]

Experimental investigation of the spectroscopy, kinetics, and reaction mechanisms of reactive intermediates is key to understanding the behaviour of such species, requiring sensitive and specific detection techniques capable of monitoring changes in concentrations during the course of reactions commonly occurring on microsecond to millisecond timescales. Flash photolysis experiments, in which a reactive species is generated rapidly by a brief pulse of light from a flashlamp or laser and then monitored throughout its subsequent reactions (further information is provided in Chapter 3), have enabled the study of many reactions of interest. However, while the flash photolysis method can be coupled to a wide range of techniques to determine the kinetics of a reaction, limitations remain, particularly surrounding the identification of reaction products and measurements of product yields.

6.1 Measuring Reactive Trace Species

For the study of fast reactions, spectroscopic or mass spectrometric techniques are typically required to provide the necessary time resolution. A detailed intercomparison of some of the most widely employed analytical detection techniques for atmospheric chemistry applications is provided in Chapter 3, therefore only a brief

discussion is given here. Laser-induced fluorescence (LIF) spectroscopy has been demonstrated to have both high sensitivity and specificity for the measurement and identification of reactants and products, but is not an absolute technique and so requires either calibration or the use of an internal standard to determine yields.[7] Moreover, LIF can only be applied to the relatively small number of species that exhibit fluorescence spectra. Mass spectrometry can be applied more widely, particularly if soft ionisation techniques such as photoionisation are employed, but such techniques can be costly and require sampling of a reaction mixture into an ionisation and detection region which can limit investigations to low pressure regimes.[8-11] Absorption techniques can therefore be beneficial as these can provide absolute measurements over a wide range of temperatures and pressures.

Absorption measurements based on ultraviolet (UV) spectroscopy have been used successfully to measure the kinetics of a wide range of reactions of interest, with advantages for radical-radical reactions where absolute concentrations are required. While UV absorption spectra can be relatively broad and featureless,[12] developments in the use of broadband light sources have enabled the separation of multiple absorbing species with overlapping spectra,[13] particularly if any of the spectra display distinctive vibronic structure, such as in experiments discussed in Chapter 4 for the determination of the UV absorption cross-sections of the simplest Criegee intermediate formaldehyde oxide, CH_2OO. Multipass[14] and cavity enhanced techniques[13] can also offer significant improvements to sensitivity. However, UV absorption experiments are typically employed to monitor changes in reactant concentrations to determine reaction kinetics, such as in experiments discussed in Chapter 5 for the determination of reaction kinetics of the CH_2OO self-reaction, $CH_2OO + CH_2OO$, and the $CH_2OO + I$ reaction, but identification of products and measurement of product yields is often not possible owing to a lack of suitable UV absorption features or low UV absorption cross-sections for product species.

There is thus interest in the development and use of infrared (IR) techniques which, despite lower absorption cross-sections compared to the UV, have the potential to be implemented more extensively since most species exhibit some features in the IR region of the spectrum. IR absorption techniques are also often advantageous over other spectroscopic methods since IR transitions are typically not dissociative,[15, 16]

and as a result do not suffer lifetime broadening or probe-induced photochemistry, and Doppler broadening in the IR is less problematic than in the UV or visible, leading to better resolution of closely spaced features.[15, 16] Furthermore, the distinct structure of ro-vibrationally resolved spectra observed in high resolution IR can avoid by-product interferences, provides high selectivity and allows for unambiguous identification of species, especially desirable when more than one species which absorbs in the same region is present. Where reaction products cannot be measured *via* UV absorption, IR absorption provides a method to detect and track product formation from which rates of reaction, identification of products and quantification of product yields can be determined.

The mid-IR region of the electromagnetic spectrum (between 2.5 and 25 μm or 4000 and 400 cm^{-1}) is of particular interest for spectroscopic measurements since it presents windows of atmospheric transmission where many molecules of interest, including but not limited to CO, CH_4, NO, N_2O, HCHO, NH_3 and SO_2,[17] have fundamental absorption bands. Furthermore, the majority of complex organic molecules (typically more than 5 atoms) have signatures between 7 and 12 μm. Absorption spectra in the mid-IR of major small atmospheric species of potential interest for atmospheric chemistry are shown in Figure 6.1. Because the absorption lines for a given gas can typically be several orders of magnitude (often 100×) stronger or more intense in the mid-IR than the near-IR overtone or combination bands (0.7-2.5 μm or 14,000-4000 cm^{-1}), there has been significant activity in recent years to develop practical, room temperature tuneable lasers to cover this region.[16]

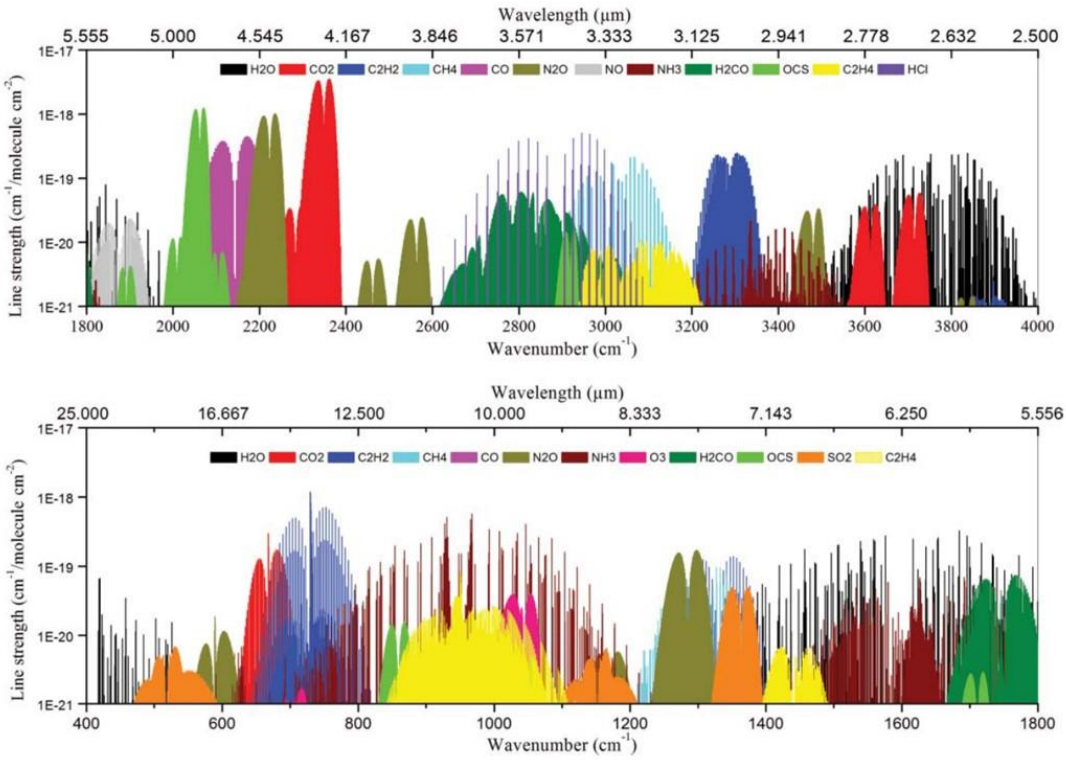

Figure 6.1: Absorption spectra in the mid-IR region (2.5-25 μm or 4000-400 cm^{-1}) for major atmospheric species as simulated from the HITRAN data base showing integrated line intensities at 296 K . Reproduced from reference 17.[17]

For many reactions of atmospheric interest, products have been determined by long-path Fourier transform infrared (FT-IR) absorption spectroscopy in atmospheric simulation chambers used to study reactions at a mechanistic level,[18-21] but this method has relatively poor time resolution compared to direct studies of elementary reactions and can be influenced by secondary chemistry and wall reactions which may transform reactive products into more stable species on the timescale of the experiment. Step-scan FT-IR experiments,[22, 23] in which spectra are recorded at successive timepoints during the course of a reaction, offer improved time resolution and aid direct identification of reaction products. However, step-scan FT-IR has relatively poor spectral resolution compared to other techniques and is not typically employed to investigate reaction kinetics owing to the length of time required to record a suitable time profile.

6.2 Quantum Cascade Lasers

Diode lasers,[15] quantum cascade lasers (QCLs),[24-28] and frequency comb lasers[29-31] can be used to give both high spectral resolution and high temporal resolution, and can be applied to measurements of transient species. Frequency comb lasers can provide extremely high resolution spectra, but there are, at present, relatively few examples[30] of their application in chemistry and chemical kinetics owing to relatively high cost and complexity of the experimental setup. In contrast to diode lasers, mid-infrared QCLs do not require cryogenic cooling operation and do not suffer issues related to uneven diode quality or unpredictable tunability.[16] The spectral output of QCLs can be tailored to transitions over a wide range, providing access to regions of the spectrum not readily accessible with diode lasers or frequency comb lasers.[26, 27, 32] QCLs have high output powers, and can reach several hundred mW to ~1 mW,[16, 26-28] compared to typical powers of a few mW for diode lasers,[16] and absorbances on the order of 10^{-6} have been reported for QCL-based infrared absorption experiments for stable species.[33] The high resolution, specificity, and sensitivity of QCL-based absorption techniques has led to the development of a number of field instruments for detection of trace species in the atmosphere,[17, 34] including CH_4,[35, 36] CO_2,[36] OCS,[35] N_2O,[35-37] H_2O,[35] HCOOH,[38] and HONO[39] which can be challenging to monitor by other methods. The high power and spectral resolution of QCL light sources, enabling sensitive and specific experiments in regions of the spectrum characterised by strong fundamental transitions, have also led to interest from the chemical kinetics community.

QCLs consist of layers of semiconductor material that create a series of coupled quantum wells in which the layer thickness determines the depth of the quantum well and thus the energy of emitted photons.[24, 26] In contrast to diode lasers, which involve electronic transitions between conduction and valence bands, laser action in QCLs involves intersubband transitions within the conduction band, typically *via* a three-level system.[26, 40, 41] In the absence of an electric field, electrons are confined in the quantum wells within an injector region. When an electric field is applied, the quantum wells within the injector region align and electrons are injected into an upper intersubband state, creating a population inversion. Relaxation of electrons to a lower intersubband state, resulting in photon emission, followed by tunnelling of electrons

from the lower intersubband state into the injector region of the next layer creates a cascade of electrons as the layer structure is traversed, leading to increased photon emission and significant optical gain.[26] This design of alternating wells and barriers, or active and injector regions, often numbering 500-1000,[26] is shown in Figure 6.2 which schematically illustrates the operating mechanism of QCLs. Broadband emission can be achieved using external cavity (EC) QCLs, which can give coverage of several hundred cm^{-1}, or Fabry-Perót (FP) QCLs, giving coverage of ~50 cm^{-1}, while single mode emission relevant to this work is achieved using distributed feedback (DFB) QCLs.[32] For emission in the mid-IR, DFB QCLs can be operated at room temperature, with control of the temperature of the semiconductor and the applied current allowing fine tuning of the laser output within a range of ~5 cm^{-1}.[32]

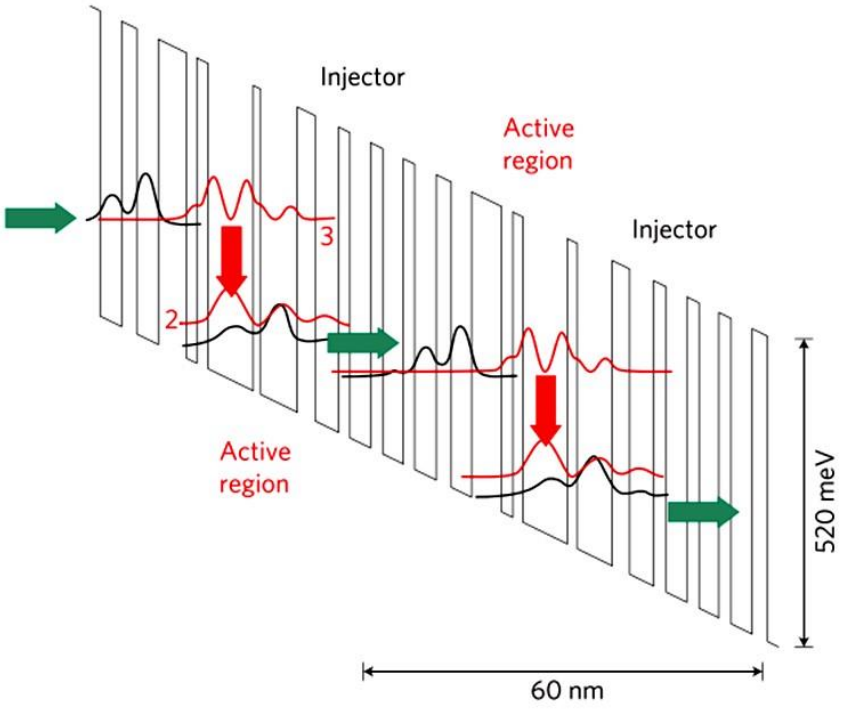

Figure 6.2: Simplified schematic of the working mechanism of QCLs, showing the conduction band structure for the QCL, where the laser transition is between subbands 3 and 2. Reproduced from reference 26.[26]

Pulsed QCLs have been used to measure the production of CO in the combustion of *n*-heptane,[42] and have been used to determine the IR absorption spectrum and cross-sections of the Criegee intermediate CH_2OO.[43-45] Quasi-continuous QCLs,

pulsed QCLs in which the pulse period is relatively long compared to the lifetime of the species under investigation, have also been used to investigate the spectra and kinetics of CH_2OO,[46] and continuous wave (cw) QCLs have been used to investigate the kinetics of not only CH_2OO[47-51] but also other larger Criegee intermediates[47] as well as the spectroscopy and kinetics of the atmospherically important peroxy radicals HO_2 [52, 53] and CH_3O_2.[54] Measurements of SO_2 and SO_3 at high sensitivity have also been demonstrated using quasi-continuous QCLs, used to detect and monitor SO_2 and SO_3 in aircraft test combustor exhausts at room temperature.[55] Figure 6.3 shows the approximate wavelength region coverage for tuneable lasers in the IR region including QCLs, and demonstrates the versatility of mid-IR QCLs since they operate at useful wavelengths for measurement of many trace atmospheric species in this region, as depicted in Figure 6.1. In recent years, the design flexibility of QCLs has further expanded the achievable wavelength range to ~3-25 μm, resulting in almost complete coverage of the mid-IR region.[26] While mid-IR QCLs have been employed to study the kinetics and spectroscopy of reactive species relevant to atmospheric chemistry, there are still few examples of the use of QCL-based techniques to identify reaction products and to determine product yields.

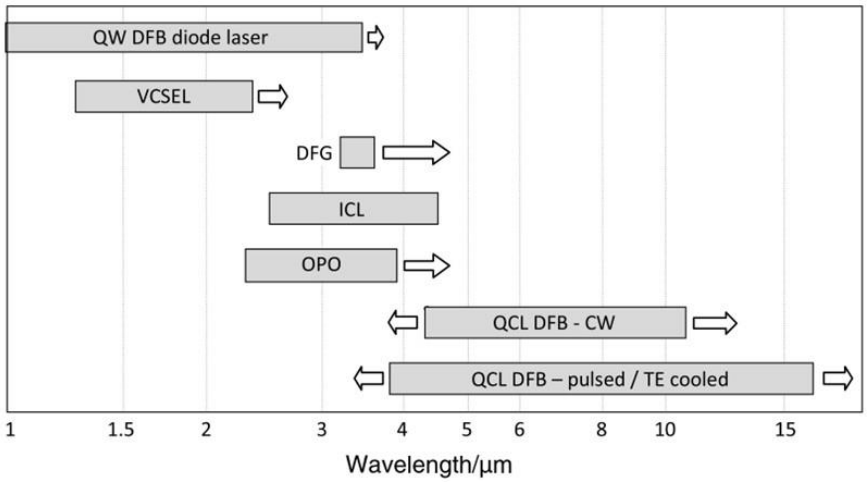

Figure 6.3: Wavelength region coverage for room temperature, solid state tuneable lasers in the IR, with arrows indicating the direction of research activity in a rapidly developing field. Key: CW- continuous wave; QW DFB- quantum well distributed feedback; VCSEL- vertical cavity surface emitting laser; DFG- difference frequency generation; ICL- interband cascade laser; OPO- optical parametric oscillator; QCL- quantum cascade laser. Reproduced from reference 16.[16]

6.3 Criegee Intermediate + SO_2 Reaction

A new experimental system has been developed in this laboratory using mid-IR QCL measurements of reactive and product species as the basis for detection. The intention of developing such an instrument is to monitor reaction kinetics and product yields of reactions of interest. One such reaction of interest is that of $CH_2OO + SO_2$, since it has potentially significant atmospheric implications, which are discussed further in this chapter and in Chapter 1. As part of the development and characterisation of the new experimental system developed in this work, it was important to study and measure a reaction with well-established kinetics using this new system to test the system's accuracy, validity and reproducibility. Since the kinetics of the reaction between CH_2OO and SO_2 are now well-established in the literature, details for which are provided below, this reaction was selected to be used as a test case for the system. Employing mid-IR QCL detection during this work also enabled the product yields of the $CH_2OO + SO_2$ reaction to be investigated, which are not as well studied and established in the literature as the kinetics of the reaction.

The reactions of Criegee intermediates with SO_2 have been demonstrated to be important in the atmosphere (refer to Chapter 1 for further information). The bimolecular reactions between Criegee intermediates and SO_2 result in the production of sulphate aerosol, secondary organic aerosols (SOA) and sulphuric acid, H_2SO_4, through oxidation of SO_2 to sulphur trioxide, SO_3, and thus influence air quality and climate.[56-61] It is essential to study these reactions to determine the kinetics and product yields, and hence quantify their impact on the atmospheric concentration and subsequent chemistry of other trace species.

The first direct measurements of the kinetics for the reaction between CH_2OO and SO_2 were carried out by Welz *et al.*[56] at 298 K in 4 Torr of He, following 248 nm photolysis of CH_2I_2 in excess O_2, and a rate coefficient of $(3.9 \pm 0.7) \times 10^{-11}$ cm^3 s^{-1} was reported with the products of the reaction predicted to be $HCHO + SO_3$. This rate coefficient was several orders of magnitude larger than previous measurements based on indirect measurements in ozonolysis reactions, with potentially significant impacts on the understanding of atmospheric oxidation of SO_2.

$$CH_2OO + SO_2 \rightarrow HCHO + SO_3 \qquad \text{(R6.1)}$$

Following the work of Welz *et al*., several studies have investigated the kinetics of the $CH_2OO + SO_2$ reaction at room temperature using the same photolytic production method of CH_2OO first proposed by Welz *et al*.[56] Various spectroscopic techniques have been employed in these subsequent studies to detect either CH_2OO,[49, 62-66] HCHO formed by the reaction,[63] or OH as a proxy for CH_2OO.[67, 68] A summary of the previously measured values reported in the literature for the rate coefficient of this reaction, $k_{6.1}$, is provided in Table 6.1.

Study	Temperature / K	Pressure / Torr	Photolysis λ / nm	Detection Technique	Bath gas	$k_{6.1}$ / 10^{-11} cm^3 s^{-1}
Welz *et al*., 2012[56]	298	4	248	PIMS	He	3.9 ± 0.7
Sheps, 2013[62]	295	5	255	UVA	He	4.1 ± 0.3
Stone *et al*, 2014[63]	295	50-450	355	LIF HCHO	N_2	3.42 ± 0.42
	295	1.5	248	PIMS	He	
Liu *et al*., 2014[67]	295	50-200	351	LIF OH	Ar	3.53 ± 0.29
Chhantyal-Pun *et al*., 2015[64]	295	30	355	CRDS	N_2	3.80 ± 0.04
Huang *et al*., 2015[65]	298	30-756	248	UVA	N_2	3.57 ± 0.28
Liu *et al*., 2017[68]	300	10	355	LIF OH	Ar	3.88 ± 0.13
Howes *et al*., 2018[66]	295	2	248	PIMS	He	3.74 ± 0.43
	295	50	248	UVA	N_2	3.87 ± 0.45
Qiu and Tonokura[49]	295	10.4	266	FT-IR	N_2	3.6 ± 0.1

Table 6.1: Summary of results for the rate coefficient of the $CH_2OO + SO_2$ reaction ($k_{6.1}$) reported in the literature in experiments using laser flash photolysis (LFP) of CH_2I_2 in the presence of excess O_2 coupled with a range of detection techniques. PIMS = photoionisation mass spectrometry; UVA = ultraviolet absorption; LIF = laser induced fluorescence; CRDS = cavity ringdown spectroscopy; FT-IR = Fourier transform infrared.

The number of photolytic experiments investigating the $CH_2OO + SO_2$ reaction employing a wide variety of detection techniques and over a range of pressure conditions, and the good agreement between the results determined from these various studies summarised in Table 6.1 suggest that the rate coefficient for this reaction at room temperature is relatively well characterised and shows no significant pressure dependence at pressures between 1.5 and 760 Torr.[69] The current IUPAC recommendation for the $CH_2OO + SO_2$ reaction is a pressure independent rate coefficient of $(3.70^{+0.45}_{-0.40}) \times 10^{-11}$ cm^3 s^{-1} at 298 K.[69]

The pressure dependence of the $CH_2OO + SO_2$ reaction was investigated by Stone *et al.*[63] over the pressure range 1.5-450 Torr and a pressure independent rate coefficient for the reaction of $(3.42 \pm 0.42) \times 10^{-11}$ cm^3 s^{-1} was reported. This experimental study employing laser induced fluorescence (LIF) detection of the HCHO produced in the reaction between CH_2OO and SO_2 (R6.1) observed HCHO production in 100 % yield, which, along with the lack of pressure dependence observed in the kinetics for this reaction, not only suggest that HCHO, and thus SO_3, are products of the reaction, but also imply that SO_3 is produced in the same yield as HCHO. The SO_3 product of the reaction has also been directly observed by photoionisation mass spectrometry (PIMS) at 4 Torr,[70] and by transient step-scan Fourier transform infrared (FT-IR) absorption spectroscopy at 110 and 214 Torr.[71]

A number of theoretical studies have also suggested that the dominant product channel of the $CH_2OO + SO_2$ reaction under atmospheric conditions is the production of HCHO and SO_3, with the reaction mechanism occurring *via* the formation of a five-membered secondary ozonide cycloadduct.[57, 72-74] Another product channel proposed by Aplincourt and Rui-López of the SO_2 catalysed isomerisation of CH_2OO to formic acid *via* production of a secondary ozonide is thus rendered a minor channel of the reaction,[75] supported by experimental studies using PIMS[70] and FT-IR absorption spectroscopy[71] in which no production of formic acid was observed, further indicating this to be a negligible product channel of the $CH_2OO + SO_2$ reaction. An investigation of the potential energy surface (PES) for the reaction between CH_2OO and SO_2 combined with Rice-Ramsperger-Kassel-Marcus (RRKM) or master equation simulations was carried out by Vereecken *et al.*[57] and Kuwata *et al.*[74] in order to predict product yields. Both studies reported the reaction to be under the low

pressure regime with negligible stabilisation of the secondary ozonide up to pressures considerably above atmospheric pressure, however Vereecken *et al*.[57] predicted a yield of 68 % HCHO + SO_3 at atmospheric pressure whereas Kuwata *et al*.[74] predicted a yield of at least 97 % at the same pressure.

Mechanisms for the formation of the secondary ozonide and the subsequent production of HCHO and SO_3 from the two studies also differed. Vereecken *et al*.[57] predicted barrierless formation of the secondary ozonide in the initial encounter between CH_2OO and SO_2, followed by homolytic cleavage of the O-O bond producing the $OCH_2OS(O)O$ biradical, and subsequent β-scission to form the dominant HCHO and SO_3 products. As well as this major product channel, minor product channels of fomyl sulfinic acid (HC(=O)OS(=O)OH) and bisoxy biradical ($H_2C(O)O$) by decomposition of the $OCH_2OS(O)O$ biradical at yields of 15 % and 17 % respectively at atmospheric pressure were predicted by Vereecken *et al*.[57] On the contrary Kuwata *et al*.,[74] in qualitative agreement with previous theoretical studies conducted by Jiang *et al*.[72] and Kurtén *et al*.,[73] predicted the barrierless formation of a pre-reaction complex in the first reaction step leading to production of the secondary ozonide, which then undergoes cycloreversion to the direct formation of predominantly HCHO + SO_3. The PES predicted by Kuwata *et al*.[74] incorporated two distinct stereochemical pathways to product formation owing to the existence of diastereomeric *endo*- and *exo*- conformers of the pre-reaction complex and the secondary ozonide. This PES predicted and described by Kuwata *et al*.[74] and produced later by Wang *et al*.[71] is shown in Figure 6.4a. A combination of the quantum chemical calculations carried out with statistical rate theory models allowed for a rate coefficient for the $CH_2OO + SO_2$ reaction of $(3.68 \pm 0.02) \times 10^{-11}$ cm^3 s^{-1} to be predicted by Kuwata *et al*., with no significant pressure dependence in the pressure range 1-760 Torr.[74] This predicted value is in good agreement with the results determined for the rate coefficient of the $CH_2OO + SO_2$ reaction from experimental measurements. Furthermore, a forthcoming publication from this laboratory[76] of the first study investigating the temperature dependence of the rate coefficient for the $CH_2OO + SO_2$ reaction in the temperature range 223-344 K and at 85 Torr, using time-resolved broadband UV absorption spectroscopy to monitor CH_2OO, has demonstrated the reaction to exhibit a negative temperature dependence, consistent with the PES of the reaction from the calculations reported by Kuwata *et al*.[74]

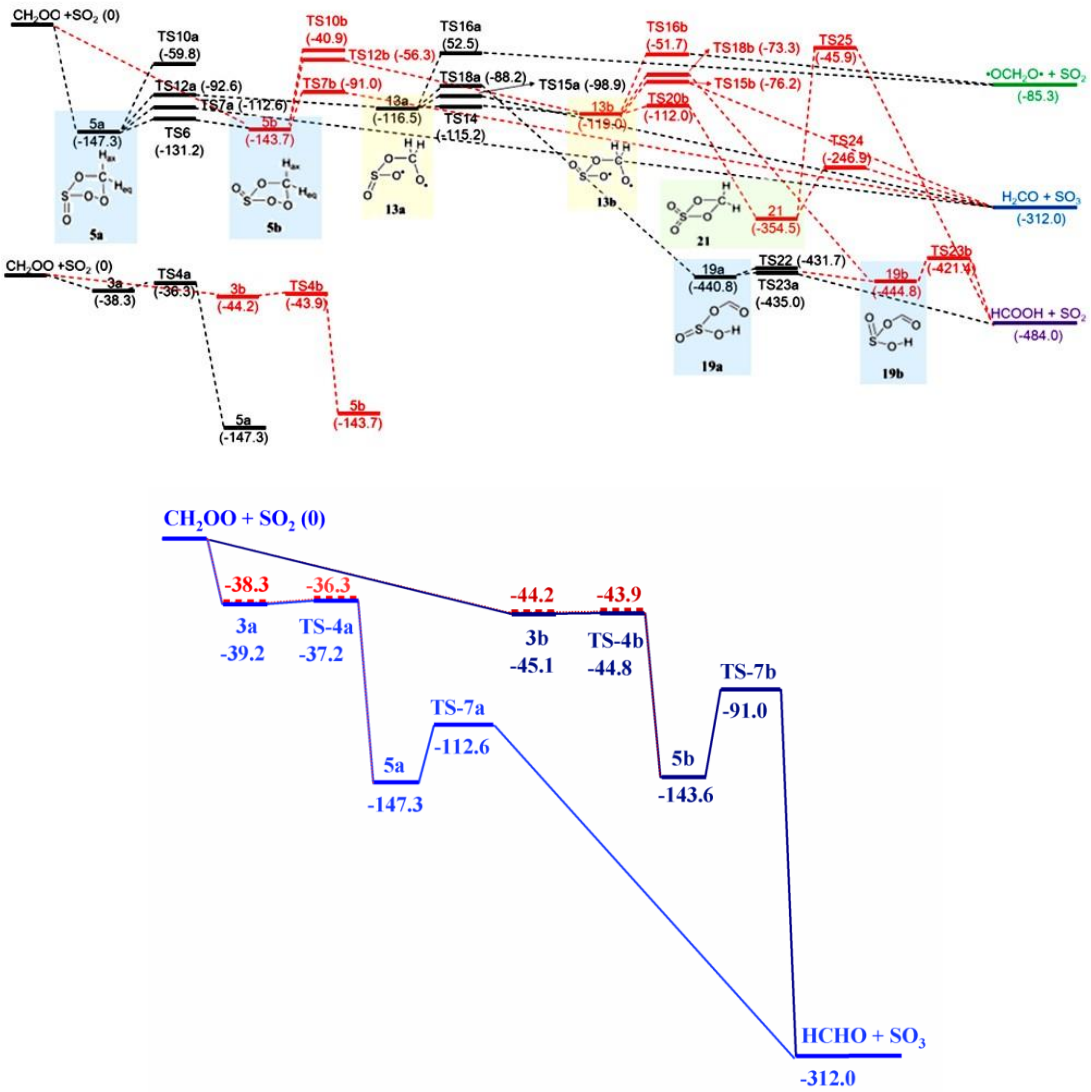

Figure 6.4: The potential energy surface (PES) of the $CH_2OO + SO_2$ reaction a) predicted by Kuwata *et al.*[74] using the B3LYP/6-311G(2d,d,p), reproduced from reference 71,[71] and b) obtained using MESMER calculations by reducing the PES determined by Kuwata *et al.*[74] to only the dominant mechanism for $HCHO + SO_3$ production, giving a simplified PES, reproduced from reference 76.[76] Two stereochemical pathways proceeding through *endo*- and *exo*-forms of species are shown distinguished by a) the black and red colours respectively, and b) the light blue and dark blue colours respectively. Calculated energies (in kJ mol^{-1}) for transition states, intermediates and products are a) from the work of Kuwata *et al.*,[74] with the initial steps to form the *endo*- and *exo*-conformers of the pre-reaction complex (3a and 3b respectively) and the secondary ozonide (5a and 5b respectively) shown in the lower left, and b) from the work of Kuwata *et al.*,[74] except for the *endo*- and *exo*-conformers of the pre-reaction complex (3a and 3b respectively) and the transition state (TS-4a and TS-4b respectively) to formation of the secondary ozonide (5a and 5b respectively), which are from MESMER calculations,[76] with energies calculated by Kuwata *et al.*[74] shown in light and dark red (for *endo*- and *exo*-conformers respectively) for comparison.

The forthcoming publication from this laboratory also includes a master equation analysis using the Master Equation Solver for Multi-Energy well Reactions (MESMER), a full description of which is given in previous work,[77-82] which was used to fit the PES for the $CH_2OO + SO_2$ reaction to the experimentally measured rate coefficients as a function of temperature.[76] These calculations were based on a PES obtained by reducing the PES determined by Kuwata *et al*.[74] to only the dominant mechanism for $HCHO + SO_3$ production *via* both stereochemical pathways owing to the existence of *endo*- and *exo*-conformers of the pre-reaction complex and the secondary ozonide,[76] with the reduced or simplified PES shown in Figure 6.4b. Simulations using MESMER showed that there was no significant loss of accuracy from reduction of the PES to only the main pathway, and that the reduced mechanism dominates the fate of the $CH_2OO + SO_2$ reaction under all conditions used in the calculations (T = 223-344 K and p = 2-760 Torr).[76]

As stated above, the formation of SO_3 from the $CH_2OO + SO_2$ reaction indicates that the reaction has potentially significant implications for the atmospheric production of H_2SO_4 and sulphate aerosol. Although the dominant tropospheric removal of CH_2OO is expected to be through reaction with the water dimer, $(H_2O)_2$ (refer to Chapter 1 for further details), the reaction of CH_2OO with SO_2 is fast enough to potentially compete with the CH_2OO + water dimer reaction and hence impact SO_2 oxidation in SO_2 rich environments and/or under conditions of low absolute humidities. As also mentioned previously, there is much interest in the investigation of atmospheric species of interest, including Criegee intermediates and SO_2/SO_3, using IR spectroscopy. Mid-IR QCL absorption spectroscopy provides an ideal method of monitoring Criegee intermediates such as CH_2OO, and detecting products of reactions of Criegee intermediates such as the SO_3 product of the $CH_2OO + SO_2$ reaction. Such IR investigations of Criegee reactions not only yield information of IR spectra but also allow reaction kinetics and product yields to be determined.

In this work, the development, characterisation, and initial results from a robust and economical experiment using laser flash photolysis coupled with time-resolved mid-infrared QCL absorption spectroscopy that can be applied to a wide range of problems in atmospheric chemistry and beyond are reported. The experimental setup is described, along with time-averaged measurements of absorption spectra of stable

species, and time-resolved measurements of photolytically generated species and reaction products that can be used to determine spectra of reactive species as well as reaction kinetics and product yields. The kinetics of the $CH_2OO + SO_2$ reaction were measured as a way of testing the experimental system.

6.4 Experimental

A schematic of the experimental setup is given in Figure 6.5. The reaction cell has been used previously in IR diode laser experiments[83-85] and consists of a central cylindrical stainless steel cell of length 70 cm and internal diameter 40 mm, connected *via* bellows at each end to stainless steel sections of length 15 cm and 7 cm internal diameter which are furnished with 60 mm diameter UV grade CaF_2 windows (Crystran). The end sections can house spherical mirrors of diameter 50 mm within the cell to enable internal alignment of a Herriott cell for the IR probe beam. The end sections of the cell are mounted on axial translation stages to enable changes of up to 5 cm to the distance between the spherical mirrors and alignment of the Herriot cell, which is facilitated by the bellows connecting the sections of the cell.

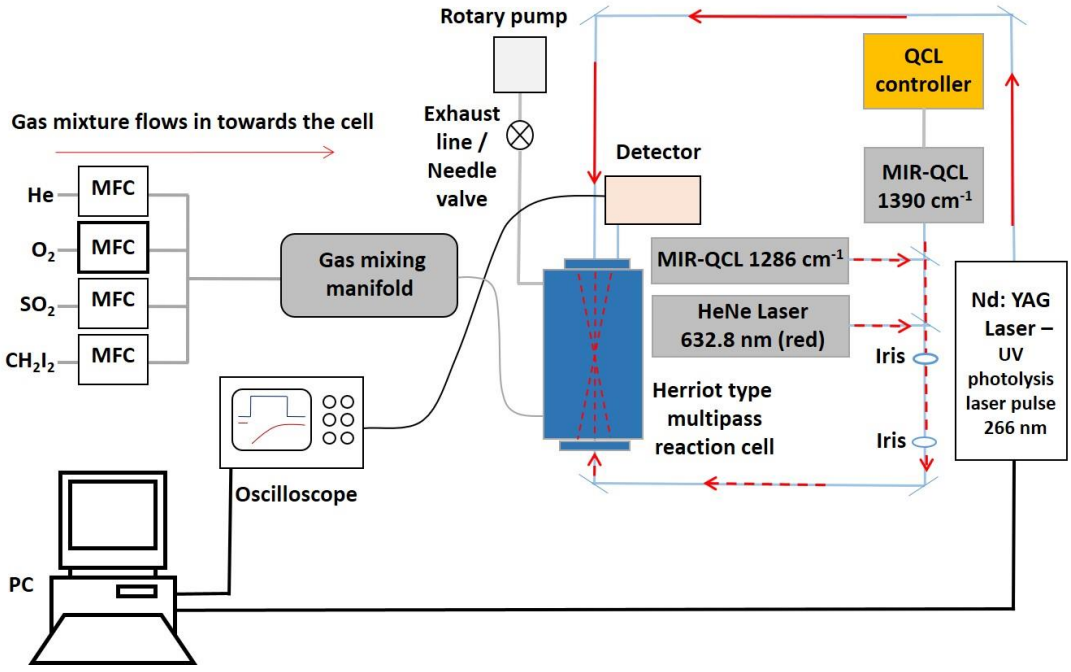

Figure 6.5: Schematic diagram of the experimental setup used in this work, with the red dashed lines showing the path of the multipass probe beam.

6.4.1 Gas Handling and Initiation of Chemistry

Reagent gases, such as NO (BOC Special Gases, 99.5 %) and SO_2 (Sigma-Aldrich, 99.9 %) (Section 6.7.2), are prepared manometrically at known concentrations in N_2 and stored in glass bulbs before mixing with N_2 (BOC, 99.99 %), and in some cases, O_2 (BOC, 99.999 %), in a stainless steel mixing line at known flow rates determined by calibrated mass flow controllers (Tylan, 2900 series) (further details are provided in Appendix 1). For experiments involving species in the liquid phase at room temperature, such as CH_3I (Sigma-Aldrich, 99 %) and CH_2I_2 (Sigma-Aldrich, 99 %) (Sections 6.7.1 and 6.7.2), the liquid is contained within a bubbler held at 0 ^oC and entrained into the vapour phase by passing a known flow of N_2 through the bubbler which is subsequently combined with the main gas flow in the mixing line. Gas mixtures prepared in the mixing line are passed into the reaction cell *via* one of the end sections, with the other end section connected to a rotary pump (Edwards 210 ED660). The total pressure in the cell is monitored by a capacitance manometer (MKS Instruments, 626A) and controlled by throttling the exit of the cell to the pump, with cell pressures from < 5 Torr to above atmospheric pressure achievable. Experiments reported in this work were performed at room temperature, although the temperature control of the reaction cell is possible by surrounding the cell with ceramic heaters (Watlow, WATROD tubular heater) or a bath filled with an appropriate solvent (e.g. methanol) chilled by a refrigerated immersion probe (LabPlant Refrigerated Immersion Probe, RP-100CD), both of which are available in this laboratory.

For experiments involving reactive species generated by photolysis, chemistry within the cell is initiated by the fourth harmonic of an Nd:YAG laser (Continuum Powerlite 8010), giving 266 nm (typical fluence 30 mJ cm^{-2}), or the third harmonic of the same Nd:YAG laser, giving 355 nm (typical fluence 150 mJ cm^{-2}). The photolysis beam has diameter ~ 1 cm and is aligned through the centre of the reaction cell using a pair of mirrors (ThorLabs NB1-K04 for operation at 266 nm and ThorLabs NB1-K08 for operation at 355 nm). For all experiments reported in this work the repetition rate of the photolysis laser was set to 1 Hz and the flow rate through the reaction cell was sufficiently high to ensure that a fresh gas mixture was photolysed for each photolysis shot.

6.4.2 Monitoring Species and Reactions

Infrared probe radiation is provided by one of several cw mid-IR DFB QCLs, depending on the application, providing radiation at centre wavenumbers of ~1286 cm^{-1} (Alpes Lasers), ~1390 cm^{-1} (ThorLabs) and ~1906 cm^{-1} (Thorlabs), with tuning of ~5-10 cm^{-1} around each centre. Temperature and current control of the QCL, which determines the precise output wavenumber of a given QCL, is controlled by a combined laser current and thermoelectric (TEC) controller (ThorLabs, ITC4002QCL). The current and TEC controller is operated in constant current mode, which provides current control up to 2 A in 0.1 mA steps with accuracy ±(0.1 % + 800 µA) and stability < 150 µA, and temperature control between 123 and 423 K in 0.001 K steps with stability < 0.002 K. For QCLs operating at ~1286 cm^{-1} and ~1390 cm^{-1}, the QCLs are housed in high heat load (HHL) packages, which are integrated with a ZnSe aspheric lens to collimate the output beam (divergence < 6 mrad), and mounted on a heatsink (Hamamatsu HHL mount, A117909-1) to dissipate excess heat. For the QCL operating at ~1906 cm^{-1}, the QCL is mounted on a two-tab C mount (ThorLabs) housed within a thermoelectrically cooled mount (ThorLabs C-Mount Laser Mount, LDMC20/M) which also accommodates a Geltech aspheric lens (focal length 1.873 mm, ThorLabs, C037TME-E) to collimate the output beam. Mounted QCLs are positioned on a pitch and yaw stage (ThorLabs, PY003/M) on an adjustable height platform (ThorLabs, C1519/M) to aid alignment through two adjustable aperture irises (ThorLabs, ID8/M) which are separated by > 70 cm. A collimated laser diode operating at 635 nm (ThorLabs, CPS635R) is co-aligned through the irises *via* a mirror (ThorLabs, PF10-03-G01) on a flip-mount (ThorLabs, FM90/M) to guide alignment of the QCL beam through the reaction cell. After the beam passes through the second iris, it is directed into the reaction cell by a pair of 1" Al mirrors (ThorLabs, PF10-03-G01), with the beam focussed into the centre of the cell by a 1" ZnSe plano-convex lens (focal length 1000 mm, ThorLabs, LA7753-G).

There are two options available for alignment of the probe IR beam through the cell in a multipass arrangement to increase the total pathlength and sensitivity, with the mirrors reflecting the probe beam located internal to the cell or external to the cell. In the internal arrangement, circular Au concave spherical mirrors (diameter 50 mm, radius of curvature 50 cm) are mounted inside the end sections of the cell. The mirrors have a central 25 mm hole to allow the UV photolysis beam to pass through the centre

of the cell, and a 6 mm hole at a radius of 20 mm to allow the IR probe beam to enter and exit the cell. Alignment of the mirrors is achieved using three adjustable screws accessible from the exterior of the end sections of the reaction cell. During experiments the mirrors are purged with a low flow (~5 sccm) of N_2 provided by ¼" entry ports in the end sections of the cell and monitored by a gas flow meter (Tylan). This design enables the alignment of a Herriott cell within the reaction cell, with >30 passes possible, maximising the total path length of the IR probe whilst minimising the number of passes through the CaF_2 mirrors.

In the external mirror arrangement, custom built mirror mounts with a central 12 mm hole are located exterior to the cell and are used to mount six Ag mirrors (12 mm diameter, 2.4 m radius of curvature, Knight Optical) in a circular arrangement at each end of the cell, similarly to the arrangement previously described for the multipass UV absorption experiment in this laboratory.[14] These mirrors can be aligned independently of each other *via* three alignment screws for each mirror, and enable up to 13 passes through the reaction cell. While this arrangement has a lower total pathlength than the internal mirror arrangement, and requires the IR beam to pass through the CaF_2 cell windows on each pass, it was found that the stability of the IR signal was improved compared to the internal mirror setup owing to impacts of vibrations on the internal mirrors that were less problematic with the external mirror array.

On the final pass of the IR probe beam through the cell, with either mirror arrangement, the beam is directed onto a 1" Au off-axis parabolic mirror (reflected focal length 4", ThorLabs, MPD149-M01) and focussed onto the detector. The detector is a DC-coupled photovoltaic Mercury-Cadmium-Telluride (MCT) detector (Vigo System, PVMI-3TE-8-2x2-TO8-wBaF2-35), integrated with a pre-amplifier (Vigo System, MIP-DC-100k-F-M4) with bandwidth up to 100 kHz. For a small number of experiments involving the detection of NO, use of an AC-coupled photovoltaic MCT detector (Vigo System, PVMI-3TE-8-2x2-TO8-wZnSeAR-35), integrated with a pre-amplifier (Vigo System, MIP-10k-50M-F-M4) with bandwidth 10 kHz to 50 MHz was also investigated. This is discussed further in Section 6.7.2. Unless stated otherwise, results shown are those obtained with the DC-coupled detector.

The signal is transferred to an oscilloscope *via* a sheathed BNC cable for data collection and processing, with the settings on the oscilloscope dictating the time resolution of the experiment. For measurements of stable species, all spectra reported in this work were recorded using a traditional oscilloscope (LeCroy Wavenumber-2, LT262, 350 MHz, 1 GS/s sample rate, 8 bit resolution), while for reactive species produced in photolytic experiments, the use of a Picoscope (Pico Technology, PicoScope 6402C, 250 MHz, 5 GS/s sample rate, 12 bit resolution) was also investigated. This is discussed further in Section 6.7.2.

Synchronisation of the photolysis laser and oscilloscope is achieved using a custom-built digital delay generator based on National Instruments hardware, with the overall experiment and data collection controlled by custom LabVIEW software. The software enables stepping of the current applied to the QCL at a set temperature to vary the output wavenumber, which is used to measure the variation in the probe intensity across the tuning range with and without a sample present to determine the spectra of stable species. For reactive species produced by, or following, photolysis, the average pre- and post-photolysis intensities are determined over specified time ranges at each current setting to give the absorption spectrum. Further details are given in Section 6.7.2.

6.5 Analysis, Results and Discussion

Experiments were carried out in this work to characterise the mid-IR QCL absorption spectroscopy instrument developed in this laboratory. Time-averaged measurements of the absorption spectra of stable species, i.e. SO_2 and CH_3I, were carried out, as well as time-resolved measurements of photolytically generated species, i.e. CH_2OO, and reaction products, i.e. SO_3, which were used to determine the absorption spectra of these reactive species as well as reaction kinetics of the $CH_2OO + SO_2$ reaction as a function of pressure and investigate the SO_3 product yield of this reaction as a function of pressure, which allowed for an estimation of the absorption cross-section for SO_3. A description of the analysis carried out at each stage is provided here along with results and a discussion of the implications of these results.

6.5.1 Time Averaged Experiments

Figure 6.6 shows the variation in the output wavenumber with current and temperature for the QCL centred at ~1390 cm^{-1}, measured by directing the output beam into a commercial FT-IR spectrometer (Bruker IFS66), with the variation in output power, measured by a thermal power sensor (ThorLabs, S401C & PM100D), with current given in Figure 6.7. The behaviour demonstrated in Figure 6.6 is typical of the DFB-QCLs used in this work, and while the resolution of the FT-IR spectrometer is significantly lower (typical resolution ~0.1 cm^{-1})[41] than that achievable with the QCL sources (typical resolution/linewidth < 0.002 cm^{-1}),[41] such measurements can provide a good indication for the current and temperature settings required to find a spectroscopic transition of interest.

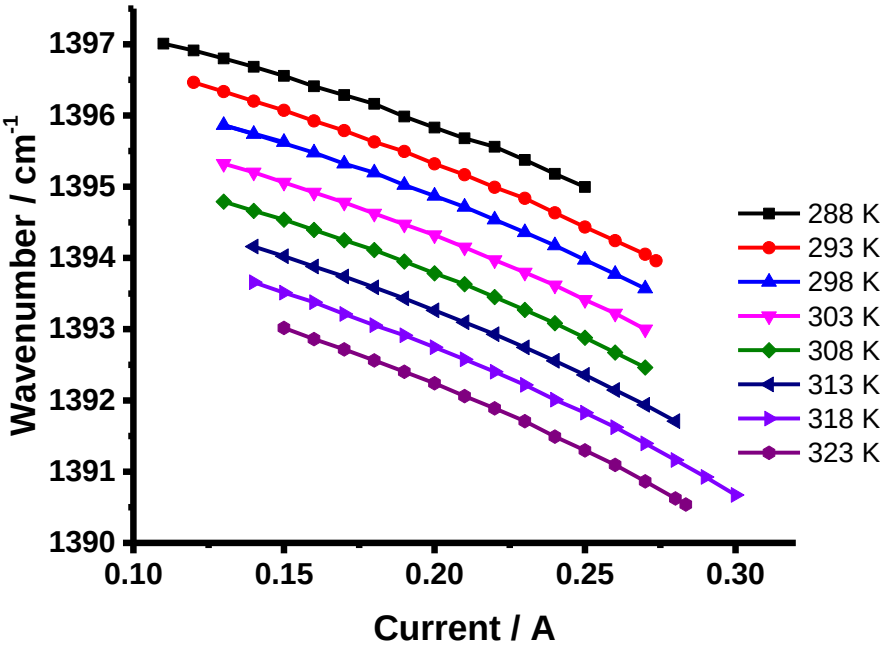

Figure 6.6: Variation in output wavenumber for the QCL centred at ~1390 cm^{-1} as a function of the current and temperature applied to the QCL. The output wavenumber was measured by a commercial FT-IR spectrometer.

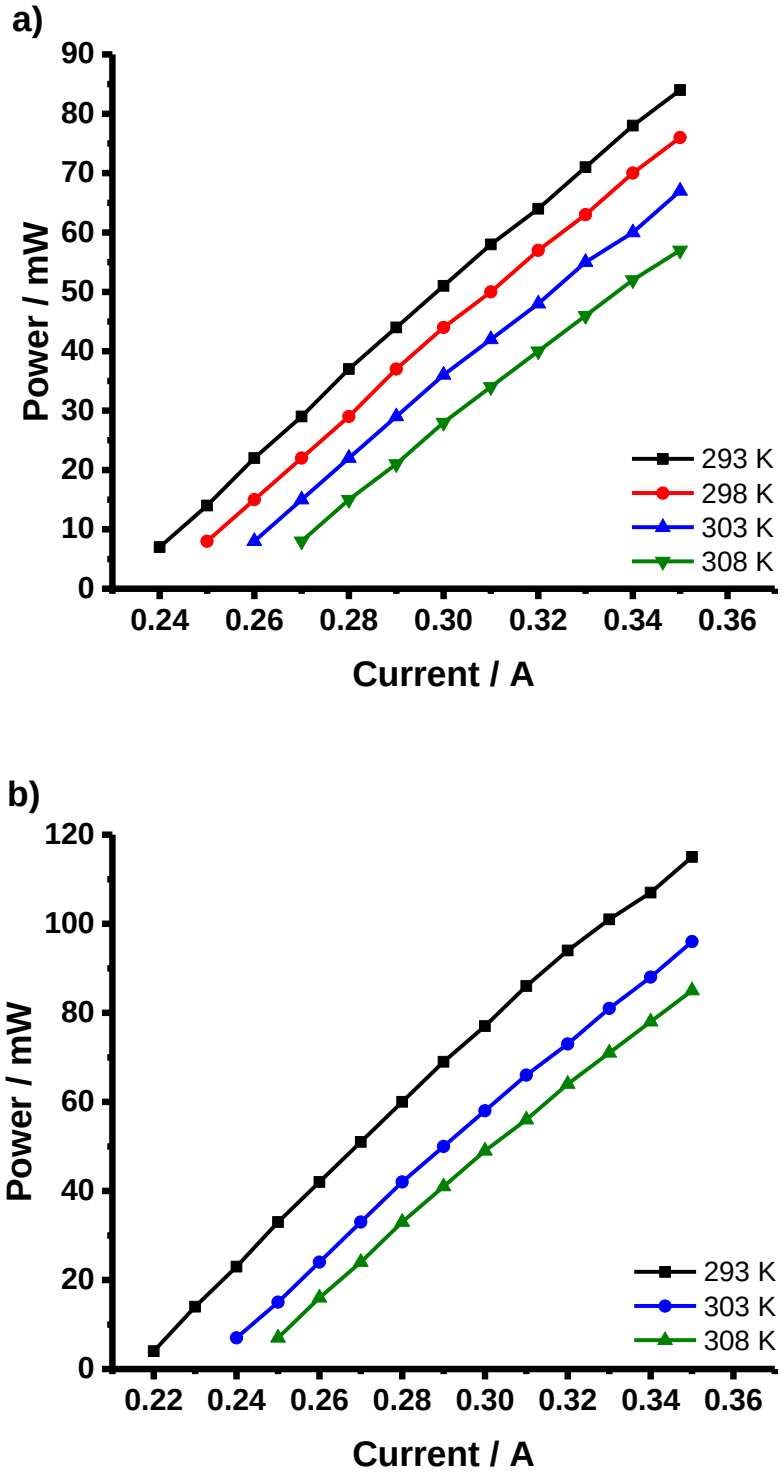

Figure 6.7: Variation in output power for the QCL centred at a) ~1390 cm^{-1} and b) ~1286 cm^{-1} as a function of the current applied to the QCL at constant temperatures of 293 K, 298 K, 303 K and 313 K.

Characterisation of the output wavenumber of the QCL can also be achieved through measurement of the absorption spectrum of a stable species with a well-defined rovibrational spectrum. Spectra for SO_2 and CH_3I were recorded using the external mirror arrangement by measuring the variation in QCL intensity across the tuning range of the QCL for the cell filled with N_2 and for the cell filled with N_2 and the species of interest under otherwise identical conditions. The absorbance, $A_{\tilde{\nu}}$, at each wavenumber $\tilde{\nu}$, was calculated from the Beer-Lambert law (refer to Chapter 2 for further information):

$$A_{\tilde{\nu}} = \ln\left(\frac{I_{\tilde{\nu},0}}{I_{\tilde{\nu}}}\right) = \sigma_{\tilde{\nu}}[\mathrm{C}]l \qquad \text{(Equation 6.1)}$$

where $I_{\tilde{\nu},0}$ and $I_{\tilde{\nu}}$ are the intensities at wavenumber $\tilde{\nu}$ without and with the species of interest present, respectively, $\sigma_{\tilde{\nu}}$ is the absorption cross-section at wavenumber $\tilde{\nu}$, [C] is the concentration, and l is the path length of the IR probe beam through the sample. In measurements of stable species in experiments in which no photolysis takes place, the total path length can be determined from the geometry of the cell and optical arrangement, and was ~13 m for the measurements discussed here.

Figure 6.8 shows the normalised observed absorbance spectra for SO_2 and CH_3I alongside the comparison to normalised spectra available on the HITRAN database[86] which were used to provide a more precise calibration of the QCL output wavenumber with the current setting than provided by the FT-IR measurements shown in Figure 6.6. The measured spectra indicate the capacity for high resolution measurements made possible by the narrow laser linewidth, with the resolution of the CH_3I measurements significantly higher than that available in the HITRAN database.

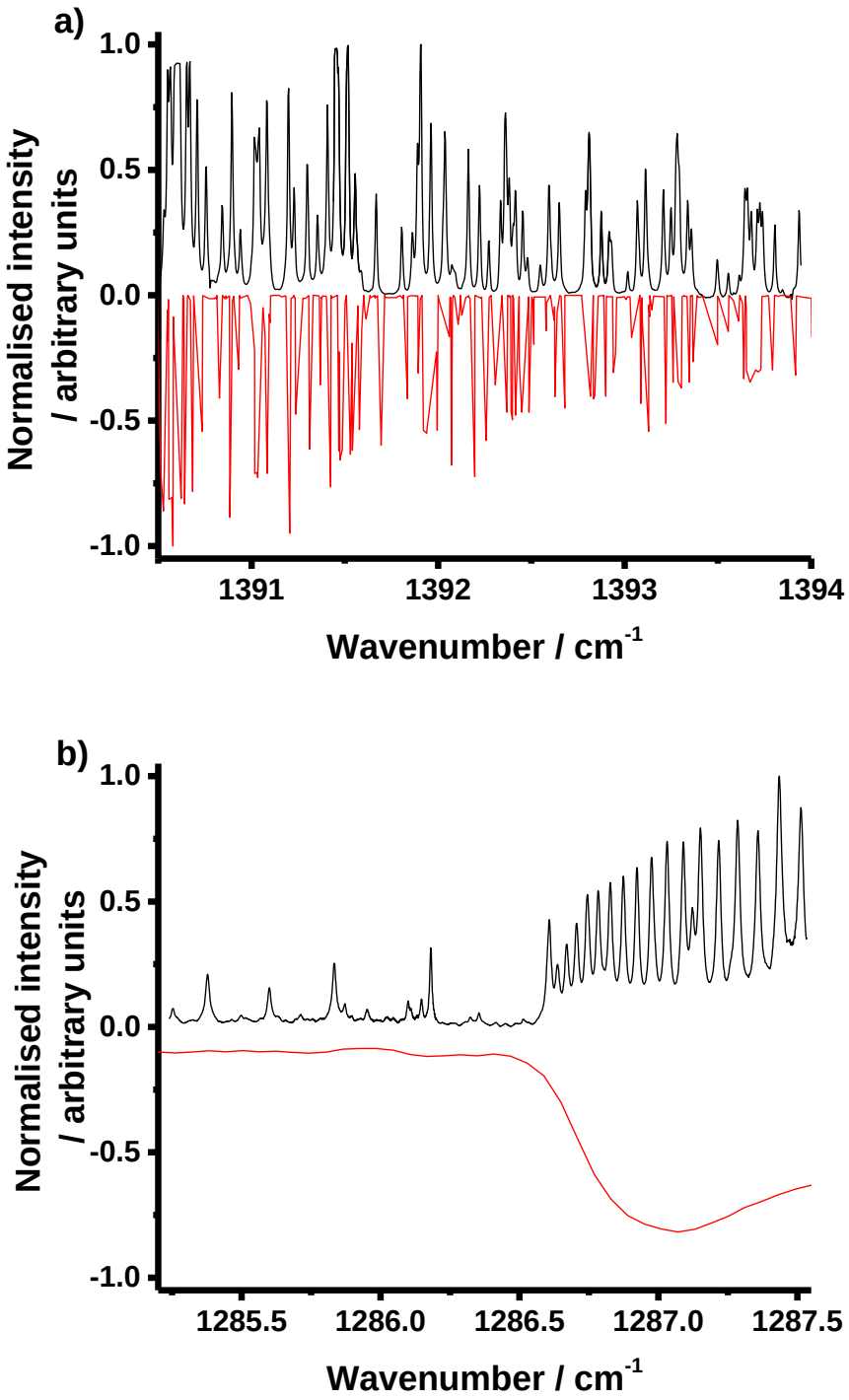

Figure 6.8: Normalised observed spectra (black) for a) SO_2 and b) CH_3I with corresponding normalised spectra reported on the HITRAN database[86] (multiplied by -1) (red). HITRAN data for SO_2 (a) are given as line intensities, and thus do not account for any line broadening, while those for CH_3I (b) are given as absorption cross-sections at 760 Torr, but at a lower resolution (0.06 cm^{-1}) and with more significant pressure broadening than measured by the QCL experiment and thus do not display the rovibronic structure evident for the higher resolution and lower pressure measurements made in this work.

6.5.2 Time Resolved Experiments

6.5.2.1 Stable Species

Photolytic experiments were initially performed for systems demonstrating a step-change in the time-resolved signal intensity at a given wavenumber on photolysis, such that a species was produced or depleted on photolysis with no significant further chemistry. Figure 6.9 shows the change in intensity by NO observed on photolysis of a flowing mixture of NO_2/N_2 at a wavelength of 355 nm obtained in experiments using the QCL centred at 1906 cm^{-1} tuned to an absorption line for NO. Measurements of the change in NO signal as a function of the initial NO_2 concentration were also made, and are shown in the inset to Figure 6.9. For the measurements of NO, the AC coupled detector was used, giving relative changes in intensity rather than absolute intensities which can be used to give absorbance. The QCL was housed in a two-tab C mount within a thermoelectrically cooled unit, and the internal spherical concave Au mirrors were used. For all other measurements reported in this work, the DC coupled detector was used, with the QCLs housed in HHL mounts with the external mirror arrangement. It was found that the internal mirror arrangement was subject to greater noise resulting from vibrations within the laboratory than the external mirror arrangement. In addition, collimation of the QCL beam exiting the two-tab C mount was more challenging than for QCLs housed in HHL mounts in which the collimation lens is integrated into the mount, and while collimation of the probe for NO was achieved, use of HHL mounted QCLs for applications such as those described here is recommended where feasible.

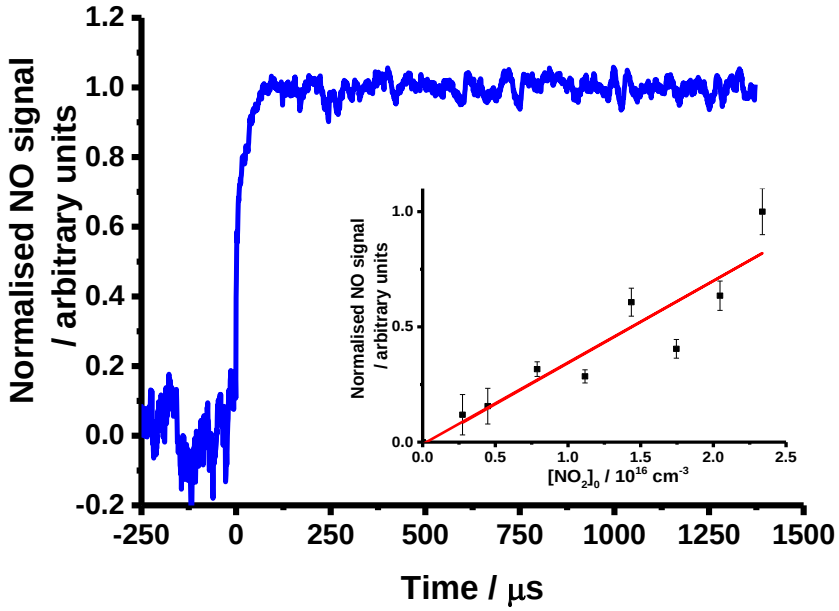

Figure 6.9: Normalised change in intensity at ~1906 cm^{-1} observed on 355 nm photolysis of NO_2. For the data shown in the main figure $[NO_2]_0 = 2.3 \times 10^{16}$ cm^{-3}, p = 50 Torr, and laser fluence 150 mJ cm^{-2}. The inset shows the normalised average post-photolysis change in intensity as a function of the initial NO_2 concentration (black points) with the line of best fit (red). The measurements shown were recorded with the AC coupled detector, giving relative changes in intensity rather than absolute intensities which can be used to give the absorbance. The data shown are the mean of 1000 photolysis shots.

Figure 6.10 shows the time-resolved absorbance observed on 266 nm photolysis of CH_3I/N_2 mixtures and the average post-photolysis change in absorbance as a function of the initial CH_3I concentration. Photolysis of CH_3I leads to a decrease in concentration, and thus an increase in signal intensity and a negative absorbance. The extent of change in absorbance reflects the absorption cross-section at the measurement wavenumber, the change in concentration, and the effective path length resulting from the overlap between the UV photolysis beam and the IR probe beam. For the 266 nm laser fluence of 30 mJ cm^{-2} and CH_3I absorption cross-section of 9.7 $\times 10^{-19}$ cm^2 at the photolysis wavelength,[87] a change in CH_3I concentration of 4 % is expected on photolysis. For the absorbance data shown in Figure 6.10 and an estimated IR cross-section of CH_3I at ~1287 cm^{-1} of 2×10^{-21} cm^2,[86] the effective path length of the IR probe beam can thus be estimated as (290 ± 30) cm.

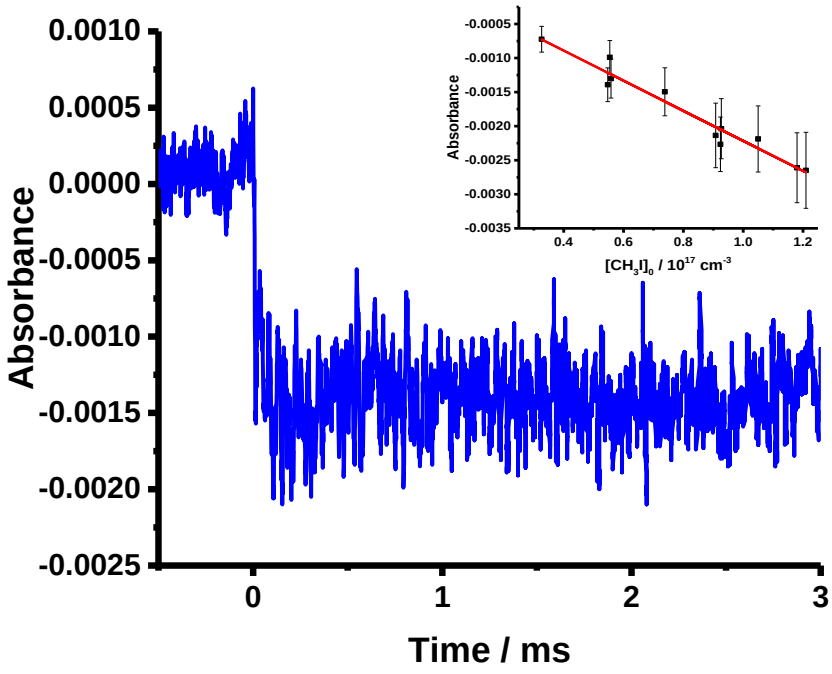

Figure 6.10: Changes in absorbance at ~1287 cm^{-1} observed on 266 nm photolysis of CH_3I. For the data shown in the main figure $[CH_3I]_0 = 5.5 \times 10^{16}$ cm^{-3}, p = 50 Torr, and laser fluence 30 mJ cm^{-2}. The inset shows the average post-photolysis change in absorbance as a function of the initial CH_3I concentration (black points) with the line of best fit (red). The data shown are the means of 200 photolysis shots.

6.5.2.2 Reactive Species

The behaviour of reactive species was investigated through 266 nm photolysis of $CH_2I_2/O_2/N_2$ and $CH_2I_2/O_2/N_2/SO_2$ mixtures,[56] resulting in the rapid production ($k_{CH2I+O2}[O_2] > 2 \times 10^5$ s^{-1}) of the Criegee intermediate CH_2OO (R6.2-R6.3), followed by its removal through the CH_2OO self-reaction (R6.4), $CH_2OO + I$ (R6.5), and, in the presence of SO_2, $CH_2OO + SO_2$ (R6.1):

$CH_2I_2 + h\nu$	$\rightarrow$	$CH_2I + I$	(R6.2)
$CH_2I + O_2$	$\rightarrow$	$CH_2OO + I$	(R6.3a)
	$\xrightarrow{+M}$	CH_2IO_2	(R6.3b)
$CH_2OO + CH_2OO$	$\rightarrow$	$2\ HCHO + O_2$	(R6.4)
$CH_2OO + I$	$\rightarrow$	CH_2IO_2	(R6.5)
$CH_2OO + SO_2$	$\rightarrow$	$HCHO + SO_3$	(R6.1)

Figure 6.11 shows the spectrum obtained in the absence of SO_2 by measuring the average pre- and post-photolysis absorbances for an observed time-profile for a given QCL current setting, and thus a given wavenumber, and then stepping to the next current setting and repeating. The step in current for these experiments was 0.1 mA, the smallest step-size available with the current controller used. The pre-photolysis region was defined as -4000 μs to -500 μs, owing to detection of some radiofrequency noise associated with the Q-switch delay of the photolysis laser which was set to 280 μs, and the post-photolysis region as 500 μs to 6000 μs, where $t = 0$ is the time at which the photolysis laser is fired. Experiments were performed at 50 Torr and each time-resolved trace was averaged for 1000 photolysis shots. The concentration of CH_2I_2 for these experiments, determined from the flow rates of gases in the cell, the vapour pressure of CH_2I_2 and measurements of the saturation of the flow with CH_2I_2 in experiments with similar flow rates (described in Chapters 4 and 5), was $\sim 2 \times 10^{14}$ cm^{-3}, and the 266 nm laser fluence was 30 mJ cm^{-2}, giving an expected initial CH_2OO concentration of $\sim 7 \times 10^{12}$ cm^{-3} using previous measurements of the yield of R6.3.[88] The CH_2OO spectrum measured in this work is in good agreement with that reported by Chang *et al*,[46] and is provided in tabulated form in Appendix 5. The resolution observed in this work is similar to the resolution of < 0.004 cm^{-1} reported by Chang *et al*.[43] based on the observation of non-overlapped peaks, although the line width of the QCLs used in this work and in that by Chang *et al*.[46] should enable higher resolution of < 0.002 cm^{-1}.

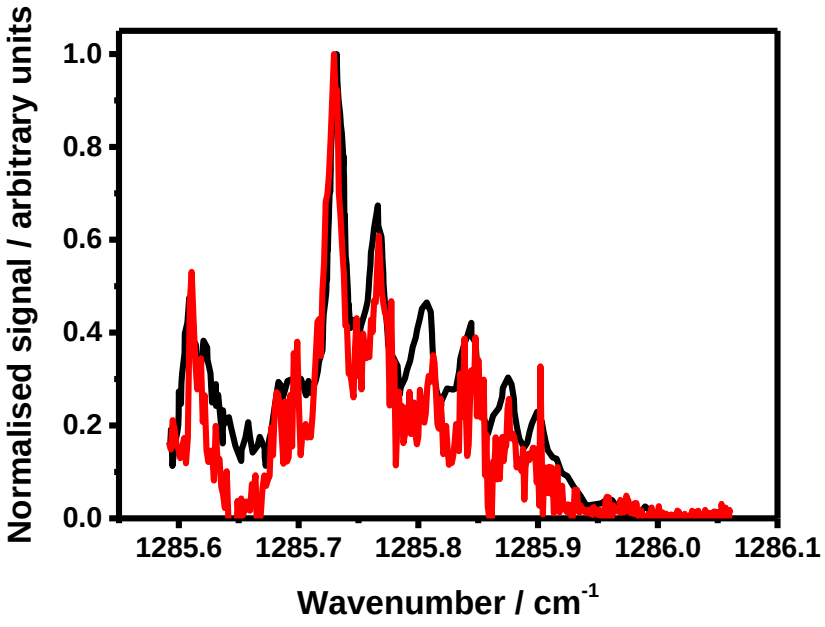

Figure 6.11: Normalised CH_2OO spectrum obtained in this work (red line) and that reported by Chang *et al.*[46] (black line). Measurements made in this work were obtained at a total pressure of 50 Torr at 298 K in the absence of SO_2, with $[CH_2I_2]$ ~2×10^{14} cm^{-3} and a laser fluence of 30 mJ cm^{-2}. The data shown are the means of 1000 photolysis shots at each current setting on the QCL with the wavenumber calibrated using the results reported by Chang *et al.*[46]

Kinetics describing the loss of CH_2OO were monitored in separate experiments with the QCL set at the peak in the CH_2OO spectrum (~1285.73 cm^{-1}). Figure 6.12 shows the decays obtained at a pressure of 50 Torr in the absence of SO_2. Previous work to determine the UV absorption cross-sections and kinetics of R6.4 and R6.5,[64, 89] including that performed in this laboratory,[90] and described in Chapters 4 and 5, has demonstrated that the loss of CH_2OO can be described by a mixed first- and second-order model:

$$[CH_2OO]_t = \frac{k_{1st}[CH_2OO]_0}{k_{1st}e^{k_{1st}t} - 2\,k_{2nd}[CH_2OO]_0 + 2\,k_{2nd}[CH_2OO]_0 e^{k_{1st}t}}$$

(Equation 6.2)

where $[CH_2OO]_t$ is the concentration of CH_2OO at time t, $[CH_2OO]_0$ is the initial concentration of CH_2OO, k_{1st} represents first-order losses of CH_2OO, such as diffusion and wall loss, and k_{2nd} represents second-order losses of CH_2OO resulting

from a combination of R6.4 and R6.5. Equation 6.2 can also be given in terms of absorbance and the absorption cross-section for CH_2OO and path length:

$$A_{\tilde{\nu},t} = \frac{k_{1st} A_{\tilde{\nu},0}}{k_{1st} e^{k_{1st} t} - 2\, k_{2nd} \left(\frac{A_{\tilde{\nu},0}}{\sigma_{\tilde{\nu}} l}\right) + 2\, k_{2nd} \left(\frac{A_{\tilde{\nu},0}}{\sigma_{\tilde{\nu}} l}\right) e^{k_{1st} t}} \qquad \text{(Equation 6.3)}$$

where $A_{\tilde{\nu},t}$ is the absorbance at time t and wavenumber $\tilde{\nu}$, $\sigma_{\tilde{\nu}}$ is the absorption cross-section for CH_2OO at wavenumber $\tilde{\nu}$, which has been determined to be (3.9 ± 0.6) × 10^{-18} cm^2 at wavenumber $\tilde{\nu}$ which corresponds to the peak of the spectrum at ~1285.73 cm^{-1} for a total pressure of 50 Torr,[44] and l is the effective path length of the IR probe beam. Results obtained in experiments described in Chapter 5 have indicated k_{2nd} = (1.30 ± 0.4) × 10^{-10} cm^3 s^{-1} at 50 Torr, and Equation 6.3 can thus be fit to the observed CH_2OO decays to determine the effective path length. Fits were performed globally for experiments in which precursor concentrations were varied in the range 0.1 – 2.0 × 10^{14} cm^{-3}, giving $[CH_2OO]_0$ in the range 0.4 – 6.0 × 10^{12} cm^{-3} for a laser fluence of ~30 mJ cm^{-2} at 50 Torr total pressure, with σ fixed at a value of 3.9 × 10^{-18} cm^2 and k_{2nd} fixed to a value of 1.30 × 10^{-10} cm^3 s^{-1}. Values for $A_{\tilde{\nu},0}$ were treated as local variables for each CH_2OO trace, with k_{1st} and l treated as global parameters and fits giving k_{1st} = (400 ± 4) s^{-1} and l = (235 ± 80) cm. While the effective path length determined from experiments involving CH_2OO ((235 ± 80) cm) is lower than that determined from experiments involving CH_3I ((290 ± 30) cm, as described above), the results are in broad agreement and the system was realigned between experiments which may explain the difference.

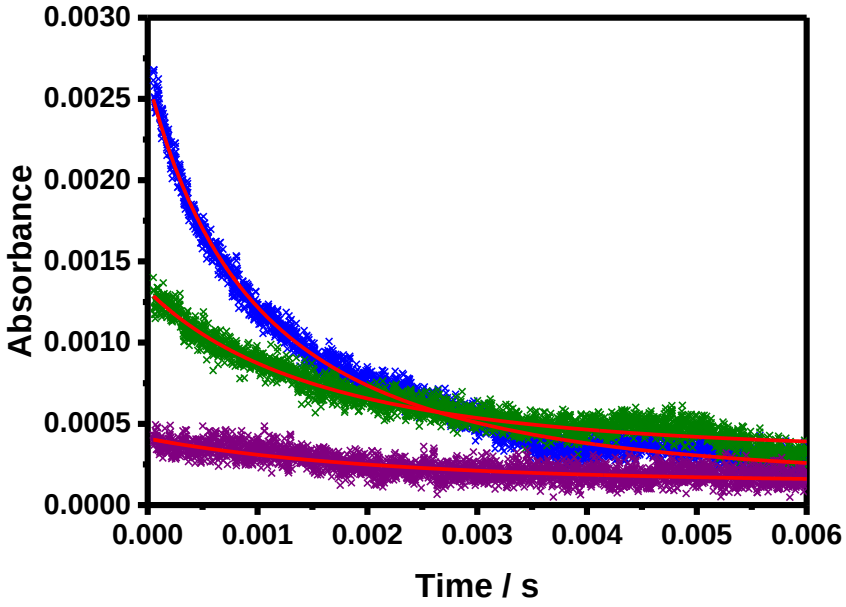

Figure 6.12: Typical time-resolved absorbance signals for CH_2OO obtained at a wavenumber of ~1285.73 cm^{-1}. Data are averages of 1000 photolysis shots at a total pressure of 50 Torr. For these data, CH_2I_2 concentrations were 2×10^{14} cm^{-3} (blue), 1.4×10^{14} cm^{-3} (green), and 2.4×10^{13} cm^{-3} (purple), and $[SO_2] = 0$. The fit to Equation 6.3 is shown by the solid red lines, which gave $k_{1st} = (400 \pm 4)$ s^{-1} and $l = (235 \pm 80)$ cm.

The 1σ limit of detection, in terms of absorbance, can be determined from the standard deviation of the post-photolysis baseline signal and was found to be 4.6×10^{-5} for a 10 μs integration time when averaging 250 photolysis shots. For the estimated path length of (235 ± 80) cm (as described above) and typical IR absorption cross-sections of ~10^{-19} cm^2, the limit of detection for these data can be estimated as ~2×10^{12} cm^{-3}. For CH_2OO, which has high absorption cross-sections at ~1285 cm^{-1} of ~10^{-18} cm^2, the limit of detection in terms of number density is thus ~2×10^{11} cm^{-3}.

In the presence of excess SO_2 the observed decays of CH_2OO are dominated by R6.1 and the loss of CH_2OO can be described by pseudo-first-order kinetics:

$$A_t = A_{t=0} \exp(-k't) \qquad \text{(Equation 6.4)}$$

where A_t is the absorbance at time t, A_0 is the absorbance at time zero, and k' is the pseudo-first-order rate coefficient, given by $k' = k_{6.1}[SO_2] + k_{phys}$ where $k_{6.1}$ is the bimolecular rate coefficient for reaction between CH_2OO and SO_2 and k_{phys} is the rate

coefficient representing physical losses of CH_2OO such as diffusion out of the probe region.

Fits of Equation 6.4 to the observed CH_2OO decays obtained in the presence of SO_2 (Figure 6.13) were performed to determine the pseudo-first-order rate coefficients, k', which can plotted against the known SO_2 concentration to give the bimolecular rate coefficient $k_{6.1}$. Figure 6.14 shows typical bimolecular plots of k' against the SO_2 concentration (experimental conditions and results are provided in Appendix 6), giving $k_{6.1} = (3.7 \pm 0.2) \times 10^{-11}$ cm^3 s^{-1} at 20 Torr, $k_{6.1} = (3.8 \pm 0.3) \times 10^{-11}$ cm^3 s^{-1} at 50 Torr, and $k_{6.1} = (4.0 \pm 0.3) \times 10^{-11}$ cm^3 s^{-1} at 100 Torr, in good agreement with the current IUPAC[69] recommended value of $(3.70^{+0.45}_{-0.40}) \times 10^{-11}$ cm^3 s^{-1} and previous work as listed in Table 6.1,[49, 56, 62-68] demonstrating that $k_{6.1}$ is independent of pressure over the range investigated. The data shown in Figures 6.12-6.14 indicate that the experiment developed in this work is able to measure the spectra and kinetics of reactive species to a high degree of accuracy and precision, and that a high dynamic range up to at least 20,000 s^{-1} can be achieved.

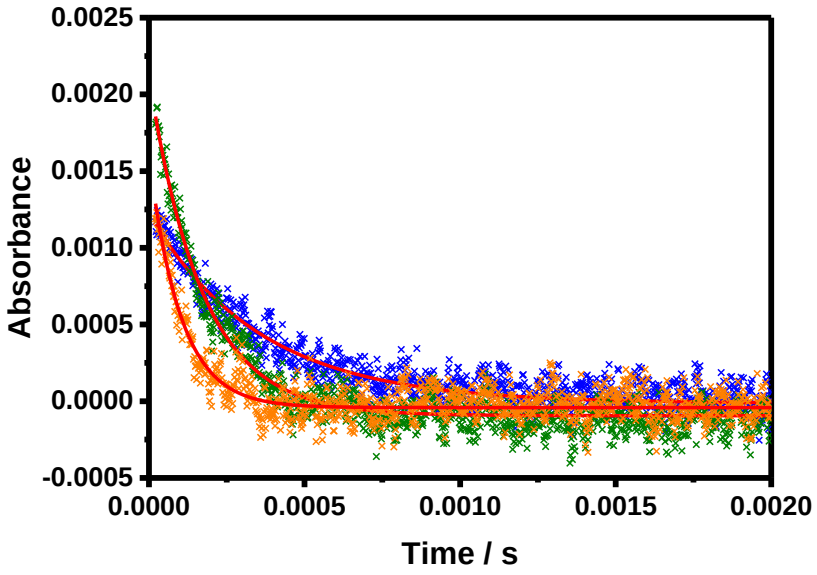

Figure 6.13: Typical time-resolved absorbance signals for CH_2OO in the presence of SO_2 obtained at a wavenumber of ~1285.73 cm^{-1}. Data are averages of 250 photolysis shots at a total pressure of 50 Torr with $[CH_2I_2] = 1.9 \times 10^{14}$ cm^{-3}. Fits to Equation 6.4 are shown by the solid red lines, which gave $k' = (2810 \pm 50)$ s^{-1} for $[SO_2] = 9.9 \times 10^{13}$ cm^{-3} (blue points), $k' = (5860 \pm 90)$ s^{-1} for $[SO_2] = 1.4 \times 10^{14}$ cm^{-3} (green points), and $k' = (9860 \pm 280)$ s^{-1} for $[SO_2] = 2.2 \times 10^{14}$ cm^{-3} (orange points).

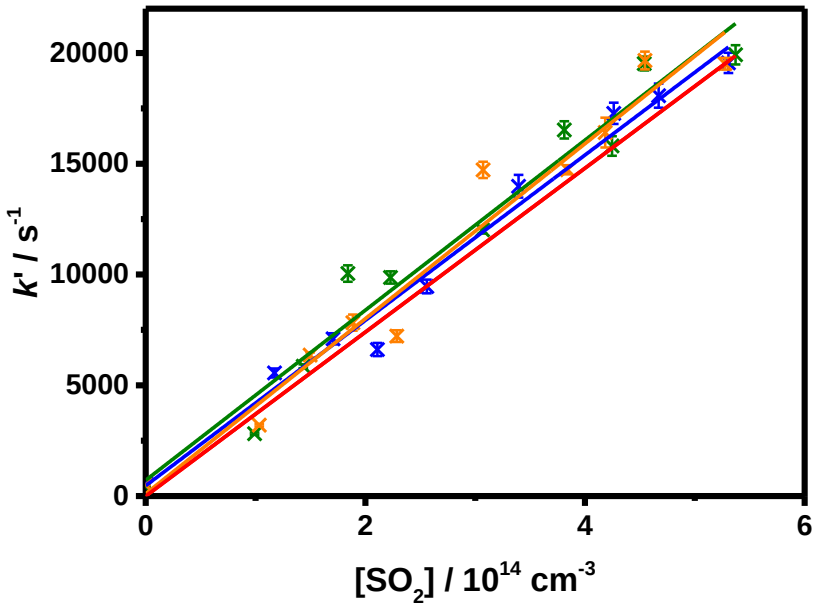

Figure 6.14: Bimolecular plots of the pseudo-first-order rate coefficents, *k*', determined from fits of Equation 6.4 to observed CH_2OO decays as a function of $[SO_2]$ at total pressures of 20 Torr (blue points and line, giving $k_{6.1} = (3.7 \pm 0.2) \times 10^{-11}$ cm^3 s^{-1}, intercept = (467 ± 605 s^{-1})), 50 Torr (green points and line, giving $k_{6.1} = (3.8 \pm 0.3) \times 10^{-11}$ cm^3 s^{-1}, intercept = (714 ± 861 s^{-1})), and 100 Torr (orange points and line, giving $k_{6.1} = (4.0 \pm 0.3) \times 10^{-11}$ cm3 s^{-1}, intercept = (106 ± 890 s^{-1})). Also shown is the current IUPAC recommendation[69] of $(3.70^{+0.45}_{-0.40}) \times 10^{-11}$ cm^3 s^{-1} (red line). For these data T = 298 K and initial CH_2I_2 concentrations were in the range 2.1-9.5 × 10^{14} cm^{-3}. Error bars are 1σ.

Further experiments were performed with the $CH_2I_2/O_2/N_2/SO_2$ system to monitor the production of SO_3 at ~1388.7 cm^{-1}. Previous work in this laboratory has demonstrated that HCHO is produced in R6.1,[63] and theory has predicted the co-production of SO_3.[57, 74] Experimental work by Wang *et al.*[71] using step-scan FT-IR spectroscopy with a resolution of 1 – 4 cm^{-1} have indicated the production of SO_3 following photolysis of $CH_2I_2/O_2/N_2/SO_2$ mixtures, but kinetics of SO_3 production have yet to be reported to confirm direct production through R6.1.

The QCL operating at ~1390 cm^{-1} was tuned to an absorption feature in the SO_3 spectrum using a sample of gaseous SO_3/N_2 in an infrared absorption cell prepared from solid SO_3 (Sigma-Aldrich, >99 %) in a glove box purged with N_2. The QCL was subsequently scanned over the absorption feature in experiments in which SO_3 was

expected to be produced following photolysis of $CH_2I_2/O_2/N_2/SO_2$ mixtures. The SO_3 spectrum obtained in photolytic experiments in this work, using the method described above for CH_2OO, is shown in Figure 6.15 and compares well to calculations[91] of the positions and relative line strengths of SO_3 absorption features reported on the HITRAN database.[86]

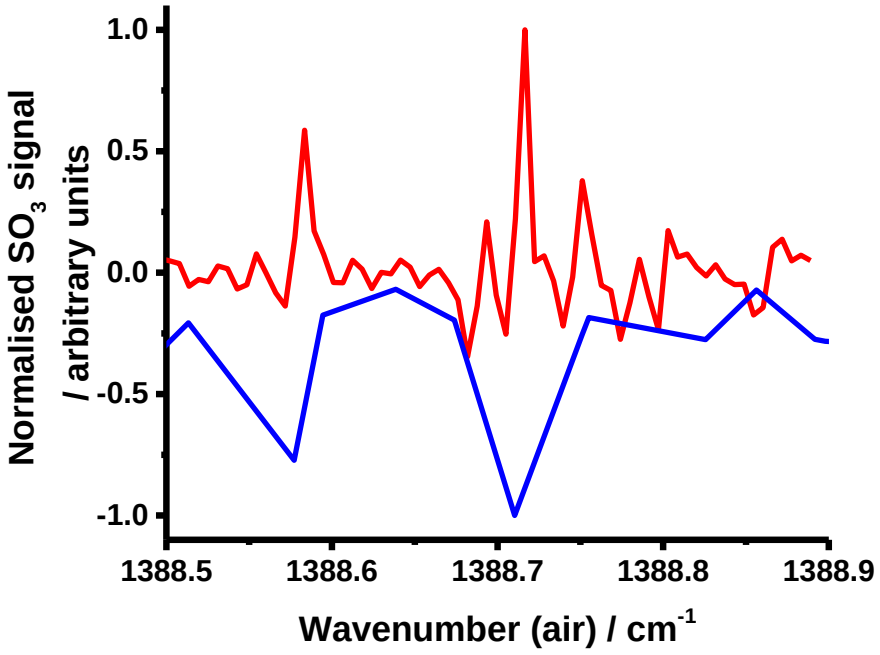

Figure 6.15: Normalised SO_3 spectrum obtained in this work (red) from experiments in which SO_3 was produced following photolysis of $CH_2I_2/O_2/N_2/SO_2$ mixtures with the normalised line intensities for SO_3 reported on the HITRAN database[86] (blue, multiplied by -1). Measurements made in this work were obtained at a total pressure of 50 Torr at 298 K, with $[CH_2I_2] = 5.4 \times 10^{14}$ cm^{-3} and $[SO_2] = 4.2 \times 10^{15}$ cm^{-3}.

For experiments to monitor the kinetics of SO_3 production, a PicoScope was used to collect the signal owing to lower absorbance signals for SO_3 compared to CH_2OO for given experimental conditions, with the faster transfer rate and memory (5 Gs/s and 12 bit, respectively) of the PicoScope compared to the traditional LeCroy oscilloscope (transfer rate 1 Gs/s and 8 bit memory) effectively decreasing the limit of detection. For experiments with the LeCroy oscilloscope described above, the 1σ limit of detection was determined to be 4.6×10^{-5} for a 10 μs integration time when averaging

250 photolysis shots, while that using the PicoScope was found to be 6.5×10^{-6} for the same conditions.

Figure 6.16 shows an example of the time-resolved SO_3 absorbance, which can be described by a pseudo-first-order growth combined with a first-order loss (Equation 6.5) and used to provide an alternative determination of $k_{6.1}$:

$$A_t = \frac{A_0 k_{growth}}{(k_{growth} - k_{loss})} \left\{ e^{-k_{loss} t} - e^{-k_{growth} t} \right\} \qquad \text{(Equation 6.5)}$$

where A_t is the absorbance at time t, A_0 is the maximum absorbance which relates to the initial radical concentration and yield of SO_3, k_{growth} is the pseudo-first-order rate coefficient describing the growth of SO_3 which is equal to $k_{6.1}[SO_2]$, and k_{loss} is the first-order rate coefficient describing the loss of SO_3 which is expected to be dominated by physical losses such as diffusion out of the probe region.

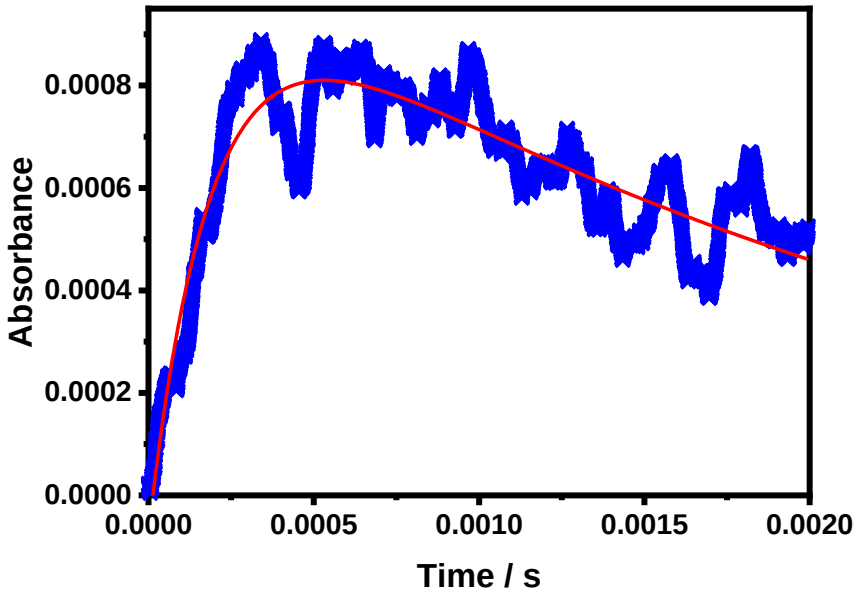

Figure 6.16: Time-resolved absorbance signals for SO_3 obtained at a wavenumber of 1388.7 cm^{-1}. Data are averages of 250 photolysis shots at a total pressure of 50 Torr at 298 K and are shown for $[SO_2] = 2.1 \times 10^{14}$ cm^{-3} (blue), with $[CH_2I_2] = 2 \times 10^{14}$ cm^{-3}. The fit to determine the kinetics describing the production and loss of SO_3 is also shown (red) and gave $k_{growth} = (8248 \pm 65)$ s^{-1} and $k_{loss} = (298 \pm 6)$ s^{-1}.

The bimolecular plots obtained through SO_3 measurements at total pressures of 20, 50, and 100 Torr are shown in Figure 6.17 (experimental conditions and results are

provided in Appendix 6) and demonstrate the capability of the instrument to measure the kinetics describing product formation to at least 25,000 s^{-1}. The bimolecular plots give $k_{6.1}$ = (3.6 ± 0.3) × 10^{-11} cm^3 s^{-1} at 20 Torr, (3.9 ± 0.3) × 10^{-11} cm^3 s^{-1} at 50 Torr, and (4.0 ± 0.2) × 10^{-11} cm^3 s^{-1} at 100 Torr, in excellent agreement with that determined through measurements of CH_2OO described above and the current IUPAC recommendation.[69] These results thus demonstrate direct production of SO_3 through R6.1.

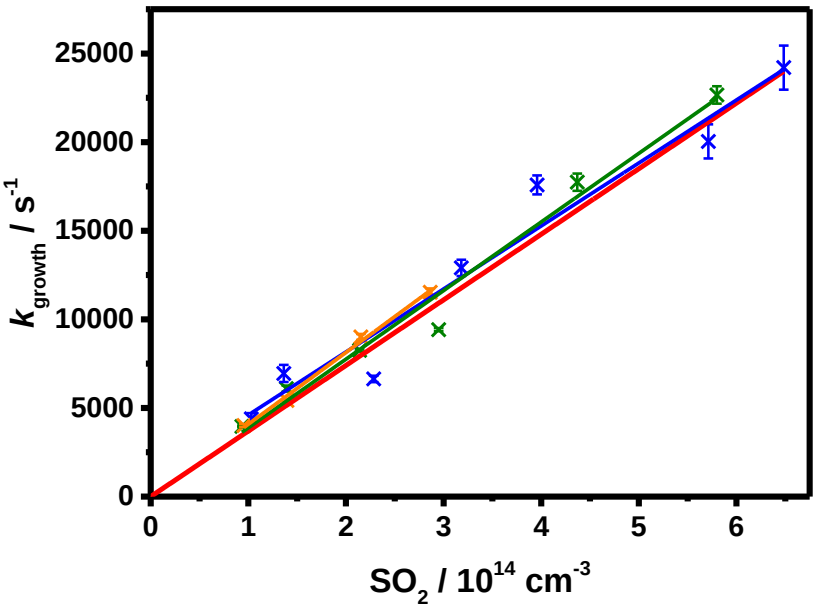

Figure 6.17: Bimolecular plots of the pseudo-first-order rate coefficents, k_{growth}, determined from the observed SO_3 profiles as a function of [SO_2]. Data were obtained at total pressure of 20 Torr (blue points and line, giving $k_{6.1}$ = (3.6 ± 0.3) × 10^{-11} cm^3 s^{-1}, intercept = (1052 ± 1364 s^{-1})), 50 Torr (green points and line, giving $k_{6.1}$ = (3.9 ± 0.3) × 10^{-11} cm^3 s^{-1}, intercept = (123 ± 941 s^{-1})), and 100 Torr (orange points and line, giving $k_{6.1}$ = (4.0 ± 0.2) × 10^{-11} cm^3 s^{-1}, intercept = (380 ± 379 s^{-1})). Also shown is the current IUPAC recommendation of [69] of ($3.70^{+0.45}_{-0.40}$) × 10-^{11} cm^3 s^{-1} (red line). Error bars are 1σ.

Observations of product formation can also be used to investigate product yields in cases where the absorption cross-sections are known. For SO_3, absorption cross-sections at the required resolution are not available, but previous measurements from this laboratory of HCHO formation[63] from R6.1 and theoretical studies[57, 74] indicate a yield of unity for HCHO and co-production of SO_3, with no significant

pressure dependence under ambient conditions. The observation of SO_3 production in this work supports these suggestions, and assuming that the yield of SO_3 is also unity over the pressure range investigated it is possible to assess the SO_3 absorption cross-section at the measurement wavenumber. Theoretical investigations[57, 74] of the reactions of larger Criegee intermediates (e.g. $(CH_3)_2COO$) with SO_2 have indicated that the kinetics and product yields of such reactions may be pressure dependent, with the potential for stabilisation of initial addition products at atmospheric pressure rather than production of SO_3. Assessment of the absorption cross-section for SO_3 from analysis of results from $CH_2OO + SO_2$ will thus provide valuable information for future studies of SO_3 product yields from reactions of SO_2 with other Criegee intermediates.

The parameter A_0 in Equation 6.5 represents the absorbance relating to the total concentration of SO_3 produced (i.e. the concentration that would be produced if there were no loss processes for SO_3 in the system). Thus, for an SO_3 yield of unity, A_0 should be equal to the initial CH_2OO concentration multiplied by the cross-section of SO_3 at the measurement wavenumber and the effective path length of the probe beam. Figure 6.18 shows the parameter A_0 as a function of pressure, normalised for the initial concentrations of CH_2OO, which depend on the initial concentration of CH_2I_2, the absorption cross-section of CH_2I_2 at the photolysis wavelength of 266 nm, the laser fluence, and the pressure-dependent yield of CH_2OO from $CH_2I + O_2$ (experimental conditions and calculation results are provided in Appendix 6). No significant dependence of the normalised A_0 on pressure is observed, providing further support to a lack of pressure dependence in the kinetics and product yields of R6.1, but also suggesting that there is little impact of pressure broadening on the SO_3 absorption line investigated in this work. Significant pressure broadening would result in a reduction in the effective absorption cross-section for SO_3 with increasing pressure, and hence a reduction in normalised A_0 with pressure. It may be that pressure broadening across the spectrum has resulted in little impact on the specific point in the spectrum at which measurements were taken, since other lines may have broadened into the measurement region to counteract broadening of the transition under investigation. However, it is still potentially useful to use the results obtained in this work to estimate the absorption cross-section for SO_3.

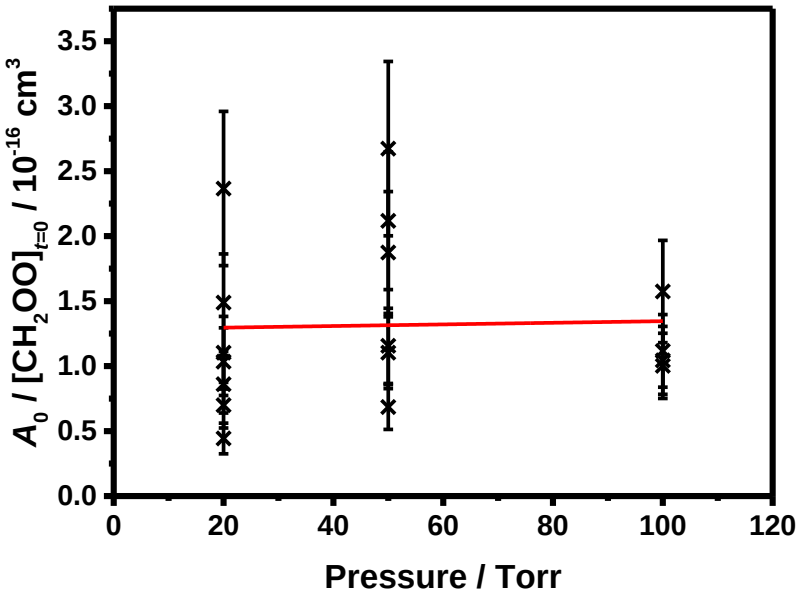

Figure 6.18: A_0 parameters obtained from fits of Equation 6.5 to SO_3 absorbance-time profiles normalised for initial concentrations of CH_2OO. The line of best fit (solid red line) has a slope of (6.2 ± 5.0) x 10^{-20} cm^3 $Torr^{-1}$ and an intercept of (1.3 ± 0.3) x 10^{-16} cm^3, which represents the product of the absorption cross-section for SO_3 at the measurement wavenumber and the effective path length of the IR probe beam. Error bars are 1σ.

Assuming a yield of unity for SO_3 and little impact of pressure broadening over the range investigated, the intercept of Figure 6.18, which has a value of (1.3 ± 0.3) × 10^{-16} cm^3, should be equal to the product of the absorption cross-section for SO_3, σ, and the path length of the probe beam, l. Using the value of l = (235 ± 80) cm determined through observations of CH_2OO, the absorption cross-section for SO_3 at the measurement wavenumber of ~1388.7 cm^{-1} can thus be estimated to be (5.5 ± 2.3) × 10^{-19} cm^2.

6.6 Conclusions

A new, robust and economical experimental system has been developed in this laboratory which uses laser flash photolysis coupled with time-resolved mid-infrared QCL absorption spectroscopy. This mid-IR QCL technique used in the instrument described in this work has applications in atmospheric chemistry and chemical

kinetics, among wider uses in trace gas analysis in industrial processes and medical diagnostics. Time-averaged measurements of absorption spectra of the stable species CH_3I and SO_2 aided characterisation of the output wavenumber of the QCLs used. Additionally, time-resolved experiments have been carried out employing 266 nm photolysis of $CH_2I_2/O_2/N_2$ and $CH_2I_2/O_2/N_2/SO_2$ gas mixtures at 298 K and pressures between 20 and 100 Torr to develop and characterise the system, and the CH_2OO + SO_2 reaction was selected as a test case for this development and characterisation. Such time-resolved measurements of photolytically generated species (CH_2OO) and reaction products (SO_3) have been used to determine spectra of reactive species (CH_2OO) as well as reaction kinetics (of the CH_2OO + SO_2 reaction) and product yields (of SO_3). Results indicate the IR absorption spectrum of CH_2OO to have defined rovibrational structure and be in good agreement with that previously reported by Chang *et al.*[46] in the wavenumber region 1285.5917-1286.0605 cm^{-1} in terms of relative peak heights and positions. A rate coefficient of $(3.8 \pm 0.5) \times 10^{-11}$ cm^3 s^{-1} has been determined for the reaction between CH_2OO and SO_2 from measurements of both the CH_2OO reactant loss and SO_3 product formation, in good agreement with the current IUPAC[69] recommended value of $(3.70^{+0.45}_{-0.40}) \times 10^{-11}$ cm^3 s^{-1} and previous work as listed in Table 6.1,[49, 56, 62-68] with no significant pressure dependence observed over the pressure range investigated. Determination of the kinetics of SO_3 production reported here confirm direct production of SO_3 from the CH_2OO + SO_2 reaction, as predicted by theory.[57, 74] The product yield of SO_3 from the reaction of CH_2OO + SO_2 has been found to be independent of pressure over the range investigated, consistent with previous measurements of the HCHO co-product yield reported by Stone *et al.*,[63] and an SO_3 absorption cross-section of $(5.5 \pm 2.3) \times 10^{-19}$ cm^2 at ~1388.7 cm^{-1} has been determined.

6.7 References

1. Blitz, M. A.; Seakins, P. W., Laboratory studies of photochemistry and gas phase radical reaction kinetics relevant to planetary atmospheres. *Chemical Society Reviews* **2012,** *41* (19), 6318-6347.

2. Herbst, E., The chemistry of interstellar space. *Chemical Society Reviews* **2001,** *30* (3), 168-176.

3. Pilling, M. J.; Robertson, S. H.; Seakins, P. W., Elementary radical reactions and autoignition. *Journal of the Chemical Society-Faraday Transactions* **1995,** *91* (23), 4179-4188.

4. Zador, J.; Taatjes, C. A.; Fernandes, R. X., Kinetics of elementary reactions in low-temperature autoignition chemistry. *Progress in Energy and Combustion Science* **2011,** *37* (4), 371-421.

5. Monks, P. S., Gas-phase radical chemistry in the troposphere. *Chemical Society Reviews* **2005,** *34* (5), 376-395.

6. von Schneidemesser, E.; Monks, P. S.; Allan, J. D.; Bruhwiler, L.; Forster, P.; Fowler, D.; Lauer, A.; Morgan, W. T.; Paasonen, P.; Righi, M.; Sindelarova, K.; Sutton, M. A., Chemistry and the linkages between air quality and climate change. *Chemical Reviews* **2015,** *115* (10), 3856-3897.

7. Carr, S. A.; Baeza-Romero, M. T.; Blitz, M. A.; Pilling, M. J.; Heard, D. E.; Seakins, P. W., OH yields from the CH_3CO+O_2 reaction using an internal standard. *Chemical Physics Letters* **2007,** *445* (4-6), 108-112.

8. Fockenberg, C.; Bernstein, H. J.; Hall, G. E.; Muckerman, J. T.; Preses, J. M.; Sears, T. J.; Weston, R. E., Repetitively sampled time-of-flight mass spectrometry for gas-phase kinetics studies. *Review of Scientific Instruments* **1999,** *70* (8), 3259-3264.

9. Blitz, M. A.; Goddard, A.; Ingham, T.; Pilling, M. J., Time-of-flight mass spectrometry for time-resolved measurements. *Review of Scientific Instruments* **2007,** *78* (3).

10. Osborn, D. L.; Zou, P.; Johnsen, H.; Hayden, C. C.; Taatjes, C. A.; Knyazev, V. D.; North, S. W.; Peterka, D. S.; Ahmed, M.; Leone, S. R., The multiplexed chemical kinetic photoionization mass spectrometer: A new approach to isomer-resolved chemical kinetics. *Review of Scientific Instruments* **2008,** *79* (10).

11. Middaugh, J. E.; Buras, Z. J.; Matrat, M.; Chu, T. C.; Kim, Y. S.; Alecu, I. M.; Vasiliou, A. K.; Goldsmith, C. F.; Green, W. H., A combined photoionization

time-of-flight mass spectrometry and laser absorption spectrometry flash photolysis apparatus for simultaneous determination of reaction rates and product branching. *Review of Scientific Instruments* **2018,** *89* (7).

12. Orlando, J. J.; Tyndall, G. S., Laboratory studies of organic peroxy radical chemistry: an overview with emphasis on recent issues of atmospheric significance. *Chemical Society Reviews* **2012,** *41* (19), 6294-6317.

13. Cossel, K. C.; Waxman, E. M.; Finneran, I. A.; Blake, G. A.; Ye, J.; Newbury, N. R., Gas-phase broadband spectroscopy using active sources: progress, status, and applications. *Journal of the Optical Society of America B-Optical Physics* **2017,** *34* (1), 104-129.

14. Lewis, T.; Heard, D. E.; Blitz, M. A., A novel multiplex absorption spectrometer for time-resolved studies. *Review of Scientific Instruments* **2018,** *89* (2).

15. Taatjes, C. A.; Hershberger, J. F., Recent progress in infrared absorption techniques for elementary gas-phase reaction kinetics. *Annual Review of Physical Chemistry* **2001,** *52*, 41-70.

16. Hodgkinson, J.; Tatam, R. P., Optical gas sensing: a review. *Measurement Science and Technology* **2013,** *24* (1).

17. Li, J. S.; Chen, W.; Fischer, H., Quantum cascade laser spectrometry techniques: A new trend in atmospheric chemistry. *Applied Spectroscopy Reviews* **2013,** *48* (7), 523-559.

18. Doussin, J. F.; Ritz, D.; DurandJolibois, R.; Monod, A.; Carlier, P., Design of an environmental chamber for the study of atmospheric chemistry: New developments in the analytical device. *Analusis* **1997,** *25* (7), 236-242.

19. Glowacki, D. R.; Goddard, A.; Hemavibool, K.; Malkin, T. L.; Commane, R.; Anderson, F.; Bloss, W. J.; Heard, D. E.; Ingham, T.; Pilling, M. J.; Seakins, P. W., Design of and initial results from a Highly Instrumented Reactor for Atmospheric Chemistry (HIRAC). *Atmospheric Chemistry and Physics* **2007,** *7* (20), 5371-5390.

20. Glowacki, D. R.; Goddard, A.; Seakins, P. W., Design and performance of a throughput-matched, zero-geometric-loss, modified three objective multipass matrix system for FTIR spectrometry. *Applied Optics* **2007,** *46* (32), 7872-7883.

21. Nilsson, E. J. K.; Eskebjerg, C.; Johnson, M. S., A photochemical reactor for studies of atmospheric chemistry. *Atmospheric Environment* **2009,** *43* (18), 3029-3033.

22. Su, Y. T.; Huang, Y. H.; Witek, H. A.; Lee, Y. P., Infrared absorption spectrum of the simplest Criegee intermediate CH_2OO. *Science* **2013,** *340* (6129), 174-176.

23. Huang, D. R.; Chu, L. K.; Lee, Y. P., Infrared absorption of gaseous CH_3OO detected with a step-scan Fourier-transform spectrometer. *Journal of Chemical Physics* **2007,** *127* (23).

24. Faist, J.; Capasso, F.; Sivco, D. L.; Sirtori, C.; Hutchinson, A. L.; Cho, A. Y., Quantum cascade laser. *Science* **1994,** *264* (5158), 553-556.

25. Hofstetter, D.; Faist, J., High performance quantum cascade lasers and their applications. In *Solid-State Mid-Infrared Laser Sources*, Sorokina, I. T.; Vodopyanov, K. L., Eds. 2003; Vol. 89, pp 61-96.

26. Yao, Y.; Hoffman, A. J.; Gmachl, C. F., Mid-infrared quantum cascade lasers. *Nature Photonics* **2012,** *6* (7), 432-439.

27. Zhang, L. Z.; Tian, G.; Li, J. S.; Yu, B. L., Applications of absorption spectroscopy using quantum cascade lasers. *Applied Spectroscopy* **2014,** *68* (10), 1095-1107.

28. Pecharroman-Gallego, R., Quantum cascade lasers: Review, applications and prospective development. *Lasers in Engineering* **2013,** *24* (5-6), 277-314.

29. Fleisher, A. J.; Bjork, B. J.; Bui, T. Q.; Cossel, K. C.; Okumura, M.; Ye, J., Mid-infrared time-resolved frequency comb spectroscopy of transient free radicals. *Journal of Physical Chemistry Letters* **2014,** *5* (13), 2241-2246.

30. Bjork, B. J.; Bui, T. Q.; Heckl, O. H.; Changala, P. B.; Spaun, B.; Heu, P.; Follman, D.; Deutsch, C.; Cole, G. D.; Aspelmeyer, M.; Okumura, M.; Ye, J., Direct

frequency comb measurement of OD + CO → DOCO kinetics. *Science* **2016,** *354* (6311), 444-448.

31. Roberts, F. C.; Lewandowski, H. J.; Hobson, B. F.; Lehman, J. H., A rapid, spatially dispersive frequency comb spectrograph aimed at gas phase chemical reaction kinetics. *Molecular Physics* **2020,** *118* (16).

32. Shahmohammadi, M.; Kapsalidis, F.; Suess, M. J.; Gini, E.; Beck, M.; Hundt, M.; Tuzson, B.; Emmenegger, L.; Faist, J., Multi-wavelength distributed feedback quantum cascade lasers for broadband trace gas spectroscopy. *Semiconductor Science and Technology* **2019,** *34* (8).

33. Borri, S.; Bartalini, S.; De Natale, P.; Inguscio, M.; Gmachl, C.; Capasso, F.; Sivco, D. L.; Cho, A. Y., Frequency modulation spectroscopy by means of quantum-cascade lasers. *Applied Physics B-Lasers and Optics* **2006,** *85* (2-3), 223-229.

34. Du, Z. H.; Zhang, S.; Li, J. Y.; Gao, N.; Tong, K. B., Mid-infrared tunable laser-based broadband fingerprint absorption spectroscopy for trace gas sensing: A review. *Applied Sciences-Basel* **2019,** *9* (2).

35. McManus, J. B.; Zahniser, M. S.; Nelson, D. D.; Shorter, J. H.; Herndon, S.; Wood, E.; Wehr, R., Application of quantum cascade lasers to high-precision atmospheric trace gas measurements. *Optical Engineering* **2010,** *49* (11).

36. Kostinek, J.; Roiger, A.; Davis, K. J.; Sweeney, C.; DiGangi, J. P.; Choi, Y.; Baier, B.; Hase, F.; Gross, J.; Eckl, M.; Klausner, T.; Butz, A., Adaptation and performance assessment of a quantum and interband cascade laser spectrometer for simultaneous airborne in situ observation of CH_4, C_2H_6, CO_2, CO and N_2O. *Atmospheric Measurement Techniques* **2019,** *12* (3), 1767-1783.

37. Banik, G. D.; Som, S.; Maity, A.; Pal, M.; Maithani, S.; Mandal, S.; Pradhan, M., An EC-QCL based N_2O sensor at 5.2 μm using cavity ring-down spectroscopy for environmental applications. *Analytical Methods* **2017,** *9* (15), 2315-2320.

38. Herndon, S. C.; Zahniser, M. S.; Nelson, D. D.; Shorter, J.; McManus, J. B.; Jimenez, R.; Warneke, C.; de Gouw, J. A., Airborne measurements of HCHO and HCOOH during the New England Air Quality Study 2004 using a pulsed quantum

cascade laser spectrometer. *Journal of Geophysical Research-Atmospheres* **2007,** *112* (D10).

39. Cui, X. J.; Yu, R. Q.; Chen, W. D.; Zhang, Z. R.; Pang, T.; Sun, P. S.; Xia, H.; Wu, B.; Dong, F. Z., Development of a quantum cascade laser-based sensor for environmental HONO monitoring in the mid-infrared at 8 μm. *Journal of Lightwave Technology* **2019,** *37* (11), 2784-2791.

40. Gmachl, C.; Capasso, F.; Sivco, D. L.; Cho, A. Y., Recent progress in quantum cascade lasers and applications. *Reports on Progress in Physics* **2001,** *64* (11), 1533-1601.

41. Curl, R. F.; Capasso, F.; Gmachl, C.; Kosterev, A. A.; McManus, B.; Lewicki, R.; Pusharsky, M.; Wysocki, G.; Tittel, F. K., Quantum cascade lasers in chemical physics. *Chemical Physics Letters* **2010,** *487* (1-3), 1-18.

42. Nasir, E. F.; Farooq, A., Cavity-enhanced absorption sensor for carbon monoxide in a rapid compression machine. *Proceedings of the Combustion Institute* **2019,** *37* (2), 1297-1304.

43. Chang, Y. P.; Merer, A. J.; Chang, H. H.; Jhang, L. J.; Chao, W.; Lin, J. J. M., High resolution quantum cascade laser spectroscopy of the simplest Criegee intermediate, CH_2OO, between 1273 cm^{-1} and 1290 cm^{-1}. *Journal of Chemical Physics* **2017,** *146* (24), 244302.

44. Chang, Y. P.; Li, Y. L.; Liu, M. L.; Ou, T. C.; Lin, J. J. M., Absolute infrared absorption cross section of the simplest Criegee intermediate near 1285.7 cm^{-1}. *Journal of Physical Chemistry A* **2018,** *122* (45), 8874-8881.

45. Luo, P. L.; Endo, Y.; Lee, Y. P., High-resolution vibration-rotational spectra and rotational perturbation of the OO-stretching (ν_6) band of CH_2OO between 879.5 and 932.0 cm^{-1}. *Physical Chemistry Chemical Physics* **2018,** *20* (40), 25806-25811.

46. Chang, Y. P.; Chang, H. H.; Lin, J. J. M., Kinetics of the simplest Criegee intermediate reaction with ozone studied using a mid-infrared quantum cascade laser spectrometer. *Physical Chemistry Chemical Physics* **2018,** *20* (1), 97-102.

47. Luo, P. L.; Endo, Y.; Lee, Y. P., Identification and self-reaction kinetics of Criegee intermediates syn-CH_3CHOO and CH_2OO via high-resolution infrared

spectra with a quantum-cascade laser. *Journal of Physical Chemistry Letters* **2018,** *9* (15), 4391-4395.

48. Luo, P. L.; Chung, C. A.; Lee, Y. P., Rate coefficient of the reaction CH_2OO + NO_2 probed with a quantum-cascade laser near 11 μm. *Physical Chemistry Chemical Physics* **2019,** *21* (32), 17578-17583.

49. Qiu, J.; Tonokura, K., Detection of the simplest Criegee intermediate CH_2OO in the v_4 band using a continuous wave quantum cascade laser and its kinetics with SO_2 and NO_2. *Chemical Physics Letters: X* **2019,** *2*, 100019.

50. Li, Y. L.; Lin, Y. H.; Yin, C. T.; Takahashi, K.; Chiang, C. Y.; Chang, Y. P.; Lin, J. J. M., Temperature-dependent rate coefficient for the reaction of CH_3SH with the simplest Criegee intermediate. *Journal of Physical Chemistry A* **2019,** *123* (19), 4096-4103.

51. Li, Y. L.; Lin, C. Y.; Lin, Y. H.; Lin, J. J. M., Temperature-dependent kinetics of the simplest Criegee intermediate reaction with dimethyl sulfoxide. *Journal of the Chinese Chemical Society* **2020,** *67* (9), 1563-1570.

52. Miyano, S.; Tonokura, K., Measurements of nitrogen-broadening coefficients in the v_3 band of the hydroperoxyl radical using a continuous wave quantum cascade laser. *Journal of Molecular Spectroscopy* **2011,** *265* (1), 47-51.

53. Sakamoto, Y.; Tonokura, K., Measurements of the absorption line strength of hydroperoxyl radical in the v_3 band using a continuous wave quantum cascade laser. *Journal of Physical Chemistry A* **2012,** *116* (1), 215-222.

54. Chattopadhyay, A.; Samanta, M.; Mondal, K.; Chakraborty, T., Mid-infrared quantum cascade laser spectroscopy probing of the kinetics of an atmospherically significant radical reaction, $CH_3O_2 + NO_2 + M \rightarrow CH_3O_2NO_2 + M$, in the gas phase. *Journal of Chemical Sciences* **2018,** *130* (5).

55. Rawlins, W. T.; Hensley, J. M.; Sonnenfroh, D. M.; Oakes, D. B.; Allen, M. G., Quantum cascade laser sensor for SO_2 and SO_3 for application to combustor exhaust streams. *Applied Optics* **2005,** *44* (31), 6635-6643.

56. Welz, O.; Savee, J. D.; Osborn, D. L.; Vasu, S. S.; Percival, C. J.; Shallcross, D. E.; Taatjes, C. A., Direct kinetic measurements of Criegee intermediate (CH_2OO) formed by reaction of CH_2I with O_2. *Science* **2012,** *335* (6065), 204-207.

57. Vereecken, L.; Hardera, H.; Novelli, A., The reaction of Criegee intermediates with NO, RO_2, and SO_2, and their fate in the atmosphere. *Physical Chemistry Chemical Physics* **2012,** *14* (42), 14682-14695.

58. Percival, C. J.; Welz, O.; Eskola, A. J.; Savee, J. D.; Osborn, D. L.; Topping, D. O.; Lowe, D.; Utembe, S. R.; Bacak, A.; McFiggans, G.; Cooke, M. C.; Xiao, P.; Archibald, A. T.; Jenkin, M. E.; Derwent, R. G.; Riipinen, I.; Mok, D. W. K.; Lee, E. P. F.; Dyke, J. M.; Taatjes, C. A.; Shallcross, D. E., Regional and global impacts of Criegee intermediates on atmospheric sulphuric acid concentrations and first steps of aerosol formation. *Faraday Discussions* **2013,** *165*, 45-73.

59. Khan, M. A. H.; Percival, C. J.; Caravan, R. L.; Taatjes, C. A.; Shallcross, D. E., Criegee intermediates and their impacts on the troposphere. *Environmental Science: Processes & Impacts* **2018,** *20* (3), 437-453.

60. Chhantyal-Pun, R.; Rotavera, B.; McGillen, M. R.; Khan, M. A. H.; Eskola, A. J.; Caravan, R. L.; Blacker, L.; Tew, D. P.; Osborn, D. L.; Percival, C. J.; Taatjes, C. A.; Shallcross, D. E.; Orr-Ewing, A. J., Criegee intermediate reactions with carboxylic acids: A potential source of secondary organic aerosol in the atmosphere. *ACS Earth and Space Chemistry* **2018,** *2* (8), 833–842.

61. Chhantyal-Pun, R.; Khan, M. A. H.; Taatjes, C. A.; Percival, C. J.; Orr-Ewing, A. J.; Shallcross, D. E., Criegee intermediates: production, detection and reactivity. *International Reviews in Physical Chemistry* **2020,** *39* (3), 383-422.

62. Sheps, L., Absolute ultraviolet absorption spectrum of a Criegee intermediate CH_2OO. *The Journal of Physical Chemistry Letters* **2013,** *4* (24), 4201–4205.

63. Stone, D.; Blitz, M.; Daubney, L.; Howes, N. U. M.; Seakins, P., Kinetics of CH_2OO reactions with SO_2, NO_2, NO, H_2O and CH_3CHO as a function of pressure. *Physical Chemistry Chemical Physics* **2014,** *16* (3), 1139-1149.

64. Chhantyal-Pun, R.; Davey, A.; Shallcross, D. E.; Percival, C. J.; Orr-Ewing, A. J., A kinetic study of the CH_2OO Criegee intermediate self-reaction, reaction with

SO_2 and unimolecular reaction using cavity ring-down spectroscopy. *Physical Chemistry Chemical Physics* **2015,** *17* (5), 3617-3626.

65. Huang, H.-L.; Chao, W.; Lin, J. J.-M., Kinetics of a Criegee intermediate that would survive high humidity and may oxidize atmospheric SO_2. *Proceedings of the National Academy of Sciences* **2015,** *112* (35), 10857-10862.

66. Howes, N. U. M.; Mir, Z. S.; Blitz, M. A.; Hardman, S.; Lewis, T. R.; Stone, D.; Seakins, P. W., Kinetic studies of C_1 and C_2 Criegee intermediates with SO_2 using laser flash photolysis coupled with photoionization mass spectrometry and time resolved UV absorption spectroscopy. *Physical Chemistry Chemical Physics* **2018,** *20* (34), 22218-22227.

67. Liu, Y.; Bayes, K. D.; Sander, S. P., Measuring rate constants for reactions of the simplest Criegee intermediate (CH_2OO) by monitoring the OH radical. *The Journal of Physical Chemistry A* **2014,** *118* (4), 741–747.

68. Liu, Y.; Liu, F.; Liu, S.; Dai, D.; Dong, W.; Yang, X., A kinetic study of the CH_2OO Criegee intermediate reaction with SO_2, $(H_2O)_2$, CH_2I_2 and I atoms using OH laser induced fluorescence. *Physical Chemistry Chemical Physics* **2017,** *19* (31), 20786-20794.

69. Cox, R. A.; Ammann, M.; Crowley, J. N.; Herrmann, H.; Jenkin, M. E.; McNeill, V. F.; Mellouki, A.; Troe, J.; Wallington, T. J., Evaluated kinetic and photochemical data for atmospheric chemistry: Volume VII – Criegee intermediates. *Atmospheric Chemistry and Physics* **2020,** *20* (21), 13497–13519.

70. Taatjes, C. A.; Welz, O.; Eskola, A. J.; Savee, J. D.; Scheer, A. M.; Shallcross, D. E.; Rotavera, B.; Lee, E. P. F.; Dyke, J. M.; Mok, D. K. W.; Osborn, D. L.; Percival, C. J., Direct measurements of conformer-dependent reactivity of the Criegee intermediate CH_3CHOO. *Science* **2013,** *340* (6129), 177-180.

71. Wang, Y.-Y.; Dash, M. R.; Chung, C.-Y.; Lee, Y.-P., Detection of transient infrared absorption of SO_3 and 1,3,2-dioxathietane-2,2-dioxide [*cyc*-$(CH_2)O(SO_2)O$] in the reaction CH_2OO+SO_2. *The Journal of Chemical Physics* **2018,** *148* (6), 064301.

72. Jiang, L.; Xu, Y.-s.; Ding, A.-z., Reaction of stabilized Criegee intermediates from ozonolysis of limonene with sulfur dioxide: Ab initio and DFT study. *The Journal of Physical Chemistry A* **2010,** *114* (47), 12452–12461.

73. Kurtén, T.; Lane, J. R.; Jørgensen, S.; Kjaergaard, H. G., A computational study of the oxidation of SO_2 to SO_3 by gas-phase organic oxidants. *The Journal of Physical Chemistry A* **2011,** *115* (31), 8669–8681.

74. Kuwata, K. T.; Guinn, E. J.; Hermes, M. R.; Fernandez, J. A.; Mathison, J. M.; Huang, K., A computational re-examination of the Criegee intermediate–sulfur dioxide reaction. *The Journal of Physical Chemistry A* **2015,** *119* (41), 10316–10335.

75. Aplincourt, P.; Ruiz-López, M. F., Theoretical investigation of reaction mechanisms for carboxylic acid formation in the atmosphere. *Journal of the American Chemical Society* **2000,** *122* (37), 8990–8997.

76. Onel, L.; Lade, R.; Mortiboy, J.; Blitz, M.; Seakins, P.; Heard, D.; Stone, D., Kinetics of the gas phase reaction of the Criegee intermediate CH_2OO with SO_2 as a function of temperature. **In production**.

77. Glowacki, D. R.; Liang, C.-H.; Morley, C.; Pilling, M. J.; Robertson, S. H., MESMER: An open-source Master Equation Solver for Multi-Energy well Reactions. *The Journal of Physical Chemistry A* **2012,** *116* (38), 9545–9560.

78. Shannon, R. J.; Caravan, R. L.; Blitz, M. A.; Heard, D. E., A combined experimental and theoretical study of reactions between the hydroxyl radical and oxygenated hydrocarbons relevant to astrochemical environments. *Physical Chemistry Chemical Physics* **2014,** *16* (8), 3466-3478.

79. Shannon, R. J.; Tomlin, A. S.; Robertson, S. H.; Blitz, M. A.; Pilling, M. J.; Seakins, P. W., Global uncertainty propagation and sensitivity analysis in the $CH_3OCH_2 + O_2$ system: Combining experiment and theory to constrain key rate coefficients in DME combustion. *The Journal of Physical Chemistry A* **2015,** *119* (28), 7430–7438.

80. Stone, D.; Au, K.; Sime, S.; Medeiros, D. J.; Blitz, M.; Seakins, P. W.; Decker, Z.; Sheps, L., Unimolecular decomposition kinetics of the stabilised Criegee intermediates CH_2OO and CD_2OO. *Physical Chemistry Chemical Physics* **2018,** *20* (38), 24940-24954.

81. Whelan, C. A.; Blitz, M. A.; Shannon, R.; Onel, L.; Lockhart, J. P.; Seakins, P. W.; Stone, D., Temperature and pressure dependent kinetics of QOOH decomposition and reaction with O_2: Experimental and theoretical investigations of

QOOH radicals derived from Cl + $(CH_3)_3COOH$. *The Journal of Physical Chemistry A* **2019,** *123* (47), 10254–10262.

82. Whelan, C. A.; Eble, J.; Mir, Z. S.; Blitz, M. A.; Seakins, P. W.; Olzmann, M.; Stone, D., Kinetics of the reactions of hydroxyl radicals with furan and its alkylated derivatives 2-methyl furan and 2,5-dimethyl furan. *The Journal of Physical Chemistry A* **2020,** *124* (37), 7416–7426.

83. Qian, H. B.; Turton, D.; Seakins, P. W.; Pilling, M. J., Dynamic frequency stabilization of infrared diode laser for kinetic studies. *Chemical Physics Letters* **2000,** *322* (1-2), 57-64.

84. Qian, H. B.; Turton, D.; Seakins, P. W.; Pilling, M. J., A laser flash photolysis/IR diode laser absorption study of the reaction of chlorine atoms with selected alkanes. *International Journal of Chemical Kinetics* **2001,** *34* (2), 86-94.

85. Choi, N.; Pilling, M. J.; Seakins, P. W.; Wang, L., Studies of site selective hydrogen atom abstractions by Cl atoms from isobutane and propane by laser flash photolysis/IR diode laser spectroscopy. *Physical Chemistry Chemical Physics* **2006,** *8* (18), 2172-2178.

86. Gordon, I. E.; Rothman, L. S.; Hill, C.; Kochanov, R. V.; Tan, Y.; Bernath, P. F.; Birk, M.; Boudon, V.; Campargue, A.; Chance, K. V.; Drouin, B. J.; Flaud, J.-M.; Gamache, R. R.; Hodges, J. T.; Jacquemart, D.; Perevalov, V. I.; Perrin, A.; Shine, K. P.; Smith, M.-A. H.; Tennyson, J.; Toon, G. C.; Tran, H.; Tyuterev, V. G.; Barbe, A.; Császár, A. G.; Devi, V. M.; Furtenbacher, T.; Harrison, J. J.; Hartmann, J. M.; Jolly, A.; Johnson, T. J.; Karman, T.; Kleiner, I.; Kyuberis, A. A.; Loos, J.; Lyulin, O. M.; Massie, S. T.; Mikhailenko, S. N.; Moazzen-Ahmadi, N.; Müller, H. S. P.; Naumenko, O. V.; Nikitin, A. V.; Polyansky, O. L.; Rey, M.; Rotger, M.; Sharpe, S. W.; Sung, K.; Starikova, E.; Tashkun, S. A.; VanderAuwera, J.; Wagner, G.; Wilzewski, J.; Wcisło, P.; Yu, S.; Zak, E. J., The HITRAN2016 molecular spectroscopic database. *Journal of Quantitative Spectroscopy and Radiative Transfer* **2017,** *203,* 3-69.

87. Atkinson, R.; Baulch, D. L.; Cox, R. A.; Crowley, J. N.; Hampson, R. F.; Hynes, R. G.; Jenkin, M. E.; Rossi, M. J.; Troe, J.; Wallington, T. J., Evaluated kinetic and photochemical data for atmospheric chemistry: Volume IV – gas phase

reactions of organic halogen species. *Atmospheric Chemistry and Physics* **2008,** *8* (15), 4141–4496.

88. Stone, D.; Blitz, M.; Daubney, L.; Ingham, T.; Seakins, P., CH_2OO Criegee biradical yields following photolysis of CH_2I_2 in O_2. *Physical Chemistry Chemical Physics* **2013,** *15* (44), 19119-19124.

89. Su, Y.-T.; Lin, H.-Y.; Putikam, R.; Matsui, H.; Lin, M. C.; Lee, Y.-P., Extremely rapid self-reaction of the simplest Criegee intermediate CH_2OO and its implications in atmospheric chemistry. *Nature Chemistry* **2014,** *6* (6), 477–483.

90. Mir, Z. S.; Lewis, T. R.; Onel, L.; Blitz, M. A.; Seakins, P. W.; Stone, D., CH_2OO Criegee intermediate UV absorption cross-sections and kinetics of CH_2OO + CH_2OO and CH_2OO + I as a function of pressure. *Physical Chemistry Chemical Physics* **2020,** *22* (17), 9448-9459.

91. Underwood, D. S.; Tennyson, J.; Yurchenko, S. N., An *ab initio* variationally computed room-temperature line list for $^{32}S^{16}O_3$. *Physical Chemistry Chemical Physics* **2013,** *15* (25), 10118-10125.

Chapter 7

Summary and Future Work

Criegee intermediates are an important class of trace species produced during atmospheric ozonolysis, i.e. the atmospheric oxidation of unsaturated volatile organic compounds by ozone.[1, 2] The chemistry of these zwitterionic species has implications for the non-photolytic atmospheric production of OH, particularly under conditions of low solar radiation such as at night and during winter,[3-6] and for production of other radicals such as HO_2 and RO_2, sulphate aerosol, secondary organic aerosol (SOA), gaseous sulphuric acid (H_2SO_4) and acid rain, thus affecting the formation of new atmospheric particles and secondary cloud condensation nuclei, and ultimately, the climate.[7-11] Since the recent introduction of the diiodoalkane photolysis method to generate Criegee intermediates and enable direct detection,[7] a number of investigations have been carried out into the spectroscopic and kinetic properties of various Criegee intermediates. The work carried out and described in this thesis has investigated the spectra and kinetics of the simplest Criegee intermediate CH_2OO.

7.1 Summary of Results

Measurements of Criegee intermediate ultraviolet (UV) absorption cross-sections of CH_2OO, the simplest Criegee intermediate, have indicated that the absorption cross-sections are relatively large, on the order of 10^{-17} cm^2,[12-15] making UV absorption spectroscopy a useful tool for the measurement of atmospherically relevant CH_2OO reaction kinetics. However, there are significant uncertainties in the UV absorption cross-sections and in the shape of the CH_2OO spectrum. Significant uncertainties have also been reported in the rate coefficient for the CH_2OO + CH_2OO self-reaction,[16-19] which is not itself atmospherically important but for which an accurate value is required since it largely influences CH_2OO kinetics under laboratory conditions, and the kinetics of which can be closely coupled to the determination of absorption cross-sections since significant changes in concentration can occur on the timescale of the absorption measurements. The CH_2OO self-reaction has the potential to impact all CH_2OO reaction kinetics determined under laboratory conditions, where

the self-reaction becomes important due to the large concentration of CH_2OO formed in such experiments, hence it is necessary to quantify the contribution of this CH_2OO self-reaction to the observed kinetics.

The UV absorption cross-sections of CH_2OO, and the kinetics of the CH_2OO self-reaction, $CH_2OO + CH_2OO$, and the reaction between CH_2OO and I have been investigated using pulsed laser flash photolysis of $CH_2I_2/O_2/N_2$ gas mixtures at 248 nm coupled with time-resolved broadband UV absorption spectroscopy at pressures between 6 and 300 Torr and a temperature of 298 K. Results indicate a broad UV absorption spectrum for CH_2OO, with a peak absorption cross-section of $(1.37 \pm 0.29) \times 10^{-17}$ cm^2 at $\lambda \sim 340$ nm and vibronic structure at wavelengths > 340 nm, in good agreement with results reported by Ting *et al.*[14] and Foreman *et al.*[15] Kinetics of the CH_2OO self-reaction have been shown to be independent of pressure over the range investigated, with a rate coefficient of $(8.0 \pm 1.1) \times 10^{-11}$ cm^3 s^{-1} over all pressures, in good agreement with the current IUPAC recommendation. The $CH_2OO + I$ reaction is significant in the reaction system, with a pressure dependent rate coefficient ranging from $(1.1\ ^{+2.2}_{-1.1}) \times 10^{-12}$ cm^3 s^{-1} at 6 Torr to $(5.5 \pm 2.1) \times 10^{-11}$ cm^3 s^{-1} at 300 Torr which can be parameterised by a Lindemann fit using $k_0 = (4.4 \pm 1.0) \times 10^{-29}$ cm^6 s^{-1} and $k_\infty = (6.7 \pm 0.6) \times 10^{-11}$ cm^3 s^{-1}. The production of IO in the system resulting from secondary I atom chemistry has also been investigated as a function of pressure. Results indicate that IO formation results from the chemistry of both the CH_2OO Criegee intermediate and the CH_2IO_2 peroxy radical, with relative contributions from CH_2OO and CH_2IO_2 chemistry varying as a function of pressure owing to the pressure-dependent yields of CH_2OO and CH_2IO_2 from $CH_2I + O_2$ and the pressure dependence of the $CH_2OO + I$ reaction. The kinetics of the $CH_2OO + I$ reaction along with its impacts in laboratory measurements of CH_2OO kinetics,[16-19] and the source of IO radicals following photolysis of CH_2I_2 in excess O_2,[18, 20-26] have long been of interest with significant discrepancies for both reported in the literature. However, results determined in this work of the pressure dependent rate coefficient for the $CH_2OO + I$ reaction and the production of IO in the system resulting from chemistry of both CH_2OO and CH_2IO_2 have resolved these discrepancies.

As is the case for many other species of atmospheric interest, infrared (IR) absorption spectroscopy, particularly in the mid-IR region of the electromagnetic spectrum and

using quantum cascade lasers (QCLs), has also been indicated to be a promising method of CH_2OO detection,[27-35] for determination of not only reaction kinetics but also product yields. The $CH_2OO + SO_2$ bimolecular reaction has potentially significant implications for the atmospheric production of sulphate aerosol, secondary organic aerosols and sulphuric acid, hence can influence air quality and climate, and can significantly impact our understanding of the atmospheric oxidation of SO_2 to SO_3.[7-11] Although the kinetics of this reaction at room temperature are well studied in the literature,[7, 13, 19, 33, 36-40] there exists a lack of experimental information on the SO_3 product yield of the reaction. Observation of the HCHO co-product in 100 % yield with a lack of pressure dependence implies SO_3 to be produced in the same yield,[36] and theory suggests that the SO_3 yield may vary for larger Criegee intermediates.

Experiments described in this thesis have enabled development and characterisation of a new, robust and economical instrument carrying the potential to be utilised in various reaction systems and be applied to a vast array of challenges in atmospheric chemistry and beyond. The development, characterisation and initial results of the instrument from experiments investigating the $CH_2OO + SO_2$ reaction are reported. The IR absorption spectrum of CH_2OO and rate coefficient $CH_2OO + SO_2$ reaction with respect to CH_2OO loss and SO_3 production have been determined using pulsed laser flash photolysis of $CH_2I_2/O_2/SO_2/N_2$ gas mixtures at 266 nm coupled with time-resolved mid-IR quantum cascade laser (QCL) absorption spectroscopy at pressures between 20 and 100 Torr and a temperature of 298 K. Results show the observed CH_2OO spectrum to have defined rovibrational structure and be in good agreement with that reported previously by Chang *et al.*[30] in terms of relative peak heights and positions in the wavenumber region 1285.5917-1286.0605 cm^{-1}. Kinetics of the $CH_2OO + SO_2$ reaction have been determined to be independent of pressure over the pressure range investigated, with a rate coefficient of $(3.8 \pm 0.5) \times 10^{-11}$ cm^3 s^{-1} from both CH_2OO and SO_3 measurements over all pressures, in good agreement with the current IUPAC recommendation. Results indicate the product yield of SO_3 from the reaction between CH_2OO and SO_2 to be independent of pressure over the range investigated, with an SO_3 absorption cross-section of $(5.5 \pm 2.3) \times 10^{-19}$ cm^2 at ~1388.7 cm^{-1}.

Results obtained in this work will provide valuable kinetic data for use in the determination of reaction kinetics of CH_2OO reactions with various atmospheric species when employing UV and IR absorption spectroscopy to detect and monitor CH_2OO, and for use in atmospheric chemistry models when accounting for CH_2OO chemistry. The new mid-IR QCL absorption spectroscopy instrument designed, developed and characterised as part of this work can be used to investigate a wide range of systems applicable to fields such as atmospheric chemistry and combustion chemistry.

7.2 Future Work

The field of Criegee chemistry is a new and exciting one, and although considerable progress has been made in the understanding of Criegee intermediates and their reactions since the introduction of the photolytic production method of Criegee intermediates, this research is far from exhaustive. To date, most investigations have been largely limited to the simplest Criegee intermediate, CH_2OO, or its methyl substituted derivatives, *syn*- and *anti*-CH_3CHOO. An extension to larger Criegee intermediates, abundantly present and important in the atmosphere, is not only desirable, but is necessary to completely comprehend the chemistry which is occurring.

Furthermore, kinetic data for the various bimolecular reactions of the various Criegee intermediates with trace atmospheric species is limited in the literature. Not only is there a lack of detailed investigations into the pressure dependence of Criegee reactions, but the kinetic analysis of reactions as a function of temperature is scarce still, and the product yields of various reaction channels of atmospherically relevant Criegee reactions also await characterisation. Both pressure and temperature dependent kinetics, along with product yields, need to be assessed to establish the effects and implications of Criegee chemistry in the real world, since, without this information it is impossible to fully appreciate the extent to which Criegee intermediate chemistry impacts atmospheric composition, air quality and climate change.

Relative rates of bimolecular reactions of Criegee intermediates determine which will play the more dominant role in the atmosphere, with the competition between reactions of $(H_2O)_2$, SO_2, NO_2 and carboxylic acids among others expected to vary dependent on the Criegee intermediate. Accurate measurements of the rate coefficients for these reactions along with their temperature and pressure dependence are vital to evaluate their atmospheric importance as potential Criegee sink processes and determine which reactions are more atmospherically relevant for each Criegee.

The reaction of CH_2OO with water is of interest since the rate of the reaction exhibits a quadratic dependence on the concentration of H_2O, suggesting a reaction with the water dimer $(H_2O)_2$. This reaction between CH_2OO and water dimer has been shown to be rapid, and is important since it is expected to be the dominant atmospheric sink for CH_2OO owing to the high concentration of H_2O and hence $(H_2O)_2$ in the atmosphere. Therefore, future experiments should focus on the kinetics of the $CH_2OO + (H_2O)_2$ reaction as a function of both pressure and temperature and determination of product yields from this reaction.

Furthermore, there is the potential to study larger Criegee intermediates *via* the methods utilised throughout this work, and hence experiments to determine absorption cross-sections and reaction kinetics of larger Criegee intermediates with atmospherically relevant co-reactant species can be investigated. For example, theoretical studies of the reactions of larger Criegee intermediates, e.g. $(CH_3)_2COO$, with SO_2 have indicated the kinetics and SO_3 product yields of these reactions to be pressure dependent, with potential stabilisation of the initial addition adducts formed during the reaction at atmospheric pressure rather than production of SO_3. Experimental determination of such reaction kinetics and product yields as a function of pressure is warranted to assess the atmospheric implications of these reactions.

7.3 References

1. Criegee, R.; Wenner, G., Die Ozonisierung des 9,10-Oktalins. *Justus Liebigs Annalen der Chemie* **1949,** *564* (1), 9-15.

2. Criegee, R., Mechanism of ozonolysis. *Angewandte Chemie International Edition* **1975,** *14* (11), 745-752.

3. Heard, D. E.; Carpenter, L. J.; Creasey, D. J.; Hopkins, J. R.; Lee, J. D.; Lewis, A. C.; Pilling, M. J.; Seakins, P. W.; Carslaw, N.; Emmerson, K. M., High levels of the hydroxyl radical in the winter urban troposphere. *Geophysical Research Letters* **2004,** *31* (18), L18112.

4. Malkin, T. L.; Goddard, A.; Heard, D. E.; Seakins, P. W., Measurements of OH and HO_2 yields from the gas phase ozonolysis of isoprene. *Atmospheric Chemistry and Physics* **2010,** *10* (3), 1441–1459.

5. Stone, D.; Whalley, L. K.; Heard, D. E., Tropospheric OH and HO_2 radicals: field measurements and model comparisons. *Chemical Society Reviews* **2012,** *41* (19), 6348-6404.

6. Stone, D.; Evans, M. J.; Walker, H.; Ingham, T.; Vaughan, S.; Ouyang, B.; Kennedy, O. J.; McLeod, M. W.; Jones, R. L.; Hopkins, J.; Punjabi, S.; Lidster, R.; Hamilton, J. F.; Lee, J. D.; Lewis, A. C.; Carpenter, L. J.; Forster, G.; Oram, D. E.; Reeves, C. E.; Bauguitte, S.; Morgan, W.; Coe, H.; Aruffo, E.; Dari-Salisburgo, C.; Giammaria, F.; Carlo, P. D.; Heard, D. E., Radical chemistry at night: comparisons between observed and modelled HO_X, NO_3 and N_2O_5 during the RONOCO project. *Atmospheric Chemistry and Physics* **2014,** *14* (3), 1299–1321.

7. Welz, O.; Savee, J. D.; Osborn, D. L.; Vasu, S. S.; Percival, C. J.; Shallcross, D. E.; Taatjes, C. A., Direct kinetic measurements of Criegee intermediate (CH_2OO) formed by reaction of CH_2I with O_2. *Science* **2012,** *335* (6065), 204-207.

8. Vereecken, L.; Hardera, H.; Novelli, A., The reaction of Criegee intermediates with NO, RO_2, and SO_2, and their fate in the atmosphere. *Physical Chemistry Chemical Physics* **2012,** *14* (42), 14682-14695.

9. Percival, C. J.; Welz, O.; Eskola, A. J.; Savee, J. D.; Osborn, D. L.; Topping, D. O.; Lowe, D.; Utembe, S. R.; Bacak, A.; McFiggans, G.; Cooke, M. C.; Xiao, P.; Archibald, A. T.; Jenkin, M. E.; Derwent, R. G.; Riipinen, I.; Mok, D. W. K.; Lee, E. P. F.; Dyke, J. M.; Taatjes, C. A.; Shallcross, D. E., Regional and global impacts of Criegee intermediates on atmospheric sulphuric acid concentrations and first steps of aerosol formation. *Faraday Discussions* **2013,** *165*, 45-73.

10. Khan, M. A. H.; Percival, C. J.; Caravan, R. L.; Taatjes, C. A.; Shallcross, D. E., Criegee intermediates and their impacts on the troposphere. *Environmental Science: Processes & Impacts* **2018,** *20* (3), 437-453.

11. Chhantyal-Pun, R.; Rotavera, B.; McGillen, M. R.; Khan, M. A. H.; Eskola, A. J.; Caravan, R. L.; Blacker, L.; Tew, D. P.; Osborn, D. L.; Percival, C. J.; Taatjes, C. A.; Shallcross, D. E.; Orr-Ewing, A. J., Criegee intermediate reactions with carboxylic acids: A potential source of secondary organic aerosol in the atmosphere. *ACS Earth and Space Chemistry* **2018,** *2* (8), 833–842.

12. Beames, J. M.; Liu, F.; Lu, L.; Lester, M. I., Ultraviolet spectrum and photochemistry of the simplest Criegee intermediate CH_2OO. *Journal of the American Chemical Society* **2012,** *134* (49), 20045-20048.

13. Sheps, L., Absolute ultraviolet absorption spectrum of a Criegee intermediate CH_2OO. *The Journal of Physical Chemistry Letters* **2013,** *4* (24), 4201-4205.

14. Ting, W.-L.; Chen, Y.-H.; Chao, W.; Smith, M. C.; Lin, J. J.-M., The UV absorption spectrum of the simplest Criegee intermediate CH_2OO. *Physical Chemistry Chemical Physics* **2014,** *16* (22), 10438-10443

15. Foreman, E. S.; Kapnas, K. M.; Jou, Y.; Kalinowski, J.; Feng, D.; Gerber, R. B.; Murray, C., High resolution absolute absorption cross sections of the B^1A'–X^1A' transition of the CH_2OO biradical. *Physical Chemistry Chemical Physics* **2015,** *17* (48), 32539-32546.

16. Su, Y.-T.; Lin, H.-Y.; Putikam, R.; Matsui, H.; Lin, M. C.; Lee, Y.-P., Extremely rapid self-reaction of the simplest Criegee intermediate CH_2OO and its implications in atmospheric chemistry. *Nature Chemistry* **2014,** *6* (6), 477–483.

17. Buras, Z. J.; Elsamra, R. M. I.; Green, W. H., Direct determination of the simplest Criegee intermediate (CH_2OO) self reaction rate. *The Journal of Physical Chemistry Letters* **2014,** *5* (13), 2224-2228.

18. Ting, W.-L.; Chang, C.-H.; Lee, Y.-F.; Matsui, H.; Lee, Y.-P.; Lin, J. J.-M., Detailed mechanism of the $CH_2I + O_2$ reaction: Yield and self-reaction of the simplest Criegee intermediate CH_2OO. *The Journal of Chemical Physics* **2014,** *141* (10), 104308.

19. Chhantyal-Pun, R.; Davey, A.; Shallcross, D. E.; Percival, C. J.; Orr-Ewing, A. J., A kinetic study of the CH_2OO Criegee intermediate self-reaction, reaction with SO_2 and unimolecular reaction using cavity ring-down spectroscopy. *Physical Chemistry Chemical Physics* **2015,** *17* (5), 3617-3626.

20. Masaki, A.; Tsunashima, S.; Washida, N., Rate constants for reactions of substituted methyl radicals (CH_2OCH_3, CH_2NH_2, CH_2I, and CH_2CN) with O_2. *The Journal of Physical Chemistry* **1995,** *99* (35), 13126-13131.

21. Enami, S.; Ueda, J.; Goto, M.; Nakano, Y.; Aloisio, S.; Hashimoto, S.; Kawasaki, M., Formation of iodine monoxide radical from the reaction of CH_2I with O_2. *The Journal of Physical Chemistry A* **2004,** *108* (30), 6347-6350.

22. Eskola, A. J.; Wojcik-Pastuszka, D.; Ratajczak, E.; Timonen, R. S., Kinetics of the reactions of CH_2Br and CH_2I radicals with molecular oxygen at atmospheric temperatures. *Physical Chemistry Chemical Physics* **2006,** *8* (12), 1416-1424.

23. Enami, S.; Sakamoto, Y.; Yamanaka, T.; Hashimoto, S.; Kawasaki, M.; Tonokura, K.; Tachikawa, H., Reaction mechanisms of IO radical formation from the reaction of CH_3I with Cl atom in the presence of O_2. *Bulletin of the Chemical Society of Japan* **2008,** *81* (10), 1250-1257.

24. Dillon, T. J.; Tucceri, M. E.; Sander, R.; Crowley, J. N., LIF studies of iodine oxide chemistry. *Physical Chemistry Chemical Physics* **2008,** *10* (11), 1540-1554.

25. Gravestock, T. J.; Blitz, M. A.; Bloss, W. J.; Heard, D. E., A multidimensional study of the reaction $CH_2I + O_2$: products and atmospheric implications. *ChemPhysChem* **2010,** *11* (18), 3928-3941.

26. Foreman, E. S.; Murray, C., Kinetics of IO production in the $CH_2I + O_2$ reaction studied by cavity ring-down spectroscopy. *The Journal of Physical Chemistry A* **2015,** *119* (34), 8981-8990.

27. Chang, Y. P.; Merer, A. J.; Chang, H. H.; Jhang, L. J.; Chao, W.; Lin, J. J. M., High resolution quantum cascade laser spectroscopy of the simplest Criegee intermediate, CH_2OO, between 1273 cm^{-1} and 1290 cm^{-1}. *Journal of Chemical Physics* **2017,** *146* (24), 244302.

28. Chang, Y. P.; Li, Y. L.; Liu, M. L.; Ou, T. C.; Lin, J. J. M., Absolute infrared absorption cross section of the simplest Criegee intermediate near 1285.7 cm^{-1}. *Journal of Physical Chemistry A* **2018,** *122* (45), 8874-8881.

29. Luo, P. L.; Endo, Y.; Lee, Y. P., High-resolution vibration-rotational spectra and rotational perturbation of the OO-stretching (v_6) band of CH_2OO between 879.5 and 932.0 cm^{-1}. *Physical Chemistry Chemical Physics* **2018,** *20* (40), 25806-25811.

30. Chang, Y. P.; Chang, H. H.; Lin, J. J. M., Kinetics of the simplest Criegee intermediate reaction with ozone studied using a mid-infrared quantum cascade laser spectrometer. *Physical Chemistry Chemical Physics* **2018,** *20* (1), 97-102.

31. Luo, P. L.; Endo, Y.; Lee, Y. P., Identification and self-reaction kinetics of Criegee intermediates *syn*-CH_3CHOO and CH_2OO *via* high-resolution infrared spectra with a quantum-cascade laser. *Journal of Physical Chemistry Letters* **2018,** *9* (15), 4391-4395.

32. Luo, P. L.; Chung, C. A.; Lee, Y. P., Rate coefficient of the reaction CH_2OO + NO_2 probed with a quantum-cascade laser near 11 μm. *Physical Chemistry Chemical Physics* **2019,** *21* (32), 17578-17583.

33. Qiu, J.; Tonokura, K., Detection of the simplest Criegee intermediate CH_2OO in the v_4 band using a continuous wave quantum cascade laser and its kinetics with SO_2 and NO_2. *Chemical Physics Letters: X* **2019,** *2*, 100019.

34. Li, Y. L.; Lin, Y. H.; Yin, C. T.; Takahashi, K.; Chiang, C. Y.; Chang, Y. P.; Lin, J. J. M., Temperature-dependent rate coefficient for the reaction of CH_3SH with the simplest Criegee intermediate. *Journal of Physical Chemistry A* **2019,** *123* (19), 4096-4103.

35. Li, Y. L.; Lin, C. Y.; Lin, Y. H.; Lin, J. J. M., Temperature-dependent kinetics of the simplest Criegee intermediate reaction with dimethyl sulfoxide. *Journal of the Chinese Chemical Society* **2020,** *67* (9), 1563-1570.

36. Stone, D.; Blitz, M.; Daubney, L.; Howes, N. U. M.; Seakins, P., Kinetics of CH_2OO reactions with SO_2, NO_2, NO, H_2O and CH_3CHO as a function of pressure. *Physical Chemistry Chemical Physics* **2014,** *16* (3), 1139-1149.

37. Liu, Y.; Bayes, K. D.; Sander, S. P., Measuring rate constants for reactions of the simplest Criegee intermediate (CH_2OO) by monitoring the OH radical. *The Journal of Physical Chemistry A* **2014,** *118* (4), 741–747.

38. Huang, H.-L.; Chao, W.; Lin, J. J.-M., Kinetics of a Criegee intermediate that would survive high humidity and may oxidize atmospheric SO_2. *Proceedings of the National Academy of Sciences* **2015,** *112* (35), 10857-10862.

39. Liu, Y.; Liu, F.; Liu, S.; Dai, D.; Dong, W.; Yang, X., A kinetic study of the CH_2OO Criegee intermediate reaction with SO_2, $(H_2O)_2$, CH_2I_2 and I atoms using OH laser induced fluorescence. *Physical Chemistry Chemical Physics* **2017,** *19* (31), 20786-20794.

40. Howes, N. U. M.; Mir, Z. S.; Blitz, M. A.; Hardman, S.; Lewis, T. R.; Stone, D.; Seakins, P. W., Kinetic studies of C_1 and C_2 Criegee intermediates with SO_2 using laser flash photolysis coupled with photoionization mass spectrometry and time resolved UV absorption spectroscopy. *Physical Chemistry Chemical Physics* **2018,** *20* (34), 22218-22227.

Appendices

Appendix 1: MFC calibrations

Calibration of all MFCs was carried out periodically by varying the gas flow into the MFC and monitoring the displacement of bubbles through a flow tube.

UV experimental setup described in Chapter 3 and experiments/results from this setup described in Chapters 4 and 5. MFC calibrations for each of the MFCs used in Chapters 4 and 5 (listed by serial number, S/N) are shown below.

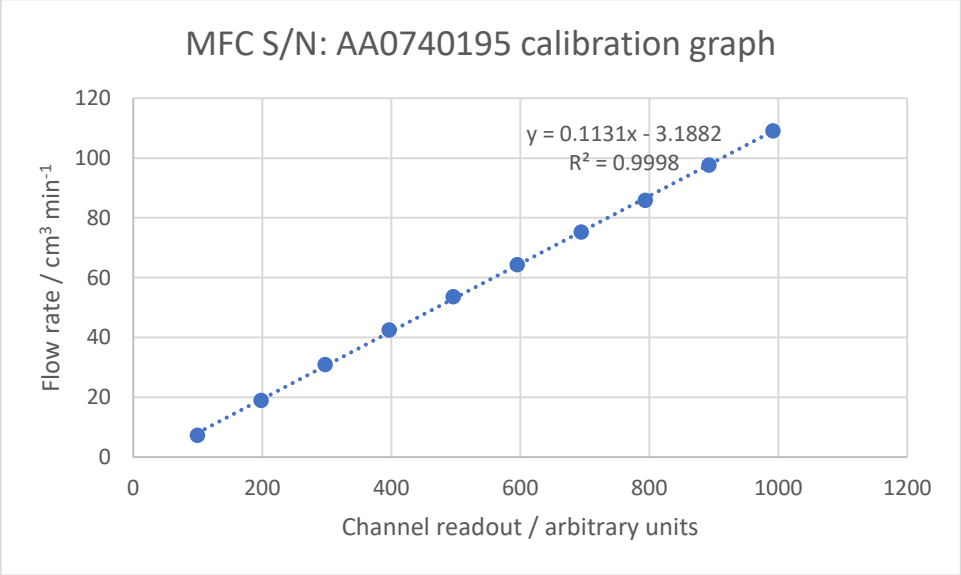

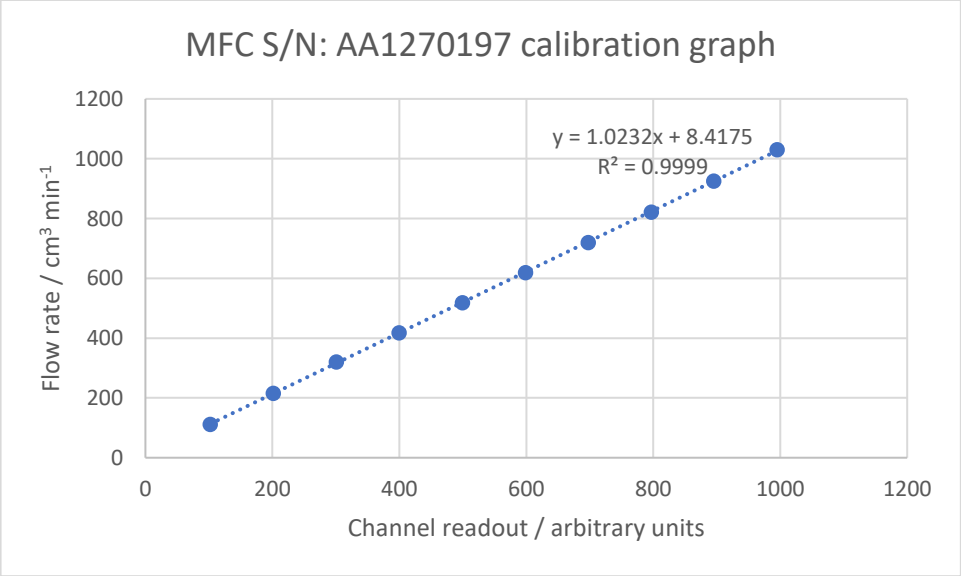

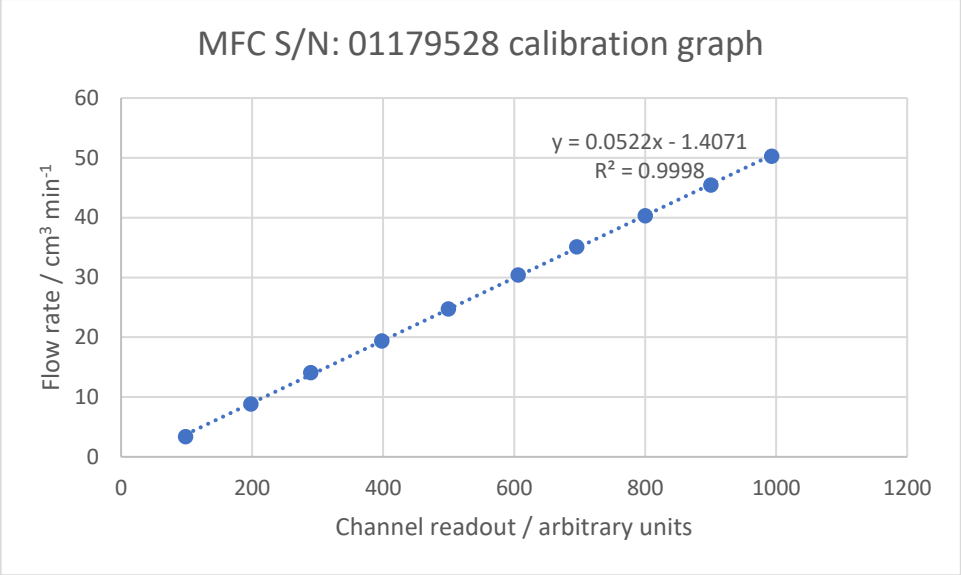

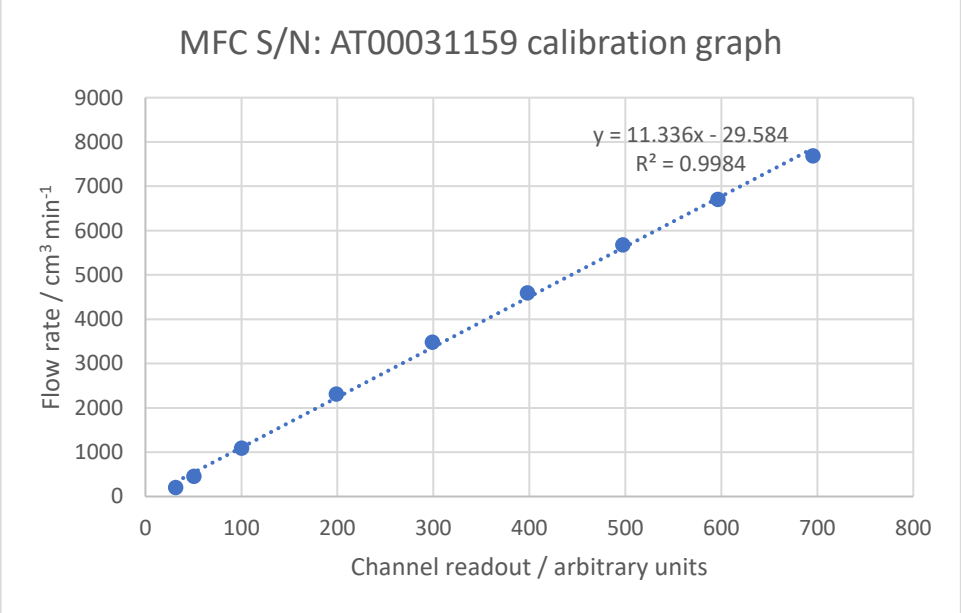

IR experimental setup and experiments/results from this setup described in Chapter 6. MFC calibrations for each of the MFCs used in Chapter 6 (listed by serial number, S/N) are shown below.

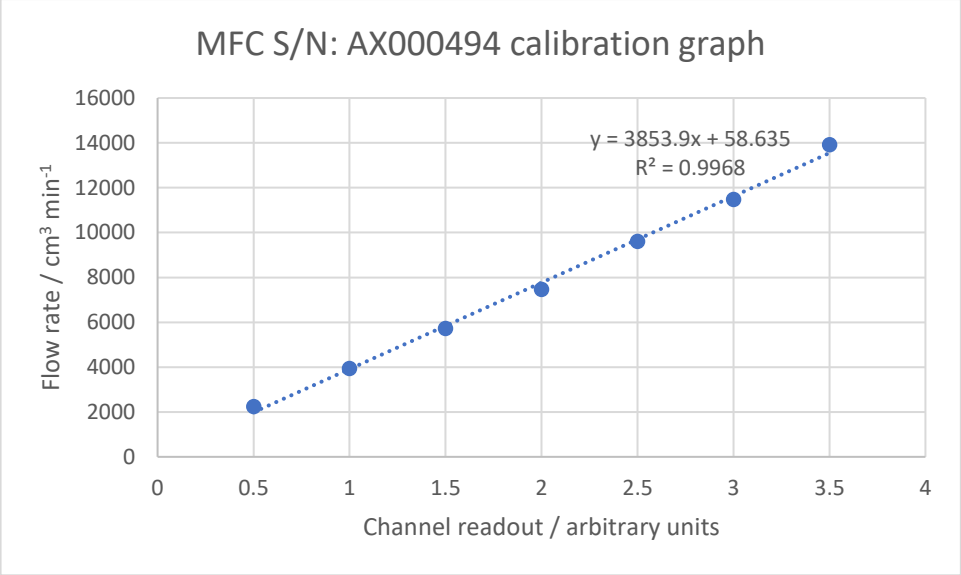
MFC S/N: AX000494 calibration graph
y = 3853.9x + 58.635
R² = 0.9968
Flow rate / cm³ min⁻¹
Channel readout / arbitrary units
0
2000
4000
6000
8000
10000
12000
14000
16000
0
0.5
1
1.5
2
2.5
3
3.5
4

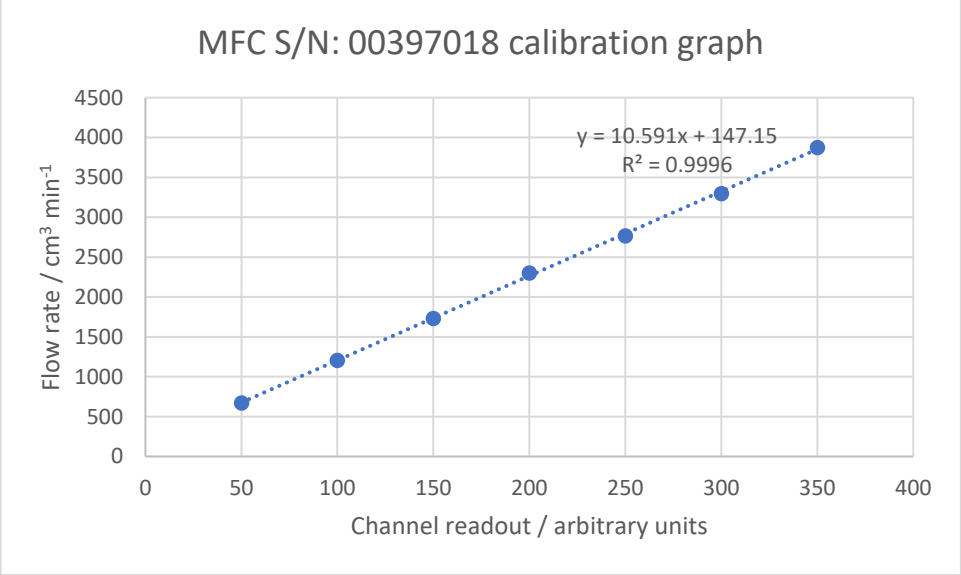
MFC S/N: 00397018 calibration graph
y = 10.591x + 147.15
R² = 0.9996
Flow rate / cm³ min⁻¹
Channel readout / arbitrary units
0
500
1000
1500
2000
2500
3000
3500
4000
4500
0
50
100
150
200
250
300
350
400

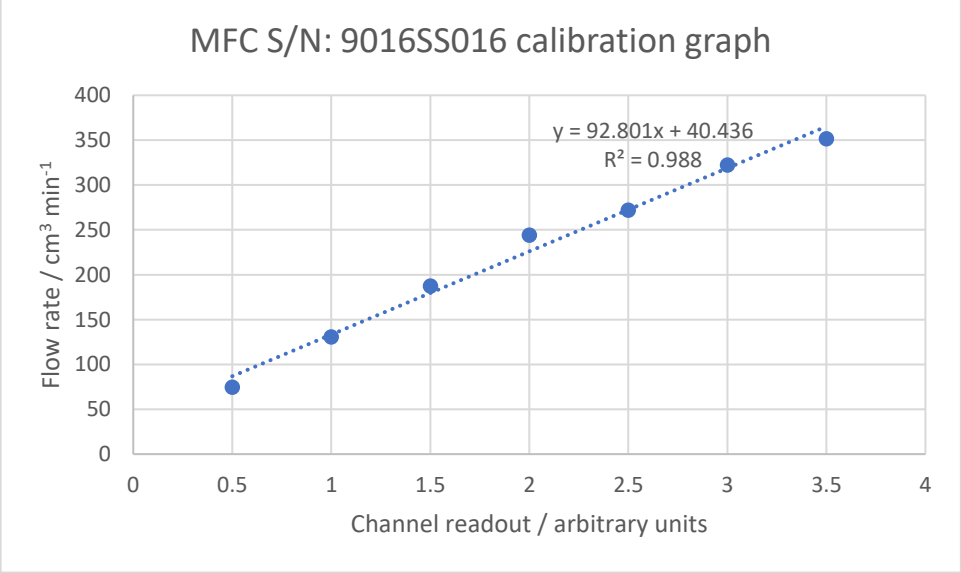
MFC S/N: 9016SS016 calibration graph
y = 92.801x + 40.436
R² = 0.988
Flow rate / cm³ min⁻¹
Channel readout / arbitrary units
0
50
100
150
200
250
300
350
400
0
0.5
1
1.5
2
2.5
3
3.5
4

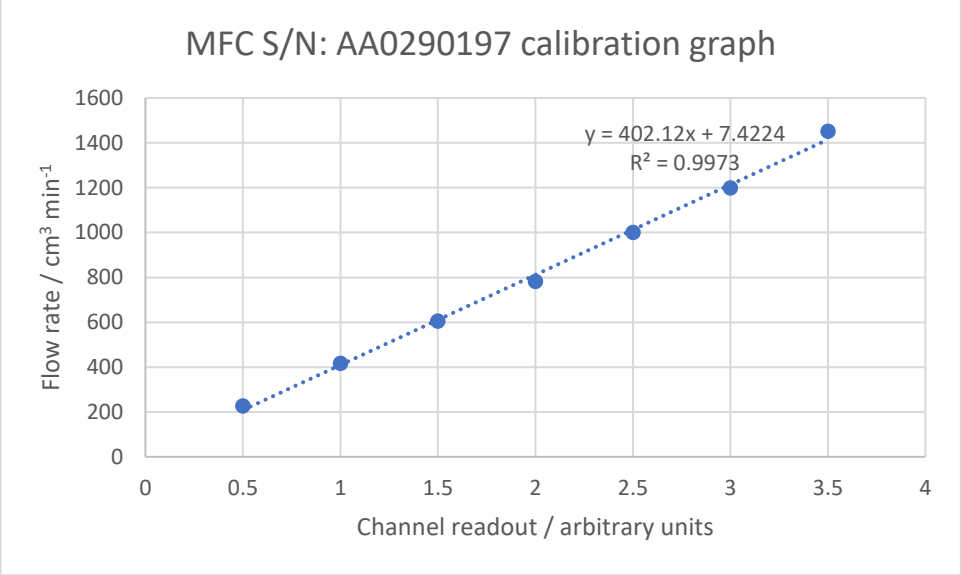

Appendix 2: Effective path length in UV experiments

In the experimental setup described in Chapter 3 and the work described in Chapters 4 and 5, the optics controlling the path of the multipass beam were arranged to give either 7 or 13 passes through the cell. The effective path length of the multipass arrangement has been determined and reported in previous work,[1] however was remeasured in this work using a different method for the 13 pass configuration. The effective path length of the multipass arrangement, *l*, was determined from experiments in which the absorbance owing to IO, which is produced by secondary chemistry in the system following photolysis of $CH_2I_2/O_2/N_2$ mixtures as described in detail in Chapter 5, observed from a single pass of the probe beam through the reaction cell, which overlapped completely with the photolysis laser and thus has a path length which is fixed, definite, and equivalent to the 150 cm length of the reaction cell, was compared to the absorbance owing to IO observed simultaneously from the multipass arrangement, as described in Chapter 3.

Due to the high CH_2I_2 concentrations (1×10^{14} – 1×10^{15} cm^{-3}) employed in experiments to determine the path length, to enable high levels of absorbance to be observed and so that excellent *S/N* ratio was obtained without the need for signal averaging (these experiments were averaged over ~5 photolysis shots), large concentrations of IO were produced in the system, resulting in absorbance owing to OIO and I_2 also being observed on the timescale of the experiment, which are most

likely produced from the subsequent chemistry of IO in the system. The time profile of the ratio of the absorbance observed in the multipass arrangement to that simultaneously observed in the single pass arrangement for each species was obtained *via* the method of data analysis described in detail in Chapter 4, in which reference spectra[2] of all the absorbing species were fit to the total absorbance observed to determine the contribution from each species. The IO time profile showed formation an instant production following photolysis, followed by a slower production over 5 ms following photolysis, followed by an overall decay over a timescale of 150 ms. The OIO time profile, like IO, was observed to be formed quickly following photolysis and subsequently appeared to slowly decay over a timescale of 150 ms. The I_2 time profile did not show I_2 to be produced instantly following photolysis, rather it was depicted to grow in slowly over a timescale of 50 ms, with the rate of growth then appearing to slow down and the concentration beginning to level off or reach a steady-state. When investigating the transient absorbance spectra collected over time, an absorbance was clearly displayed in the 400-650 nm range, with distinct vibronic structure on the high wavelength side, growing in on the same timescale as the IO decay, as shown in the figure below. Despite similarities in the wavelength range over which I_2 and OIO exhibit UV absorption spectra, both species were able to be fit to the overall absorbance, however due to the lack of regular structure in the OIO spectrum, both reference and observed, the absorbance owing to OIO was not used to determine the path length.

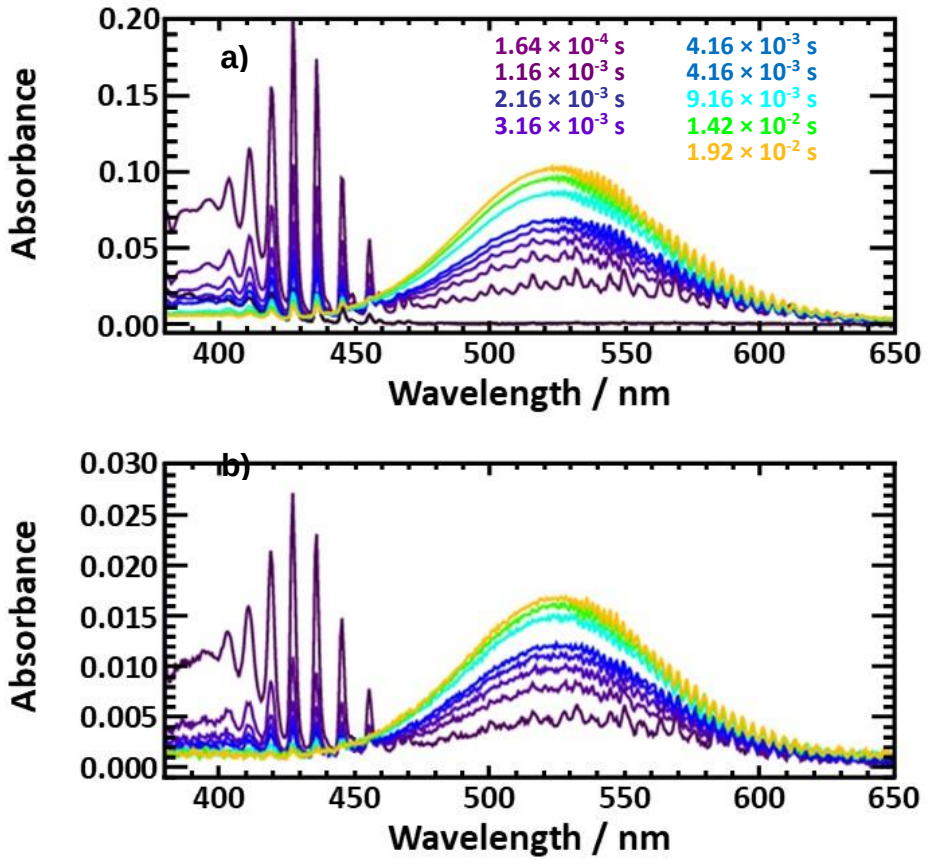

Figure showing the transient absorbance spectra with contributions from CH_2OO (380-450 nm), IO (400-450 nm), OIO and I_2 (400-650 nm) at various time points following photolysis in experiments to determine the path length observed from a) the multipass arrangement comprising 13 passes and b) the single pass arrangement.

Since the wavelength grids for the two cameras detecting light from the single pass and multipass arrangements respectively were different, the analysis required reference spectra of each of the absorbing species to be fit to the total observed absorbance, in order to perform an interpolation of the two wavelength grids. The ratio of the absorbance of IO in the first 5 ms following photolysis and of I_2 in the time range of 100-105 ms following photolysis, i.e. a short period of time over which the concentration of both species was not rapidly changing, measured using the single pass and multipass arrangements was determined. The average of 15 individual experiments along with the standard deviation between them were concluded to be the value and error for the path length of the configuration comprising 13 passes of the probe beam. An example of the absorbance observed owing to IO in one of these

experiments in both the single pass and multipass arrangements is shown in the figure below. The effective path length of l = (443 ± 21) cm was obtained from the 7 pass arrangement of the probe beam through the reaction cell in previous work,[1] and l = (1136 ± 143) cm was obtained from the 13 pass arrangement of the probe beam through the reaction cell using the method described here, when considering the total overlap between the photolysis and probe beams.

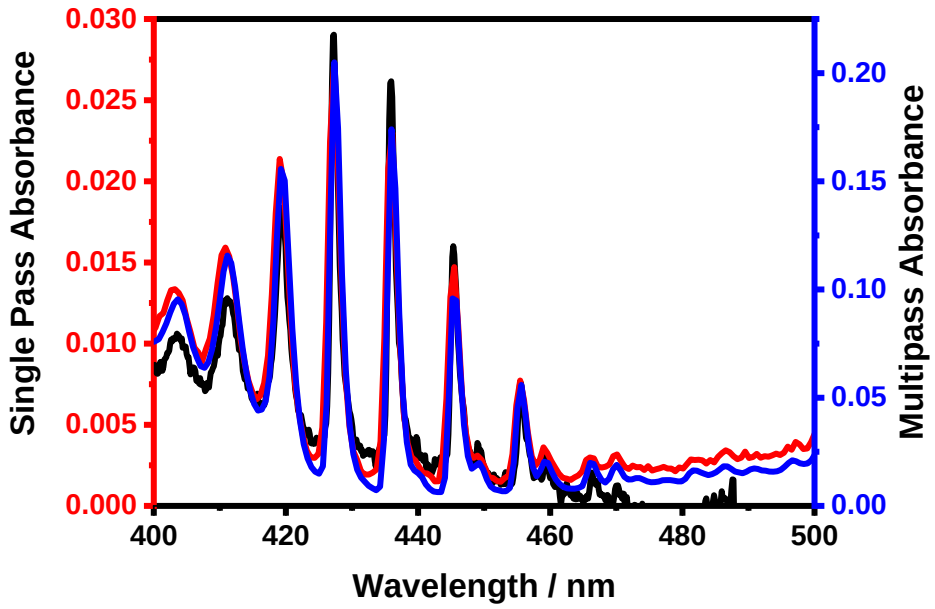

Figure showing the simultaneously observed IO absorbance in the single pass (red) and multipass (blue) arrangement along with the reference IO spectrum[2, 3] (black) which was fit to the observed absorbance.

Appendix 3: CH_2OO UV absorption cross-sections

Table summarising the CH_2OO UV absorption cross-sections described in Chapter 4.

Wavelength / nm	Absorption cross-section / 10^{-17} cm^2
280.5	0.25
281.1	0.25
281.6	0.25
282.2	0.27
282.8	0.25
283.3	0.28
283.9	0.30
284.5	0.28

Wavelength / nm	Absorption cross-section / 10^{-17} cm^2
285.0	0.29
285.6	0.29
286.2	0.30
286.7	0.31
287.3	0.33
287.9	0.32
288.4	0.36
289.0	0.35

Wavelength / nm	Absorption cross-section / 10^{-17} cm^2
289.6	0.36
290.1	0.38
290.7	0.38
291.3	0.40
291.8	0.38
292.4	0.39
293.0	0.40
293.5	0.41
294.1	0.43
294.7	0.47
295.2	0.47
295.8	0.48
296.4	0.48
296.9	0.50
297.5	0.52
298.1	0.53
298.6	0.55
299.2	0.54
299.8	0.56
300.3	0.58
300.9	0.58
301.5	0.60
302.0	0.62
302.6	0.63
303.2	0.64
303.7	0.66
304.3	0.67
304.9	0.70
305.4	0.72
306.0	0.73
306.6	0.75
307.1	0.77
307.7	0.78
308.3	0.79
308.8	0.80
309.4	0.82
310.0	0.82
310.5	0.85
311.1	0.88
311.7	0.87
312.3	0.89
312.8	0.90
313.4	0.93
314.0	0.94
314.5	0.95
315.1	0.96
315.7	0.98
316.2	0.99
316.8	1.01
317.4	1.02
317.9	1.04

Wavelength / nm	Absorption cross-section / 10^{-17} cm^2
318.5	1.04
319.1	1.06
319.6	1.07
320.2	1.10
320.8	1.10
321.3	1.11
321.9	1.13
322.5	1.14
323.0	1.17
323.6	1.17
324.2	1.18
324.7	1.19
325.3	1.19
325.9	1.22
326.4	1.23
327.0	1.22
327.6	1.25
328.1	1.25
328.7	1.26
329.3	1.27
329.8	1.28
330.4	1.28
331.0	1.30
331.5	1.30
332.1	1.31
332.7	1.32
333.2	1.32
333.8	1.34
334.4	1.34
334.9	1.35
335.5	1.34
336.1	1.36
336.6	1.35
337.2	1.35
337.8	1.36
338.3	1.36
338.9	1.36
339.5	1.36
340.0	1.37
340.6	1.37
341.2	1.37
341.7	1.38
342.3	1.37
342.9	1.38
343.5	1.37
344.0	1.37
344.6	1.37
345.2	1.36
346.9	1.35
347.4	1.36
348.0	1.36

Wavelength / nm	Absorption cross-section / 10^{-17} cm^2
348.6	1.36
349.1	1.34
349.7	1.34
350.3	1.34
350.8	1.33
351.4	1.32
353.1	1.27
353.7	1.29
354.2	1.29
354.8	1.28
355.4	1.28
355.9	1.27
357.6	1.26
358.2	1.23
358.8	1.21
359.3	1.19
359.9	1.19
360.5	1.16
361.0	1.17
361.6	1.16
362.2	1.17
362.7	1.17
363.3	1.18
363.9	1.17
364.4	1.16
365.0	1.14
365.6	1.11
366.1	1.08
366.7	1.03
368.4	0.97
369.0	0.97
369.5	0.99
370.1	1.00
370.7	1.02
371.2	1.02
371.8	1.01
372.4	0.99
372.9	0.96
373.5	0.92
374.1	0.88
374.7	0.85
375.2	0.81
375.8	0.80
376.4	0.78
376.9	0.78
377.5	0.78
379.2	0.84
379.8	0.84
380.3	0.83
380.9	0.81
381.5	0.77

Wavelength / nm	Absorption cross-section / 10^{-17} cm^2
382.0	0.74
382.6	0.69
383.2	0.64
383.7	0.61
384.3	0.57
384.9	0.57
385.4	0.57
386.0	0.58
386.6	0.59
387.1	0.63
387.7	0.65
388.3	0.66
390.0	0.61
390.5	0.56
391.1	0.53
391.7	0.49
392.2	0.45
392.8	0.42
394.5	0.40
395.1	0.39
395.6	0.41
396.2	0.43
396.8	0.44
397.3	0.47
397.9	0.46
398.5	0.46
399.0	0.44
400.7	0.37
401.3	0.33
401.9	0.31
402.4	0.28
403.0	0.26
403.6	0.25
405.3	0.26
405.9	0.27
406.4	0.28
407.0	0.30
407.6	0.31
408.1	0.30
408.7	0.31
409.3	0.31
409.8	0.27
410.4	0.25
411.0	0.25
411.5	0.21
412.1	0.19
412.7	0.18
413.2	0.18
413.8	0.17
414.4	0.16
416.1	0.17

Wavelength / nm	Absorption cross-section / 10^{-17} cm^2
416.6	0.16
417.2	0.17
417.8	0.18
418.3	0.18
418.9	0.17
419.5	0.17
420.0	0.16
420.6	0.16
421.2	0.16
421.7	0.15
422.3	0.15
422.9	0.14
423.4	0.14
424.0	0.12
424.6	0.11
425.1	0.12
426.8	0.07
427.4	0.06
428.0	0.08
428.5	0.09
429.1	0.09
429.7	0.10
430.2	0.11
430.8	0.12
431.4	0.12
431.9	0.12
432.5	0.11
433.1	0.10
433.6	0.10
434.2	0.09
434.8	0.08
435.4	0.06
435.9	0.05
437.6	0.06
438.2	0.07
438.8	0.08
439.3	0.08
439.9	0.06
440.5	0.07
441.0	0.06
441.6	0.06
442.2	0.06
442.7	0.07
443.3	0.07
443.9	0.08
444.4	0.06
445.0	0.05
445.6	0.05
446.1	0.05
446.7	0.07
447.3	0.06
447.8	0.05
448.4	0.05
449.0	0.04
449.5	0.05

Appendix 4: UV experiments investigating CH_2OO + CH_2OO and CH_2OO + I reactions

Table summarising the conditions and numerical integration results of all experiments carried out using broadband time-resolved UV absorption spectroscopy to determine kinetics for the CH_2OO + CH_2OO and CH_2OO + I reactions, as described in Chapter 5. The table shows the summary for all experiments at a single pressure, with experiments conducted at a total of nine pressures in the range 6-300 Torr. All experiments were carried out at a temperature of 298 K. In the table, $k_{5.3}$ refers to the rate coefficient for the CH_2OO self-reaction, $k_{5.4}$ refers to the rate coefficient for the CH_2OO + I reaction, and $k_{5.5}$ refers to the rate coefficient for the first-order CH_2OO loss.

Pressure / Torr	$[CH_2I_2]$ / cm^{-3}	$[O_2]$ / cm^{-3}	$[CH_2OO]_{t=0}$ / cm^{-3}	$k_{5.3}$ / $cm^3\ s^{-1}$	$k_{5.4}$ / $cm^3\ s^{-1}$	$k_{5.5}$ / s^{-1}
6	5.46E+12	1.51E+16	1.67E+11	7.58E-11	6.03E-12	37.935
6	1.73E+13	1.71E+16	4.29E+11	7.04E-11	6.21E-15	50.254
6	4.86E+12	1.49E+16	1.83E+11	7.32E-11	6.30E-13	53.111
6	8.86E+12	1.35E+16	1.30E+12	8.56E-11	8.18E-13	36.591
6	3.54E+12	1.49E+16	4.28E+11	7.04E-11	6.21E-15	50.254
6	5.99E+12	1.33E+16	8.94E+11	8.56E-11	8.18E-13	36.591
6	1.59E+13	1.22E+16	1.94E+12	7.58E-11	6.03E-12	37.935
6	1.26E+13	1.39E+16	1.76E+12	7.04E-11	6.21E-15	50.254
6	1.75E+12	1.56E+16	2.14E+11	7.42E-11	5.07E-13	53.312
6	8.36E+12	1.40E+16	1.11E+12	7.58E-11	6.03E-12	37.935
6	1.38E+13	1.36E+16	1.84E+12	8.56E-11	8.18E-13	36.591
6	4.19E+12	1.11E+16	6.09E+11	7.32E-11	6.30E-13	53.111
6	1.46E+13	1.11E+16	1.70E+12	7.58E-11	6.03E-12	37.935
6	8.68E+12	1.13E+16	1.14E+12	7.42E-11	5.07E-13	53.312
6	1.77E+13	1.11E+16	1.45E+12	8.42E-11	7.08E-15	43.572
6	5.94E+12	1.28E+16	6.49E+11	8.42E-11	7.08E-15	43.572
6	1.14E+13	1.41E+16	1.04E+12	7.32E-11	6.30E-13	53.111
6	3.37E+12	1.45E+16	3.97E+11	8.42E-11	7.08E-15	43.572
6	1.80E+13	1.39E+16	7.19E+11	8.88E-11	1.29E-14	46.184
6	5.40E+12	1.66E+16	2.47E+11	8.42E-11	7.08E-15	43.572
6	3.00E+12	1.83E+16	1.38E+11	8.88E-11	1.29E-14	46.184
6	1.42E+13	1.64E+16	5.90E+11	8.88E-11	1.29E-14	46.184
6	9.76E+12	1.74E+16	3.24E+11	7.32E-11	6.30E-13	53.111
6	1.52E+13	1.62E+16	3.97E+11	7.42E-11	5.07E-13	53.312
6	6.87E+12	1.72E+16	2.58E+11	8.88E-11	1.29E-14	46.184
6	2.06E+13	1.60E+16	6.11E+11	7.42E-11	5.07E-13	53.312
15	3.89E+12	1.58E+17	2.29E+11	7.22E-11	3.17E-11	6.229
15	5.44E+12	8.92E+16	3.13E+11	8.81E-11	1.80E-11	4.971
15	4.11E+12	8.99E+16	2.50E+11	7.22E-11	3.17E-11	6.229
15	1.52E+12	9.07E+16	1.18E+11	7.21E-11	1.02E-11	16.453
15	2.13E+12	8.58E+16	7.53E+10	8.81E-11	1.80E-11	4.971
15	1.27E+12	8.55E+16	1.21E+11	7.24E-11	1.23E-11	17.415
15	4.44E+12	4.55E+16	3.01E+11	7.09E-11	3.54E-11	7.974
15	4.63E+12	4.75E+16	2.89E+11	7.21E-11	1.02E-11	16.453
15	3.65E+12	4.63E+16	1.94E+11	7.24E-11	1.23E-11	17.415
15	2.10E+12	4.83E+16	1.17E+11	7.09E-11	3.54E-11	7.974
15	5.16E+12	4.39E+16	2.42E+11	7.24E-11	1.23E-11	17.415
15	3.41E+12	4.75E+16	1.75E+11	8.81E-11	1.80E-11	4.971
15	2.63E+12	4.63E+16	3.35E+10	7.22E-11	3.17E-11	6.229
15	5.49E+12	4.67E+16	1.53E+11	7.22E-11	3.17E-11	6.229
15	7.38E+12	4.74E+16	2.28E+11	7.09E-11	3.54E-11	7.974
15	7.12E+12	4.32E+16	2.47E+11	8.81E-11	1.80E-11	4.971
15	8.86E+12	4.40E+16	1.12E+11	7.21E-11	1.02E-11	16.453
30	7.08E+12	1.40E+17	2.57E+11	7.56E-11	7.11E-13	19.285
30	7.54E+12	1.38E+17	2.15E+11	7.56E-11	7.11E-13	19.285
30	4.62E+12	1.38E+17	1.73E+11	7.18E-11	3.69E-11	0.004
30	1.97E+12	1.33E+17	9.88E+10	7.56E-11	7.11E-13	19.285
30	1.01E+12	1.35E+17	4.27E+10	7.56E-11	7.11E-13	19.285
30	7.19E+12	8.49E+16	4.38E+11	9.33E-11	2.34E-11	0.168

Pressure / Torr	$[CH_2I_2]$ / cm^{-3}	$[O_2]$ / cm^{-3}	$[CH_2OO]_{t=0}$ / cm^{-3}	$k_{5.3}$ / $cm^3\ s^{-1}$	$k_{5.4}$ / $cm^3\ s^{-1}$	$k_{5.5}$ / s^{-1}
30	9.02E+12	8.68E+16	3.35E+11	7.18E-11	3.69E-11	0.004
30	4.60E+12	8.58E+16	2.37E+11	7.96E-11	3.29E-11	0.860
30	8.26E+12	8.31E+16	5.70E+11	7.96E-11	3.29E-11	0.860
30	9.29E+12	8.62E+16	4.69E+11	7.18E-11	3.69E-11	0.004
30	2.51E+13	8.59E+16	8.90E+11	9.33E-11	2.34E-11	0.168
30	2.36E+13	8.89E+16	8.04E+11	7.18E-11	3.69E-11	0.004
30	1.67E+13	8.81E+16	6.98E+11	7.96E-11	3.29E-11	0.860
30	1.55E+13	8.56E+16	5.30E+11	9.33E-11	2.34E-11	0.168
30	1.02E+13	8.47E+16	4.42E+11	7.96E-11	3.29E-11	0.860
30	8.16E+12	8.36E+16	3.68E+11	9.33E-11	2.34E-11	0.168
70	7.25E+12	1.50E+17	3.08E+11	8.10E-11	5.01E-11	0.146
70	8.13E+12	1.51E+17	3.60E+11	8.86E-11	4.19E-11	8.512
70	8.86E+12	1.49E+17	3.82E+11	8.73E-11	4.42E-11	0.009
70	1.91E+13	1.49E+17	5.24E+11	7.93E-11	5.04E-11	1.000
70	4.83E+12	1.51E+17	2.16E+11	8.14E-11	3.42E-11	4.253
70	6.15E+12	1.50E+17	3.35E+11	7.88E-11	3.50E-11	0.001
70	8.53E+12	1.51E+17	2.85E+11	8.10E-11	5.01E-11	0.146
70	9.97E+12	1.50E+17	6.27E+11	8.14E-11	3.42E-11	4.253
70	9.45E+12	1.48E+17	5.61E+11	7.88E-11	3.50E-11	0.001
70	1.28E+13	1.49E+17	5.57E+11	9.50E-11	4.37E-11	0.030
70	1.54E+13	1.48E+17	5.77E+11	8.86E-11	4.19E-11	8.512
70	1.57E+13	1.49E+17	6.77E+11	9.50E-11	4.37E-11	0.030
70	1.29E+13	1.48E+17	6.25E+11	8.14E-11	3.42E-11	4.253
70	5.81E+12	2.11E+17	6.31E+11	9.50E-11	4.37E-11	0.030
70	3.69E+12	2.18E+17	5.64E+11	8.10E-11	5.01E-11	0.146
70	5.73E+12	2.18E+17	5.80E+11	8.73E-11	4.42E-11	0.009
70	6.98E+12	2.19E+17	6.05E+11	8.10E-11	5.01E-11	0.146
70	4.85E+12	2.22E+17	6.81E+11	7.93E-11	5.04E-11	1.000
70	9.72E+12	2.19E+17	7.27E+11	9.50E-11	4.37E-11	0.030
70	1.16E+13	2.22E+17	6.79E+11	7.93E-11	5.04E-11	1.000
70	4.36E+13	2.04E+17	2.36E+12	7.88E-11	3.50E-11	0.001
70	6.44E+12	2.07E+17	6.19E+11	8.86E-11	4.19E-11	8.512
70	1.13E+13	5.51E+16	9.42E+11	8.73E-11	4.42E-11	0.009
70	5.64E+12	5.53E+16	5.59E+11	8.14E-11	3.42E-11	4.253
70	8.95E+12	2.08E+17	1.49E+12	7.88E-11	3.50E-11	0.001
120	6.00E+12	1.79E+17	6.04E+11	8.68E-11	3.53E-11	4.368
120	1.66E+13	1.78E+17	6.19E+11	7.30E-11	4.92E-11	9.541
120	1.61E+13	1.79E+17	6.66E+11	7.30E-11	4.92E-11	9.541
120	1.77E+13	1.79E+17	6.79E+11	7.73E-11	5.06E-11	0.142
120	1.59E+13	1.76E+17	5.38E+11	8.37E-11	4.41E-11	9.031
120	1.43E+13	1.77E+17	5.88E+11	7.73E-11	5.06E-11	0.142
120	1.43E+13	1.78E+17	5.45E+11	9.18E-11	3.45E-11	2.922
120	1.65E+13	1.77E+17	6.24E+11	8.37E-11	4.41E-11	9.031
120	1.63E+13	1.76E+17	6.25E+11	9.18E-11	3.45E-11	2.922
120	1.87E+13	1.78E+17	6.92E+11	8.37E-11	4.41E-11	9.031
120	3.42E+12	1.76E+17	6.92E+11	8.68E-11	3.53E-11	4.368
120	3.33E+13	1.78E+17	7.86E+11	9.18E-11	3.45E-11	2.922
120	2.25E+12	2.15E+17	3.68E+11	7.30E-11	4.92E-11	9.541
120	3.65E+12	2.19E+17	2.79E+11	8.68E-11	3.53E-11	4.368

Pressure / Torr	$[CH_2I_2]$ / cm^{-3}	$[O_2]$ / cm^{-3}	$[CH_2OO]_{t=0}$ / cm^{-3}	$k_{5.3}$ / $cm^3\ s^{-1}$	$k_{5.4}$ / $cm^3\ s^{-1}$	$k_{5.5}$ / s^{-1}
120	1.50E+12	2.19E+17	2.35E+11	9.18E-11	3.45E-11	2.922
120	1.85E+12	2.21E+17	2.38E+11	7.73E-11	5.06E-11	0.142
120	1.28E+12	2.21E+17	1.72E+11	7.30E-11	4.92E-11	9.541
120	1.70E+12	2.27E+17	1.85E+11	8.37E-11	4.41E-11	9.031
160	2.72E+13	1.76E+17	8.80E+11	8.59E-11	5.96E-11	1.872
160	3.05E+13	1.77E+17	9.62E+11	7.52E-11	4.44E-11	0.151
160	3.17E+13	1.77E+17	9.12E+11	8.31E-11	4.62E-11	4.915
160	2.31E+13	1.75E+17	6.00E+11	7.52E-11	4.44E-11	0.151
160	2.02E+13	1.76E+17	5.96E+11	8.31E-11	4.62E-11	4.915
160	1.30E+13	1.76E+17	6.59E+11	9.23E-11	4.57E-11	2.800
160	1.19E+13	1.76E+17	4.70E+11	7.52E-11	4.44E-11	0.151
160	1.25E+13	1.76E+17	4.42E+11	8.59E-11	5.96E-11	1.872
160	6.56E+12	1.77E+17	6.48E+11	8.48E-11	4.15E-11	0.014
160	1.49E+13	1.76E+17	5.06E+11	7.68E-11	7.69E-11	0.316
160	4.00E+12	1.77E+17	4.87E+11	8.31E-11	4.62E-11	4.915
160	9.48E+12	1.77E+17	6.41E+11	7.68E-11	7.69E-11	0.316
160	1.23E+13	1.76E+17	3.84E+11	7.68E-11	7.69E-11	0.316
160	1.63E+13	1.76E+17	5.89E+11	8.59E-11	5.96E-11	1.872
160	1.53E+13	1.76E+17	4.52E+11	8.48E-11	4.15E-11	0.014
160	1.57E+13	1.76E+17	4.79E+11	9.32E-11	4.49E-11	0.104
160	1.71E+13	1.77E+17	5.21E+11	8.48E-11	4.15E-11	0.014
160	2.85E+13	1.75E+17	6.38E+11	9.32E-11	4.49E-11	0.104
160	3.09E+12	2.62E+17	2.62E+11	8.59E-11	5.96E-11	1.872
160	1.38E+13	2.62E+17	3.92E+11	9.32E-11	4.49E-11	0.104
160	9.43E+12	2.65E+17	2.87E+11	8.31E-11	4.62E-11	4.915
160	8.74E+12	2.64E+17	3.43E+11	7.52E-11	4.44E-11	0.151
160	2.95E+12	2.66E+17	1.73E+11	9.23E-11	4.57E-11	2.800
160	2.08E+12	2.66E+17	1.50E+11	8.48E-11	4.15E-11	0.014
160	4.47E+12	4.02E+17	9.57E+11	7.68E-11	7.69E-11	0.316
160	4.17E+12	1.90E+17	4.54E+11	9.23E-11	4.57E-11	2.800
160	3.04E+12	3.53E+17	5.36E+11	9.23E-11	4.57E-11	2.800
200	8.63E+12	1.77E+17	3.17E+11	7.52E-11	3.90E-11	4.614
200	9.59E+12	1.77E+17	4.93E+11	7.25E-11	6.67E-11	1.054
200	1.12E+13	1.76E+17	3.65E+11	6.39E-11	8.31E-11	0.089
200	1.07E+13	1.76E+17	3.35E+11	8.61E-11	5.43E-11	0.332
200	1.17E+13	1.76E+17	3.38E+11	8.16E-11	7.88E-11	0.937
200	1.24E+13	1.77E+17	4.46E+11	6.39E-11	8.31E-11	0.089
200	1.59E+13	1.76E+17	3.51E+11	7.25E-11	6.67E-11	1.054
200	1.22E+13	1.75E+17	3.87E+11	7.25E-11	6.67E-11	1.054
200	9.55E+12	1.75E+17	4.13E+11	8.05E-11	5.25E-11	0.001
200	4.92E+12	1.77E+17	3.85E+11	7.52E-11	3.90E-11	4.614
200	7.38E+12	1.77E+17	4.24E+11	8.16E-11	7.88E-11	0.937
200	1.08E+13	1.76E+17	3.02E+11	8.61E-11	5.43E-11	0.332
200	1.09E+13	1.76E+17	3.24E+11	8.05E-11	5.25E-11	0.001
200	1.16E+13	1.76E+17	3.96E+11	8.16E-11	7.88E-11	0.937
200	1.42E+13	1.75E+17	4.06E+11	8.61E-11	5.43E-11	0.332
200	1.26E+13	1.76E+17	3.78E+11	8.05E-11	5.25E-11	0.001
200	2.73E+13	2.07E+17	6.79E+11	6.39E-11	8.31E-11	0.089
200	2.40E+12	2.07E+17	4.09E+11	7.52E-11	3.90E-11	4.614

Pressure / Torr	$[CH_2I_2]$ / cm^{-3}	$[O_2]$ / cm^{-3}	$[CH_2OO]_{t=0}$ / cm^{-3}	$k_{5.3}$ / $cm^3\ s^{-1}$	$k_{5.4}$ / $cm^3\ s^{-1}$	$k_{5.5}$ / s^{-1}
200	4.44E+13	2.07E+17	1.60E+12	8.16E-11	7.88E-11	0.937
200	7.58E+12	2.06E+17	1.01E+12	8.05E-11	5.25E-11	0.001
200	4.40E+12	2.07E+17	8.03E+11	7.52E-11	3.90E-11	4.614
250	3.85E+12	1.77E+17	2.69E+11	6.81E-11	7.08E-11	0.002
250	9.53E+12	1.77E+17	4.15E+11	6.81E-11	7.08E-11	0.002
250	1.43E+13	1.77E+17	4.76E+11	6.75E-11	6.28E-11	0.512
250	2.04E+13	1.77E+17	4.95E+11	8.84E-11	3.32E-11	6.041
250	1.70E+13	1.77E+17	3.74E+11	8.67E-11	5.25E-11	4.867
250	1.03E+13	1.76E+17	3.07E+11	8.42E-11	4.98E-11	5.743
250	1.07E+13	1.77E+17	3.02E+11	8.67E-11	5.25E-11	4.867
250	9.69E+12	1.77E+17	3.07E+11	6.81E-11	7.08E-11	0.002
250	3.66E+12	1.77E+17	2.01E+11	6.75E-11	6.28E-11	0.512
250	6.86E+12	1.77E+17	1.92E+11	6.81E-11	7.08E-11	0.002
250	8.70E+12	1.77E+17	2.51E+11	8.42E-11	4.98E-11	5.743
250	1.24E+13	1.77E+17	2.61E+11	8.84E-11	3.32E-11	6.041
250	8.47E+12	1.76E+17	2.98E+11	8.67E-11	5.25E-11	4.867
250	1.00E+13	1.76E+17	3.22E+11	6.75E-11	6.28E-11	0.512
250	1.06E+13	1.76E+17	3.34E+11	8.42E-11	4.98E-11	5.743
250	1.64E+13	3.19E+17	3.27E+11	8.84E-11	3.32E-11	6.041
250	9.58E+12	3.22E+17	1.73E+11	8.42E-11	4.98E-11	5.743
250	1.79E+13	3.21E+17	2.88E+11	6.75E-11	6.28E-11	0.512
250	3.10E+13	3.20E+17	2.52E+11	8.84E-11	3.32E-11	6.041
250	1.85E+13	3.21E+17	1.58E+11	8.67E-11	5.25E-11	4.867
300	3.28E+12	1.77E+17	2.65E+11	8.44E-11	4.52E-11	2.363
300	6.20E+12	1.76E+17	1.85E+11	7.01E-11	6.08E-11	7.329
300	7.21E+12	1.77E+17	1.59E+11	7.01E-11	6.08E-11	7.329
300	7.67E+12	1.77E+17	2.59E+11	7.53E-11	5.15E-11	4.393
300	1.13E+13	1.77E+17	1.92E+11	8.42E-11	6.07E-11	0.044
300	8.35E+12	1.76E+17	2.80E+11	7.09E-11	4.91E-11	8.302
300	8.69E+12	1.76E+17	3.70E+11	7.09E-11	4.91E-11	8.302
300	1.30E+13	1.76E+17	3.50E+11	7.53E-11	5.15E-11	4.393
300	7.96E+12	1.76E+17	2.62E+11	7.01E-11	6.08E-11	7.329
300	4.46E+12	1.77E+17	2.57E+11	8.42E-11	6.07E-11	0.044
300	2.88E+12	3.32E+17	2.85E+11	7.08E-11	6.32E-11	0.112
300	8.10E+12	3.31E+17	2.44E+11	7.09E-11	4.91E-11	8.302
300	4.68E+12	3.32E+17	1.79E+11	7.53E-11	5.15E-11	4.393
300	9.78E+11	3.30E+17	1.61E+11	7.09E-11	4.91E-11	8.302
300	7.46E+12	1.35E+17	2.44E+11	8.44E-11	4.52E-11	2.363
300	9.06E+12	1.35E+17	2.46E+11	7.08E-11	6.32E-11	0.112
300	1.43E+13	1.35E+17	2.77E+11	8.42E-11	6.07E-11	0.044
300	1.08E+13	1.34E+17	1.98E+11	7.08E-11	6.32E-11	0.112
300	7.79E+12	1.35E+17	2.10E+11	8.44E-11	4.52E-11	2.363
300	1.24E+13	1.35E+17	2.36E+11	7.53E-11	5.15E-11	4.393
300	1.60E+13	1.35E+17	2.55E+11	7.01E-11	6.08E-11	7.329

Appendix 5: Normalised CH_2OO IR absorption spectrum

Table summarising the normalised CH_2OO IR absorption spectrum described in Chapter 6.

Current / A	Wavenumber / cm^{-1}	Normalised signal / arbitrary units
0.3120	1285.5917	0.1644
0.3119	1285.5933	0.1483
0.3118	1285.5949	0.2114
0.3117	1285.5965	0.1895
0.3116	1285.5981	0.1555
0.3115	1285.5996	0.1495
0.3114	1285.6012	0.1297
0.3113	1285.6028	0.1549
0.3112	1285.6044	0.1729
0.3111	1285.6060	0.1187
0.3110	1285.6075	0.1728
0.3109	1285.6091	0.4635
0.3108	1285.6107	0.5307
0.3107	1285.6122	0.4291
0.3106	1285.6138	0.3362
0.3105	1285.6153	0.2778
0.3104	1285.6169	0.2992
0.3103	1285.6185	0.3443
0.3102	1285.6200	0.2077
0.3101	1285.6216	0.2652
0.3100	1285.6231	0.1478
0.3099	1285.6246	0.1212
0.3098	1285.6262	0.1454
0.3097	1285.6277	0.1455
0.3096	1285.6293	0.0816
0.3095	1285.6308	0.1991
0.3094	1285.6323	0.1168
0.3093	1285.6339	0.1277
0.3092	1285.6354	0.0676
0.3091	1285.6369	0.0520
0.3090	1285.6384	0.0221
0.3089	1285.6400	0.1014
0.3088	1285.6415	-0.0109
0.3087	1285.6430	-0.0292
0.3086	1285.6445	-0.0291
0.3085	1285.6460	-0.0386
0.3084	1285.6475	-0.0787
0.3083	1285.6490	0.0374
0.3082	1285.6505	-0.0225
0.3081	1285.6520	0.0427
0.3080	1285.6535	0.0064
0.3079	1285.6550	0.0192
0.3078	1285.6565	0.0362
0.3077	1285.6580	0.0191
0.3076	1285.6595	0.0167
0.3075	1285.6610	0.0737
0.3074	1285.6625	0.0608
0.3073	1285.6640	0.0929
0.3072	1285.6654	-0.0394
0.3071	1285.6669	-0.0159
0.3070	1285.6684	0.0090
0.3069	1285.6699	0.0636
0.3068	1285.6713	0.0926
0.3067	1285.6728	0.0698
0.3066	1285.6743	0.0819
0.3065	1285.6757	0.0912
0.3064	1285.6772	0.1962
0.3063	1285.6787	0.1358
0.3062	1285.6801	0.2346
0.3061	1285.6816	0.2715
0.3060	1285.6830	0.2658
0.3059	1285.6845	0.2392
0.3058	1285.6859	0.1812
0.3057	1285.6874	0.1176
0.3056	1285.6888	0.2521
0.3055	1285.6902	0.1223
0.3054	1285.6917	0.1314
0.3053	1285.6931	0.2657
0.3052	1285.6945	0.1545
0.3051	1285.6960	0.3557
0.3050	1285.6974	0.2454
0.3049	1285.6988	0.3806
0.3048	1285.7002	0.2396
0.3047	1285.7017	0.1361
0.3046	1285.7031	0.1782
0.3045	1285.7045	0.1811
0.3044	1285.7059	0.2033
0.3043	1285.7073	0.1740
0.3042	1285.7087	0.1966
0.3041	1285.7101	0.1744
0.3040	1285.7115	0.2197
0.3039	1285.7129	0.2806
0.3038	1285.7143	0.3478
0.3037	1285.7157	0.4232
0.3036	1285.7171	0.4289
0.3035	1285.7185	0.3496
0.3034	1285.7199	0.4900
0.3033	1285.7213	0.5482

Current / A	Wavenumber / cm^{-1}	Normalised signal / arbitrary units
0.3032	1285.7227	0.6817
0.3031	1285.7241	0.6982
0.3030	1285.7254	0.7409
0.3029	1285.7268	0.8212
0.3028	1285.7282	0.9064
0.3027	1285.7296	1.0000
0.3026	1285.7309	0.9154
0.3025	1285.7323	0.9220
0.3024	1285.7337	0.7013
0.3023	1285.7350	0.6493
0.3022	1285.7364	0.5863
0.3021	1285.7377	0.5268
0.3020	1285.7391	0.4149
0.3019	1285.7404	0.4146
0.3018	1285.7418	0.3114
0.3017	1285.7431	0.3140
0.3016	1285.7445	0.2890
0.3015	1285.7458	0.2605
0.3014	1285.7472	0.3684
0.3013	1285.7485	0.4310
0.3012	1285.7498	0.3071
0.3011	1285.7512	0.3577
0.3010	1285.7525	0.2779
0.3009	1285.7538	0.3978
0.3008	1285.7552	0.3726
0.3007	1285.7565	0.3446
0.3006	1285.7578	0.3565
0.3005	1285.7591	0.3471
0.3004	1285.7604	0.4279
0.3003	1285.7618	0.4012
0.3002	1285.7631	0.4692
0.3001	1285.7644	0.4649
0.3000	1285.7657	0.5443
0.2999	1285.7670	0.6083
0.2998	1285.7683	0.5490
0.2997	1285.7696	0.4858
0.2996	1285.7709	0.4615
0.2995	1285.7722	0.4428
0.2994	1285.7735	0.4329
0.2993	1285.7748	0.4018
0.2992	1285.7761	0.2429
0.2991	1285.7773	0.4676
0.2990	1285.7786	0.2624
0.2989	1285.7799	0.3382
0.2988	1285.7812	0.1140
0.2987	1285.7825	0.2056
0.2986	1285.7837	0.2729
0.2985	1285.7850	0.2097
0.2984	1285.7863	0.2421
0.2983	1285.7875	0.1618
0.2982	1285.7888	0.1806

Current / A	Wavenumber / cm^{-1}	Normalised signal / arbitrary units
0.2981	1285.7901	0.2386
0.2980	1285.7913	0.1882
0.2979	1285.7926	0.2722
0.2978	1285.7938	0.1815
0.2977	1285.7951	0.1967
0.2976	1285.7963	0.2495
0.2975	1285.7976	0.1804
0.2974	1285.7988	0.1595
0.2973	1285.8001	0.1758
0.2972	1285.8013	0.2768
0.2971	1285.8025	0.2491
0.2970	1285.8038	0.2169
0.2969	1285.8050	0.2060
0.2968	1285.8062	0.2254
0.2967	1285.8075	0.2844
0.2966	1285.8087	0.3067
0.2965	1285.8099	0.2937
0.2964	1285.8111	0.3105
0.2963	1285.8124	0.3512
0.2962	1285.8136	0.3343
0.2961	1285.8148	0.2687
0.2960	1285.8160	0.2034
0.2959	1285.8172	0.1932
0.2958	1285.8184	0.2584
0.2957	1285.8196	0.2143
0.2956	1285.8208	0.1384
0.2955	1285.8220	0.1505
0.2954	1285.8232	0.1990
0.2953	1285.8244	0.1511
0.2952	1285.8256	0.1153
0.2951	1285.8268	0.1372
0.2950	1285.8280	0.1193
0.2949	1285.8292	0.1351
0.2948	1285.8303	0.1634
0.2947	1285.8315	0.2031
0.2946	1285.8327	0.1728
0.2945	1285.8339	0.1447
0.2944	1285.8350	0.3117
0.2943	1285.8362	0.2185
0.2942	1285.8374	0.2572
0.2941	1285.8385	0.3867
0.2940	1285.8397	0.2247
0.2939	1285.8409	0.1344
0.2938	1285.8420	0.1571
0.2937	1285.8432	0.2570
0.2936	1285.8443	0.3186
0.2935	1285.8455	0.2746
0.2934	1285.8466	0.2968
0.2933	1285.8478	0.3896
0.2932	1285.8489	0.2197
0.2931	1285.8501	0.3414

Current / A	Wavenumber / cm^{-1}	Normalised signal / arbitrary units
0.2930	1285.8512	0.2804
0.2929	1285.8523	0.2171
0.2928	1285.8535	0.2551
0.2927	1285.8546	0.2986
0.2926	1285.8557	0.0928
0.2925	1285.8569	0.1800
0.2924	1285.8580	0.0262
0.2923	1285.8591	0.0032
0.2922	1285.8602	0.0527
0.2921	1285.8613	0.0001
0.2920	1285.8625	0.1224
0.2919	1285.8636	0.1096
0.2918	1285.8647	0.1744
0.2917	1285.8658	0.0840
0.2916	1285.8669	0.1393
0.2915	1285.8680	0.0846
0.2914	1285.8691	0.1509
0.2913	1285.8702	0.1750
0.2912	1285.8713	0.1233
0.2911	1285.8724	0.1494
0.2910	1285.8735	0.1566
0.2909	1285.8746	0.2350
0.2908	1285.8756	0.2571
0.2907	1285.8767	0.1734
0.2906	1285.8778	0.1721
0.2905	1285.8789	0.1824
0.2904	1285.8800	0.1752
0.2903	1285.8810	0.1616
0.2902	1285.8821	0.1097
0.2901	1285.8832	0.1285
0.2900	1285.8842	0.1140
0.2899	1285.8853	0.1063
0.2898	1285.8864	0.1010
0.2897	1285.8874	0.1501
0.2896	1285.8885	0.0402
0.2895	1285.8895	0.1094
0.2894	1285.8906	0.1292
0.2893	1285.8916	0.1386
0.2892	1285.8927	0.1252
0.2891	1285.8937	0.1409
0.2890	1285.8948	0.1412
0.2889	1285.8958	0.1522
0.2888	1285.8969	0.1512
0.2887	1285.8979	0.1235
0.2886	1285.8989	0.0771
0.2885	1285.9000	0.1189
0.2884	1285.9010	0.0272
0.2883	1285.9020	0.3272
0.2882	1285.9030	0.1411
0.2881	1285.9041	0.0086
0.2880	1285.9051	0.1012

Current / A	Wavenumber / cm^{-1}	Normalised signal / arbitrary units
0.2879	1285.9061	0.1095
0.2878	1285.9071	0.0761
0.2877	1285.9081	0.0543
0.2876	1285.9091	0.1109
0.2875	1285.9101	0.0537
0.2874	1285.9111	0.1098
0.2873	1285.9121	0.1004
0.2872	1285.9131	0.0111
0.2871	1285.9141	0.0385
0.2870	1285.9151	0.0304
0.2869	1285.9161	0.1103
0.2868	1285.9171	0.0308
0.2867	1285.9181	0.0128
0.2866	1285.9191	0.0337
0.2865	1285.9201	0.0704
0.2864	1285.9210	0.0297
0.2863	1285.9220	0.0265
0.2862	1285.9230	0.0181
0.2861	1285.9240	0.0134
0.2860	1285.9249	0.0301
0.2859	1285.9259	0.0276
0.2858	1285.9269	0.0282
0.2857	1285.9278	0.0037
0.2856	1285.9288	0.0001
0.2855	1285.9298	0.0190
0.2854	1285.9307	0.0615
0.2853	1285.9317	0.0243
0.2852	1285.9326	0.0612
0.2851	1285.9336	0.0182
0.2850	1285.9345	0.0122
0.2849	1285.9355	0.0279
0.2848	1285.9364	0.0226
0.2847	1285.9373	0.0150
0.2846	1285.9383	0.0189
0.2845	1285.9392	0.0140
0.2844	1285.9401	0.0121
0.2843	1285.9411	0.0182
0.2842	1285.9420	0.0119
0.2841	1285.9429	0.0169
0.2840	1285.9438	0.0092
0.2839	1285.9448	0.0212
0.2838	1285.9457	0.0074
0.2837	1285.9466	0.0241
0.2836	1285.9475	0.0190
0.2835	1285.9484	0.0137
0.2834	1285.9493	0.0161
0.2833	1285.9502	0.0070
0.2832	1285.9511	0.0186
0.2831	1285.9520	0.0065
0.2830	1285.9529	0.0029
0.2829	1285.9538	0.0035

Current / A	Wavenumber / cm^{-1}	Normalised signal / arbitrary units
0.2828	1285.9547	0.0033
0.2827	1285.9556	0.0192
0.2826	1285.9565	0.0372
0.2825	1285.9574	0.0464
0.2824	1285.9583	0.0015
0.2823	1285.9592	0.0452
0.2822	1285.9600	0.0135
0.2821	1285.9609	0.0216
0.2820	1285.9618	0.0026
0.2819	1285.9627	0.0283
0.2818	1285.9635	0.0141
0.2817	1285.9644	0.0220
0.2816	1285.9653	0.0152
0.2815	1285.9661	0.0198
0.2814	1285.9670	0.0145
0.2813	1285.9678	0.0244
0.2812	1285.9687	0.0398
0.2811	1285.9695	0.0117
0.2810	1285.9704	0.0284
0.2809	1285.9712	0.0175
0.2808	1285.9721	0.0127
0.2807	1285.9729	0.0212
0.2806	1285.9738	0.0490
0.2805	1285.9746	0.0410
0.2804	1285.9754	0.0387
0.2803	1285.9763	0.0240
0.2802	1285.9771	0.0115
0.2801	1285.9779	0.0142
0.2800	1285.9788	0.0138
0.2799	1285.9796	0.0098
0.2798	1285.9804	0.0323
0.2797	1285.9812	0.0093
0.2796	1285.9820	0.0328
0.2795	1285.9829	0.0143
0.2794	1285.9837	0.0076
0.2793	1285.9845	0.0001
0.2792	1285.9853	0.0097
0.2791	1285.9861	0.0175
0.2790	1285.9869	0.0038
0.2789	1285.9877	0.0076
0.2788	1285.9885	0.0036
0.2787	1285.9893	0.0002
0.2786	1285.9901	0.0001
0.2785	1285.9909	0.0050
0.2784	1285.9917	0.0029
0.2783	1285.9924	0.0102
0.2782	1285.9932	0.0031
0.2781	1285.9940	0.0067
0.2780	1285.9948	0.0232
0.2779	1285.9956	0.0112
0.2778	1285.9963	0.0036

Current / A	Wavenumber / cm^{-1}	Normalised signal / arbitrary units
0.2777	1285.9971	0.0080
0.2776	1285.9979	0.0052
0.2775	1285.9986	0.0126
0.2774	1285.9994	0.0002
0.2773	1286.0002	0.0066
0.2772	1286.0009	0.0260
0.2771	1286.0017	0.0006
0.2770	1286.0024	0.0071
0.2769	1286.0032	0.0010
0.2768	1286.0039	0.0130
0.2767	1286.0047	0.0067
0.2766	1286.0054	0.0083
0.2765	1286.0062	0.0066
0.2764	1286.0069	0.0101
0.2763	1286.0076	0.0051
0.2762	1286.0084	0.0067
0.2761	1286.0091	0.0074
0.2760	1286.0098	0.0067
0.2759	1286.0106	0.0026
0.2758	1286.0113	0.0082
0.2757	1286.0120	0.0034
0.2756	1286.0127	0.0038
0.2755	1286.0135	0.0020
0.2754	1286.0142	0.0081
0.2753	1286.0149	0.0039
0.2752	1286.0156	0.0029
0.2751	1286.0163	0.0167
0.2750	1286.0170	0.0073
0.2749	1286.0177	0.0143
0.2748	1286.0184	0.0052
0.2747	1286.0191	0.0080
0.2746	1286.0198	0.0035
0.2745	1286.0205	0.0050
0.2744	1286.0212	0.0041
0.2743	1286.0219	0.0033
0.2742	1286.0226	0.0098
0.2741	1286.0233	0.0030
0.2740	1286.0239	0.0054
0.2739	1286.0246	0.0001
0.2738	1286.0253	0.0004
0.2737	1286.0260	0.0005
0.2736	1286.0266	0.0068
0.2735	1286.0273	0.0005
0.2734	1286.0280	0.0000
0.2733	1286.0286	0.0163
0.2732	1286.0293	0.0032
0.2731	1286.0300	0.0025
0.2730	1286.0306	0.0016
0.2729	1286.0313	0.0008
0.2728	1286.0319	0.0142
0.2727	1286.0326	0.0022

Current / A	Wavenumber / cm^{-1}	Normalised signal / arbitrary units
0.2726	1286.0332	0.0030
0.2725	1286.0339	0.0162
0.2724	1286.0345	0.0040
0.2723	1286.0352	0.0020
0.2722	1286.0358	0.0000
0.2721	1286.0364	0.0072
0.2720	1286.0371	0.0064
0.2719	1286.0377	0.0005
0.2718	1286.0383	0.0054
0.2717	1286.0390	0.0049
0.2716	1286.0396	0.0181
0.2715	1286.0402	0.0130
0.2714	1286.0408	0.0093
0.2713	1286.0414	0.0037
0.2712	1286.0421	0.0000
0.2711	1286.0427	0.0116
0.2710	1286.0433	0.0061
0.2709	1286.0439	0.0002
0.2708	1286.0445	0.0108
0.2707	1286.0451	0.0007
0.2706	1286.0457	0.0089
0.2705	1286.0463	0.0001
0.2704	1286.0469	0.0148
0.2703	1286.0475	0.0031

Current / A	Wavenumber / cm^{-1}	Normalised signal / arbitrary units
0.2702	1286.0481	0.0142
0.2701	1286.0487	0.0062
0.2700	1286.0492	0.0131
0.2699	1286.0498	0.0001
0.2698	1286.0504	0.0115
0.2697	1286.0510	0.0006
0.2696	1286.0516	0.0009
0.2695	1286.0521	0.0007
0.2694	1286.0527	0.0010
0.2693	1286.0533	0.0309
0.2692	1286.0538	0.0218
0.2691	1286.0544	0.0052
0.2690	1286.0550	0.0021
0.2689	1286.0555	0.0050
0.2688	1286.0561	0.0071
0.2687	1286.0566	0.0230
0.2686	1286.0572	0.0089
0.2685	1286.0577	0.0067
0.2684	1286.0583	0.0013
0.2683	1286.0588	0.0170
0.2682	1286.0594	0.0009
0.2681	1286.0599	0.0183
0.2680	1286.0605	0.0112

Appendix 6: IR experiments investigating $CH_2OO + SO_2$ reaction

Tables summarising the conditions and results of all experiments carried out using time-resolved mid-IR QCL absorption spectroscopy to develop and characterise this experimental setup, determine kinetics of the $CH_2OO + SO_2$ reaction by monitoring both the CH_2OO reactant and the SO_3 product, and determine the SO_3 yield and hence absorption cross-section, as described in Chapter 6. Tables show the summary for all experiments at a single pressure, with experiments conducted at a total of 3 pressures in the range 20-100 Torr. All experiments were carried out at a temperature of 298 K.

For experiments monitoring CH_2OO, A_0 is the absorbance at time zero and k' is the pseudo-first-order rate coefficient for the reaction between $CH_2OO + SO_2$ at a particular $[SO_2]$. For experiments monitoring SO_3, A_0 is the maximum absorbance which relates to the initial radical concentration and yield of SO_3, k_{growth} is the pseudo-first-order rate coefficient for the reaction between $CH_2OO + SO_2$ at a particular $[SO_2]$ describing the growth of SO_3, and k_{loss} is the first-order rate

coefficient describing the loss of SO_3. For determination of the SO_3 IR absorption cross-section, assuming an SO_3 yield of unity for the reaction between $CH_2OO + SO_2$, the parameter A_0, which represents the absorbance relating to the total concentration of SO_3 produced, is equal to the product of the initial CH_2OO concentration, the SO_3 IR cross-section at the measurement wavenumber, and the effective path length of the IR probe beam. Following from this, normalisation of the parameter A_0 for the initial CH_2OO concentration at all pressures, A_0 / $[CH_2OO]_0$, provides information on the pressure dependence, if any, of the kinetics and product yields of the $CH_2OO + SO_2$ reaction. Furthermore, assuming an SO_3 yield of unity and with knowledge of the path length of the probe beam, A_0 / $[CH_2OO]_0$ also allows estimation of the IR absorption cross-section of SO_3 at the measurement wavenumber.

Data at 20 Torr monitoring CH_2OO

$[SO_2]$ / cm^{-3}	A_0	error	k' / s^{-1}	error
0.00E+00	0.00145	0.00001	559	6
1.17E+14	0.00124	0.00003	5555	203
1.71E+14	0.00109	0.00003	7094	251
2.11E+14	0.00095	0.00003	6613	295
2.56E+14	0.00153	0.00004	9463	309
3.40E+14	0.00086	0.00002	13983	512
4.26E+14	0.00109	0.00003	17276	482
4.67E+14	0.00106	0.00003	18072	544
5.31E+14	0.00141	0.00003	19555	457

Data at 50 Torr monitoring CH_2OO

$[SO_2]$ / cm^{-3}	A_0	error	k' / s^{-1}	error
0.00E+00	0.00168	0.00001	424	5
9.92E+13	0.00124	0.00002	2813	53
1.43E+14	0.00221	0.00002	5859	86
1.84E+14	0.00117	0.00004	10044	373
2.23E+14	0.00164	0.00004	9864	277
3.07E+14	0.00161	0.00002	12018	169
3.81E+14	0.00123	0.00003	16529	388
4.25E+14	0.00101	0.00003	15804	441
4.54E+14	0.00224	0.00003	19523	313
5.37E+14	0.00162	0.00003	19918	435

Data at 100 Torr monitoring CH_2OO

$[SO_2]$ / cm^{-3}	A_0	error	k' / s^{-1}	error
0.00E+00	0.00369	0.00001	505	5
1.03E+14	0.00152	0.00002	3199	58
1.50E+14	0.00236	0.00003	6362	122
1.89E+14	0.00104	0.00004	7828	362
2.29E+14	0.00132	0.00003	7218	264
3.07E+14	0.00110	0.00002	14722	369
3.84E+14	0.00095	0.00001	14729	204
4.18E+14	0.00080	0.00003	16408	674
4.55E+14	0.00158	0.00003	19660	404
5.27E+14	0.00228	0.00003	19513	265

Data at 20 Torr monitoring SO_3

$[SO_2]$ / cm^{-3}	A_0	error	k_{growth} / s^{-1}	error	k_{loss} / s^{-1}	error
1.03E+14	0.000217	0.000005	4390	320	-548	11
1.36E+14	0.000319	0.000009	6947	483	81	9
2.28E+14	0.000336	0.000014	6638	181	-266	9
3.18E+14	0.000468	0.000012	12908	458	-129	5
3.96E+14	0.000138	0.000013	17586	538	-237	31
5.71E+14	0.000750	0.000015	20041	965	196	6
6.49E+14	0.000270	0.000016	24205	1244	-257	13

Data at 50 Torr monitoring SO_3

$[SO_2]$ / cm^{-3}	A_0	error	k_{growth} / s^{-1}	error	k_{loss} / s^{-1}	error
9.34E+13	0.001230	0.000004	3961	47	394	10
1.39E+14	0.000403	0.000012	6095	169	288	9
2.14E+14	0.001090	0.000005	8248	65	298	6
2.95E+14	0.001600	0.000036	9423	88	203	4
4.37E+14	0.000645	0.000009	17741	489	279	7
5.80E+14	0.000675	0.000005	22662	493	898	13

Data at 100 Torr monitoring SO_3

$[SO_2]$ / cm^{-3}	A_0	error	k_{growth} / s^{-1}	error	k_{loss} / s^{-1}	error
9.55E+13	0.000961	0.000008	4007	83	3	6
1.40E+14	0.001500	0.000008	5425	74	334	6
2.15E+14	0.000994	0.000010	9007	171	21	3
2.86E+14	0.001050	0.000011	11526	219	-23	3

SO_3 yield and IR absorption cross-section

Pressure / Torr	$[CH_2I_2]$ / cm^{-3}	error	$[CH_2OO]_0$ / cm^{-3}	error	$[SO_2]$ / cm^{-3}	A_0	error	$A_0/[CH_2OO]_0$ / cm^3	error
20	8.70E+13	2.18E+13	3.10E+12	7.75E+11	1.03E+14	0.000217	0.000005	6.99E-17	1.75E-17
20	8.66E+13	2.16E+13	3.08E+12	7.71E+11	1.36E+14	0.000319	0.000009	1.03E-16	2.60E-17
20	8.54E+13	2.14E+13	3.04E+12	7.60E+11	2.28E+14	0.000336	0.000014	1.10E-16	2.80E-17
20	8.83E+13	2.21E+13	3.14E+12	7.86E+11	3.18E+14	0.000468	0.000012	1.49E-16	3.74E-17
20	8.73E+13	2.18E+13	3.11E+12	7.77E+11	3.96E+14	0.000138	0.000013	4.43E-17	1.18E-17
20	8.90E+13	2.23E+13	3.17E+12	7.93E+11	5.71E+14	0.000750	0.000015	2.37E-16	5.93E-17
20	8.80E+13	2.20E+13	3.14E+12	7.84E+11	6.49E+14	0.000270	0.000016	8.60E-17	2.21E-17
50	1.90E+14	4.75E+13	5.81E+12	1.45E+12	9.34E+13	0.001230	0.000004	2.12E-16	5.30E-17
50	1.92E+14	4.81E+13	5.89E+12	1.47E+12	1.39E+14	0.000403	0.000012	6.85E-17	1.72E-17
50	1.90E+14	4.75E+13	5.82E+12	1.45E+12	2.14E+14	0.001090	0.000005	1.87E-16	4.69E-17
50	1.96E+14	4.89E+13	5.99E+12	1.50E+12	2.95E+14	0.001600	0.000036	2.67E-16	6.71E-17
50	1.91E+14	4.78E+13	5.85E+12	1.46E+12	4.37E+14	0.000645	0.000009	1.10E-16	2.76E-17
50	1.91E+14	4.77E+13	5.84E+12	1.46E+12	5.80E+14	0.000675	0.000005	1.16E-16	2.89E-17
100	3.88E+14	9.69E+13	9.60E+12	2.40E+12	9.55E+13	0.000961	0.000008	1.00E-16	2.51E-17
100	3.85E+14	9.62E+13	9.53E+12	2.38E+12	1.40E+14	0.001500	0.000008	1.57E-16	3.94E-17
100	3.84E+14	9.61E+13	9.51E+12	2.38E+12	2.15E+14	0.000994	0.000010	1.04E-16	2.61E-17
100	3.80E+14	9.50E+13	9.40E+12	2.35E+12	2.86E+14	0.001050	0.000011	1.12E-16	2.79E-17

References

1. Lewis, T.; Heard, D. E.; Blitz, M. A., A novel multiplex absorption spectrometer for time-resolved studies. *Review of Scientific Instruments* **2018,** *89* (2), 024101.

2. Keller-Rudek, H.; Moortgat, G. K.; Sander, R.; Sörensen, R., The MPI-Mainz UV/VIS spectral atlas of gaseous molecules of atmospheric interest. *Earth System Science Data* **2013,** *5* (2), 365–373.

3. Harwood, M. H.; Burkholder, J. B.; Hunter, M.; Fox, R. W.; Ravishankara, A. R., Absorption cross sections and self-reaction kinetics of the IO radical. *The Journal of Physical Chemistry A* **1997,** *101* (5), 853-863.